



ISSN 1343-2230

CNS-REP-94
February, 2016

Annual Report 2014

Center for Nuclear Study,
Graduate School of Science, the University of Tokyo

Editors

Taku Gunji

Yukino Kishi

Center for Nuclear Study

CNS Reports are available from:

Wako-Branch at RIKEN

Center for Nuclear Study,

Graduate School of Science, the University of Tokyo

2-1 Hirosawa, Wako

351-0198, Japan

Tel: +81-48-464-4191

Fax: +81-48-464-4554

Annual Report 2014

Center for Nuclear Study,
Graduate School of Science, the University of Tokyo

Preface

This is the annual report of the Center for Nuclear Study (CNS), Graduate School of Science, the University of Tokyo, for the fiscal year 2014 (April 2014 through March 2015). During this period, a lot of research activities in various fields of nuclear physics have been carried out and a wide variety of fruitful results have been obtained at CNS. This report summarizes research such activities. I hereby mention some highlights of the report.

The Center for Nuclear Study (CNS) aims to elucidate the nature of nuclear system by producing the characteristic states where the Isospin, Spin and Quark degrees of freedom play central roles. These researches lead to the understanding of the matter based on common natures of many-body systems in various phases. We also aim at elucidating the explosion phenomena and the evolution of the universe by the direct measurements simulating nuclear reactions in the universe. In order to advance the nuclear science with heavy-ion reactions, we develop AVF upgrade, CRIB and SHARAQ facilities in the large-scale accelerators laboratories RIBF. We started a new project OEDO for a new energy-degrading scheme, where a RF deflector system is introduced to obtain a good quality of low-energy beam. We promote collaboration programs at RHIC-PHENIX and ALICE-LHC with scientists in the world. We also provide educational opportunities to young scientists in the heavy-ion science through the graduate course as a member of the department of physics in the University of Tokyo and through hosting the international summer school.

The NUSPEQ (NUclear SPectroscopy for Extreme Quantum system) group studies exotic structures in high-isospin and/or high-spin states in nuclei. The GRAPE (Gamma-Ray detector Array with Position and Energy sensitivity) is a major apparatus for high-resolution in-beam gamma-ray spectroscopy. Missing mass spectroscopy using the SHARAQ is used for another approach on exotic nuclei. In 2014, the following progress has been made. Experimental data taken in 2013 under the EURICA collaboration are being analyzed for studying octupole deformation in neutron-rich nuclei. Gamow-Teller transitions of ^8He were studied by the (p,n) reaction in inverse kinematics, where a prominent sharp peak at $E_x \sim 8$ MeV was found to be the Gamow-Teller resonance. Exochemic charge exchange reactions ($^8\text{He}, ^8\text{Li}^*(1+)$) on ^4He are being analyzed for studying spin-dipole response of few-body system on the photon line. The tetra-neutron system was studied by the $^4\text{He}(^8\text{He}, ^8\text{Be})4n$ reaction, which shows a candidate of the ground state of the tetra neutrons just above the $4n$ threshold as well as continuum at higher excitation energy. The readout system of 14 detectors of the GRAPE was upgraded, where digital pulse data taken by sampling ADCs are analyzed by FPGAs on boards.

The nuclear astrophysics group in CNS is working for experimental researches using the low-energy RI beam separator CRIB. The call for CRIB proposals at the NP-PAC has been resumed, and 3 new proposals have been approved in the NP-PAC meetings in the fiscal year 2014. In May 2014, a measurement of the elastic scattering of $^8\text{B}+\text{Pb}$ was performed in collaboration with INFN-LNL (Padova). It was made possible by the special development of intense and energy-enhanced ^6Li beam. A unique beam of ^8B at 50 MeV and 10^4 pps was produced, and the measurement was successfully completed.

Main goal of the quark physics group is to understand the properties of hot and dense nuclear matter created by colliding heavy nuclei at relativistic energies. The group has been involved in the PHENIX experiment at Relativistic Heavy Ion Collider (RHIC) at Brookhaven National Laboratory, and the ALICE experiment at Large Hadron Collider (LHC) at CERN. As for PHENIX, the group has been concentrating on the physics analysis involving leptons and photons; dielectron measurement in Au+Au collisions. As for ALICE, the group has involved in the data analyses, which include the measurements of low-mass dielectron pairs, charmed baryons, and long-range rapidity correlations. The group has involved in the ALICE-TPC upgrade using a Gas Electron Multiplier (GEM). Performance evaluation of the MicroMegas + GEM systems for the upgrade is performed.

The Exotic Nuclear Reaction group studies various exotic reactions induced by beams of unstable

nuclei. In 2014, a parity transfer probe of the (^{16}O , $^{16}\text{F}(\text{g.s.})$) reaction was demonstrated on ^{12}C at SHARAQ. The proton from the subsequent instant decay of $^{16}\text{F}(\text{g.s.}) \rightarrow ^{15}\text{F}+p$ was detected by a MWDC newly introduced. The kinematical reconstruction of ^{16}F was successful. At SAMURAI, a measurement of knockout reactions from Borromean nuclei, ^{11}Li and ^{14}Be was performed to study the two-neutron correlation. Analysis of the $^{22,24}\text{O}(p,2p)$ reaction data obtained in 2012 was almost finished and the spin-orbit splitting of proton $0p$ orbitals in ^{22}O was derived.

The OEDO/SHARAQ group promoted high-resolution experimental studies of RI beams by using the high-resolution beamline and SHARAQ spectrometer. The mass measurement by TOF-Br technique was performed for very neutron-rich calcium isotopes around $N=34$. For the experiment, we introduced new detector devices into the experiment. Diamond detectors, which were developed as timing counters with extreme resolution, were installed for measuring time of flight at the first and final foci of the beam line. Clover-type Ge detectors were installed at the final focal plane of the SHARAQ spectrometer for the first time, enabling particle identification of RI beams by probing delayed gamma rays from known isomeric states of specific nuclei. We have started ion optical development for achievement of high-quality RI beams with energies lower than 100 MeV/u. This project was named OEDO (Optimized Energy-Degrading Optics for RI beam) and the basic magnet arrangement and ion optics was discussed based on the existing high-resolution beamline and SHARAQ spectrometer.

In a project of active target development launched as an intergroup collaboration in 2009, two types of active target, called GEM-MSTPC and CAT, respectively, have been developed. The (α,p) reactions on ^{18}Ne , ^{22}Mg and ^{30}S , and the alpha emission following the beta decay of ^{16}N have been measured using GEM-MSTPC. The deuteron inelastic scattering off ^{132}Xe was measured by using the CAT with 106-particles-per-spill ^{132}Xe beam at HIMAC accelerator facility in Chiba.

One of the major tasks of the accelerator group is the AVF upgrade project that includes development of ion sources, upgrading the AVF cyclotron of RIKEN and the beam line to CRIB. Development of ECR heavy ion sources is to provide new HI beams, higher and stable beams of metallic ions, and to improve the control system. The Hyper ECR and the Super ECR sources provide all the beams for the AVF cyclotron and support not only CRIB experiments but also a large number of RIBF experiments. Injection beam monitoring and control are being developed. Detailed study of the optics from the ion sources are expected to improve transmission and qualities of beams for the RIBF facility.

The nuclear theory group has been promoting the CNS-RIKEN collaboration project on large-scale nuclear structure calculations since 2001 and maintaining its PC cluster. This group has revealed that the 4^{+1} of ^{44}S is high-K isomer, and discussed the deformation properties of the high-spin states of neutron-rich Cr and Fe isotopes utilizing shell-model calculations. A memorandum of understanding on this collaboration has been made between CNS and RIKEN in March 2014. In parallel, this group participated in activities of HPCI Strategic Programs for Innovative Research (SPIRE) Field 5 " The origin of matter and universe " since 2011.

The 13th CNS-EFES International Summer School (CNS-EFES14) has been organized in August 2014 with many invited lecturers including four foreign distinguished physicists.

Finally, I thank Mr. Yoshimura and other administrative staff members for their heartfelt contributions throughout the year.

Takaharu Otsuka
Director of CNS



Table of Contents

1a. Experimental Nuclear Physics: Low and Intermediate Energies

Development for re-measurement of isobaric analog resonances of ^{35}Si	3
<i>N. Imai, S. Hayakawa, Y. Hirayama, Y. Ichikawa, H.S. Jung, D. Kahl, S. Michimasa, H. Miya, H. Miyatake, S. Ota, S. Shimizu, S. Shimoura, T. Teranishi, H. Ueno, Y. Utsuno, Y.X. Watanabe, H. Yamaguchi, and K. Yoneda</i>	
The parity-transfer ($^{16}\text{O}, ^{16}\text{F}$) reaction for studies of the spin-dipole 0^- mode	5
<i>M. Dozono, T. Uesaka, K. Fujita, N. Fukuda, M. Ichimura, N. Inabe, S. Kawase, K. Kisamori, Y. Kiyokawa, K. Kobayashi, M. Kobayashi, T. Kubo, Y. Kubota, C. S. Lee, M. Matsushita, S. Michimasa, H. Miya, A. Ohkura, S. Ota, H. Sagawa, S. Sakaguchi, H. Sakai, M. Sasano, S. Shimoura, Y. Shindo, L. Stuhl, H. Suzuki, H. Tabata, M. Takaki, H. Takeda, H. Tokieda, T. Wakasa, K. Yako, M. Yamagami, Y. Yanagisawa, J. Yasuda, R. Yokoyama, K. Yoshida, and J. Zenihiro</i>	
Tetraneutron state populated by the $^4\text{He}(^8\text{He}, ^8\text{Be})$ reaction	7
<i>K. Kisamori, S. Shimoura, H. Miya, M. Assie, H. Baba, T. Baba, D. Beaumel, M. Dozono, T. Fujii, N. Fukuda, S. Go, F. Hammache, E. Ideguchi, N. Inabe, M. Itoh, D. Kameda, S. Kawase, T. Kawabata, M. Kobayashi, Y. Kondo, T. Kubo, Y. Kubota, M. Kurata-Nishimura, C. S. Lee, Y. Maeda, H. Matsubara, S. Michimasa, K. Miki, T. Nishi, S. Noji, S. Ota, S. Sakaguchi, H. Sakai, Y. Sasamoto, M. Sasano, H. Sato, Y. Shimizu, A. Stolz, H. Suzuki, M. Takaki, H. Takeda, S. Takeuchi, A. Tamii, L. Tang, H. Tokieda, M. Tsumura, T. Uesaka, K. Yako, Y. Yanagisawa and R. Yokoyama</i>	
Search for a double Gamow-Teller giant resonance in ^{48}Ti via heavy-ion double charge exchange ($^{12}\text{C}, ^{12}\text{Be}$) reaction	9
<i>M. Takaki, T. Uesaka, S. Shimoura, N. Aoi, M. Dozono, T. Furuno, C. Iwamoto, T. Kawabata, M. Kobayashi, Y. Matsuda, M. Matsushita, S. Michimasa, S. Ota, M. Sasano, L. Stuhl, A. Tamii, M. Tsumura, R. Yokoyama, and J. Zenihiro</i>	
Study of spin-dipole response of ^4He by using ($^8\text{He}, ^8\text{Li}^*(1^+)$) reaction	11
<i>H. Miya, S. Shimoura, K. Kisamori, M. Assie, H. Baba, T. Baba, D. Beaumel, M. Dozono, T. Fujii, N. Fukuda, S. Go, F. Hammache, E. Ideguchi, N. Inabe, M. Ito, D. Kameda, S. Kawase, T. Kawabata, M. Kobayashi, Y. Kondo, T. Kubo, Y. Kubota, C. S. Lee, Y. Maeda, H. Matsubara, S. Michimasa, K. Miki, T. Nishi, M. Kurata-Nishimura, S. Ota, H. Sakai, S. Sakaguchi, M. Sasano, H. Sato, Y. Shimizu, H. Suzuki, A. Stolz, M. Takaki, H. Takeda, S. Takeuchi, A. Tamii, H. Tokieda, M. Tsumura, T. Uesaka, K. Yako, Y. Yanagisawa, and R. Yokoyama</i>	
Direct mass measurements of neutron-rich Ca isotopes beyond $N = 34$	13
<i>M. Kobayashi, S. Michimasa, Y. Kiyokawa, H. Baba, G.P.A. Berg, M. Dozono, N. Fukuda, T. Furuno, E. Ideguchi, N. Inabe, T. Kawabata, S. Kawase, K. Kisamori, K. Kobayashi, T. Kubo, Y. Kubota, C.S. Lee, M. Matsushita, H. Miya, A. Mizukami, H. Nagakura, D. Nishimura, H. Oikawa, S. Ota, H. Sakai, S. Shimoura, A. Stolz, H. Suzuki, M. Takaki, H. Takeda, S. Takeuchi, H. Tokieda, T. Uesaka, K. Yako, Y. Yamaguchi, Y. Yanagisawa, R. Yokoyama, and K. Yoshida</i>	
Spectroscopic factors of $^{23,25}\text{F}(p,2p)$ reaction	15
<i>T. L. Tang, S. Kawase, T. Uesaka, D. Beaumel, M. Dozono, T. Fujii, N. Fukuda, T. Fukunaga, A. Galindo-Uribarri, S. H. Hwang, N. Inabe, D. Kameda, T. Kawahara, W. Y. Kim, K. Kisamori, M. Kobayashi, T. Kubo, Y. Kubota, K. Kusaka, C. S. Lee, Y. Maeda, H. Matsubara, S. Michimasa, H. Miya, T. Noro, A. Obertelli, S. Ota, E. Padilla-Rodal, S. Sakaguchi, H. Sakai, M. Sasano, S. Shimoura, S. S. Stepanyan, H. Suzuki, M. Takaki, H. Takeda, H. Tokieda, T. Wakasa, T. Wakui, K. Yako, Y. Yanagisawa, J. Yasuda, R. Yokoyama, K. Yoshida, J. Zenihiro, for SHARAQ04 collaboration</i>	
Spectroscopy of single-particle states in oxygen isotopes via $^4\text{O}(\vec{p}, 2p)$ reaction with polarized protons	17
<i>S. Kawase, T. L. Tang, T. Uesaka, D. Beaumel, M. Dozono, T. Fujii, N. Fukuda, T. Fukunaga, A. Galindo-Uribarri, S. H. Hwang, N. Inabe, D. Kameda, T. Kawahara, W. Kim, K. Kisamori, M. Kobayashi, T. Kubo, Y. Kubota, K. Kusaka, C. S. Lee, Y. Maeda, H. Matsubara, S. Michimasa, H. Miya, T. Noro, A. Obertelli, S. Ota, E. Padilla-Rodal, S. Sakaguchi, H. Sakai, M. Sasano, S. Shimoura, S. Stepanyan, H. Suzuki, M. Takaki, H. Takeda, H. Tokieda, T. Wakasa, T. Wakui, K. Yako, Y. Yanagisawa, J. Yasuda, R. Yokoyama, K. Yoshida, and J. Zenihiro</i>	
Investigation of the octupole correlations of neutron-rich $Z \sim 56$ isotopes by β - γ spectroscopy	19

R. Yokoyama, E. Ideguchi, G. Simpson, Mn. Tanaka, S. Nishimura, P. Doornenbal, P.-A. Söderström, G. Lorusso, Z.Y. Xu, J. Wu, T. Sumikama, N. Aoi, H. Baba, F. Bello, F. Browne, R. Daido, Y. Fang, N. Fukuda, G. Gey, S. Go, S. Inabe, T. Isobe, D. Kameda, K. Kobayashi, M. Kobayashi, T. Komatsubara, T. Kubo, I. Kuti, Z. Li, M. Matsushita, S. Michimasa, C.B. Moon, H. Nishibata, I. Nishizuka, A. Odahara, Z. Patel, S. Rice, E. Sahin, L. Sinclair, H. Suzuki, H. Takeda, J. Taprogge, Zs. Vajta, H. Watanabe, and A. Yagi

Experimental study on two-neutron correlation in Borromean nuclei via the (p, pn) reaction with the SAMURAI spectrometer 21

Y. Kubota, A. Corsi, G. Authelet, H. Baba, C. Caesar, D. Calvet, A. Delbart, M. Dozono, J. Feng, F. Flavigny, J.-M. Gheller, J. Gibelin, A. Gillibert, K. Hasegawa, T. Isobe, Y. Kanaya, S. Kawakami, D. Kim, Y. Kiyokawa, M. Kobayashi, N. Kobayashi, T. Kobayashi, Y. Kondo, Z. Korkulu, S. Koyama, V. Lapoux, Y. Maeda, F. M. Marqués, T. Motobayashi, T. Miyazaki, T. Nakamura, N. Nakatsuka, Y. Nishio, A. Obertelli, A. Ohkura, N. A. Orr, S. Ota, H. Otsu, T. Ozaki, V. Panin, S. Paschalis, E. C. Pollacco, S. Reichert, J.-Y. Roussé, A. Saito, S. Sakaguchi, M. Sako, C. Santamaria, M. Sasano, H. Sato, M. Shikata, Y. Shimizu, Y. Shindo, L. Stuhl, T. Sumikama, M. Tabata, Y. Togano, J. Tsubota, T. Uesaka, Z. Yang, J. Yasuda, K. Yoneda, and J. Zenihiro

Isomer spectroscopy in the vicinity of ^{54}Ca at SHARAQ 23

Y. Kiyokawa, S. Michimasa, M. Kobayashi, R. Yokoyama, D. Nishimura, A. Mizukami, H. Oikawa, K. Kobayashi, H. Baba, G.P.A. Berg, M. Dozono, N. Fukuda, T. Furuno, E. Ideguchi, N. Inabe, T. Kawabata, S. Kawase, K. Kisamori, T. Kubo, Y. Kubota, C.S. Lee, M. Matsushita, H. Miya, H. Nagakura, S. Ota, H. Sakai, S. Shimoura, A. Stolz, H. Suzuki, M. Takaki, H. Takeda, S. Takeuchi, H. Tokieda, T. Uesaka, K. Yako, Y. Yamaguchi, Y. Yanagisawa, and K. Yoshida

Interaction of ^8B , unstable-loosely-bound, with ^{208}Pb : scattering and breakup 25

C. Signorini, A. Boiano, C. Boiano, M. La Commara, C. Manea, M. Mazzocco, C. Parascandolo, D. Pierroutsakou, A.M. Sanchez-Benitez, E. Strano, D. Torresi, H. Yamaguchi, D. Kahl, Y. Hirayama, H. Ishiyama, N. Imai, N. Iwasa, S.C. Jeong, S. Kimura, Y.H. Kim, S. Kubono, H. Miyatake, M. Mukai, T. Nakao, Y. Sakaguchi, T. Teranishi, Y. Wakabayashi, Y.X. Watanabe, C.J. Lin, H.M. Jia, L. Yang and Y.Y. Yang

New resonances in ^{34}Ar via $^{30}\text{S}+\alpha$ elastic scattering 27

D. Kahl, A. A. Chen, S. Kubono, H. Yamaguchi, D. N. Binh, J. Chen, S. Cherubini, N. N. Duy, T. Hashimoto, S. Hayakawa, N. Iwasa, H. S. Jung, S. Kato, Y. K. Kwon, S. Michimasa, S. Nishimura, S. Ota, K. Setoodehnia, T. Teranishi, H. Tokieda, T. Yamada, C. C. Yun, L. Y. Zhang

Progress of analysis for searching for linear-chain cluster states in ^{14}C 29

Y. Sakaguchi, H. Yamaguchi, D. Kahl, T. Nakao, S. Hayakawa, A. Kim, D. H. Kim, P. S. Lee, S. M. Cha, K. Y. Chae, M. S. Gwak, J. H. Lee, Y. H. Kim

Momentum distribution of the α - ^{16}O inter-cluster motion in ^{20}Ne nucleus 31

S. Hayakawa, C. Spitaleri, N. Burtebayev, A. Aimaganbetov, P. Figuera, M. Fisichella, G. L. Guardo, S. Igamov, I. Indelicato, G. Kiss, S. Kliczewski, M. La Cognata, L. Lamia, M. Lattuada, E. Piasecki, G. G. Rapisarda, S. Romano, S. B. Sakuta, R. Siudak, A. Trzcińska, A. Tumino, and A. Urkinbayev

1b. Experimental Nuclear Physics: PHENIX Experiment at BNL-RHIC and ALICE Experiment at CERN-LHC

Upgrade of the TPC Readout Control Unit for Run2 35

T. Gunji, H. Hamagaki, Y. Sekiguchi, J. Alme, C. Zhao, T. Alt, L. Bratrud, F. Costa, E. David, T. Kiss, C. Lippmann, A. Ur Rehman

Heavy baryon measurements at LHC-ALICE 37

Y.S. Watanabe for the ALICE collaboration

Measurement of dielectrons from charm and bottom quark decays in p -Pb collisions with the ALICE detector 39

S. Hayashi, H. Hamagaki, and T. Gunji on behalf of the ALICE Collaboration

Two particle correlations of V^0 particles in p -Pb collisions with the ALICE detector 41

Y. Sekiguchi, H. Hamagaki, and T. Gunji for the ALICE Collaboration

Dielectron measurements in Au+Au collisions at $\sqrt{s_{NN}} = 200$ GeV using the PHENIX detector 43

2. Accelerator and Instrumentation

Construction of OEDO beamline	47
<i>S. Michimasa, S. Shimoura, M. Matsushita, N. Imai, H. Yamaguchi, S. Ota, E. Ideguchi, and K. Yamada</i>	
Simulation study of a new energy-degrading beamline, OEDO	49
<i>M. Matsushita, S. Shimoura, S. Michimasa, S. Ota, K. Yako, H. Yamaguchi, N. Imai, E. Ideguchi, and K. Yamada</i>	
High intensity heavy-ion beam injection in CNS Active Target (CAT) and measurement of $^{132}\text{Xe}(d,d')$	51
<i>S. Ota, C.S. Lee, H. Tokieda, Y.N. Watanabe, Y. Aramaki, M. Dozono, U. Garg, Y. Guputa, N. Imai, S. Kawakami, S. Kawase, Y. Kiyokawa, M. Kobayashi, Y. Kubota, M. Matsushita, S. Michimasa, N. Nakatsuka, T. Peach, R. Saiseau, M. Takaki, K. Wimmer, J. Zenihiro, E. Takada</i>	
Study of Track Finding Algorithm for CNS Active Target	53
<i>H. Tokieda, S. Ota, C. S. Lee, Y. N. Watanabe, and T. Uesaka</i>	
Pressure dependence and long-term stability of effective gas gain of THGEM in deuterium gas	55
<i>C. S. Lee, S. Ota, H. Tokieda, R. Kojima, Y.N. Watanabe, R. Saiseau, and T. Uesaka</i>	
Performance Evaluation of the MICROMEGAS for the Application of the TPC	57
<i>K. Terasaki, H. Hamagaki, and T. Gunji</i>	
Emittance measurement of mixed ion beam in Hyper ECR ion source	59
<i>Y. Ohshiro, Y. Kotaka, S. Watanabe, H. Muto, H. Yamaguchi, N. Imai and S. Shimoura</i>	
THE PEFFORMANCE OF PEEPER-POT EMITTANCE MONITOR	61
<i>Y. Kotaka, Y. Ohshiro, S. Watanabe, H. Muto, H. Yamaguchi, N. Imai, S. Shimoura, K. Kase, and K.Hatanaka</i>	
Observation of Ti getter pump effect by a grating monochromator	63
<i>H. Muto, Y. Ohshiro, Y. Kotaka, S. Yamaka, S. Watanabe, M. Oyaizu, H. Yamaguchi, K. Kobayashi, M. Nichimura, S. Kubono, M. Kase, T. Hattori, and S. Shimoura</i>	

3. Theoretical Nuclear Physics

Shell Model Study of Triaxial Deformation in Xenon and Barium Isotopes	67
<i>N. Shimizu, T. Otsuka, T. Mizusaki, Y. Utsuno, and M. Honma</i>	
Shell-model calculation for first-forbidden beta decay in neutron-rich K isotopes	69
<i>Y. Utsuno, N. Shimizu, T. Togashi, T. Otsuka, T. Suzuki, and M. Honma</i>	
Fundamentals of matrix element for neutrinoless double beta decay	71
<i>Y. Iwata, J. Menéndez, N. Shimizu, T. Otsuka, Y. Utsuno, M. Honma, T. Abe</i>	
Microscopic description of shell model Hamiltonian and neutron-rich nuclei	73
<i>N. Tsunoda, T. Otsuka, N. Shimizu</i>	
Study of unnatural-parity states in neutron-rich Cr and Fe isotopes by large-scale shell-model calculations	75
<i>T. Togashi, N. Shimizu, Y. Utsuno, T. Otsuka, and M. Honma</i>	
Structure of Be isotopes based on Monte Carlo shell model with $N_{\text{shell}} > 4$ model space	77
<i>T. Yoshida, N. Shimizu, T. Abe, and T. Otsuka</i>	

4. Other Activities

Laboratory exercise for undergraduate students	81
<i>S. Ota, K. Yako, M. Niikura, T. Miyazaki, S. Momiyama, H. Sakurai, S. Shimoura</i>	

The 13th CNS International Summer School (CNSSS14)	83
<i>S. Michimasa, Y. Iwata, S. Ota, T. Gunji, S. Shimoura, T. Otsuka, H. Sakai, H. Hamagaki, T. Nakatsukasa, H. Sakurai, N. Shimizu, T. Uesaka, Y. Utsuno, H. Utsunomiya, K. Yako, and N. Imai</i>	

Appendices

Symposium, Workshop, Seminar, PAC and External Review	87
CNS Reports	88
Publication List	89
Talks and Presentations	95
Personnel	102

Experimental Nuclear Physics: Low and Intermediate Energies

Development for re-measurement of isobaric analog resonances of ^{35}Si

N. Imai, S. Hayakawa, Y. Hirayama^a, Y. Ichikawa^b, H.S. Jung^a, D. Kahl, S. Michimasa, H. Miya, H. Miyatake^a, S. Ota, S. Shimizu, S. Shimoura, T. Teranishi^c, H. Ueno^b, Y. Utsuno^d, Y.X. Watanabe^a, H. Yamaguchi, and K. Yoneda^b

Center for Nuclear Study, Graduate School of Science, University of Tokyo
^aIPNS, KEK

^bRIKEN Nishina Center

^bDepartment of Physics, Kyushu University

^dASRC, JAEA

Isobaric analog resonance (IAR) is a well-known phenomenon of atomic nucleus. In the case of a neutron-rich nucleus, the IAR is observed at the un-bound region in isobaric nucleus. The IAR has the same configuration of the valence proton as that of the neutron in the parent state. Hence, if we can determine the wave function of the IAR, giving rise to the indirect determination of the configuration of the parent state. The IAR had been observed by measuring the excitation function of the proton elastic scattering at a given scattering angle by changing the proton energy with a small energy step.

We measured the proton resonance elastic scattering off ^{34}Si beams of about 5 MeV/nucleon under the inverse kinematic condition in order to observe the IARs of ^{35}Si [1], aiming to understand the single particle structure around the island of inversion. We observed eight resonances and identified six IARs among them. At that time, only four bound states were known via β decay studies [2] so that our experiment revealed the possible two bound states in ^{35}Si .

Recently, the experiment of $d(^{34}\text{Si},p)^{35}\text{Si}$ reaction was performed at GANIL [3]. The recoiled protons were measured in coincidence with the de-excitation γ rays. They observed three bound states which includes a new bound state of $l = 1$ around 2 MeV in ^{35}Si . The energy of the second $l = 1$ which is consistent with our measurement of the IARs. The spectroscopic factor S for the ground state of $f_{7/2}$ is also reproduced. However, the S for the two $l = 1$ states are found not to be consistent. Table 1 is our previous assignment of J^π and S together with the result of (d,p) reaction data. For the inconsistency of the first $l = 1$ state at $E^{pp} = 984$ keV, we guess that there is un-resolved resonance around the $l = 1$ IAR due to the bad energy resolution of 130 keV in the laboratory frame in our previous experiment. Concerning the second one, a recent shell model calculation predicts that there are three $l = 1$ states around 2 MeV. Their excitation energies are 2.0, 2.239, and 2.34 MeV. Their respective S are calculated to be 0.0027, 0.0579, 0.9304. According to the theory, the GANIL's data corresponds to the last one, while our S is consistent with either the first or the second one, suggesting that when we search for other resonances with wider energy range we may find another $l = 1$ resonance with a large S . To solve the inconsistency, we are going to measure the excitation function of $p(^{34}\text{Si},p)^{34}\text{Si}$ reaction in inverse kinematics with the better resolution and with the wider energy range of recoiled proton

In addition, in the next experiment we are also going to search for an inelastic channel of $p(^{34}\text{Si},p)^{34}\text{Si}(0_2^+)$. The second 0^+ state in ^{34}Si was discovered to be placed at the excitation energy of 2.719 MeV [4], which is located below

the first 2^+ state of 3.327 MeV. While the ground 0^+ state in ^{34}Si is regarded as spherical, the second 0^+ state is considered as deformed. Since the Coulomb penetrability to the second 0^+ state from IAR around $E_{ex}^{pp} \simeq 2$ MeV is reasonably large, we may have chance to see a large decay width to the second 0^+ state. If there is a large overlap between the IAR and the second 0^+ state, which may tell us about the shape co-existence in ^{35}Si . In fact, the inelastic channel of the IARs of ^{139}Ba was used to deduce S between the IAR and the first 2^+ state in ^{138}Ba [5]. Since the overlap of a neutron bound state relative to the excited core state is not feasible for (d,p) reaction. The next experiment would provide us unique physical quantity.

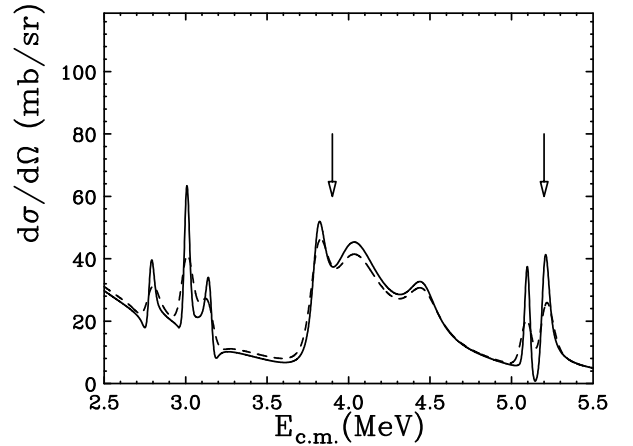


Figure 1: Excitation function of the proton resonance elastic scattering off ^{34}Si in the previous experiment (dashed line). The excitation function expected for the next experiment (solid line). The arrows indicate the resonance energies which were assigned as $l = 1$ in our last experi-

One of the causes of the bad resolution in the previous experiment was attributed to the energy resolution of the Micron Pad type detector of 1.5 mm thickness. We developed a system to cool the guard ring of the SSD by using a chiller of ethanol of 5 degrees in Celsius. The SSD is attached to a cooled aluminum frame via electrically non-conductive but thermally conductive material. Using the cooling, the 32 keV energy resolution is achieved for ^{241}Am standard α source. In the next experiment, we may observe protons of around 20 MeV with 60 keV energy resolution in total, which is about half of the previous resolution. Figure 1 compares the expected excitation function with the previous our experimental result. The arrows indicate the resonance energies which were assigned as $l = 1$ in our last experi-

Table 1: Parameters of eight resonances obtained by R -matrix analysis assuming the angular momenta listed in the second column. The third column represents the energy difference relative to the second resonance which is regarded as the IAR of the ground state in ^{35}Si . The fourth and fifth column stand for the proton width and the total widths, respectively. The $S^{p,p}$ shows the spectroscopic factor deduced from the IAR while the $S^{d,p}$ represent those by (d,p) reaction.

No.	l	E_R (keV)	E_{ex}^{pp} (keV)	Γ_p (keV)	Γ_{total} (keV)	$S^{p,p}$ [1]	$S^{d,p}$ [3]
1	0	2783(24)	-223(24)	4.6(28)	4.6(81)	0.04(2)	-
2	3	3006(2)	0.0	1.6(4)	1.6(28)	0.63(16)	0.56(6)
3	2	3151(24)	145(24)	3.3(27)	10.4(203)	0.19(15)	-
4	2	3809(18)	803(18)	26.7(69)	84.0(250)	0.79(20)	-
5	1	3990(36)	984(36)	184.8(430)	353.8(867)	1.37(32)	0.69(10)
6	0	4450(44)	1444(44)	58.4(367)	215.4(1513)	0.45(28)	-
7	2	5099(12)	2093(12)	3.8(9)	3.8(78)	0.04(1)	-
8	1	5200(15)	2194(15)	20.9(123)	32.0(224)	0.12(7)	0.73(10)

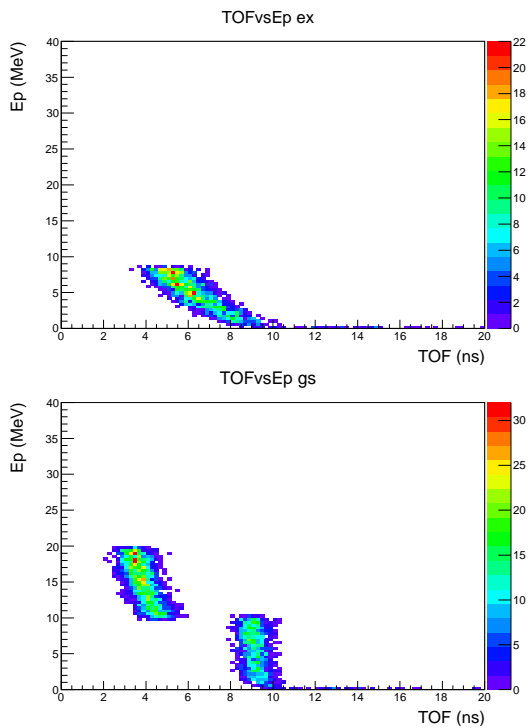


Figure 2: (Down panel) E_p (Yaxis) vs ToF (Xaxis) for the elastic channel. (Upper) E_p (Yaxis) vs ToF (Xaxis) for the inelastic channel.

ment. To expand the dynamic range of the recoiled protons, we increase the number of layers of telescope from three to four. As a result, the thickness in total varies from 3.5 mm to 4.3 mm. With the telescope, we can measure the protons upto 27 MeV ($E_{c.m} = 6.75$ MeV).

We will divide the polyethylene target to two lasers, 50 and 150 μm in order to distinguish the inelastic channel from the elastic one. The thinner one will be placed at the original target position, while the thicker one will be placed in front of the SSD telescope, which is 20 cm downstream from the first target. Due to the difference between the velocity of the ^{34}Si beam and that of recoiled proton, we can distinguish the inelastic and elastic channel by selecting the incident beam energy. Figure 2 shows the simulated correlation between the proton energies and the TOF of the protons after the beam hits the first target for the

5 ± 1 MeV/nucleon ^{34}Si beam. When the IAR decays to the ground state, there is no event from 5 to 8.5 ns. Whereas, in the case of the decay to the second 0^+ state, there are events from 5 to 8.5 ns. The time resolution of SSD of 1 ns (σ) is taken into account the simulation. The simulation demonstrates that we can distinguish the inelastic channels from the elastic channel.

References

- [1] N. Imai *et al.*, Phys. Rev. C **85**, 034313 (2012).
- [2] S. Nummela *et al.*, Phys. Rev. C **63**, 044316 (2001).
- [3] G. Burgeunder *et al.*, Phys. Rev. Lett. **112**, 042502 (2014).
- [4] F. Rotaru *et al.*, Phys. Rev. Lett. **109**, 092503 (2012).
- [5] S.A.A. Zaidi, P.Von Brentano, D. Rikek, and J.P. Wurn, Physics Letters **19**, 45 (1965).

The parity-transfer (^{16}O , ^{16}F) reaction for studies of the spin-dipole 0^- mode

M. Dozono, T. Uesaka^a, K. Fujita^b, N. Fukuda^a, M. Ichimura^a, N. Inabe^a, S. Kawase, K. Kisamori, Y. Kiyokawa, K. Kobayashi^c, M. Kobayashi, T. Kubo^a, Y. Kubota, C. S. Lee, M. Matsushita, S. Michimasa, H. Miya, A. Ohkura^b, S. Ota, H. Sagawa^{a,d}, S. Sakaguchi^b, H. Sakai^a, M. Sasano^a, S. Shimoura, Y. Shindo^b, L. Stuhl^a, H. Suzuki^a, H. Tabata^b, M. Takaki, H. Takeda^a, H. Tokieda, T. Wakasa^b, K. Yako, M. Yamagami^d, Y. Yanagisawa^a, J. Yasuda^b, R. Yokoyama, K. Yoshida^a, and J. Zenihiro^a

Center for Nuclear Study, Graduate School of Science, University of Tokyo

^aRIKEN Nishina Center

^bDepartment of Physics, Kyushu University

^cRikkyo University

^dCenter for Mathematics and Physics, University of Aizu

Spin-dipole (SD) states excited with $\Delta L = 1$, $\Delta S = 1$, and $\Delta J^\pi = 0^-, 1^-, 2^-$, have recently attracted theoretical attention owing to its strong relevance in the tensor correlations in nuclei. For example, self-consistent HF+RPA calculations in Ref. [1] predict that the tensor correlations produce a strong hardening (shifting toward higher excitation energy) effect on the 0^- resonance. It is also predicted that the effect is sensitive to the magnitude of the tensor strength. Thus experimental data of the SD 0^- distribution enable us to examine the tensor correlation effects quantitatively.

In spite of its interesting properties described above, experimental information on 0^- states is limited. This is because, as a recent polarization transfer experiment for the $^{208}\text{Pb}(p, n)$ reaction shows [2], 0^- states are populated only weakly compared with 1^- and 2^- states and they are strongly fragmented over a wide range of excitation energy. A well-suited experimental tool to probe the 0^- states is definitely desired.

We propose a new probe, the parity-transfer (^{16}O , $^{16}\text{F}(0^-, \text{g.s.})$) reaction, for 0^- studies [3]. The parity-transfer reaction selectively excites unnatural-parity states for a 0^+ target nucleus, which is an advantage over the other reactions used thus far. In order to establish the parity-transfer reaction as a new tool for 0^- studies, we measured the $^{12}\text{C}(^{16}\text{O}, ^{16}\text{F}(0^-, \text{g.s.}))^{12}\text{B}$ reaction. We demonstrate the effectiveness of this reaction by identifying the known 0^- state at $E_x = 9.3$ MeV in ^{12}B [4].

The experiment was performed at the RIKEN RI Beam Factory (RIBF) by using the SHARAQ spectrometer and the high-resolution beam line. Figure 1 shows a schematic layout of the experimental setup. A primary ^{16}O beam at 250 MeV/nucleon and 10^7 pps from the superconducting RING cyclotron (SRC) was transported to the S0 target position. The beam line to the spectrometer was set up for dispersion-matched transport. We used a segmented plastic scintillation detector as an active ^{12}C target. This detector consisted of 16 plastic scintillators with a size of $30 \text{ mm} \times 5 \text{ mm} \times 1 \text{ mm}$, and it was used to determine the x -position of the beam on the target. The outgoing $^{15}\text{O} + p$ particles produced by the decay of ^{16}F were measured in coincidence. The particles were momentum analyzed by using the SHARAQ spectrometer. The ^{15}O particles were detected with two low-pressure multi-wire drift chambers (LP-MWDCs) [5] at the S2 focal plane, while the protons were detected with two MWDCs [6] at the S1 focal plane, which has been newly designed and located at

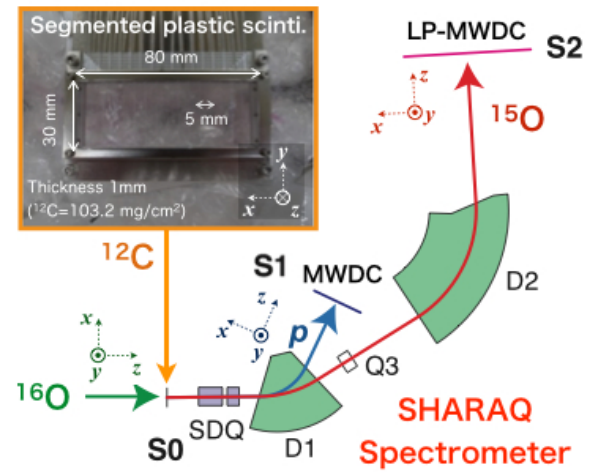


Figure 1: Schematic layout of the experimental setup.

the low-momentum side of the exit of the first dipole magnet.

In order to study the ion-optical properties between S0 and S1, the data for a proton beam were also taken. A secondary proton beam was produced by the BigRIPS using a primary ^{16}O beam in a 4-mm thick Be target. We measured the beam trajectories from S0 to S1 by using LP-MWDCs at S0 and MWDCs at S1. The transfer matrix elements from S0 to S1 were obtained by the correlations of the measured beam trajectories at S0 and S1. For example, a correlation between the horizontal angle at S0 (a_{S0}) and the horizontal angle at S1 (a_{S1}) provides us with a measure of the $\langle a|a \rangle$ element. The left panel in Fig. 2 shows the correlation between a_{S1} and a_{S0} . The gradient of the correlation corresponds to the $\langle a|a \rangle$ element. The second order gradient is also seen, which corresponds to the $\langle a|aa \rangle$ element. Thus, $\langle a|a \rangle = -3.03$ rad/rad and $\langle a|aa \rangle = -24$ rad/rad² are obtained in this case. We also determined the δ dependent terms of the matrix elements by scaling the magnet field of the spectrometer because scaling of the magnet field changes δ effectively. The right panel in Fig. 2 shows the a_{S1} - a_{S0} correlations for various magnetic field settings. Five loci in the figure represent the events for scaling factors of 0.930, 0.965, 1.000, 1.035, and 1.070, which correspond to $\delta = +7.0\%$, $+3.5\%$, 0.0% , -3.5% , -7.0% , respectively. The difference of the gradients between the five loci is due

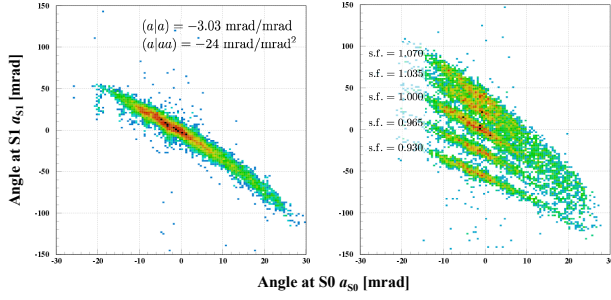


Figure 2: Correlation between the angle at the focal plane S1 and the angle at the focal plane S0 for a proton beam.

	x	a	y
$(x x)$	-0.35	$(a x)$ -1.43	$(y y)$ -9.55
	(-0.36)	(-1.53)	(-9.00)
$(x a)$	0.01	$(a a)$ -3.03	$(y b)$ -4.70
	(0.00)	(-2.75)	(-4.50)
$(x \delta)$	-1.57	$(a \delta)$ -0.70	
	(-1.56)	(-0.75)	
$(x aa)$	0.80	$(a aa)$ -24	$(y ab)$ -36
$(x a\delta)$	0.40	$(a a\delta)$ 11	$(y y\delta)$ 34
$(x \delta\delta)$	-7.3	$(a \delta\delta)$ 1.5	$(y b\delta)$ 24
$(x aaa)$	-820	$(a aad)$ 80	$(y ab\delta)$ 230
$(x a\delta\delta)$	-57	$(a a\delta\delta)$ -12	$(y b\delta\delta)$ 24
$(x \delta\delta\delta)$	-29	$(a \delta\delta\delta)$ 7.8	

Table 1: Measured transfer matrix elements from S0 to S1. For the first order terms, the design values are also shown in the parentheses. Units for lengths and angles are in meter and radian, respectively.

to the matrix elements such as $(a|a\delta)$ and $(a|aa\delta)$. The matrix elements such as $(a|\delta)$ and $(a|\delta\delta)$ are also obtained from the shift of the a_{S1} positions at $a_{S0} = 0$ mrad.

Table 1 summarize the measured matrix elements from S0 to S1. For the first order terms, the measured matrix elements are in good agreement with the design values, which were obtained from ion-optical calculations with COSY INFINITY [7], in the parentheses. It was also found that the effects of the higher order terms are sufficiently large to change the trajectories, and that these effects should be correctly taken into account.

We are now analyzing the $(^{16}\text{O}, ^{16}\text{F})$ data by using the measured transfer matrix elements in Table 1. Fig. 3 shows the preliminary result of the relative energy E_{rel} between the ^{15}O and the proton. The obtained E_{rel} resolution was 150 keV in FWHM at $E_{\text{rel}} = 535$ keV, and the 0^- g.s. of ^{16}F was clearly separated from other excited states. In order to identify the $^{12}\text{B}(0^-, 9.3 \text{ MeV})$ state, the data analysis for obtaining the $^{12}\text{C}(^{16}\text{O}, ^{16}\text{F}(0^-, \text{g.s.}))$ spectrum and its angular distributions is in progress.

References

- [1] H. Sagawa and G. Colò, Prog. Part. Nucl. Phys. **76**, 76 (2014).
- [2] T. Wakasa *et al.*, Phys. Rev. C **85**, 064606 (2012).
- [3] M. Dozono *et al.*, RIKEN Accel. Prog. Rep. **45**, 10 (2012).
- [4] H. Okamura *et al.*, Phys. Rev. C **66**, 054602 (2002).
- [5] H. Miya *et al.*, Nucl. Instr. Meth. B **317**, 701 (2013).

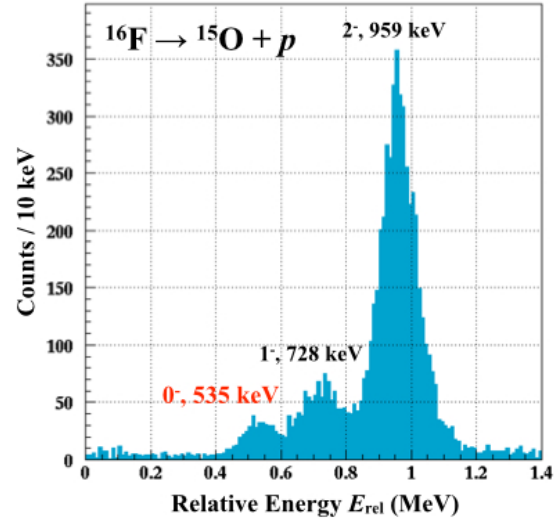


Figure 3: Preliminary result of the relative energy between the ^{15}O nucleus and the proton from the decay of ^{16}F .

[6] M. Dozono *et al.*, RIKEN Accel. Prog. Rep. **47**, 22 (2014).

[7] K. Makino *et al.*, Nucl. Instr. Meth. A **558**, 346 (2006).

Tetraneutron state populated by the ${}^4\text{He}({}^8\text{He}, {}^8\text{Be})$ reaction

K. Kisamori, S. Shimoura, H. Miya, M. Assie^a, H. Baba^b, T. Baba^c, D. Beaumel^a, M. Dozono^b, T. Fujii, N. Fukuda^b, S. Go, F. Hammache^a, E. Ideguchi^d, N. Inabe^b, M. Itoh^e, D. Kameda^b, S. Kawase, T. Kawabata^c, M. Kobayashi, Y. Kondo^f, T. Kubo^b, Y. Kubota, M. Kurata-Nishimura^b, C. S. Lee, Y. Maeda^g, H. Matsubara^k, S. Michimasa, K. Miki^d, T. Nishi^h, S. Nojiⁱ, S. Ota, S. Sakaguchi^j, H. Sakai^b, Y. Sasamoto, M. Sasano^b, H. Sato^b, Y. Shimizu^b, A. Stolz^a, H. Suzuki^b, M. Takaki, H. Takeda^b, S. Takeuchi^b, A. Tamii^d, L. Tang, H. Tokieda, M. Tsumura^c, T. Uesaka^b, K. Yako, Y. Yanagisawa^b and R. Yokoyama

Center for Nuclear Study, Graduate School of Science, University of Tokyo

^aIPN, Orsay, France

^bRIKEN (The Institute of Physical and Chemical Research)

^cDepartment of Physics, Kyoto University

^dResearch Center Nuclear Physics, Osaka University

^eCyclotron and Radioisotope Center, Tohoku University

^fDepartment of Physics, Tokyo Institute of Technology

^gFaculty of Engineering, University of Miyazaki

^hDepartment of Physics, University of Tokyo

ⁱNational Superconducting Cyclotron Laboratory, Michigan State University, USA

^jFaculty of Sciences, Kyushu University

^kNational Institute of Radiological Sciences

Since the report on candidates of a bound tetraneutron system [1], multi-neutron systems in nuclei have attracted considerable attention on both the experimental and theoretical fronts. On the other hand, later theoretical studies using *ab-initio* calculations [2] have suggested that the tetraneutron cannot exist as a bound system but possibly as a resonance system.

We performed missing-mass spectroscopy of the tetraneutron system via the exothermic double-charge exchange (DCX) reaction ${}^4\text{He}({}^8\text{He}, {}^8\text{Be})$ [3]. In order to produce the tetraneutron system with a small momentum transfer of less than 20 MeV/c, a secondary beam of ${}^8\text{He}$ with a large internal energy was used. The experiment was performed at the RIKEN RI Beam Factory (RIBF) using the SHARAQ spectrometer and a liquid He target system [4]. We measured the momentum of the ${}^8\text{He}$ beam at BigRIPS-F6 with the High-Resolution Beamline and the momenta of two alpha particles, which were the decay products of the ${}^8\text{Be}$ ejectile, with the SHARAQ spectrometer. The incident beam energy of ${}^8\text{He}$ was 186 MeV/u.

Events resulting from the ${}^4\text{He}({}^8\text{He}, {}^8\text{Be})$ reaction were selected. Two α particles from the ${}^8\text{Be}$ ejectile were detected simultaneously at the final focal plane of the SHARAQ spectrometer. Furthermore, a method to reconstruct trajectories for more than two particles under a high-intensity beam (~ 2 MHz) was developed [5]. In order to obtain a good signal-to-noise ratio, it was important to identify multi-particles in one bunch, which have the possibility to create the background events. These events were rejected using the Multi-Wire Drift Chamber (MWDC) at F6.

We obtained the missing-mass spectrum of a tetraneutron system, as shown in Fig. 1 (a). The spectrum contains 27 events including background events. The missing mass of tetraneutron E_{4n} was calculated on an event-by-event basis from the momentum of ${}^8\text{He}$ and the sum of the two α particles. The background events were estimated from the the

number of events that was not identified as multi-particle in one bunch in the MWDC at F6. There were only 2.2 ± 1.0 events in the whole spectrum region, which is almost negligible compared to the selected 27 events. The shape of the background was reconstructed by selecting two independent single- α events identified at S2 at random. The dashed line (blue) in Fig. 1 (a) represents the estimated background magnified by 10 times for visualization. The missing-mass spectrum was calibrated using the peak position of the ${}^8\text{Li}(1^+)$ state and the scale of magnetic rigidity of the SHARAQ spectrometer. ${}^8\text{Li}$ was produced by the inverse kinematics of the (p, n) reaction of ${}^8\text{He}$. The systematic error of the energy was 1.3 MeV at the one sigma level. The experimental resolution of the spectrum was 1.2 MeV at the one sigma level.

Two components are clearly observed in this spectrum in spite of the relatively low statistics. One is the broad continuum in the $E_{4n} > 2$ MeV region, whereas the other is the peak at the low-energy region $0 < E_{4n} < 2$ MeV. To interpret this spectrum, we employed two different types of states. One is the direct decay with the final-state interaction between the two correlated neutron pairs. This direct decay contributes to the continuum in the spectrum. The other is a possible resonant state of the tetraneutron system.

The continuum spectrum was calculated taking into account the initial structure of the target nuclei, reaction mechanism, few-body effects, and final-state interaction in the studies of unbound states for analyzing the present data were all incorporated in the calculation. After the DCX reaction of ${}^4\text{He}$, the four-neutron wave packet with the angular momentum $J = 0$ is assumed to be $\Phi[(0s)^2(0p)^2]$. The final-state interactions between the two neutrons in the ${}^1\text{S}_0$ neutron pair (dineutron) and between the two dineutrons were also considered. The experimentally observed distribution at approximately 30 MeV was well reproduced

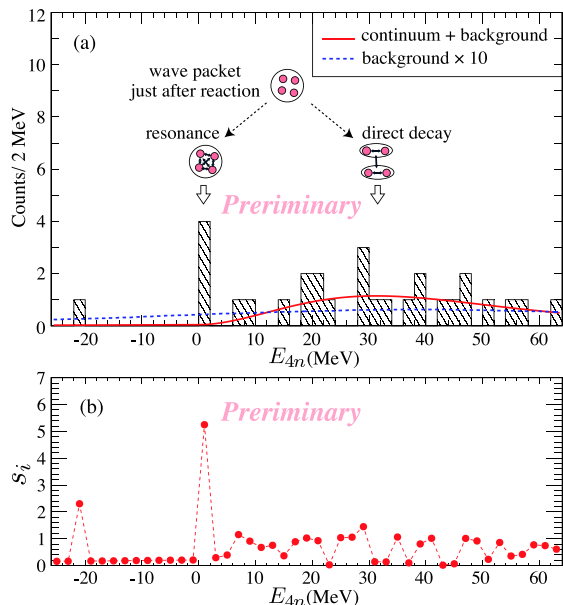


Figure 1: (a) Missing-mass spectrum of the tetraneutron system. The solid (red) curve represents the sum of the direct decay of correlated two-neutron pairs and estimated background. The dashed (blue) curve represents the estimated background multiplied by a factor of 10. (b) Evaluation of the goodness-of-fit for each bin using the likelihood ratio test. The s_i were defined in the text.

by the calculation. Note that contributions from the non-resonant direct decay to dineutron pairs are very small near the threshold.

To demonstrate the significance of the yields near the threshold, we fitted the experimental data with a trial function assuming the absence of the resonant state and estimated the goodness-of-fit with a statistical analysis. The trial function is defined as

$$af_{\text{cont}}(E_{4n}) + f_{\text{BG}}(E_{4n}),$$

where $f_{\text{cont}}(E_{4n})$ is the continuum obtained by the theoretical calculation described above, $f_{\text{BG}}(E_{4n})$ is the estimated experimental background, and a is the parameter for a factor of the continuum. We fitted the data such that the likelihood ratio test [6] was minimized. Figure 1 (b) shows the bin-by-bin goodness-of-fit s_i defined as

$$s_i = \sqrt{2[y_i - n_i + n_i \ln(n_i/y_i)]},$$

where n_i is the number of events in the i -th bin and y_i is the number of events predicted by the trial function in the i -th bin. An enhancement of $s_i = 5.2$ at $0 < E_{4n} < 2$ MeV can be clearly observed. This clear disagreement between the fitted curve and experimental data means that events at $0 < E_{4n} < 2$ MeV can be hardly explained by the direct decay to dineutron pairs and can be a candidate of state of tetraneutron system because the fitted curve assumes no resonant state. Except for the $0 < E_{4n} < 2$ MeV region, the s_i is consistent with the statistical distribution. The event at $-22 < E_{4n} < -20$ MeV is considered to be the contribution from the experimental background because an upper limit of the binding energy is 3.1 MeV provided by the particle stability of ${}^8\text{He}$, which does not decay into $\alpha + {}^4\text{n}$.

To estimate the significance of the peak at $0 < E_{4n} < 2$ MeV more carefully, we considered the “look elsewhere effect” [7]. The significance of observing a local excess of events should be obtained by considering the probability that such an excess originated from fluctuations of the continuum elsewhere in the region. According to this evaluation, the significance of the peak at low energies was 4.9σ , indicating that a contribution other than the continuum and experimental background is needed.

In conclusion, the four events in the $0 < E_{4n} < 2$ MeV region are the candidates for a resonant state of the tetraneutron system. Because of the small contribution of the continuum and experimental background, the significance level of the peak is 4.9σ compared with the continuum that assumes no resonant state. The mean energy of the events is evaluated to be 0.8 ± 0.7 MeV with an additional systematic uncertainty of 1.3 MeV due to that in the missing mass calibration. The upper limit of width of the peak is estimated to be 2.6 MeV (FWHM) which is mainly determined by the experimental missing-mass resolution. The cross section of the peak is estimated to be $3.8^{+2.9}_{-1.8}$ nb for integration up to $\theta_{\text{CM}} < 5.4^\circ$, where the θ_{CM} is the scattering angle in the center-of-mass system of the DCX reaction.

References

- [1] F. Marques *et al.*, Phys. Rev. C **65**, 044006 (2002).
- [2] S. Pieper, Phys. Rev. Lett. **90**, 252501 (2003).
- [3] K. Kisamori *et al.*, CNS Ann. Rep. 2011 (2013).
- [4] M. Kurata-Nishimura *et al.*, Accelerator Progress Rep. **46** (2013).
- [5] K. Kisamori *et al.*, CNS Ann. Rep 2012 (2014).
- [6] S. Baker *et al.*, Nucl. Inst. and Meth. in Phys. Res. **221**, 437 (1984).
- [7] E. Gross and O. Vitells, The Euro. Phys. Jour. C **70**, 525 (2010).

Search for a double Gamow-Teller giant resonance in ^{48}Ti via heavy-ion double charge exchange ($^{12}\text{C}, ^{12}\text{Be}$) reaction

M. Takaki, T. Uesaka^a, S. Shimoura, N. Aoi^b, M. Dozono, T. Furuno^c, C. Iwamoto^b, T. Kawabata^c,
M. Kobayashi, Y. Matsuda^d, M. Matsushita, S. Michimasa, S. Ota, M. Sasano^a, L. Stuhl^a,
A. Tamii^b, M. Tsumura^c, R. Yokoyama, and J. Zenihiro^a

Center for Nuclear Study, Graduate School of Science, University of Tokyo

^a*RIKEN (The Institute of Physical and Chemical Research)*

^b*Research Center for Nuclear Physics, Osaka University*

^c*Department of Physics, Kyoto University*

^d*Department of Physics, Konan University*

Among two-phonon excitation modes in atomic nuclei [1], a double Gamow-Teller resonance (DGTR) is a missing piece for better understanding the mechanism of two-phonon states in terms of the nuclear spin-dependent correlations. Experimental observation of the DGTR will pin down if the DGT transitions are just superpositions of single GT excitations, or, if the correlations cause further changes to structures and responses of DGT states.

Relevances to the $\beta\beta$ -decay make the DGTR study more stimulating. Both DGT transitions and the $2\nu\beta\beta$ -decay are driven by the spin-isospin operator, $\sigma\tau\sigma\tau$. As one can find from its quite long half-life [2], the $2\nu\beta\beta$ -decay covers only a small portion of about $10^{-4} - 10^{-3}$ for a total DGT strength. On the other hand, the most of the strength should concentrate in the DGTR, and thus the DGTR will provide fruitful information on *double* spin-isospin properties of nuclei.

The possible existence of the DGTR was first proposed by Auerbach, Zamick and Zheng in 1989 [3]. However, conclusive experimental signatures were not obtained so far. Observation of DGT transitions will be difficult because there are no simple probes. The DGT transitions are characterized by quantum numbers of $\Delta L = 0$, $\Delta S = 0$ or 2, and $\Delta T = 2$. Thus, a spin-flip isotensor probe is necessary. Particularly for a collective DGTR search, a $\beta^-\beta^-$ type probe is much more effective for medium or heavy nuclei appearing large collectivity, while a $\beta^+\beta^+$ type probe excites DGT states only weakly due to the Pauli blocking [4].

In 2011, we conducted a HIDCX $^{12}\text{C}(^{18}\text{O}, ^{18}\text{Ne})^{12}\text{Be}$ reaction experiment and found a large cross section for the second 0^+ (0_2^+) state in ^{12}Be at 0^+ [5]. This is probably because all the initial $^{12}\text{C}(0_{g.s.}^+)$, intermediate $^{12}\text{B}(1_{g.s.}^+)$, and final $^{12}\text{Be}(0_2^+)$ states are dominated by a $0\hbar\omega$ configuration [6–8], and consequently we can expect relatively large cross section of the DGT excitation. This is hardly satisfied in other stable beam induced reactions. This result led us to have a new idea to use the ($^{12}\text{C}, ^{12}\text{Be}(0_2^+)$) reaction as a probe to investigate DGTRs. The probe has another remarkable advantage: identification of the ($^{12}\text{C}, ^{12}\text{Be}(0_2^+)$) reaction event is possible by detecting the delayed γ -rays from the $^{12}\text{Be}(0_2^+)$ state. Figure 1 shows the level scheme of ^{12}Be below the neutron threshold. The $^{12}\text{Be}(0_2^+)$ state is known as a long life isomer with a lifetime of 331 ns [9]. The long lifetime enables us to detect the decay γ -rays downstream of a focal plane of a spectrometer. This makes an experiment feasible because a γ -ray background level should be lower than that around a target position. Moreover, the decay of the $^{12}\text{Be}(0_2^+)$ state is predominantly by the e^+e^- de-

cay which emits two 511-keV γ -rays back-to-back resulting from the positron annihilation. These γ -rays emitted back-to-back should provide a better signal-to-noise ratio.

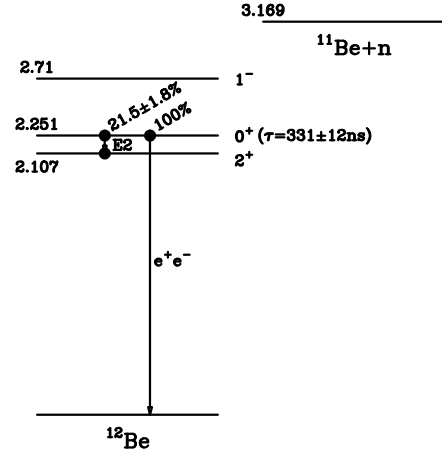


Figure 1: Level scheme of ^{12}Be below the neutron threshold and the decay property of the $^{12}\text{Be}(0_2^+)$ state [9].

As a first physics case, we have applied the method to ^{48}Ca to search for the DGTR in ^{48}Ti . The experiment was performed by using a magnetic spectrometer, Grand Raiden (GR), at RCNP, Osaka University. A 10 mg/cm² ^{48}Ca was bombarded with a primary ^{12}C beam with an incident energy of 100 MeV/nucleon. An average beam intensity was 17 pA. Outgoing particles were momentum-analyzed by GR and detected with two drift chambers for tracking and two plastic scintillators for ΔE and timing. Excitation energies of residual nuclei were measured by a missing mass method. ^{12}Be was implanted in a plastic scintillator stopper placed 1-m downstream of the GR focal plane. Two NaI(Tl) detector arrays were placed above and below the stopper in order to measure the annihilation γ rays of 511 keV followed by the isomeric decay of $^{12}\text{Be}(0_2^+)$ state. The array consisted 42 NaI(Tl) detectors with the crystal size of $45 \times 80 \times 160$ mm³ each. At the end of the detector system, we put a veto counter to improve the particle identification capability of ^{12}Be . All the ^{12}Be particles were stopped in the stopper while the lighter particles penetrated and fired the veto counter.

Figure 2 is a scatter plot of energy losses in the plastic scintillators. The horizontal axis is the energy loss in the first plastic scintillator (ΔE_1) and the vertical axis is the energy loss in the stopper ($\Delta E_{\text{stopper}}$). We can find that huge

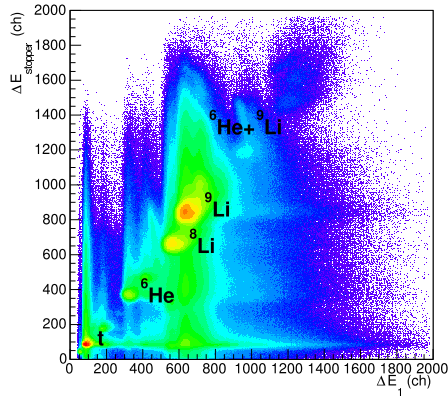


Figure 2: A scatter plot of energy losses in the stopper scintillator ($\Delta E_{\text{stopper}}$) versus in the first plastic scintillator (ΔE_1). Several lighter isotopes are identified and indicated in the figure.

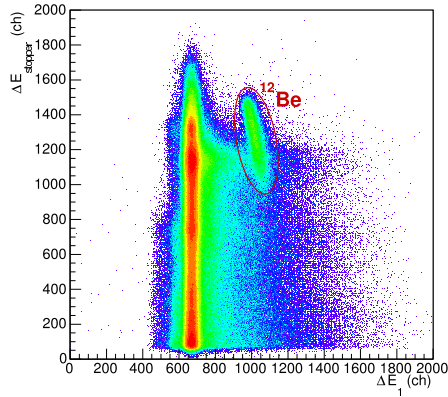


Figure 3: Same as Fig. 2 but with elimination of lighter isotopes by using the veto counter information. The locus of ^{12}Be indicated by a red circle is seen.

amount of lighter isotopes reached at the focal plane and a part of their pile-up events overlapped with the ^{12}Be region around 1000 ch and 1300 ch in ΔE_1 and $\Delta E_{\text{stopper}}$, respectively. Then, we selected the event which did not fire the veto counter. The result is shown in Fig. 3. The figure shows the same plot of Fig 2 but the event selection was applied. More than 97% of the lighter isotopes events were eliminated. After the elimination, we found the locus of ^{12}Be . We also succeeded in the identification of the $^{12}\text{Be}(0_2^+)$ state. Figure 4 shows count rates of the γ -rays as a function of the time after the implantation into the stopper. In the figure, the particle identification of ^{12}Be and the coincidence detection of two 511-keV γ -rays are required. The decay spectrum was fitted with a function of $A + B \exp(-t/\tau)$. The result is shown by the red solid line. The lifetime (τ) was deduced to be 335 ± 8.6 ns which is consistent with the known lifetime of 331 ns. It should be noted that there are a flat background from the β^+ -decay of ^{11}C produced by nuclear reactions of ^{12}C in the stopper. Further analysis is ongoing.

References

[1] Ph. Chomaz and N. Frascaria, Physics Reports **252**, 275 (1995).

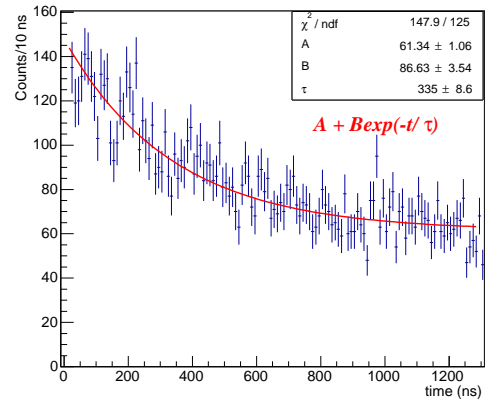


Figure 4: A γ -rays count rate spectrum. The particle identification of ^{12}Be and the coincidence detection of two 511-keV γ -rays are required. The red curve shows the result of the fitting with a common exponential decay parameter.

- [2] S. R. Elliot and P. Vogel, Annu. Rev. Nucl. Part. Sci. **52**, 115 (2002).
 [3] N. Auerbach, L. Zamick and D.C. Zheng, Annals of Physics **192**, 77 (1989).
 [4] J. Blomgren *et al.*, Phys. Lett. B **362**, 34 (1995).
 [5] M. Takaki *et al.*, RIKEN Accel. Prog. Rep. **46**, 29 (2013).
 [6] H. Fortune and R. Sherr, Phys. Rev. C **74**, 024301 (2006).
 [7] S.D. Pain *et al.*, Phys. Rev. Lett **96**, 032502 (2006).
 [8] R. Meharchant *et al.*, Phys. Rev. Lett. **108**, 122501 (2012).
 [9] S. Shimoura *et al.*, Phys. Lett. B **560**, 31 (2003); *ibid* **654**, 87 (2007).

Study of spin-dipole response of ${}^4\text{He}$ by using (${}^8\text{He}, {}^8\text{Li}^*(1^+)$) reaction

H. Miya, S. Shimoura, K. Kisamori, M. Assié^a, H. Baba^b, T. Baba^c, D. Beaumel^b, M. Dozono^b, T. Fujii, N. Fukuda^b, S. Go, F. Hammache^b, E. Ideguchi^d, N. Inabe^b, M. Ito^e, D. Kameda^b, S. Kawase, T. Kawabata^c, M. Kobayashi, Y. Kondo^f, T. Kubo^b, Y. Kubota, C. S. Lee, Y. Maeda^g, H. Matsubara^b, S. Michimasa, K. Miki^d, T. Nishi^h, M. Kurata-Nishimura^b, S. Ota, H. Sakai^b, S. Sakaguchiⁱ, M. Sasano^b, H. Sato^b, Y. Shimizu^b, H. Suzuki^b, A. Stolz^j, M. Takaki, H. Takeda^b, S. Takeuchi^b, A. Tamii^d, H. Tokieda, M. Tsumura^c, T. Uesaka^b, K. Yako, Y. Yanagisawa^b, and R. Yokoyama

Center for Nuclear Study, Graduate School of Science, the University of Tokyo

^aInstitut de Physique Nucléaire, Orsay, France

^bRIKEN (The Institute of Physical and Chemical Research)

^cDepartment of Physics, Kyoto University

^dResearch Center for Nuclear Physics, Osaka University

^eCyclotron and Radioisotope Center, Tohoku University

^fDepartment of Physics, Tokyo Institute of Technology

^gDepartment of Applied Physics, University of Miyazaki

^hDepartment of Physics, the University of Tokyo

ⁱDepartment of Physics, Kyushu University

^jNational Superconducting Cyclotron Laboratory, Michigan State University, USA

1. Introduction

Isovector spin dipole (SD) response ($\Delta L = \Delta S = 1$) is one of the Spin-Isospin responses. The SD response has a connection with the weak interaction process such as β -decay and neutrino-nucleus reaction. The neutrino-nucleus reaction is important for the study of the neutrinosynthesis in the supernova. Since it is difficult to measure the neutrino-nucleus response in laboratories due to very small cross section, the data of charge exchange reactions are important because the information of neutrino-nucleus responses can be extracted. The SD responses of ${}^4\text{He}$, which is the lightest double-closed nucleus, was studied.

We performed the exothermic charge-exchange reaction of ${}^4\text{He}({}^8\text{He}, {}^8\text{Li}^*(1^+)){}^4\text{H}$. The reaction probe has high spin-flip selectivity. The energy of ${}^8\text{He}$ beam was 190 MeV/nucleon in order to select a suitable region for the spin-isospin responses [1]. As the present results, the excitation energy spectra and the angular distribution on ${}^4\text{He}({}^8\text{He}, {}^8\text{Li}^*(1^+))$ reaction are reported in this article.

2. Experimental setup

The reaction was measured at the RIKEN RIBF facility by using the BigRIPS, the High-Resolution Beamline, and the SHARAQ spectrometer [2, 3]. A schematic view of the BigRIPS, the High-Resolution Beamline, and the SHARAQ spectrometer is shown in Fig. 1. A ${}^8\text{He}$ beam at 190 MeV/nucleon was produced via the projectile fragmentation reaction of the ${}^{18}\text{O}$ beam at 230 MeV/nucleon with a Be target at F0. The intensity of ${}^8\text{He}$ beam was approximately 2×10^6 cps at S0, where the secondary targets of liquid ${}^4\text{He}$ were installed. The ${}^4\text{He}$ target was made using CRYPTA system [4]. The target thickness was 120 mg/cm². The beam trajectory was measured by μ -hodoscope [5] and low-pressure multi-wire drift chambers [6] (LP-MWDCs) in the BigRIPS and the High-Resolution Beamline. The μ -hodoscope was installed at F3 to measure beam position

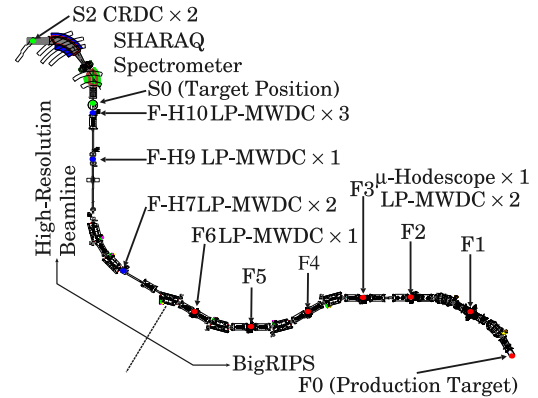


Figure 1: Schematic view of BigRIPS, High-Resolution Beamline, and SHARAQ Spectrometer.

whose spot size was as small as 1 cm in full width at half maximum. The momentum of ${}^8\text{He}$ was measured at F6, which was a momentum dispersive focal plane. At S0, the beam position and the incident angle of ${}^8\text{He}$ into the targets were determined. The scattered ${}^8\text{Li}$ was momentum analyzed with the SHARAQ spectrometer and detected by cathode readout drift chambers [7] at S2. The 980-keV γ -rays emitted from ${}^8\text{Li}$ were detected by the NaI (TI) detector array DALI2 [8] located around the target position to identify the transition from ${}^8\text{He}$ to 1^+ state of ${}^8\text{Li}$.

Figure 2 shows the excitation energy distribution of the (${}^8\text{He}, {}^8\text{Li}$) reaction (black line). The contribution of both the ${}^4\text{He}$ target and hydrogen is included in this spectrum. The regions around 10 MeV and -17 MeV show the ${}^4\text{He} \rightarrow {}^4\text{H}$ and ${}^1\text{H} \rightarrow n$ reactions, respectively. The ${}^1\text{H} \rightarrow n$ reaction originates at the plastic scintillator installed at FH10. The amount of contamination (green line) was estimated by using the energy loss of the LP-MWDC placed between the scintillator and the target. Thus, the ${}^4\text{He}({}^8\text{He}, {}^8\text{Li}){}^4\text{H}$ reac-

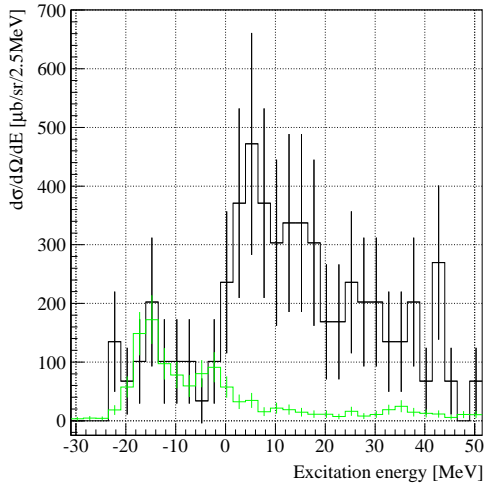


Figure 2: Excitation energy distribution of ${}^4\text{H}$ obtained using missing mass method. The green line shows the background estimated from the contamination of the excitation energy distribution.

tion was obtained.

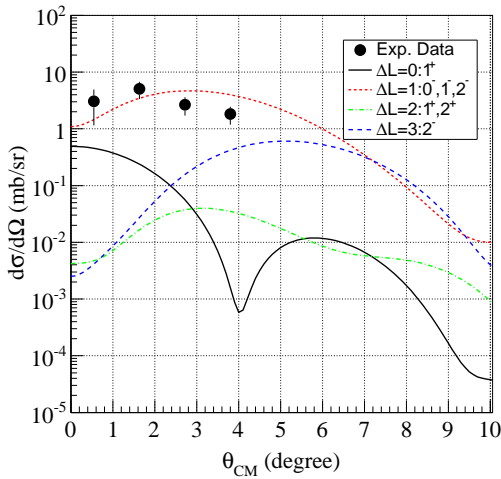


Figure 3: Angular distribution of the differential cross section of ${}^4\text{He}({}^8\text{He}, {}^8\text{Li}^*(1^+)){}^4\text{H}$ reaction.

Figure 3 shows the angular distribution of the differential cross section of ${}^4\text{He}({}^8\text{He}, {}^8\text{Li}^*(1^+)){}^4\text{H}$ reaction. The differential cross section was integrated the excitation distribution from 0 MeV to 30 MeV. The horizontal and vertical axes indicate scattering angle in center-of-mass frame and the differential cross section, respectively. The closed points with error bar are the experimental data. The curves are the result of the calculation with distorted wave born approximation (DWBA) code of FOLD [9] for various multipole components ($\Delta L = 0, 1, 2, 3$). The experimental data clearly show the angular distribution of Delta $L = 1$. Since the beam energy emphasizes the spin-flip components of the nuclear response, one can expect that the SD excitation is the main component of the cross section.

References

- [1] W. G. Love and M. A. Franey: Phys. Rev. C **24**, 1073 (1981).
- [2] T. Uesaka *et al.*: Prog. Theor. Exp. Phys. (2012) 03C007.

- [3] S. Michimasa *et al.*: Nucl. Instr. Meth. B **317** (2013) 305-310.
- [4] H. Ryuto *et al.*: Nucl. Instr. Meth. A **555** (2005) 1-5.
- [5] S. Ota *et al.*: CNS Ann Rep. 2011 (2013).
- [6] H. Miya *et al.*: Nucl. Instr. Meth. B **317** (2013) 710-713.
- [7] K. Kisamori *et al.*: CNS Ann. Rep. 2011 (2013).
- [8] T. Takeuchi *et al.*: Nucl. Instr. Meth. A **763** (2014) 1-8.
- [9] J. Cook *et al.*: Computer Code fold/dwhi, Florida state University (1988).

Direct mass measurements of neutron-rich Ca isotopes beyond $N = 34$

M. Kobayashi, S. Michimasa, Y. Kiyokawa, H. Baba^a, G.P.A. Berg^b, M. Dozono, N. Fukuda^a, T. Furuno^c, E. Ideguchi^d, N. Inabe^a, T. Kawabata^c, S. Kawase, K. Kisamori, K. Kobayashi^e, T. Kubo^a, Y. Kubota, C.S. Lee, M. Matsushita, H. Miya, A. Mizukami^f, H. Nagakura^e, D. Nishimura^f, H. Oikawa^f, S. Ota, H. Sakai^a, S. Shimoura, A. Stolz^g, H. Suzuki^a, M. Takaki, H. Takeda^a, S. Takeuchi^a, H. Tokieda, T. Uesaka^a, K. Yako, Y. Yamaguchi^e, Y. Yanagisawa^a, R. Yokoyama, and K. Yoshida^a

Center for Nuclear Study, Graduate School of Science, University of Tokyo

^a*RIKEN Nishina Center*

^b*JINA and the Department of Physics, University of Notre Dame*

^c*Department of Physics, Kyoto University*

^d*Research Center for Nuclear Physics, Osaka University*

^e*Department of Physics, Rikkyo University*

^f*Department of Physics, Tokyo University of Science*

^g*National Superconducting Cyclotron Laboratory, Michigan State University*

1. Introduction

The shell evolution in nuclei far from stability is one of the main subjects of nuclear physics. The nuclear mass is one of the fundamental quantities in investigating nuclear structure properties, such as shell closures and new magic numbers. The neutron numbers of 32 and 34 have been suggested to be candidates of new magic numbers in the Ca isotopes [1]. Recently the masses of ⁵³Ca and ⁵⁴Ca were measured, and the prominent shell closure at $N = 32$ was established [2]. Moreover, the excitation energy of the 2_1^+ state in ⁵⁴Ca was reported [3]. The result suggests the existence of a $N = 34$ shell closure in ⁵⁴Ca. For establishment of the closed-shell nature of ⁵⁴Ca, mass measurements of the Ca isotopes beyond $N = 34$ are essential.

As an indicator of nuclear shell evolution, we use the Δ_3 values [4]:

$$\Delta_3^N = \frac{(-1)^N}{2} [M(N-1) + M(N+1) - 2M(N)]c^2, \quad (1)$$

where $M(N)$ is a mass excess of a nucleus with N neutrons. Figure 1 shows systematics of the Δ_3 values for the Ar, K, Ca, Sc, and Ti isotopes. Here, the Δ_3 values are calculated using the atomic mass data listed in the 2012 Atomic Mass Evaluation [5] and, in addition, those in the more recent measurements of ^{53,54}Ca [2]. In this figure, peaks appear clearly at the conventional magic numbers of $N = 20$ and 28, and also at $N = 32$ in the Ca and Sc isotopes, which indicates shell closure at $N = 32$. The Δ_3 values can be obtained from the mass excesses obtained in this experiment. We will be able to discuss shell evolution in neutron-rich pf shell nuclei based on the Δ_3 values.

The present work aims at studying the nuclear shell evolution at $N = 32$ and 34 by direct mass measurements of neutron-rich nuclei in the vicinity of ⁵⁴Ca.

2. Experiment

The masses were measured directly by the time-of-flight-magnetic-rigidity (TOF- $B\rho$) technique. The mass-to-charge ratio m/q is derived from the following equation:

$$\frac{m_0}{q} = \frac{B\rho}{\gamma L/t}, \quad (2)$$

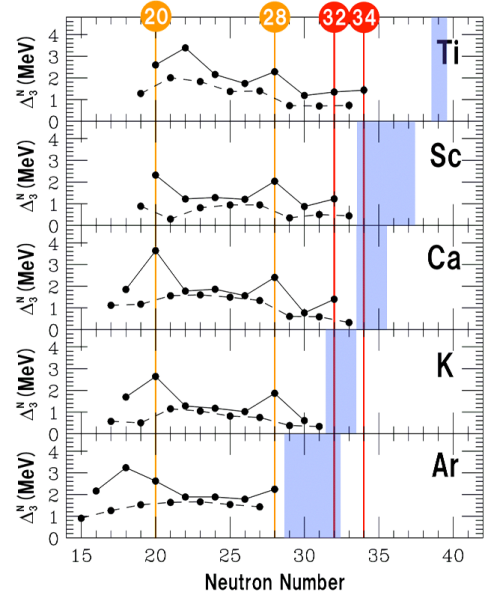


Figure 1: Systematics of Δ_3 values for the Ar, K, Ca, Sc, and Ti isotopes. Solid (dashed) lines connects neighboring even (odd) N isotopes. The shaded areas indicate nuclei to be measured in the present experiment.

where m_0 is the rest mass, γ is the Lorentz factor, L is the flight length, and t is the flight time.

The experiment was performed at the RIKEN RI Beam Factory (RIBF). A schematic view of the beamline with the detectors used in the experiment is shown in Fig. 2.

Neutron-rich isotopes were produced by fragmentation of a 345 MeV/nucleon ⁷⁰Zn primary beam impinging on a beryllium target. The fragments were transmitted in the BigRIPS separator, and then sent to the SHARAQ spectrometer through the High Resolution Beam Line. The beam line and SHARAQ were operated in the dispersion matching mode allowing a momentum resolution of 1/14700.

Timing measurements were performed by newly developed diamond detectors [6] installed at BigRIPS-F3 and the final focal plane of SHARAQ (S2). The flight path length between F3 and S2 is ~ 105 m along the central ray, and the

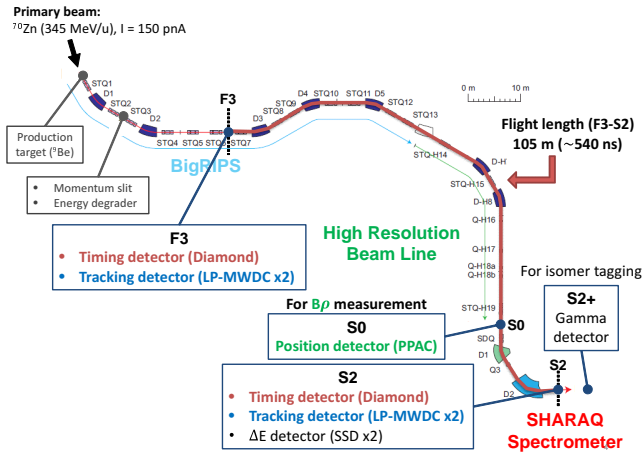


Figure 2: Schematic view of the beamline and the detectors used in the experiment.

typical flight time is ~ 540 ns. We installed two low pressure multi-wire drift chambers (LP-MWDCs) [7] at both F3 and S2 to correct the flight pass lengths using the tracking information on an event-by-event basis. The $B\rho$ value of each ion was determined by position measurement using a parallel plate avalanche counter (PPAC) located at the dispersive focus at the target position of SHARAQ (S0). At S2, we mounted two silicon strip detectors (SSDs) for identification of the atomic numbers of the fragments. To identify the isomers, which lead to a systematic shift of the obtained mass values towards higher masses, we placed a γ -detector array consisting of 2 Ge clover and 16 NaI(Tl) detectors downstream of S2. Details of this system can be found in Ref. [8].

3. Results

Figure 3 shows the preliminary particle identification of the secondary beams. The total yield of ^{55}Ca was on the order of several thousands. Many species of reference nuclei over a broad range of A and Z were observed, which were used in the mass calibration. Ion-optical correction to achieve extremely good mass resolution is being performed. Further analysis is in progress.

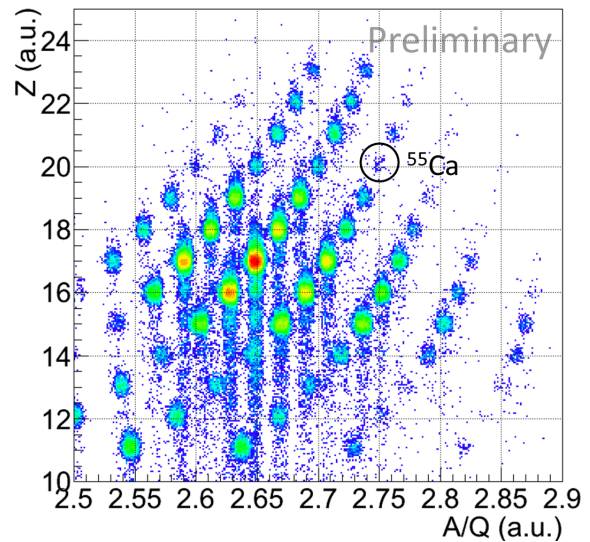


Figure 3: Particle identification of the secondary beams.

References

- [1] T. Otsuka *et al.*, Phys. Rev. Lett. **87**, 082502 (2001).
- [2] F. Wienholtz *et al.*, Nature **498**, 349 (2013).
- [3] D. Steppenbeck *et al.*, Nature **502**, 207 (2013).
- [4] W. Satula *et al.*, Phys. Rev. Lett. **81**, 3599 (1998).
- [5] G. Audi *et al.*, Chinese Physics C **36**, 1287 (2012).
- [6] S. Michimasa *et al.*, Nucl. Instr. Meth. B **317**, 305 (2013).
- [7] H. Miya *et al.*, Nucl. Instr. Meth. B **317**, 317 (2013).
- [8] Y. Kiyokawa *et al.*, in this report.

Spectroscopic factors of $^{23,25}\text{F}(p,2p)$ reaction

T. L. Tang, S. Kawase, T. Uesaka^a, D. Beaumel^g, M. Dozono^a, T. Fujii, N. Fukuda^a, T. Fukunaga^d, A. Galindo-Uribarriⁱ, S. H. Hwang^e, N. Inabe^a, D. Kameda^a, T. Kawahara^b, W. Y. Kim^e, K. Kisamori, M. Kobayashi, T. Kubo^a, Y. Kubota, K. Kusaka^a, C. S. Lee, Y. Maeda^f, H. Matsubara^a, S. Michimasa, H. Miya, T. Noro^d, A. Obertelli^h, S. Ota, E. Padilla-Rodal^j, S. Sakaguchi^d, H. Sakai^a, M. Sasano^a, S. Shimoura, S. S. Stepanyan^e, H. Suzuki^a, M. Takaki, H. Takeda^a, H. Tokieda, T. Wakasa^d, T. Wakui^c, K. Yako, Y. Yanagisawa^a, J. Yasuda^d, R. Yokoyama, K. Yoshia^a, J. Zenihiro^a, for SHARQA04 collaboration

Center for Nuclear Study, Graduate School of Science, University of Tokyo

^a*RIKEN (The Institute of Physical and Chemical Research)*

^b*Department of Physics, Toho University*

^c*Cyclotron and Radioisotope Center, Tohoku University*

^d*Department of Physics, Kyushu University*

^e*Department of Physics and Energy Science, Kyungpook National University*

^f*University of Miyazaki*

^g*Institut de physique nucleaire d'Orsay*

^h*CEA Saclay*

ⁱ*Oak Ridge National Laboratory*

^j*Instituto de Ciencias Nucleares, Universidad Nacional Autónoma de México*

1. Introduction

Independent particle model (IPM) plays an important role in understanding the microscopic nuclear structure and provides the foundation of nuclear shell model. Knockout reaction can be used to obtain the spectroscopic factor (SF), which represents the single particle strength and may validate the description of the state with IPM.

2. Experimental setup

The SHARQA04 experiment was performed with using the SHARQA spectrometer system at the RIBF of the RIKEN Nishina Center. A detailed explanation on the target and experimental setup are given in Ref. [1] [2]. The setup around the target system is shown on Fig. 1.

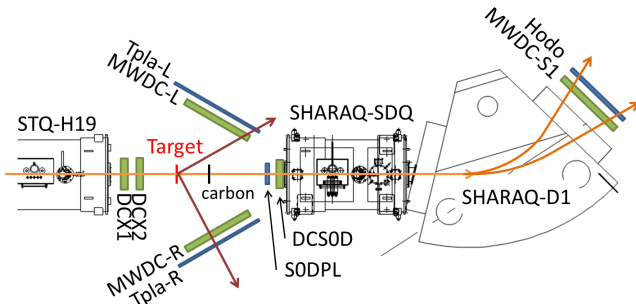


Figure 1: The setup of the detectors in the SHARQA04 experiment. The beam was coming from left to right.

A ^{23}F (^{25}F) cocktail beam at 290A MeV (277A MeV) was delivered by the BigRIPS to the SHARQA spectrometer. Scattered protons were detected by using two sets of particle detectors, composed of a multi-wire drift chamber (MWDC) and a plastic scintillator (Tpla), placed on the left and right side of the target. The residual nuclei were detected by a MWDC-S1 and a plastic hodoscopes (Hodo) at

focal plane D1 of SHARQA spectrometer.

3. Reaction Identification

The fluorine nucleus ^{25}F (^{25}F) was identified by using $\Delta E(\text{F3}) - \text{TOF}(\text{F3-FH9})$ method, where F3 and FH9 are focal planes on the BigRIPS beam line. The two scattered protons from (p,2p) reaction were detected by Tpla-L and Tpla-R coincidentally. The location of the target crystal (made of C_{10}H_8) was gated by reaction vertex, which was reconstructed by trackings of DCX1, DCX2, MWDC-L and R. In addition, a TOF(S0D-D1) gate was imposed, so that slow residues originated from target holder were ruled out. The carbon background came from the crystal was estimated by selecting the carbon target from reaction vertex. The oxygen residues were identified by downstream PID, which was deduced from DCS0D, MWDC-S1, and Hodo.

4. Excitation energy spectrum

The excitation energy E_x of ^{22}O (or ^{24}O) was determined using the following equation,

$$E_x = m(P_F + P_T - P_1 - P_2) + m(P_2) - m(P_F) - S_p(P_F), \quad (1)$$

where P_i are the 4-momentum of the i particle. The subscript F stands for fluorine, T for target, 1 for scattered proton, and 2 for knocked-out proton. $m()$ is the mass of the 4-momentum inside the bracket. $S_p()$ is the proton separation energy.

Figure. 2 and Figure. 3 show the excitation function of Oxygen isotopes from $^{23}\text{F} + p$ reaction and $^{25}\text{F} + p$ reaction, respectively. Since the 1-neutron threshold of ^{22}O is just 6.8 MeV, ^{21}O channel opens up above this excitation energy. Similarly, lighter oxygen isotopes will be detected if the excitation energy excess multiple-neutron threshold. Nitrogen and carbon residues were checked, but there is no strength on the energy spectrum.

The orbital angular momentums of each peak were analyzed using the missing momentum in the rest frame of fluorine nucleus. The experimental momentum distribution of

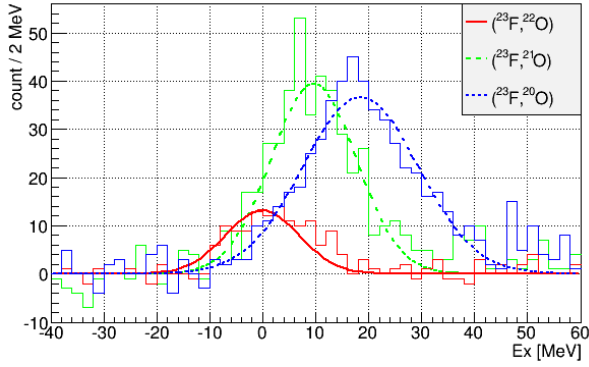


Figure 2: The excitation energy spectra for ^{22}O for $^{23}\text{F}(p,2p)$ reaction. The red, green, and blue line are Gaussian fits for $(^{23}\text{F},^{22}\text{O})$, $(^{23}\text{F},^{21}\text{O})$, and $(^{23}\text{F},^{20}\text{O})$ respectively.

residue was compared with the theoretical momentum distribution from code THREEDEE [3]. The momentum analysis shows that the $(^{23}\text{F},^{22}\text{O})$, $(^{25}\text{F},^{24}\text{O})$, and $(^{25}\text{F},^{23}\text{O})$ peaks are from d-shell. The other peaks show p-shell nature. Table 1 shows the fitted mean, standard deviation (s.d.), and cross section for each peaks. The statistic and systematic uncertainty were included in the error of the cross section.

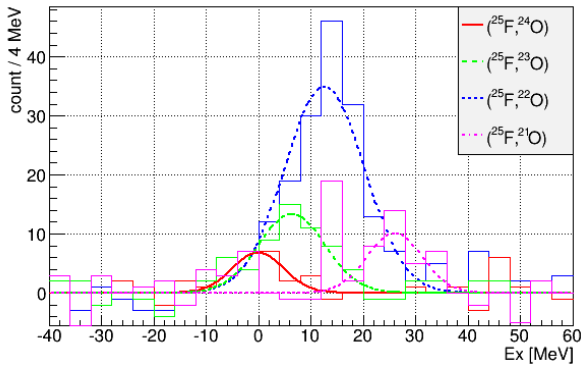


Figure 3: The excitation energy spectra for ^{24}O for $^{25}\text{F}(p,2p)$ reaction. The red, green, blue, and pink line are Gaussian fits for $(^{25}\text{F},^{24}\text{O})$, $(^{25}\text{F},^{23}\text{O})$, $(^{25}\text{F},^{22}\text{O})$, and $(^{25}\text{F},^{21}\text{O})$ respectively.

The known energy levels also support for the angular momentum assignment. All known energy level of ^{22}O are positive parity (one unknown at 5.8 MeV) below the 1-neutron thresholds and are all negative parity above it (except a 4^+ state at 6.9 MeV). Therefore, with the missing momentum distribution, the $(^{23}\text{F},^{22}\text{O})$ strength should come from $1d_{5/2}$ shell. And the $(^{23}\text{F},^{21}\text{O})$ and $(^{23}\text{F},^{20}\text{O})$ strength should be dominated by p-shell. Similar arguments was used in $^{25}\text{F}(p,2p)$ reaction.

5. Spectroscopic factor

The theoretical cross section σ_{th} was calculated with DWIA method by the code THREEDEE. The Dirac phenomenological potential with EDAD2 parameters set [4] was used. The results are summarized in Table. 1. The SF of s-d shell proton on ^{23}F is only 0.4. This could be due to deformation induced configuration mixing [5]. In deformed case, the theoretical cross section could be incorrect, because the EDAD2 parameters set was fitted for spherical isotopes. The proton-neutron pairing could also

Table 1: Cross section and Spectroscopic factor

peak	mean [MeV]	s.d. [MeV]	σ_{exp} [μb]	σ_{th} [μb]	SF
$(^{23}\text{F},^{22}\text{O})$	1.0(8)	6.0(6)	61(14)	166	0.4(1)
$(^{23}\text{F},^{21}\text{O})$	9.5(4)	7.9(4)	213(44)	95	2.2(5)
$(^{23}\text{F},^{20}\text{O})$	18.0(5)	9.7(5)	243(50)	92	2.6(5)
$(^{25}\text{F},^{24}\text{O})$	-0.5(1.1)	4.8(1.3)	34(11)	149	0.23(7)
$(^{25}\text{F},^{23}\text{O})$	6.5(1.4)	6.3(9)	90(25)	125	0.7(2)
$(^{25}\text{F},^{22}\text{O})$	12.7(6)	7.6(6)	268(70)	81	3.3(9)
$(^{25}\text{F},^{21}\text{O})$	26.1(1.2)*	5.2(1.2)*	83(27)	78	1.1(3)

* not accurate.

reduced the SF. In contrast, the sum of SF of s-d shell proton on ^{25}F is 0.9(2). This can be understood as the neutron magic number $N=16$. This new magic number was confirmed in ^{24}O [6].

The sum of SF for p-shell of ^{23}F and ^{25}F are 4.8(7) and 4.4(9) respectively, which are 75% of IPM limit. This result agrees with that of stable isotopes from $(e,e'p)$ reactions. The p-shell strength should be fragmented, but we are not able to observe it due to poor resolution.

6. Conclusion

The SF of s-d shell of ^{23}F requires further investigation, such as the effect of deformation, proton-neutron pairing, or better theoretical cross section calculation. The s-d shell proton of ^{25}F shows single particle nature as ^{24}O is double magic. A comparison to SF from shell model calculation is needed in future analysis.

References

- [1] S. Kawase *et al.*, CNS annual report 2012, **13** (2013).
- [2] T. L. Tang *et al.*, CNS annual report 2012, **59** (2013).
- [3] N. S. Chant *et al.*, PRC **15** (1977) 57
- [4] E. D. Cooper *et al.*, PRC **47** (1993) 297
- [5] M. K. Sharma *et al.*, CPC **39** (2015) 064102
- [6] R. V. F. Janssens, Nature **459** (2009) 1069

Spectroscopy of single-particle states in oxygen isotopes via $^{A}\text{O}(\vec{p}, 2p)$ reaction with polarized protons

S. Kawase, T. L. Tang, T. Uesaka^a, D. Beaumel^b, M. Dozono^a, T. Fujii, N. Fukuda^a, T. Fukunaga^c, A. Galindo-Uribarri^d, S. H. Hwang^e, N. Inabe^a, D. Kameda^a, T. Kawahara^f, W. Kim^e, K. Kisamori, M. Kobayashi, T. Kubo^a, Y. Kubota^a, K. Kusaka^a, C. S. Lee^a, Y. Maeda^g, H. Matsubara^a, S. Michimasa, H. Miya^a, T. Noro^c, A. Obertelli^h, S. Ota, E. Padilla-Rodalⁱ, S. Sakaguchi^c, H. Sakai^a, M. Sasano^a, S. Shimoura, S. Stepanyan^e, H. Suzuki^a, M. Takaki, H. Takeda^a, H. Tokieda, T. Wakasa^c, T. Wakui^j, K. Yako, Y. Yanagisawa^a, J. Yasuda^c, R. Yokoyama, K. Yoshida^a, and J. Zenihiro^a

Center for Nuclear Study, Graduate School of Science, the University of Tokyo

^a*RIKEN (The Institute of Physical and Chemical Research)*

^b*Institut de Physique Nucléaire d'Orsay, France*

^c*Department of Physics, Kyushu University*

^d*Oak Ridge National Laboratory, USA*

^e*Department of Physics and Energy Sciences, Kyungpook National University, Korea*

^f*Department of Physics, Toho University*

^g*Department of Physics, University of Miyazaki*

^h*CEA Saclay, France*

ⁱ*Instituto de Ciencias Nucleares, Universidad Nacional Autónoma de México, México*

^j*Cyclotron and Radioisotope Center, Tohoku University*

We performed $^{14,22-24}\text{O}(\vec{p}, 2p)$ reaction measurements (SHARAQ04 experiment) with a polarized proton target at RIBF to measure single-particle spectra of $^{14,22-24}\text{O}$ nuclei. The goal of this study is to determine the spin-orbit splitting of 1p proton single-particle orbits in $^{14,22-24}\text{O}$ as a function of their neutron number. For the experimental setup, see ref. [1]. In this report, current status of the analysis is described.

The $(p, 2p)$ reaction was identified via the particle identifications of incident nuclei and two scattered protons. Particles were identified via the Time-of-Flight(TOF)- ΔE method on an event-by-event basis. Then the proton separation energy of the incident nuclei and the excitation energy of the residual nuclei were calculated from scattering angles and TOF of scattered protons.

Hit position and TOF from the target are also measured for the residual nuclei at a focal plane S1 at the downstream of the D1 dipole magnet of SHARAQ after the reaction point in order to improve the S/N ratio and to separate the excited states of residual nitrogen nuclei.

Figure 1 shows the particle identification (PID) plot of the residual particles in the $^{22}\text{O}(p, 2p)$ run. The mass-charge ratio A/Q was deduced from the scattering angle after the target, the position at S1, and TOF from the target to S1. The proton number Z was obtained from the light output signal of the plastic scintillators at S1 allowing good separation for the nitrogen isotopes as shown in the plot.

Figure 2 shows the excitation energy spectra of ^{21}N with different residual PID gates for nitrogen isotopes. The red histograms show the background originated from the carbon contamination of the polarized target estimated from the measurement taken with a pure carbon target. The lower limit of the excitation energy distribution for each nitrogen isotope is consistent with the multi-neutron separation energy of ^{21}N .

The experimental cross sections for the nitrogen ground states were compared with the distorted wave impulse ap-

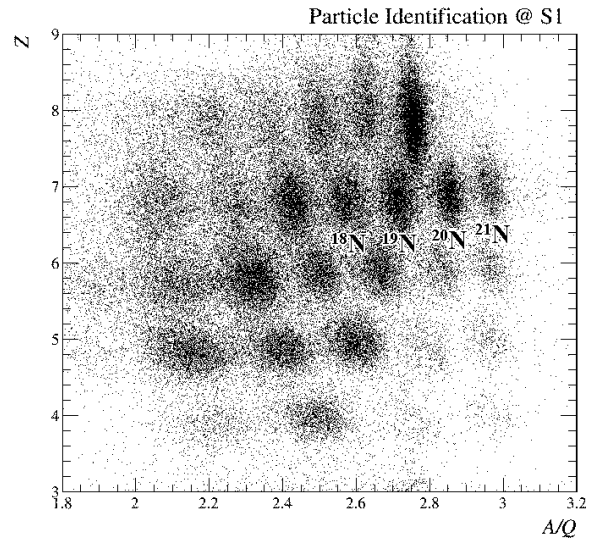


Figure 1: Particle identification plot of the residual particles in $^{22}\text{O}(p, 2p)$ run.

proximation (DWIA) calculations using the computer code THREEDEE [2]. In these calculations, nucleon-nucleus optical potential based on energy-dependent atomic-mass-number-dependent Dirac phenomenology obtained by Cooper [3] and the NN scattering amplitude obtained from phase shift analysis by Arndt [4] were used.

Since there are no excited states of ^{13}N and ^{23}N below particle thresholds, the cross sections of $^{14}\text{O}(p, 2p)^{13}\text{N}_{\text{g.s.}}$ and $^{24}\text{O}(p, 2p)^{23}\text{N}_{\text{g.s.}}$ in the experimental acceptance were obtained from yields of the events in which ^{13}N and ^{23}N were identified in S1, respectively. For the $^{22}\text{O}(p, 2p)^{21}\text{N}$ case, ^{21}N has excited states below particle threshold. In this study, the ratio of spectroscopic factors for such states was estimated from the shell model calculation using the SFO

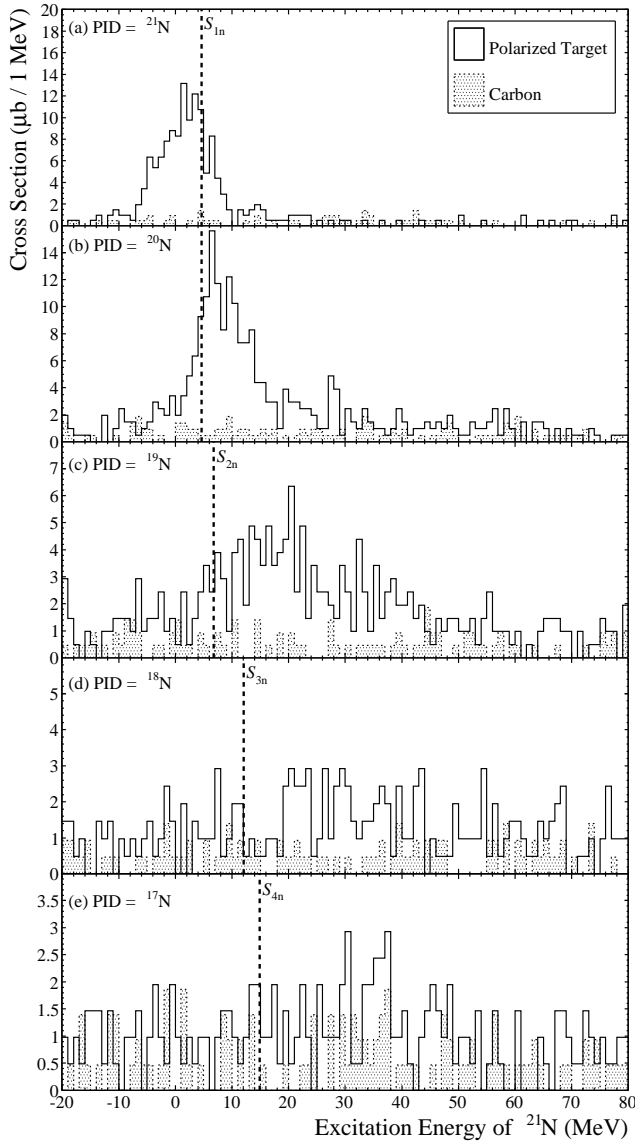


Figure 2: Excitation energy spectrum for $^{22}\text{O}(p,2p)$ for each residual PID gate at downstream. The red histograms show the background estimated from the $2p$ coincidence events occurred in the carbon target. The multi-neutron separation energies S_n , S_{2n} , S_{3n} , and S_{4n} of ^{21}N are indicated by dotted lines.

Table 1: Experimental value of C^2S for the ground states of the nitrogen isotopes obtained from the $(p,2p)$ reaction measurement. σ_{exp} is the experimental cross section and σ_{th} is the cross section calculated by using THREEDEE.

	$\sigma_{\text{exp}} (\mu\text{b})$	$\sigma_{\text{th}} (\mu\text{b})$	C^2S
$^{14}\text{O}(p,2p)^{13}\text{N}_{\text{g.s.}}$	337 ± 15	293.0	1.15 ± 0.05
$^{22}\text{O}(p,2p)^{21}\text{N}_{\text{g.s.}}$	124 ± 9	97.43	1.27 ± 0.09
$^{24}\text{O}(p,2p)^{23}\text{N}_{\text{g.s.}}$	113 ± 28	80.86	1.4 ± 0.4

interaction [5].

Table 1 shows the experimental (σ_{exp}) and the calculated cross sections (σ_{th}) and the spectroscopic factors $C^2S = \sigma_{\text{exp}}/\sigma_{\text{th}}$. The errors in the table include only statis-

tical errors. The spectroscopic factors for $^{14}\text{O}(p,2p)^{13}\text{N}_{\text{g.s.}}$, $^{22}\text{O}(p,2p)^{21}\text{N}_{\text{g.s.}}$, and $^{24}\text{O}(p,2p)^{23}\text{N}_{\text{g.s.}}$ are consistent with each other.

A more detailed analysis such as the model dependence of the DWIA calculation and the comparison of spectroscopic factors with the shell model calculations will be done in near future.

References

- [1] S. Kawase, *et al.*, CNS Annual Report 2013, 9.
- [2] N. S. Chant and P. G. Roos, *et al.*, Phys. Rev. C **15** (1977) 57.
- [3] E. D. Cooper, *et al.*, Phys. Rev. C **47** (1993) 297.
- [4] R. A. Arndt, *et al.*, Phys. Rev. D **35** (1987) 128.
- [5] T. Suzuki, R. Fujimoto, and T. Otsuka, Phys. Rev. C **67** (2003) 044302.

Investigation of the octupole correlations of neutron-rich $Z \sim 56$ isotopes by β - γ spectroscopy

R. Yokoyama, E. Ideguchi^a, G. Simpson^b, Mn. Tanaka^a, S. Nishimura^c, P. Doornenbal^c, P.-A. Söderström^c, G. Lorusso^c, Z.Y. Xu^d, J. Wu^{c,e}, T. Sumikama^f, N. Aoi^a, H. Baba^c, F. Bello^g, F. Browne^{h,c}, R. Daidoⁱ, Y. Fangⁱ, N. Fukuda^c, G. Gey^{b,c,j}, S. Go, S. Inabe^c, T. Isobe^c, D. Kameda^c, K. Kobayashi^k, M. Kobayashi, T. Komatsubara^l, T. Kubo^c, I. Kuti^m, Z. Li^e, M. Matsushita, S. Michimasa, C.B. Moonⁿ, H. Nishibataⁱ, I. Nishizuka^f, A. Odaharaⁱ, Z. Patel^{c,o}, S. Rice^{c,o}, E. Sahin^g, L. Sinclair^{c,p}, H. Suzuki^c, H. Takeda^c, J. Taprogge^{q,r}, Zs. Vajta^m, H. Watanabe^s, and A. Yagiⁱ

Center for Nuclear Study, the University of Tokyo

^a*Research Center for Nuclear Physics, Osaka University*

^b*LPSC, UJF, INP Grenoble, CNRS/IN2P3*

^c*RIKEN Nishina Center*

^d*Department of Physics, the University of Tokyo*

^e*Department of Physics, Peking University*

^f*Department of Physics, Tohoku University*

^g*Department of Physics, University of Oslo*

^h*School of Computing Engineering and Mathematics, University of Brighton*

ⁱ*Department of Physics, Osaka University*

JILL, Grenoble

^k*Department of Physics, Rikkyo University*

^l*Department of Physics, University of Tsukuba*

^m*MTA Atomki*

ⁿ*Department of Display Engineering, Hoseo University*

^o*Department of Physics, University of Surrey*

^p*Department of Physics, University of York*

^q*Instituto de Estructura de la Materia, CSIC*

^r*Departamento de Física Teórica, Universidad Autónoma de Madrid*

^s*Department of Physics, Beihang University*

It has long been a question as to whether there exist nuclei with static octupole deformation, a parity-violating collective mode. The interaction between orbits with $\Delta J = \Delta I = 3$ is responsible for strong octupole correlations and these effects are expected to be strongest for nuclei with such orbits close to the Fermi surface. Possible nucleon numbers where this occurs are Z or $N \sim 34, 56, 88$ and 134 . A recent study on $Z \sim 88, N \sim 134$ region [1] revealed that there exists static octupole deformation in ^{224}Ra and ^{220}Rn , which attracted much attention. The neutron-rich Ba isotopes ($Z = 56, N \sim 88$) are also expected to have strong octupole correlations and are good candidates for octupole deformation. The even-even Ba isotopes from $A = 140$ to 148 have been studied by using large arrays of Ge detectors and spontaneous fission sources, such as ^{248}Cm [2]. These nuclei possess low-lying positive- and negative- parity doublet bands which are characteristic of octupole collectivity. The observation of enhanced $E1$ transition rates of γ decays are one of the indication of such octupole correlations. Although the intuition that ^{144}Ba ($Z = 56, N = 88$) should show the largest $E1$ rates, Ref. [2] revealed that ^{148}Ba seems to have $B(E1)$ as large as those of ^{144}Ba , while ^{146}Ba has much smaller ones. In order to understand this discrepancy, an investigation of more neutron-rich Ba isotopes will be useful. The available theoretical calculations provide different answers for the magnitude of octupole correlations in this region. For example, a calculation by microscopic-

macroscopic method [3] predicts large β_3 values in ^{150}Ba while a Hartree-Fock calculation [4] argues that there is no state with a dipole moment in ^{150}Ba . Therefore, an experimental investigation is required to resolve this problem.

We performed β - γ spectroscopy of the neutron-rich $Z \sim 56$ isotopes at the RI Beam Factory (RIBF) of the RIKEN Nishina Center. The neutron-rich isotopes were produced by using the in-flight fission of $345\text{ MeV/u } ^{238}\text{U}$ beam bombarding a 3-mm thick Be production target. The typical intensity of the primary ^{238}U beam was $\sim 6\text{ pnA}$. Individual fission fragments were separated and identified in the BigRIPS in-flight separator [5] on an event-by-event basis by measurements of A/Q and Z . The A/Q value was obtained from the time-of-flight (TOF) and magnetic rigidity ($B\rho$) measured in the second stage of the BigRIPS separator (between F3 and F7 focal planes). The Z value was obtained from the energy loss (ΔE) measured in an ionization chamber at the final focal plane, F11. The schematic view of the beam line is shown in Fig.1 (a). The TOF was obtained from the time difference between plastic scintillators at F3 and F7 focal planes. The $B\rho$ value was obtained by the trajectory reconstruction from the position and angular information measured by position-sensitive parallel plate avalanche counters (PPACs) at F3, F5 and F7. A detailed explanation of the particle identification procedure at the BigRIPS is found in [6].

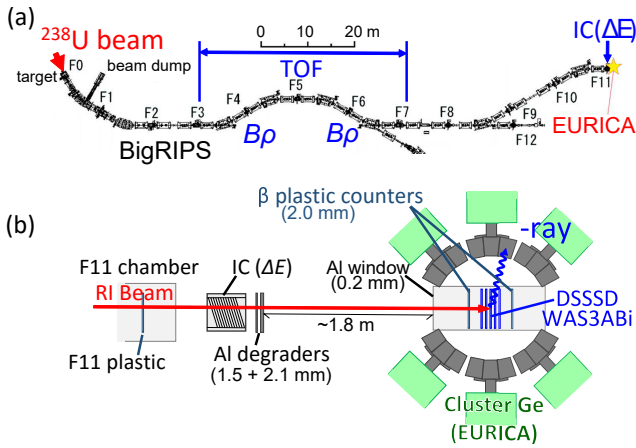


Figure 1: Schematic diagrams of the BigRIPS and ZeroDegree spectrometer beam line (a), and the stopper and detector setups at F11 (b).

The detector setups for the β - γ measurement at F11 are shown in Fig.1 (b). The secondary beam was implanted into an active stopper WAS3ABi [7] which consists of five layers of Double-Sided-Silicon-Strip Detectors (DSSSDs) with 40×60 strips, each 1-mm in width. WAS3ABi was used in order to measure the positions of the ion implantation and β -ray emission. This allows β - γ measurements with particle identification with a total implantation rate of up to ~ 100 Hz. The γ rays from the implanted ions were detected by the EURICA [8] array, consisting of 12-cluster Ge detectors. Each cluster contains seven Ge crystals, enabling the add back of Compton-scattered events in the neighboring crystals. The total detection efficiency of the array for photons of 1332 keV was 8.4%.

Figure 2 (a) shows a γ -ray spectrum obtained following the β -decay of ^{152}La ions. Three known γ rays are confirmed at 80.5, 182.5 and 274.6 keV; these have previously been reported as $E2$ decays from the 2^+ , 4^+ and 6^+ members of the ground-state band of ^{152}Ce [9]. The results for ^{152}Ce demonstrate the correctness of our measurement and analysis techniques.

Figure 2 (b) shows a preliminary γ -ray energy spectrum obtained from the β -decay of implanted ^{150}Cs ions. Some candidates for peaks are present at energies of 100, 217 and 597 keV, though the statistics are low. The peaks at 100 and 217 keV can be interpreted as the 2^+ to 0^+ and 4^+ to 2^+ γ decays, respectively, from the systematics of the 4^+ and 2^+ state energies in the neighboring even-even Ba isotopes. The position of the 597-keV transition in the decay scheme is uncertain with the current statistics. The energies of the proposed 2^+ and 4^+ levels of ^{150}Ba are lower than the equivalent ones in ^{148}Ba , indicating an increase in quadrupole deformation at ^{150}Ba . Data analysis is continuing in an effort to improve the γ -ray statistics.

References

- [1] L. P. Gaffney *et al.*, Nature **497** (2013) 199.
- [2] W. Urban *et al.*, Nucl. Phys. A **613** (1997) 107.
- [3] P. A. Butler and W. Nazarewicz, Nucl. Phys. A **533** (1991) 249.
- [4] J. Egido and L. Robledo, Nucl. Phys. A **545** (1992) 589.
- [5] T. Kubo *et al.*, NIM B **204** (2003) 97.
- [6] T. Ohnishi *et al.*, J. Phys. Soc. Jpn. **79** (2010) 073201.
- [7] S. Nishimura *et al.*, Nucl. Phys. News **22** (2012) No.3.

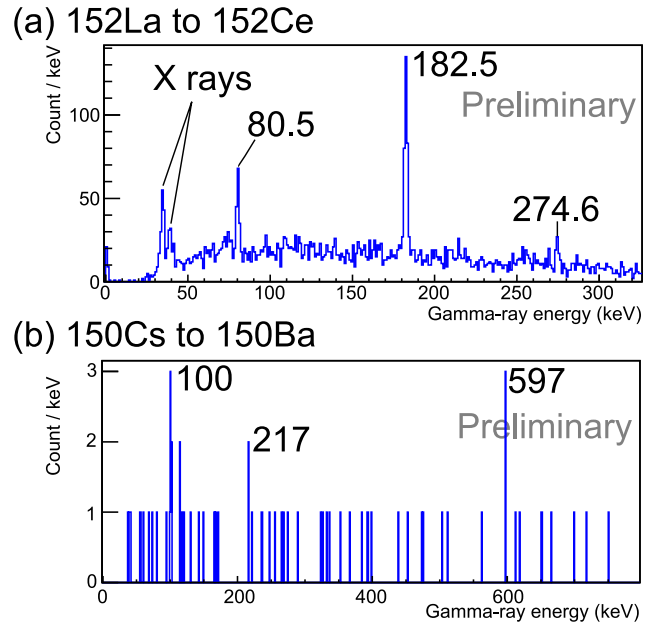


Figure 2: (a) A preliminary γ -ray energy spectrum obtained from the β -decay of ^{152}La to ^{152}Ce , up to 100 ms after ion implantation. The low-energy peaks around 34 and 39 keV are Ce K_{α} and K_{β} X rays, respectively, emitted following electron conversion. (b) A preliminary γ -ray spectrum of the β decay of ^{150}Cs to ^{150}Ba .

- [8] S. Nishimura *et al.*, RIKEN Accel. Prog. Rep. **46** (2013) 182.
- [9] H. J. Li *et al.*, Phys. Rev. C **86** (2012) 067302.

Experimental study on two-neutron correlation in Borromean nuclei via the (p, pn) reaction with the SAMURAI spectrometer

Y. Kubota^{a,b}, A. Corsi^c, G. Authelet^c, H. Baba^b, C. Caesar^d, D. Calvet^c, A. Delbart^c, M. Dozono^a, J. Feng^e, F. Flavigny^f, J.-M. Gheller^c, J. Gibelin^g, A. Gillibert^c, K. Hasegawa^h, T. Isobe^b, Y. Kanayaⁱ, S. Kawakamiⁱ, D. Kim^j, Y. Kiyokawa^a, M. Kobayashi^a, N. Kobayashi^k, T. Kobayashi^h, Y. Kondo^l, Z. Korkulu^m, S. Koyama^k, V. Lapoux^c, Y. Maedaⁱ, F. M. Marqués^g, T. Motobayashi^b, T. Miyazaki^k, T. Nakamura^l, N. Nakatsuka^{n,b}, Y. Nishio^o, A. Obertelli^c, A. Ohkura^o, N. A. Orr^g, S. Ota^a, H. Otsu^b, T. Ozaki^l, V. Panin^b, S. Paschalis^d, E. C. Pollacco^c, S. Reichert^p, J.-Y. Roussé^c, A. Saito^l, S. Sakaguchi^o, M. Sako^b, C. Santamaria^c, M. Sasano^b, H. Sato^b, M. Shikata^l, Y. Shimizu^b, Y. Shindo^o, L. Stuhl^b, T. Sumikama^h, M. Tabata^o, Y. Togano^l, J. Tsubota^l, T. Uesaka^b, Z. Yang^e, J. Yasuda^o, K. Yoneda^b, and J. Zenihiro^b

^aCenter for Nuclear Study, Graduate School of Science, University of Tokyo

^bRIKEN Nishina Center

^cCEA, Saclay

^dDepartment of Physics, Technische Universität Darmstadt

^eDepartment of Physics, Peking University

^fIPN Orsay

^gLPC Caen

^hDepartment of Physics, Tohoku University

ⁱDepartment of Applied Physics, University of Miyazaki

^jDepartment of Physics, Ehwa Womans University

^kDepartment of Physics, University of Tokyo

^lDepartment of Physics, Tokyo Institute of Technology

^mMTA Atomki

ⁿDepartment of Physics, Kyoto University

^oDepartment of Physics, Kyushu University

^pDepartment of Physics, Technische Universität München

Dineutron correlation is one of the symbolic phenomena expected to appear in neutron drip-line nuclei. Since theoretical predictions were made by Bertsch and Esbensen [1], considerable experimental efforts were devoted using different approaches, such as the transfer reaction, the break up reaction, and the nuclear-induced knockout reaction. However, currently available data seem to be insufficient to study the neutron-neutron correlation in terms of (i) the decomposition of high-angular-momentum components, the fraction of which is very small, (ii) the extraction of a core excitation, and (iii) the effect of final state interactions (FSIs) [2]. In this study, (i) the MINOS [3] was used for higher luminosity, (ii) γ rays were detected to tag the core excitation, and (iii) the proton-induced quasi-free (p, pn) reaction was employed to minimize the FSI.

The experiment was performed at the RIKEN RI Beam Factory (RIBF). Secondary beam produced by the fragmentation of a ^{48}Ca primary beam of 345 MeV/nucleon were separated by the BigRIPS. The typical intensity of the ^{48}Ca beam was 400 pnA. The primary target of either 20 mm or 30 mm thickness was used. They were detected and identified using plastic scintillators at the focal planes F3, F5, F7, and F13 and multi-wire drift chambers (MWDCs) at F13 (BDC). For their diagnostics, position-sensitive parallel plate avalanche counters (PPACs) installed at F3, F5, F7 were used. The sufficient number of beam particles were obtained, as listed in Table 1. The ratio of ^3H as a contaminant in the beam was typically 14% at F13.

Table 1: Number of beam particles on the secondary target. $\Delta p/p$ denotes the momentum acceptance of the BigRIPS.

Beam	Energy [MeV/nucleon]	$\Delta p/p$ [%]	Number of beam particles	
			Required	Obtained
^{11}Li	246	3.2	9.5×10^9	1.6×10^{10}
^{14}Be	265	3.2	1.8×10^9	2.3×10^9
^{17}B	277	3.2	8.6×10^7	1.6×10^9
^{19}B	224	3.2	4.3×10^7	9.8×10^6

Figure 1 shows a schematic view of the experimental setup. The active collimator consists of plastic scintillator and 30-cm-thick lead was placed just before the target to protect the MINOS time projection chamber (TPC) from ^3H . The reaction point in a 15-cm-thick liquid hydrogen target was determined as an intersection of the trajectories of the beam and the recoil proton, reconstructed respectively by the BDC and the MINOS TPC. The momenta of decay neutrons, a knocked-out neutron, and a recoil proton were determined respectively by the NEBULA, [4] the WINDS, [5] and a recoil proton detector (RPD) setup consisting of an MWDC and a plastic scintillator array. The charged fragments were identified and momentum analyzed by the SAMURAI spectrometer [6] using the two MWDCs (FDC1 and FDC2) followed by the hodoscopes (HODF and

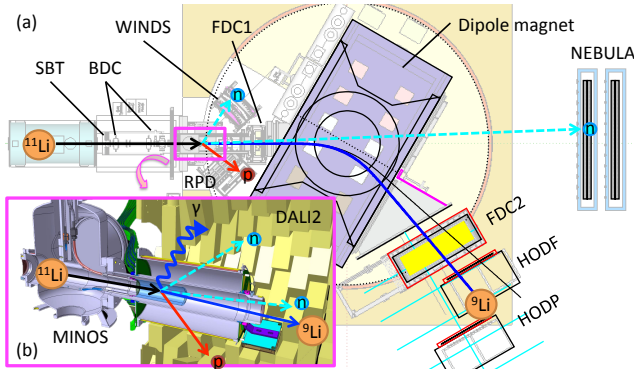


Figure 1: (a) Schematic view of the setup. Trajectories of particles are shown by arrows. (b) Schematic view of the MINOS surrounded by the DALI2.

HODP). γ rays emitted from the excited beam residue were detected by the DALI2 [7].

The beam velocity was determined by using the time-of-flight (TOF) from F7 to F13 with a typical rigidity resolution of 1/1000. The rigidity of the beam residue was derived by using FDC1, FDC2, and reaction position information. A particle is traced in the SAMURAI magnet starting from the incoming vector using the Runge-Kutta method for the best position matching with the outgoing vector. The magnetic field calculated by the TOSCA is used for tracing the particle in the SAMURAI magnet. As for the analysis of the beam particle in the non-reacting channel, the rigidity resolution of 1/700 was obtained as designed. The overall momentum resolution in the reaction channel of 1/100 was obtained by employing the momentum conservation law, since it is difficult to evaluate the momentum resolution independently for decay neutron, knocked-out neutron and recoil proton. Detailed analysis is currently in progress.

We thank the staff of accelerators and BigRIPS for their effort and support. The theoretical support and discussion provided by Y. Kikuchi and K. Ogata are highly appreciated.

References

- [1] G. Bertsch and H. Esbensen, *Ann. Phys.* **209**, 327 (1991).
- [2] Y. Kikuchi *et al.*, *Phys. Rev. C* **87**, 034606 (2013).
- [3] A. Obertelli *et al.*, *Eur. Phys. Jour. A* **50**, 8 (2014).
- [4] Y. Kondo *et al.*, *RIKEN Accel. Prog. Rep.* **45**, 131 (2012).
- [5] K. Yako *et al.*, *RIKEN Accel. Prog. Rep.* **45**, 137 (2012).
- [6] T. Kobayashi *et al.*, *Nucl. Instr. Meth.* **B317**, 294 (2013).
- [7] S. Takeuchi *et al.*, *Nucl. Instr. Meth. A* **763**, 596 (2014).

Isomer spectroscopy in the vicinity of ^{54}Ca at SHARAQ

Y. Kiyokawa, S. Michimasa, M. Kobayashi, R. Yokoyama, D. Nishimura^a, A. Mizukami^a, H. Oikawa^a, K. Kobayashi^b, H. Baba^c, G.P.A. Berg^d, M. Dozono, N. Fukuda^c, T. Furuno^e, E. Ideguchi^f, N. Inabe^c, T. Kawabata^e, S. Kawase, K. Kisamori, T. Kubo^c, Y. Kubota, C.S. Lee, M. Matsushita, H. Miya, H. Nagakura^b, S. Ota, H. Sakai^c, S. Shimoura, A. Stolz^g, H. Suzuki^c, M. Takaki, H. Takeda, S. Takeuchi^c, H. Tokieda, T. Uesaka^c, K. Yako, Y. Yamaguchi^b, Y. Yanagisawa^c, and K. Yoshida^c

Center for Nuclear Study, Graduate School of Science, University of Tokyo

^a*Department of Physics, Tokyo University of Science*

^b*Department of Physics, Rikkyo University*

^c*RIKEN Nishina Center*

^d*JINA and the Department of Physics, University of Notre Dame*

^e*Department of Physics, Kyoto University*

^f*Research Center for Nuclear Physics, Osaka University*

^g*National Superconducting Cyclotron Laboratory, Michigan State University*

Several studies have reported that neutron rich isotopes around the neutron number $N = 34$ have isomeric states [1–5]. Known isomers are highlighted in the nuclear chart in Fig 1. They locate in the nuclear region of $A/Q < 2.7$, more neutron-rich nuclei have been not reported yet. Since short-lived nuclei in the vicinity of $^{54}_{20}\text{Ca}_{34}$ were produced and identified in the SHARAQ03 experiment [6], we measured the γ -rays emitted from those nuclei at the focal plane of SHARAQ (S2), which allowed one to study isomeric states around the $N = 34$ region. Moreover, we note that the mass measurement needs the information on the isomeric states that might cause a systematic shift of a nuclear mass.

^{55}Cr	^{56}Cr	^{57}Cr	^{58}Cr	^{59}Cr	^{60}Cr	^{61}Cr	^{62}Cr	^{63}Cr	^{64}Cr
^{54}V	^{55}V	^{56}V	^{57}V	^{58}V	^{59}V	^{60}V	^{61}V	^{62}V	^{63}V
^{53}Ti	^{54}Ti	^{55}Ti	^{56}Ti	^{57}Ti	^{58}Ti	^{59}Ti	^{60}Ti	^{61}Ti	^{62}Ti
^{52}Sc	^{53}Sc	^{54}Sc	^{55}Sc	^{56}Sc	^{57}Sc	^{58}Sc	^{59}Sc	^{60}Sc	^{61}Sc
^{51}Ca	^{52}Ca	^{53}Ca	^{54}Ca	^{55}Ca	^{56}Ca	^{57}Ca	^{58}Ca		
^{50}K	^{51}K	^{52}K	^{53}K	^{54}K	^{55}K	^{56}K	^{57}K		

Figure 1: Nuclear chart around $N = 34$ region. Known isomers are highlighted.

The experiment was performed at the RIKEN RI Beam Factory (RIBF). Neutron-rich isotopes in the vicinity of ^{56}Sc were produced by projectile fragmentation of ^{70}Zn at 345 MeV/nucleon by bombarding a ^9Be target. Nuclei were separated and particles were identified on an event-by-event basis by the TOF-B ρ -dE method. Details of the experimental setup for particle identification can be found in Ref. [6].

Delayed γ rays were measured by a γ -ray detector array consisting of 2 HPGe and 16 NaI(Tl) detectors, installed outside the vacuum chamber at the downstream side of the final focal plane (S2) of the SHARAQ beam line. Figure 2 shows a schematic view of the γ -ray detector array and the detectors around S2. A 20-mm-thick plastic scintillator was placed as a beam stopper for Sc isotopes at the center of the detector array. A 12-mm-thick aluminum de-

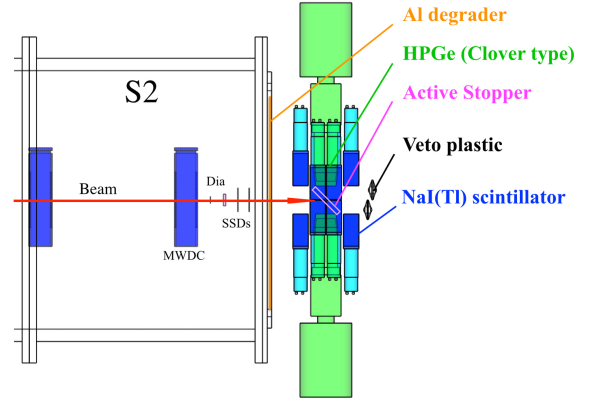


Figure 2: Schematic view of the isomer tagging system at the downstream side of the final focal plane of SHARAQ(S2).

grader was installed upstream to adjust the stopping range of the nuclei of interest. A veto scintillator was installed at the downstream side of the γ -ray detector array to reject events where the nuclei penetrated the stopper.

The dynamic range of the HPGe and NaI(Tl) detectors covers γ -rays up to 3 MeV. The energy resolution of the HPGe [NaI(Tl)] detectors was about 4 keV [83 keV] at 1333 keV [662 keV] in FWHM. The full-energy peak efficiency of the HPGe detectors was 0.6% for 1333 keV γ rays. The decay time window for γ -ray spectra was set to 100 ns – 15 μ s after the particles arrived at stopper.

The data acquisition (DAQ) system for the γ -ray detector array was separated from the one for the particle identification, and operated with single triggers from the HPGe or NaI(Tl) detectors. Hence, the data of delayed γ -rays were recorded without changing the trigger logic of mass measurement at S2. Every data in each DAQ system is labeled by a common timestamp so that one can correlate the γ -ray data with the data of particle identified by SHARAQ. The data rates on each DAQ were 2 kcps for particle identification, and 8 kcps for γ -ray detector array.

Figure 3 shows the particle identification of the secondary beams. Gamma-ray energy spectra were obtained

Table 1: γ -ray energies and half-lives of previously known isomers observed in the present work. The previously reported γ -ray energies and half-lives are presented for comparison along with the references.

Isomers	E_γ (keV)	$T_{1/2}(\mu\text{s})$	Literature		
			E_γ	$T_{1/2}(\mu\text{s})$	Ref.
$^{50}\text{K}^m$	127;171	0.125	44;70;101;127.4;171.4	0.125(40)	[3]
$^{43}\text{S}^m$	320.4	0.415	319	0.478(48)	[4]
$^{59}\text{Ti}^m$	110	0.400	109	0.587(57)	[5]

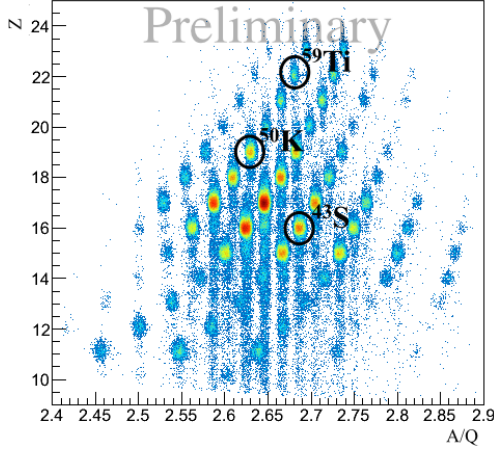


Figure 3: Particle identification of the secondary beams.

after reconstructing the event from the data according to the timestamps.

The microsecond isomers that we have observed in the present experiment are summarized in Table 1. The energies and half-lives of the observed γ -rays were consistent with those of previous measurements [3–5]. The γ -ray spectra are shown in Fig.4. The left panels show the delayed γ -ray energy spectra for (a) ^{50}K , (b) ^{43}S , and (c) ^{59}Ti after the prompt γ -ray emission (see caption for details). Peaks of the delayed γ -rays were clearly identified at 171 keV for ^{50}K , 320 keV for ^{43}S , and 110 keV for ^{59}Ti . The right panels show the γ -ray energy-time correlation with the insets showing the decay spectra obtained by gating on the γ -ray peaks.

Further analysis of the identification of new isomeric states, half-lives, and isomer ratios is in progress.

References

- [1] M. N. Mineva *et al.*, Eur. Phys. J. A **11**, 9 (2001).
- [2] H. L. Crawford *et al.*, Phys. Rev. C **82**, 014311 (2010).
- [3] J.M. Daugas *et al.*: Phys. Rev. C. **81**, 034304 (2010).
- [4] F. Sarazin *et al.*, Phys. Rev. Lett. **84**, 5062 (2000).
- [5] D. Kameda *et al.*: Phys. Rev. C. **86**, 054319 (2012).
- [6] M. Kobayashi *et al.*: in this report.

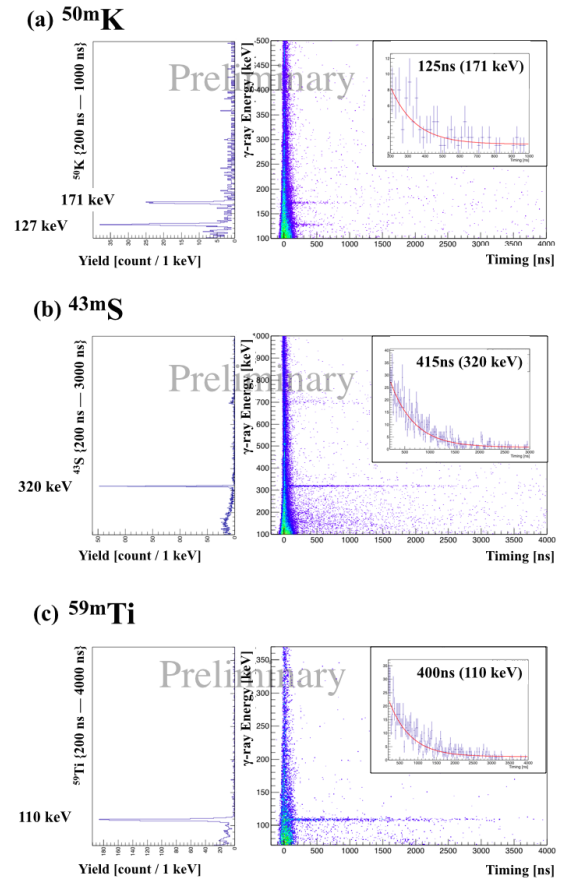


Figure 4: Left panels show the energy spectra of delayed γ -rays measured by the HPGe in (a) ^{50}K (gated by 200 – 1000 ns), (b) ^{43}S (gated by 200 –3000 ns), and (c) ^{59}Ti (gated by 200 –4000 ns). Right panels show the γ -ray energy-time correlation, where the insets indicate decay spectra for (a) ^{50}K (gated on 171 keV γ -rays), (b) ^{43}S (gated on 320 keV), and (c) ^{59}Ti (gated on 110 keV).

Interaction of ^8B , unstable-loosely-bound, with ^{208}Pb : scattering and breakup

C. Signorini^a, A. Boiano^b, C. Boiano^c, M. La Commara^b, C. Manea^d, M. Mazzocco^d,
C. Parascandolo^b, D. Pierroutsakou^b, A.M. Sanchez-Benitez^e, E. Strano^d, D. Torresi^d,
H. Yamaguchi^f, D. Kahl^f, Y. Hirayama^g, H. Ishiyama^g, N. Imai^{f,g}, N. Iwasa^h, S.C. Jeong^{g,m},
S. Kimura^g, Y.H. Kim^g, S. Kubono^{f,i}, H. Miyatake^g, M. Mukai^g, T. Nakao^g, Y. Sakaguchi^f,
T. Teranishi^j, Y. Wakabayashiⁱ, Y.X. Watanabe^g, C.J. Lin^k, H.M. Jia^k, L. Yang^k and Y.Y. Yang^l

^a INFN, LNL, viale dell'Università 2, I-35020 Legnaro (Padova), Italy

^b Department of Physics and INFN, via Cinthia, I-80126 Napoli, Italy

^c INFN-Sezione di Milano, via Celoria 16, I-20133, Milano, Italy

^d Dept. of Physics and Astronomy and INFN, Via Marzolo 8, I-35131 Padova, Italy

^e University of Lisbon, Nuclear Physics Centre, Avda. Prof. Gama Pinto 2, 1649-003, Lisbon, Portugal

^f CNS University of Tokyo, RIKEN campus, 2-1 Hirosawa, Wako, Saitama 351-0198, Japan

^g KEK, 1-1 Oho, Tsukuba, Ibaraki 305-0801, Japan

^h Department of Physics, Tohoku University, Aoba, Sendai, Miyagi 980-8578, Japan

ⁱ RIKEN Nishina Center, 2-1 Hirosawa, Wako, Saitama 351-0198, Japan

^j Department of Physics, Kyushu University, 6-10-1 Hakozaki, Fukuoka 812-8581, Japan

^k China Institute of Atomic Energy, P.O. Box 275(10), Beijing 102413, China

^l Institute of Modern Physics, Chinese Academy of Sciences, Lanzhou 730000, China

^m Institute for Basic Science, 70, Yuseong-daero 1689-gil, Yuseong-gu, Daejeon 305-811, Republic of Korea

The main motivation of this experiment was the investigation of the reaction dynamics induced by the radioactive ion-beam ^8B , extremely loosely bound with $S_p = 137.5$ keV, at Coulomb barrier energy: i.e. reaction cross section deduced from elastic scattering, as well as the transfer and/or breakup processes.

The ^8B beam, provided by the CRIB facility, was produced via the inverse kinematics reaction $^3\text{He}(^6\text{Li}, ^8\text{B})\text{n}$. The primary ^6Li beam intensity was ranging from 1 to 3 e μA , resulting in a ^8B intensity of $\sim 10^4$ Hz, with an energy of 50 ± 1 MeV. The ^6Li ion source had to be retuned twice due to the total consumption of the lithium material. This resulted in two days of beamtime lost, allowing us to accumulate statistics of four days beamtime on target. As expected, the ^8B beam was contaminated by ^7Be , via the $^3\text{He}(^6\text{Li}, ^7\text{Be})\text{d}$ reaction, by ^3He , recoiling from the ^3He material of the production gas target, and by some ^6Li halo (originating from the primary beam, that was around 10^8 times more intense than the secondary one); thus, the achieved ^8B beam purity was around 20%. The contaminations did not constitute a problem since each beam species was identified via a time of flight technique with respect to the cyclotron radiofrequency. Light charged particles produced in the reaction were detected and identified with six ΔE -E telescopes, consisting of a $40\text{-}50 \mu\text{m} + 300 \mu\text{m}$ Double Sided Silicon Strip detectors. The detectors were arranged symmetrically around the target at a distance of around 11 cm. All the detectors with the related electronics were brought from Italy [1]. For the E-detectors we utilized for the first time ASIC digital electronics, while for the ΔE detectors low-noise electronics was employed, also fully developed in Italy [2,3]. The charged particles iden-

tified were ^8B , ^7Be , ^6Li , ^4He , ^3He and protons, confirming our preliminary estimates: namely, the existence of a consistent amount of transfer (p transferred with ^7Be out) and breakup processes ($^8\text{B} \rightarrow ^7\text{Be} + \text{p}$, and possible subsequent ^7Be breakup $\rightarrow ^3\text{He} + ^4\text{He}$).

Preliminary data from the angular distribution of the ^8B elastic scattering, shown in Fig. 1, with a total reaction cross section larger than 1500 mb(!), confirm our expectations of a strong absorption occurring in the ^8B -induced reactions.

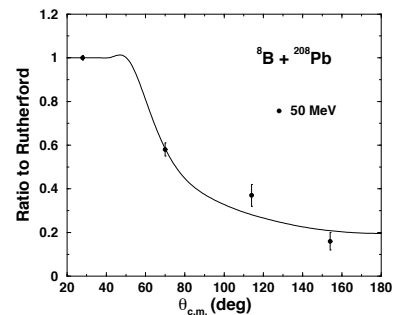


Figure 1. Elastic scattering angular distribution (preliminary).

References

- [1] E. Strano *et al.*, Nucl. Instr. and Meth. B **317** (2013) 657.
- [2] C. Boiano *et al.*, IEEE Nucl. Science Symposium and Medical Imaging Conference **14-34** (2012) 865.
- [3] C. Boiano *et al.*, IEEE Nucl. Science Symposium, Conference Records **1-173** (2009) 1399.

New resonances in ^{34}Ar via $^{30}\text{S}+\alpha$ elastic scattering

D. Kahl, A. A. Chen^a, S. Kubono, H. Yamaguchi, D. N. Binh, J. Chen^a, S. Cherubini^b, N. N. Duy^c,
T. Hashimoto, S. Hayakawa, N. Iwasa^d, H. S. Jung^e, S. Kato^f, Y. K. Kwon^e, S. Michimasa,
S. Nishimura^g, S. Ota, K. Setoodehnia^a, T. Teranishi^h, H. Tokieda, T. Yamada^d, C. C. Yun^e,
L. Y. Zhangⁱ

Center for Nuclear Study, Graduate School of Science, University of Tokyo, Japan

^a*Department of Physics & Astronomy, McMaster University, Canada*

^b*Department of Physics, University of Catania & INFN-LNS, Italy*

^c*Institute of Physics, Vietnam*

^d*Department of Physics, Tohoku University, Japan*

^e*Department of Physics, Chung-Ang University, Korea*

^f*Department of Physics, Yamagata University, Japan*

^g*RIKEN (The Institute of Physical and Chemical Research), Japan*

^h*Department of Physics, Kyushu University, Japan*

ⁱ*Institute of Modern Physics, Chinese Academy of Sciences, China*

1. Introduction

X-ray bursts (XRBs) arise from thermonuclear runaway on the surface of accreting neutron star binaries, and are the most frequent thermonuclear explosions in the galaxy. Although the nuclear reaction network includes hundreds of species and thousands of nuclear transmutations, it is actually only a small subset of these nuclear transmutations which need to be known precisely, as they make a predominant contribution to the nuclear trajectory to higher mass and energy generation.

The $^{30}\text{S}(\alpha, p)$ reaction is identified as one such important reaction, contributing more than 5% to the total energy generation [1], influencing the neutron star crustal composition [2] relevant to compositional inertia, moving material away from the ^{30}S waiting point [3], and possibly accounting for double-peaked XRBs [4].

Unfortunately, there is very little experimental information on the $^{30}\text{S}(\alpha, p)$ stellar reaction rate nor the structure of ^{34}Ar above the alpha-threshold, essentially limited to a preliminary report on a transfer reaction study of the compound nucleus ^{34}Ar at high excitation energy [5] and a time-reversal study [6]. The present work is the first experimental investigation using the entrance channel $^{30}\text{S}+\alpha$.

2. Experiment

We performed a measurement of ^{30}S alpha resonant elastic scattering using the thick-target inverse-kinematics technique using CRIB [7]. The radioactive ^{30}S beam was produced in-flight via the $^3\text{He}(^{28}\text{Si}, ^{30}\text{S})n$ reaction [8]. The ^{30}S beam arrived on target at 1.6 MeV/u, an average of 30% purity, and with an intensity of 10^4 particles per second.

The beam was tracked by two parallel plate avalanche counters (PPACs), before impinging on a newly developed active target system [9]. The active target system was filled with 90% He and 10% CO₂ at 194 Torr, comprised of a field cage, a low-gain region surrounded on three sides by a high-gain region and silicon strip detector telescopes. Between the field cage and the backgammon-type readout pads were gas electron multiplier (GEM) foils to control the specific gain. Each portion of the active target can measure the three-dimensional position of ionizing radiation (using pad number, charge comparison on two opposite sides, and electron drift time, respectively) as well as the local

energy loss ΔE (total charge collected on one pad). We measured scattered alpha particles over laboratory angles of $10^\circ \leq \theta_{\text{lab}} \leq 25^\circ$ and center-of-mass energies from 1.8 MeV $\leq E_{\text{cm}} \leq 5.5$ MeV.

3. Results

We determined the center-of-mass energy event-by-event for scattered alpha particles to produce the $^{30}\text{S}+\alpha$ spectrum. The resulting excitation function is shown as the blue data points in Figure 1, where the errors are statistical.

To extract the parameters of the observed resonances, we used an *R*-Matrix formalism [10] computed via the SAMMY8 code [11]. The location of the resonance is determined by the resonance energy E_r , the shape of the resonance from the angular momentum transfer ℓ , the height of the resonance from the alpha partial width Γ_α , and the width of the resonance from the total width Γ . The total width Γ is the sum of the proton and alpha partial widths, as the gamma width is negligible in comparison so far above the particle thresholds. To estimate the proton width Γ_p , we considered the spectroscopic factor θ_i^2 for each channel, and introduced a universal spectroscopic ratio ξ for the three resonances:

$$\theta_\alpha^2 = \Gamma_\alpha / W_{\Gamma\alpha}; \quad \theta_p^2 = \Gamma_p / W_{\Gamma p}; \quad (1)$$

$$\xi \equiv \theta_p^2 / \theta_\alpha^2; \quad \therefore \Gamma_p = \xi \theta_\alpha^2 W_{\Gamma p}. \quad (2)$$

Two acceptable *R*-Matrix fits are shown in Figure 1 along with the case of pure Coulomb scattering. The adopted level parameters are shown in Table 1, where we found the best fit for $\xi = 0.8\%$.

Table 1: Adopted level parameters for new states in ^{34}Ar from the present work, derived from the best fit in Figure 1.

E_r (MeV)	ℓ_α	J_r^π	Γ_α (keV)	Γ_p (keV)	θ_α^2 %
4.35 ± 0.07	2, 3	$(2^+, 3^-)$	$0.8_{-0.4}^{+0.4}$	1.3	15
4.75 ± 0.08	2	2^+	12_{-6}^{+6}	9.7	30
5.52 ± 0.13	1	(1^-)	290_{-200}^{+0}	65	> 99

It is useful to include the preliminary results from RCNP [5] in a calculation of the $^{30}\text{S}(\alpha, p)$ stellar reaction rate.

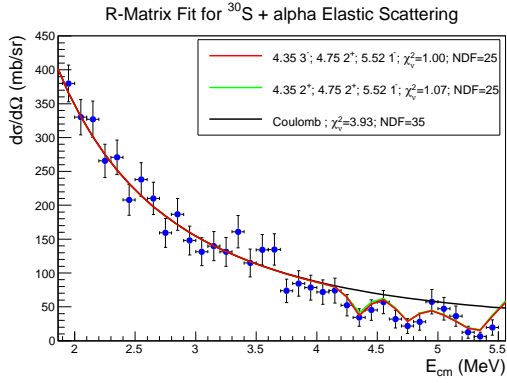


Figure 1: $^{30}\text{S}+\alpha$ elastic scattering excitation function. The bumps observed around 3.5 MeV correspond to a region of large alpha-background which are a component of the cocktail beam; even introducing resonances with the Wigner limit do not make a noticeable change to the R -Matrix curve in this region.

However, the preliminary results from RCNP only provide us with rough resonance energies, and some assumptions are required. We assumed that each state has $J_r^\pi = 0^+$, and that $\Gamma_\alpha = \frac{1}{2}W_{\Gamma_\alpha}$, where the Wigner limit $W_{\Gamma_\alpha} = 3\hbar/\mu R^2 P_l$, with μ the reduced mass, R the channel radius, and P_l the penetrability. We also use the standard simplification that $\gamma = (\Gamma_\alpha \Gamma_p)/(\Gamma_\alpha + \Gamma_p) \approx \Gamma_\alpha$ when $\Gamma_\alpha \ll \Gamma_p$. The resulting resonance strength $\omega\gamma$ is constant within a factor of around two to three for $J \leq 3$ (although it quickly drops off for $J \geq 4$); this is because we parameterize the width based on the Wigner limit, and the penetrability P_l decreases with increasing J , whereas for the $^{30}\text{S}+\alpha$ entrance channel $\omega = 2J_r + 1$. While the contribution from an individual resonance calculated in this manner will be unreliable, the sum of these contributions can be considered an upper limit under an extreme assumption.

The calculated rates are plotted and compared against the NON-SMOKER [12] Hauser-Feshbach statistical model in Figure 2. The XRB model of the double-peaked structure required a reaction rate a factor of 10^2 greater than the statistical model to quench the proposed waiting point near ^{30}S [4]. Our new reaction rate evaluated with all known level structure of ^{34}Ar is inconsistent with a reaction rate deviating more than a factor of around 2 larger than the statistical model rate.

4. Summary

We investigated the alpha-cluster structure of ^{34}Ar for the first time, using ^{30}S alpha resonant elastic scattering. Several new levels with large alpha-widths were discovered. The work demonstrates that while strong alpha resonances exist above the alpha-threshold in ^{34}Ar , they do not cause the stellar reaction rate to increase in a significant manner, vindicating the ^{30}S waiting point evidenced in many models assuming the statistical reaction rate.

References

- [1] A. Parikh, J. José, F. Moreno, C. Iliadis, *The Astrophysical Journal Supplement Series* **178** (2008) 110.
- [2] H. Schatz, K.E. Rehm, *Nuclear Physics A* **777** (2006) 601.
- [3] C. Iliadis, P.M. Endt, N. Prantzos, W.J. Thompson, *The Astrophysical Journal* **524** (1999) 434.
- [4] J.L. Fisker, F.K. Thielemann, M. Wiescher, *The Astro-*

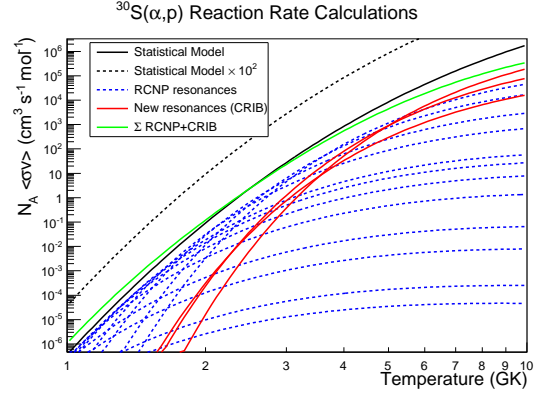


Figure 2: Calculations of the $^{30}\text{S}(\alpha, p)$ stellar reaction rate. The statistical model rate (increased by a factor of 10^2) from NON-SMOKER [12] is shown as the solid (dashed) black line. The dashed blue lines represent resonances from a preliminary report of an experiment [5], where we made many assumptions about their quantum properties. The solid red lines represent our new higher-energy resonances. The sum of the RCNP and CRIB resonant contributions is shown in green.

- physical Journal, Letters **608** (2004) L61.
- [5] S. O'Brien *et al.*, *American Institute of Physics Conference Series* **1090** (2009) 288.
- [6] C.M. Deibel *et al.*, *Phys. Rev. C* **84** (2011) 045802.
- [7] Y. Yanagisawa *et al.*, *Nuclear Instruments and Methods in Physics Research A* **539** (2005) 74.
- [8] D. Kahl *et al.*, *American Institute of Physics Conference Series* **1213** (2010) 208.
- [9] D. Kahl *et al.*, *American Institute of Physics Conference Series* **1594** (2014) 163.
- [10] A.M. Lane, R.G. Thomas, *Reviews of Modern Physics* **30** (1958) 257.
- [11] N. Larson (2000), ORNL/TM-9179/R5 (Unpublished).
- [12] T. Rauscher, F.K. Thielemann, *Atomic Data and Nuclear Data Tables* **79** (2001) 47.

Progress of analysis for searching for linear-chain cluster states in ^{14}C

Y. Sakaguchi, H. Yamaguchi, D. Kahl, T. Nakao, S. Hayakawa^a, A. Kim^b, D. H. Kim^b, P. S. Lee^c, S. M. Cha^d, K. Y. Chae^d, M. S. Gwak^d, J. H. Lee^d, Y. H. Kim^{e,f},

Center for Nuclear Study, Graduate School of Science, University of Tokyo

^a*Department of Physics, University of Catania & INFN, Italy*

^b*Department of Physics, Ewha Womans University, Korea*

^c*Department of Physics, Chung-Ang University, Korea*

^d*Department of Physics, ShungKyunKwan University, Korea*

^e*Department of Physics & Astronomy, Seoul National University, Korea*

^f*KEK, Japan*

1. Introduction

In spite of long history of the study for linear-chain cluster state, there is no clear evidence of linear-chain states. By using AMD method, Suhara and En'yo [1, 2] obtained a band (0_5^+ , 2_6^+ , 4_6^+) in which the levels can be explained as linear-chain cluster states, and the levels are located at a few MeV above the $^{10}\text{B}+\alpha$ threshold in ^{14}C .

The excited states in ^{14}C have been studied by various reactions [3–8] for the interest of the cluster states, but only the energies are determined. In order to discuss the structure precisely, we need more information of resonant parameters such as J^π and α widths.

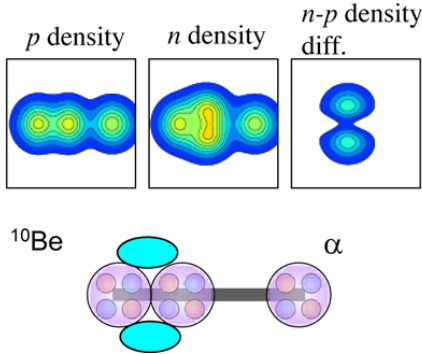


Figure 1: The AMD wave function which was calculated [1] [2]. This intuitive picture of the linear-chain cluster state 0_5^+ in ^{14}C in the bottom.

The configuration of the 0_5^+ state in the band is shown in Figure 1. The intuitive configuration implies we can access the state by the $^{10}\text{Be}+\alpha$ resonant scattering.

In January 2014, we conducted experiment for the ^{10}Be beam production and the $^{10}\text{Be}+\alpha$ scattering. This was the test experiment for the $^{10}\text{Be}+\alpha$ scattering experiment in May 2015. We analyzed roughly and obtain a histogram which has some peaks possibly made from $^{10}\text{Be}+\alpha$ resonant elastic scattering.

2. Experimental Method

CRIB, the RI beam separator, was used. The primary beam $^{11}\text{B}^{5+}$ had an energy of 5.0MeV/u. The reaction to make the ^{10}Be beam was $^{11}\text{B}(d,^3\text{He})^{10}\text{Be}$. ^{10}Be beam was selected by using the double achromatic system and Wien filter in CRIB. The ^{10}Be beam entered into our reaction chamber in which we filled He gas. $^{10}\text{Be}+\alpha$ resonant elastic scattering occurred in the reaction chamber.

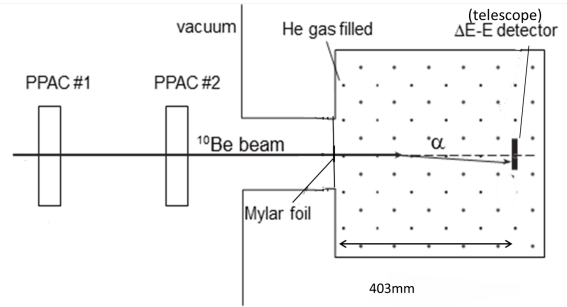


Figure 2: Setup in our reaction chamber

The thick target method in inverse kinematics was applied. The beam energy decreased gradually in the thick target, and we obtained the excitation function at certain energy range by a single initial beam energy.

Figure 2 shows the reaction chamber setup. The distance between the window and the telescope in reaction chamber was 403 mm. The telescope was composed of 2 layers. The first layer was 20 μm Si detector, and the second layer was 480 μm Si detector. The both detectors had a surface area of 50 x 50 mm^2 . The first detector had 16 strips and it has X-direction (horizontal) position sensitivity by these strip. The second detector had 16 strips in X direction and 16 strips in Y direction (vertical direction). It had XY-direction position sensitivity by these strips.

3. Result

We succeeded in making ^{10}Be beam. The purity was about 60 %, and the intensity was 1.47×10^4 cps.

We had a problem about the calibration before the experiment. α particles which have certain energies above about 4.4 MeV penetrated the first thin detector, so the α particles didn't lose their all energies in the first thin detector. The deposited energies were not same with the original energies of the α particles. We were not able to know how much the α particles lost energies in the first thin detector. We didn't have the relation between the deposited energies in channel scale and the actual energy loss in scale of MeV, so the calibration was impossible if we set our α source which emits 4.780, 5.480 and 5.795 MeV α particles. We set the thin detectors so that the α particles enter into the thin detector not perpendicularly but very obliquely. By this way, the α particles passed through the longer active area in the thin detector, and the α particles whose energies were more decreased stopped at the thin detector.

We calculated the energy losses of the α particles by using the extra thickness of the dead layer made by this

method as a parameter with a program for calculation, *enewz* which is composed of codes made by Ziegler et al. [9]. The α particles from the source which was set very obliquely stopped in the thin detector, and lost their all energies, so we obtained the correspondence between the energy losses revealed as channel scale and the exact energy losses in MeV. However the α particles we would like to detect in the $^{10}\text{Be}+\alpha$ reactions entered into the detector almost perpendicularly. If α particles enter into the detector obliquely, the α particles pass through a longer dead layer on the detector, and there are more energy losses than perpendicularly. So this calibration parameters didn't reproduce the energies of α particles which entered perpendicularly. We used the extra thickness of the dead layer as a parameter, calculated the extra energy loss with changing it, and checked whether offsets, calibration parameters, were acceptable values. By this method, we found that the extra thickness was $1.6\ \mu\text{m}$, and determined the calibration parameters for the first thin detector.

We calibrated the thin detector and the thick detector. After that we put together these detectors as the telescope and calibrated the telescope by the α source. There was a dead layer between these detectors, so particles lost energies in the layer. We treated the thickness of this dead layer as a parameter, calculated the energy losses with changing a value of the parameter, checked whether those reproduced α particles energies from the source when we summed not only the energies from the detectors but also the energy losses in the dead layer, and determined the thickness. The thickness was $0.8\ \mu\text{m}$. The reaction chamber was filled with He gas, and there was a distance of 16 mm between the first detector and the second detector, so there was an energy loss caused by the He gas between them. In order to modify this energy loss, we calculated the energy loss by the He gas, and modified this. We succeeded in reproducing the peaks of 4.780, 5.480 and 5.795 MeV from the α source within about 100keV in histograms.

We eliminated the data of contaminations by using the PPACs data and the telescope data in our reaction chamber (Figure 2). In order to select the ^{10}Be beam, we used two kinds of data. Firstly, we used the duration time between the time at which a trigger was made at PPACs and the time at which a signal came from our AVF cyclotron. Secondly, the flight time of particles which passed through the PPAC#1 and PPAC#2. Besides these selection for the ^{10}Be beam, we needed to exclude the data of the particles which didn't enter into reaction chamber. The diameter of the window on the upstream side of reaction chamber was 4 cm. We extrapolated the beam at the window position by using the position data of PPAC#1 and PPAC#2, and excluded the data of particles which didn't pass through the window on the upstream side of the reaction chamber.

We needed to find the scattered α particles out from particles which reached the telescope. We made a two dimensional plot whose one axis revealed the deposited energies and the other axis revealed the total energies. The locus of α particles on that plot had been known, so we succeeded in find α particles. After that we needed to distinguish if the α particles were scattered or not, because α particles were made in the upstream in CRIB. The scattered α duration time between the time when particles reached the PPACs and the time when particles hit the detectors had a certain range. We distinguish the scattered α particles by this duration time.

By these selections, we identified the $^{10}\text{Be}+\alpha$ resonant elastic scattering. Some peaks which were possibly made from the resonant scattering are shown in Figure 3.

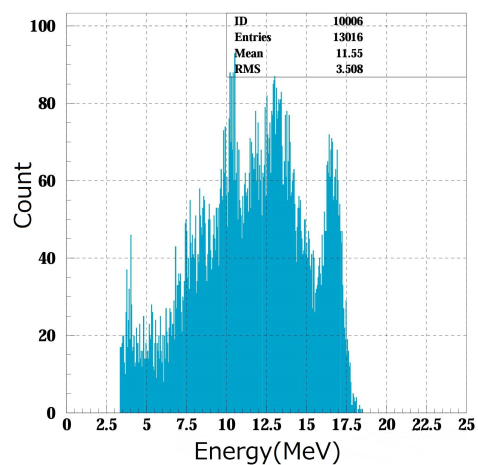


Figure 3: Preliminary energy spectrum of the scattered α particles. ^{10}Be beam intensity was 1.47×10^4 cps. This histogram includes about 14 hours run.

References

- [1] T. Suhara and Y.Kanada-En'yo, Phys. Rev. C **82**, 044301 (2010).
- [2] T. Suhara and Y.Kanada-En'yo, Phys. Rev. C **84**, 024328 (2011).
- [3] N.Soic *et al*, Phys. Rev.C **68**, 014321 (2003).
- [4] W. Oertzen *et al*, Phys. J. A **21**, 193 (2004).
- [5] M. Milin *et al*, Nucl. Phys. A **730**, 285 (2004).
- [6] D. Price *et al*, Nucl. Phys. A **765**, 263 (2006).
- [7] D. L. Price *et al*, Phys. Rev. C **75**, 014305 (2007).
- [8] P. J. Haigh *et al*, Phys. Rev. C **78**, 014319 (2008).
- [9] J.F. Ziegler *et al*, " The Stopping and Range of Ions in Solids ", Pergamon Press, New York (1985).

Momentum distribution of the α - ^{16}O inter-cluster motion in ^{20}Ne nucleus

S. Hayakawa, C. Spitaleri^{a,b}, N. Burtebayev^c, A. Aimaganbetov^d, P. Figuera^a, M. Fisichella^a, G. L. Guardo^a, S. Igamov^e, I. Indelicato^a, G. Kiss^f, S. Kliczewski^g, M. La Cognata^a, L. Lamia^b, M. Lattuada^{ab}, E. Piasecki^h, G. G. Rapisarda^b, S. Romano^{a,b}, S. B. Sakuta^g, R. Siudak^g, A. Trzcińska^h, A. Tumino^{a,i}, and A. Urkinbayev^d

Center for Nuclear Study, Graduate School of Science, University of Tokyo

^aLaboratori Nazionali del Sud, Istituto Nazionale di Fisica Nucleare

^bDepartment of Physics and Astronomy, University of Catania

^cInstitute of Nuclear Physics, National Nuclear Center

^dGumilyov Eurasian National University

^eInstitute of Nuclear Physics, Academy of Science of Uzbekistan

^fATOMKI

^gThe H. Niewodniczański Institute of Nuclear Physics PAN

^hHeavy Ion Laboratory, Univ. of Warsaw

ⁱKore University of Enna

The $^{16}\text{O}+^{16}\text{O}$ fusion reaction is important in terms of the explosive oxygen burning process during late evolution stage of massive stars as well as understanding of the mechanism of heavy-ion fusion reactions at low energies. The astrophysical S -factor of such a heavy-ion fusion strongly depends on energy at corresponding stellar temperatures far below the Coulomb barrier. There are large discrepancies among different experiments [1–4], and among theoretical predictions [5, 6], and is a lack of data below $E_{\text{cm}} = 7$ MeV.

We aim to determine the excitation function of the most major products, $\alpha+^{28}\text{Si}$ and $p+^{31}\text{P}$, of the $^{16}\text{O}+^{16}\text{O}$ reaction at stellar energies by means of the Trojan Horse Method (THM) [7]. This is an indirect technique with advantage to measure an astrophysical two-body reaction approaching the Gamow-peak energy region through a three-body reaction performed at a beam energy, which allows us to overcome the Coulomb barrier in the reaction entrance channel as well as the electron screening due to atomic electrons.

We have performed THM measurements via the $^{16}\text{O}(^{20}\text{Ne}, \alpha\alpha)^{28}\text{Si}$ and $^{16}\text{O}(^{20}\text{Ne}, p\alpha)^{31}\text{P}$ three-body reactions at two different ^{20}Ne beam energies; 45 MeV at the Heavy Ion Laboratory, and 35 MeV at Gumilyov Eurasian National University. These beams are able to cover center-of-mass energy ranges of 8–15 MeV and of 5–11 MeV respectively. The higher-energy measurement was mainly in purpose of normalization of the THM cross section to known excitation functions in the higher part of this energy range, while the lower energy measurement aims at exploring the new data below $E_{\text{cm}} = 7$ MeV. In these three-body reactions, the α particles in the exit channels may act as the “spectator” through the quasi-free mechanism, where the momentum transfer of α decaying from the possible α cluster state in the projectile ^{20}Ne is sufficiently small.

The simplest expression of the three-body reaction cross section $d^3\sigma/d\Omega_1 d\Omega_2 dE_1$ by THM in the framework of the Plain Wave Impulse Approximation (PWIA) [8] has been successfully applied for several lighter nuclear systems [7];

$$\frac{d^3\sigma}{d\Omega_1 d\Omega_2 dE_1} \propto (\text{KF}) |\phi(p_s)|^2 \frac{d\sigma(E)^{\text{HOES}}}{d\Omega} \quad (1)$$

where (KF) is the kinematic factor, $|\phi(p_s)|^2$ is the momentum distribution of the spectator, and $d\sigma/d\Omega^{\text{HOES}}$ is the half-off-energy-shell (HOES) binary reaction of our in-

terest. For the projectile-breakup measurement, the momentum of the spectator is defined by subtraction of the beam velocity contribution from the momentum of α ; $\mathbf{p}_s \equiv \mathbf{p}_\alpha - m_\alpha/m_{^{20}\text{Ne}} \times \mathbf{p}_{^{20}\text{Ne}}$. To guarantee quasi-free mechanism, the two-cluster α - ^{16}O system in the nucleus ^{20}Ne should preferably be in s state, so that the momentum distribution $|\phi(p_s)|^2$ of the spectator α has a largest peak at $p_s = 0$. This is not obvious for our case since it is the first application of the THM to such a heavy nuclear system, in which more realistic treatment such as Distorted-Wave Born Approximation (DWBA) and Continuum Discretized Coupled Channels (CDCC) might be more appropriate [9] rather than PWIA. Here we report the analysis status of the higher-energy experiment for the momentum distribution investigated for the first time.

For the higher-energy measurement, a $^{20}\text{Ne}^{3+}$ beam was provided at 45 MeV from the $K = 160$ cyclotron with a typical intensity around 20 nA on target, and the production run was performed for about 180 hours in total. The experimental setup is illustrated in Fig. 1. For the beam col-

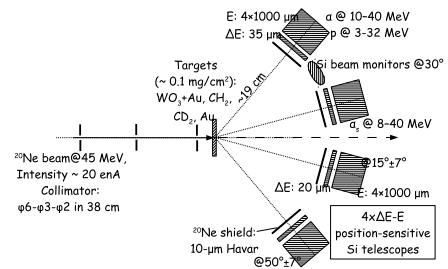


Figure 1: Schematic view of the experimental setup.

limator, a $\phi 6$ -, a $\phi 3$ - and a $\phi 2$ -mm hole are laid straight on the beam axis within a distance of 380 mm from the upstream, respectively. We utilized WO_3 evaporated onto a Au backing as solid oxygen target with a typical thickness of 116 mg/cm^2 for WO_3 and 193 mg/cm^2 for Au. Three silicon beam monitoring detectors were installed at 30° . For the reaction product measurement, four ΔE -E silicon telescopes were mounted symmetrically with respect to the beam axis at 15° and 50° . The thickness of each ΔE layer

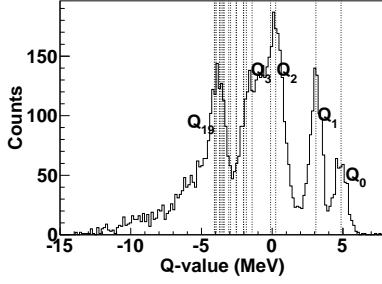


Figure 2: Q -value spectrum of the $^{16}\text{O}(^{20}\text{Ne}, \alpha\alpha)^{28}\text{Si}$ channel. The dotted lines corresponds to the excited states of ^{28}Si .

at 15° was $20\ \mu\text{m}$ in order to measure low-energy spectator α , while that at 50° was $35\ \text{mm}$ focusing on higher energy up to $40\ \text{MeV}$ of α of the coincidence pair. Each E layer consisted of a stack of four 1-mm-thick silicon detectors for high-energy proton up to $32\ \text{MeV}$. The first E layer was position-sensitive by charge division, and the distances from the target were typically $190\ \text{mm}$. We put a 10-mm Havar foil right in front of each ΔE layer to shield beam scattering and heavy-ion products. During the production run with the WO_3 target, Multiplicative particles were mostly identified as protons and α particles with the ΔE -E telescopes.

By selecting α - α coincident data, we confirmed that the peaks found in the Q -value spectrum which is defined by $Q = E_{28\text{Si}} - E_{20\text{Ne}} + E_{\alpha 1} + E_{\alpha 2}$ correspond well to the excited energy of ^{28}Si nucleus as shown in Fig. 2, which evinces the $^{16}\text{O}(^{20}\text{Ne}, \alpha\alpha)^{28}\text{Si}$ reaction. As for the $^{16}\text{O}(^{20}\text{Ne}, p\alpha)^{31}\text{P}$ channel, Q -value spectrum looks more smooth possibly because of poorer resolution of higher energy protons which punch through many layers of the silicon detectors, but the Q -value range is still reasonable.

To determine the momentum distribution $|\phi(p_s)|^2$, one needs to calculate Eq. 1 in sufficiently small energy and angular ranges where $d\sigma/d\Omega^{\text{HOES}}$ is approximately constant, since this value is unknown for most cases. However, since we had limited statistics and momentum range, we investigated the angular and energy distributions of the HOES cross section to apply to Eq. 1. We firstly checked one of the previous data of $^{16}\text{O} + ^{16}\text{O}$ reaction of Ref. [1]. They measured the total cross section of the $^{16}\text{O} + ^{16}\text{O}$ reaction by proton and α spectroscopy and also showed the angular distribution of $d\sigma/d\Omega^{\text{HOES}}$ at limited energies. Since their angular distribution of the $^{16}\text{O}(^{16}\text{O}, \alpha)^{28}\text{Si}$ reaction cross section is symmetric about 90° , we fitted it by Legendre polynomials of even orders up to $n = 6$. As shown in Fig. 3, we normalized this fitted function to our angular distribution of ^{28}Si - α relative angle at each energy bin of 2 MeV from 7 to 21 MeV, assuming the angular distribution is approximately common at any energy. Thus we calculated the momentum distribution $|\phi(p_s)|^2$ from Eq. 1. Figure 4 shows the preliminary momentum distribution. The fact that the momentum distribution does not have the maximum value around $p_s = 0$ suggests that the three-body reactions $^{16}\text{O}(^{20}\text{Ne}, \alpha\alpha)^{28}\text{Si}$ and $^{16}\text{O}(^{20}\text{Ne}, p\alpha)^{31}\text{P}$ might not proceed through the 0^+ ground state of ^{20}Ne dominantly but the 2^+ first excited state. By further data analysis, we aim to investigate whether a more realistic treatment mentioned above is needed, and how much statistics is confirmed as

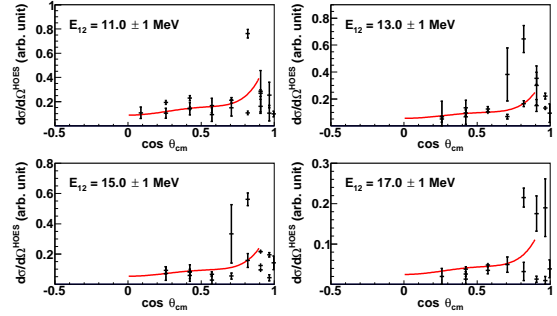


Figure 3: Example of the angular distribution of the $^{16}\text{O}(^{16}\text{O}, \alpha)^{28}\text{Si}$ reaction cross section fitted by the Legendre polynomials from 11 to 17 MeV.

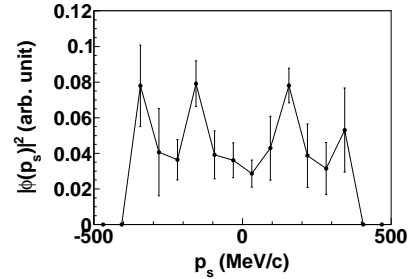


Figure 4: Preliminary momentum distribution of α in ^{20}Ne .

the quasi-free kinematics.

References

- [1] H. Spinka and H. Winkler, Nucl. Phys. **233** (1974) 456.
- [2] G. Hulke, C. Rolfs, and H. P. Trautvetter, Zeitschrift für Physik A, Atoms and Nuclei, **297** (1980) 161.
- [3] S. C. Wu and C. A. Barnes, Nucl. Phys. A, **422** (1984) 373.
- [4] J. Thomas *et al.*, Phys. Rev. C, **33** (1986) 1679.
- [5] C. L. Jiang *et al.*, Phys. Rev. C, **75** (2007) 1.
- [6] A. Diaztorres, L. Gasques, and M. Wiescher, Phys. Lett. B, **652** (2007) 255.
- [7] C. Spitaleri *et al.*, Phys. Atom. Nucl., **74** (2011) 1725.
- [8] G. F. Chew and G. C. Wick, Phys. Rev. **85** (1952) 636.
- [9] R. Tribble *et al.*, Rep. Prog. Phys. **77** (2014) 106901.

**Experiment Nuclear Physics: PHENIX
Experiment at BNL-RHIC and ALICE
Experiment at CERN-LHC**

Upgrade of the TPC Readout Control Unit for Run2

T. Gunji, H. Hamagaki, Y. Sekiguchi, J. Alme^a, C. Zhao^b, T. Alt^c, L. Bratrud^d, F. Costa^e, E. David^f,
T. Kiss^f, C. Lippmann^g, A. Ur Rehman^h

Center for Nuclear Study, Graduate School of Science, The University of Tokyo, Japan

^a Bergen University College, Norway

^b University of Oslo, Norway

^c Goethe University Frankfurt, Germany

^d Vestfold University College, Norway

^e CERN, Switzerland

^f Cerntech, Hungary

^g GSI Helmholtzzentrum für Schwerionenforschung, Germany

^h University of Bergen, Norway

1. Introduction

The ALICE experiment has been built to explore the new state of QCD matter by colliding the heavy-ions at nearly speed of light [1]. The Time Projection Chamber (TPC) is the main tracking and particle identification device in the central barrel of the ALICE detector. The TPC has a cylindrical fiducial volume of 88 m³ filled with Ne/CO₂(85/15) and is divided into two drift regions by the central electrode. The signal amplification is provided through an avalanche in the vicinity of the anode wires and the positive ions created in the avalanche induce a positive current signal on the pad plane. The TPC includes 557 568 readout pads and 4356 Front-End-Electronics (FECs), where a custom-made front-end chips consisted of charge sensitive preamplifier and shaping amplifier and ALTRO (ALice Tpc ReadOut chip) for ADC and DSP are mounted. 18 to 25 FECs are connected to one Readout Control Unit (RCU) via a multi-drop Gunning Transistor Logic (GTL) Bus and this RCU finally transfers data to ALICE DAQ system through the optical interface called as Detector Data Link (DDL). More details can be found in Ref. [3].

2. TPC RCU Upgrade

Currently, ALICE data taking rate in heavy-ion collisions is limited by the available bandwidth of the TPC. After the LHC Long Shutdown 1 (LS1), center-of-mass energy of the colliding beams will be increased to 13 TeV in *pp* and 5 TeV in Pb-Pb collisions, respectively. As a result, the event size is expected to increase by 40 % due to larger multiplicities and the radiation load on the TPC electronics will increase from 0.8 kHz/cm² to 3.0 kHz/cm². To improve the readout speed and radiation tolerance for Run2, the present RCU needs to be upgraded. As shown in Fig. 1, the upgrade to the RCU2 includes following aspects: the GTL bus is divided into four branches from the current two branches, the speed of the DDL is increased from 1.28 Gbps, the flash based and radiation tolerant Micorsemi Smartfusion2 (SF2) FPGA is used [4].

Figure 2 shows the picture of the RCU2 board, where the main components are SF2 FPGA as the main FPGA described below, ProASIC3 FPGA for the radiation monitoring and SECEDED (single error corrected and double error detection) operation, SFP interface for the data transfer, ethernet part for the ALICE Detector Control System, and the optical interface with the ALICE Trigger System (TTC).

Figure 3 shows the overview of the system in the SF2 FPGA of the RCU2. The RCU2 FPGA consists of two major components, the Readout System which is implemented

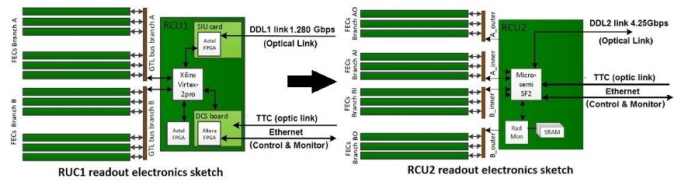


Figure 1: Upgrade from RCU1 and RCU2

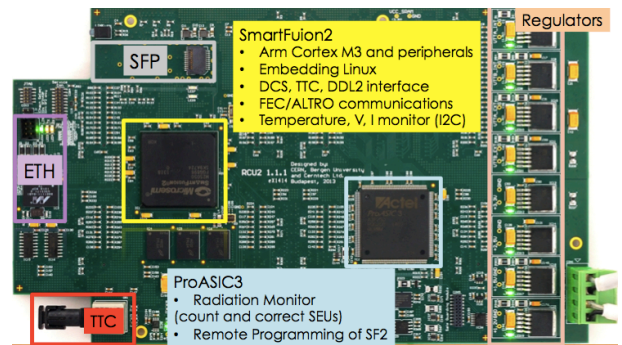


Figure 2: System Overview of the RCU2

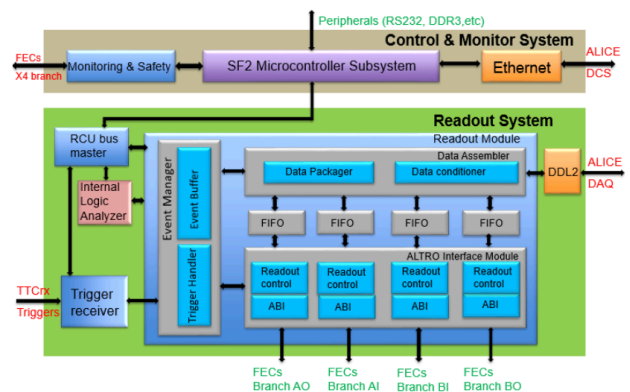


Figure 3: System Overview of the RCU2

in the fabric of SF2 FPGA and the Control and Monitoring System which runs on the SF2 Microcontroller Subsystem (MSS) [5]. The Readout System mainly consists of Trigger Receiver module and Readout Module, where Trigger

Receiver module processes the trigger sequence provided by the ALICE Central Trigger Processor (CTP) System and Readout module is responsible for reading data from four branches, checking data, merging, packaging into the ALICE data format, and sending through DDL2.

The Control and Monitoring System runs on SF2 Microcontroller Subsystem (MSS). The MSS provides I²C, SPI, Ethernet MAC, GPIO, UART, and RTC (real-time counter) peripherals. There are three DDR3 SDRAM memories (256 MB x 2 and one for SECDED) on the RCU2 and a tailored embedding Linux system is operated in the ARM-Cortex M3 in the MSS together with these three DDR3 memories. The Monitoring and Safety module runs on the Linux, obtains the voltage, current, and temperature readings from the FECs via a customized APB Bus protocol (the RCU2 bus), and sends them to the ALICE Detector Control System (DCS) via the ethernet (10M/100M). Figure 4 shows temperature, voltages, currents, and states for all 25 FECs shown at the Central DCS system, where the monitoring values are sent from RCU2.

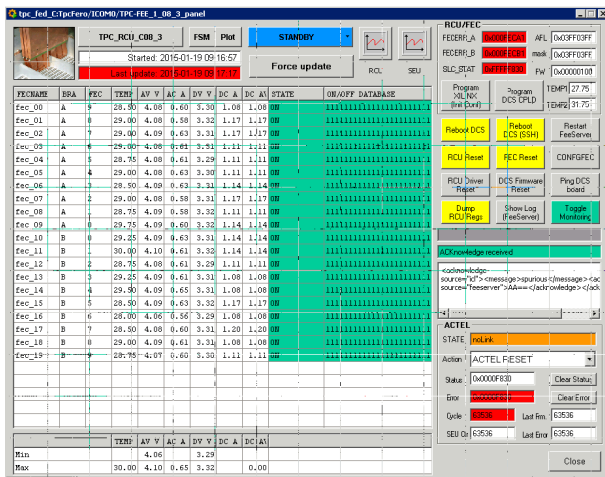


Figure 4: FEC Monitoring through the MSS of the RCU2

There is 256 kB Embedded Nonvolatile Memory (eNVM) inside the MSS, where the bootstrap applications for configuring ethernet and executing the In-System Programming of the FPGA (remote upgrade of the FPGA firmware), and uBoot firmware are stored. CNS has a charge of developing the bootstrap applications for In-System Programming, uBoot with new In-System Programming functionality, embedding Linux, and Linux application software such as FEC monitoring for the ALICE DCS, SPI, I²C applications.

3. Linux stability under Irradiation

Irradiation test of the RCU2 was performed at The Svedberg Laboratory (TSL) in Uppsala in Sweden using a 170 MeV proton beam with the proton fluence of $\sim 1\text{-}100$ MHz/cm² and ϕ of 24 mm. During this irradiation campaign, stability of the readout and Linux were tested. While Linux was being tested, two kinds of errors were observed: sometimes the Linux rebooted and in some cases the Linux was frozen. There were 7 and 3 errors for rebooting Linux and freezing Linux in 2.7×10^{10} p/cm², respectively. If we assume the particle dose of 3 kHz/cm² in Run 2, MBFT (mean time between failure) for Linux reboot and freeze is 1.7 and 3.9 hours, respectively. It should be noted that the

sequence of data readout is completely independent from the MSS. Rebooting/freezing the Linux will not stop the data taking. The possible reason of these failures may be γ single-event upsets (SEUs) and multi-bit upsets (MBUs) in the DDR SDRAMs and in the ARM processor, which may lead to the kernel panic. The protection of this failure with SECDED operation is under investigation.

4. Summary and Outlook

The upgrade of the ALICE-TPC Readout Control Unit is in progress to improve readout speed by a factor of 2-4 and radiation tolerance. Linux and related software (bootstrap application, uBoot with In-System Programming, Linux application programs for DCS) have been developed by CNS. Now the readout firmware of the FPGA Fabric is under preparation and is being extensively tested. The RCU2 will be installed in the ALICE cavern during the winter shutdown of 2015-2016.

References

- [1] ALICE Collaboration, JINST **3**, (2008), S08002.
- [2] B. Abelev *et al.*, for the ALICE Collaboration, Int. J. Mod. Phys. **A 29**, (2014) 1430044
- [3] J. Alme *et al.*, for the ALICE Collaboration, Nucl. Instr. and Meth. **A 622** (2010) 316-367.
- [4] J. Alme for the ALICE Collaboration, JINST **8**, (2013), C12032
- [5] Microsemi Corporation, SmartFusion2 Microcontroller Subsystem User 's Guide

Heavy baryon measurements at LHC-ALICE

Y.S. Watanabe for the ALICE collaboration

Center for Nuclear Study, Graduate School of Science, University of Tokyo

1. Introduction

Years of relativistic heavy ion collision experiments provide compelling evidence for the existence of a new form of matter made of deconfined quarks and gluons, quark-gluon plasma (QGP). In the course of development, heavy flavor, charm and bottom, measurements has played an important role to characterize such matter. The mass of charm and bottom quark is much larger than the temperature of QGP and thus expected to be produced only at the initial stage of the collisions. Therefore, the information concerning the whole system evolution is imprinted on the final heavy flavor observables.

So far, from the experimental side, only the measurements of heavy flavor mesons are commonly reported and little has been reported about heavy flavor baryons. However, the interest in the heavy baryon measurements is growing due to the expectation that such measurements could provide information about the correlation between light quarks inside QGP. For example, according to Ref. [1], the existence of diquark correlations in QGP enhances the production of Λ_c^+ by a factor of ~ 5 compared to the case without the diquark correlations.

Major challenges in the measurements of heavy baryons include their small cross sections and large combinatorial backgrounds. These difficulties can be, at least partially, overcome by the LHC-ALICE experiment for the following reasons:

- Large charm and bottom cross section at the LHC energies. The cross sections of charm and bottom quarks are ~ 10 and ~ 100 times larger than the RHIC energies.
- Large acceptance covering 2π in azimuth.
- PID capabilities down to low p_T provided by Time Projection Chamber (TPC) and Time-of-Flight detector (TOF).
- Precise decay vertex information provided by Inner Tracking System (ITS). The lifetimes of charm and bottom hadrons range from $\sim 100 \mu\text{m}/c$ to $\sim 500 \mu\text{m}/c$ and thus can be identified by requiring the daughter tracks to originate at a displaced secondary vertex.

This report presents various attempts to measure heavy baryons in $p\text{Pb}$ and PbPb collisions using the ALICE detectors. Properties of charm and bottom baryons shown in this report are summarized in Table 1.

	Λ_c^+	Ξ_c^+	Ω_b
Mass (GeV/c^2)	2.286	2.468	6.049
Life time ($\mu\text{m}/c$)	59.9	132	330

Table 1: Properties of charm and bottom baryons presented in this report [2].

2. Experimental apparatus

In this section, only a brief description of the ALICE subsystems relevant for the reconstruction of decay tracks at midrapidity ($|\eta| < \sim 0.8$) is given: ITS, TPC, TOF and Transition Radiation Detector (TRD). A more detailed description of the ALICE detectors can be found in Ref. [3,4].

The trajectories of the heavy baryon decay particles are reconstructed from their hits in ITS and in TPC. ITS consists of 6 cylindrical layers of silicon detectors placed between 3.9 and 43 cm from the interaction point. TPC is a large cylindrical gas detector, which has an inner and outer radius of 85 cm and 247 cm, and provides track reconstruction with up to 159 three-dimensional space points. They are placed in a 0.5 T magnetic field parallel to the beam axis and give a momentum resolution of $\sim 1\%$ at $p_T \sim 1 \text{ GeV}/c$. They also provide the measurement of the track impact parameter in the transverse plane (d_0), i.e. the distance of closest approach of the track to the primary vertex, with a resolution of $\sim 65 \mu\text{m}$ at $p_T \sim 1 \text{ GeV}/c$.

TOF is made of multigap resistive plate chambers placed at radii from 370 to 390 cm. The time-of-flight resolution is $\sim 80 \text{ ps}$, including the contribution from electronics and calibration, the uncertainty in the start time of the event, and the momentum resolution.

TRD consists of 6 layers of multiwire proportional chambers and radiators placed at radii from 290 cm to 368 cm. It provides electron identification for momenta above 1 GeV/c . TRD can also be used as a trigger detector due to its fast response time.

3. Data analysis

The analysis of the following decay modes of heavy baryons is presented in this section:

- $\Lambda_c^+ \rightarrow pK_s^0 \rightarrow p(\pi^+\pi^-)$
- $\Xi_c^+ \rightarrow \pi^+\pi^+\Xi^- \rightarrow \pi^+\pi^+(\pi^-p\pi^-)$
- $\Omega_b^- \rightarrow J/\psi\Omega^- \rightarrow (e^+e^-)(K^-p\pi^-)$

The antiparticles of those heavy baryons are also analyzed and included in the corresponding particle spectra.

The analysis of $\Lambda_c^+ \rightarrow pK_s^0$ is performed using two data sets: 100M events of the $p\text{Pb}$ minimum bias collisions from 2013 and 20M events of the PbPb central collisions from 2011. The analysis procedures are basically the same for the two data sets and are described below.

First, protons are identified using the dE/dx information of TPC and the time-of-flight information of TOF. K_s^0 decays weakly into $\pi^+\pi^-$ with $c\tau \sim 2.7 \text{ cm}$. These pions do not originate from the primary collision vertex, and thus can be easily identified by requiring d_0 to be non-zero. Once protons and K_s^0 s are selected, their invariant mass $m_{pK_s^0}$ is calculated as:

$$m_{pK_s^0} = ((\vec{p}_p^2 + m_p^2) + (\vec{p}_{K_s^0}^2 + m_{K_s^0}^2)) - (\vec{p}_p + \vec{p}_{K_s^0})^2 \quad (1)$$

where $\vec{p}_{p(K_s^0)}$ is the three momentum measured by ITS and TPC and $m_{p(K_s^0)}$ is the mass of proton (K_s^0) from Ref. [2].

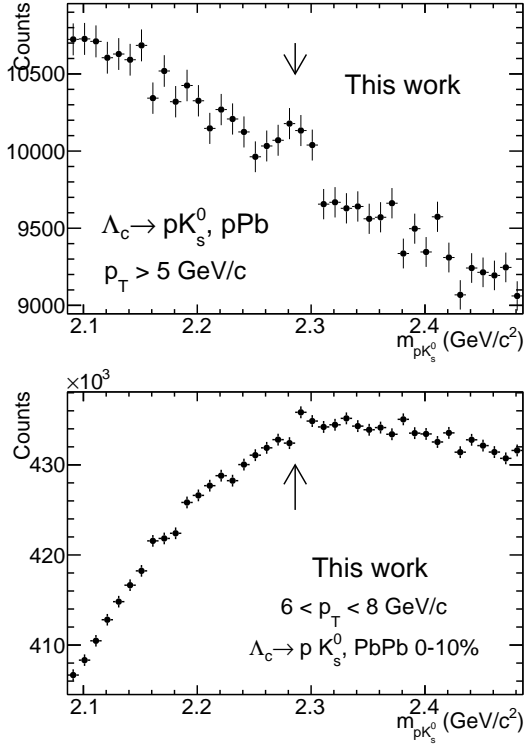


Figure 1: Invariant mass distributions of $\Lambda_c \rightarrow pK_s^0$ candidates in the p Pb collisions (top) and in the PbPb collisions (bottom). The arrows indicate the mass of Λ_c^+ in Ref. [2].

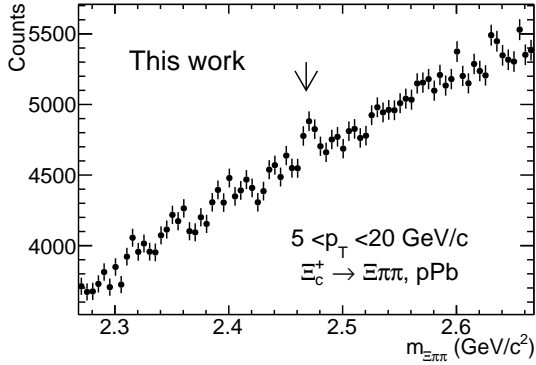


Figure 2: Invariant mass distribution of $\Xi_c^+ \rightarrow \Xi^- \pi^+ \pi^+$ candidates in the p Pb collisions. The arrow indicates the mass of Ξ_c^+ in Ref. [2].

Figure 1 shows the mass spectra in p Pb and PbPb collisions. Peak structures are visible at the mass of Λ_c^+ in Ref. [2] on top of smooth combinatorial background distributions.

Similar analysis is performed for $\Xi_c^+ \rightarrow \Xi^- \pi^+ \pi^+$ and the measured mass spectrum in p Pb collisions is shown in Fig. 2. A peak structure is visible on top of huge background contributions. The position of the peak is consistent with the Ξ_c^+ mass in Ref. [2].

The analysis of $\Omega_b^- \rightarrow J/\psi(\rightarrow ee)\Omega^-$ uses the TRD trigger data set collected during the 2013 p Pb collision runs. The TRD trigger data set contains almost a factor of two larger number of high p_T J/ψ compared to the minimum bias data set collected during the same period. The invariant mass spectrum of $J/\psi\Omega^-$ is shown in Fig. 3. A peak structure at the Ω_b^- mass is observed.

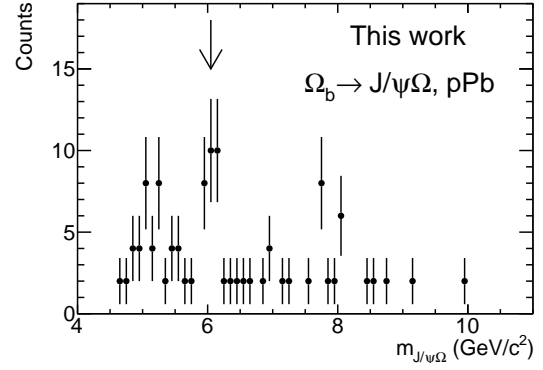


Figure 3: Invariant mass distributions $\Omega_b^- \rightarrow J/\psi\Omega^-$ candidates in the p Pb collisions. The arrow indicates the mass of Ω_b^- in Ref. [2]

4. Summary and outlook

The first attempts to measure various heavy flavor baryons using the ALICE detector are presented. Although peak-like structures are observed at the right positions in mass, the statistics and the signal-to-background ratio are not sufficient for further analysis. The current analysis procedure can be improved by refining the particle identification cuts and also exploiting the decay topologies of the heavy baryons.

References

- [1] S. H. Lee, K. Ohnishi, and S. Yasui, I. Yoo and C. M. Ko, Phys. Rev. Lett. **100** (2008) 222301.
- [2] K.A. Olive *et al.* (Particle Data Group), Chin. Phys. C **38** (2014) 090001.
- [3] K. Aamodt *et al.*, JINST **3** (2008) S08002.
- [4] B. B. Abelev *et al.*, Int. J. Mod. Phys. A **29** (2014) 1430044.

Measurement of dielectrons from charm and bottom quark decays in p -Pb collisions with the ALICE detector

S. Hayashi, H. Hamagaki, and T. Gunji on behalf of the ALICE Collaboration

Center for Nuclear Study, Graduate School of Science, University of Tokyo

1. Introduction

The principal aim of the heavy ion collisions at the Large Hadron Collider (LHC) is to investigate the properties of the deconfined matter, composed of quark and gluons, the Quark-Gluon-Plasma (QGP). Charm and bottom quarks are produced in the initial hard scattering between gluons and can hardly be created in QGP. Therefore the measurements of the yields and correlations of $c\bar{c}$ and $b\bar{b}$ provide the key information on their thermalization and energy loss mechanisms in the medium [1].

At the LHC energy, cold nuclear matter effects such as gluon shadowing, gluon saturation, and Cronin effect cannot be negligible for the heavy quark production [2]. In order to study the cold nuclear matter effects, p -A collisions are suitable. In p -Pb collisions at the LHC, the modification of the transverse momentum spectra of open heavy flavors ($p_T > 1$ GeV/ c) from the results of pp collisions can be described by Next-to-Leading order QCD calculation including EPOS09 nuclear modification of CTEQ6M parton distribution function, the calculation based on the color glass condensate (CGC), or the calculation which includes the initial energy loss, nuclear shadowing, and k_T broadening [2–5]. For more detail study of heavy flavor production in p -Pb collisions, it is very important to measure the heavy quark pair correlations to see the modification of them from the results in pp collisions and cover a wider phase space region with pair variables like invariant mass, pair p_T , the azimuthal angle, and so on. Electron and charged hadron correlation from heavy flavor decays in high multiplicity p -Pb collisions shows the long-range azimuthal correlation ($|\delta\eta| < 1.6$) which may be due to the gluon saturation or collective expansion of the system [6]. Electron-positron pairs from semi-leptonic decays of heavy quarks are dominant at $m_{ee} > 1$ GeV/ c^2 in the dielectron mass spectrum. Through the differential measurements of the invariant mass and pair p_T of dielectrons, the contributions from $c\bar{c} \rightarrow e^+e^-$ and $b\bar{b} \rightarrow e^+e^-$ can be separated since dielectrons from bottom quarks contributions are dominant in much higher mass ($m_{ee} > 3$ GeV/ c^2) or higher pair p_T regions.

ALICE is one of the main experiments at the LHC and is dedicated for the study of QGP. For the dielectron measurements from heavy quark decays, the online electron triggers provided by Transition Radiation Detector (TRD) are used to enhance electron samples at $p_T > 2$ GeV/ c in 2013, the data of p -Pb collisions at $\sqrt{s_{NN}} = 5.02$ TeV. The integrated luminosity of the TRD triggered data is 1.4 nb^{-1} . The statistics is twenty times larger than the minimum bias data (0.067 nb^{-1}). In this report, the status of the dielectron analysis with TRD triggered data is described.

2. TRD trigger performance

TRD consists of 6 layers of MWPCs filled with Xe/CO₂ (85/15) and the radiators (polypropylene fiber mat) for the transition radiation [7]. During p -Pb runs in 2013, two different electron triggers with TRD were available. One

(HSE) is the single electron trigger for $p_T > 3$ GeV/ c with online electron identification. The other is the single electron trigger with tighter online electron identification for $p_T > 2$ GeV/ c (HQU). Data taken by both triggers are used in the analysis.

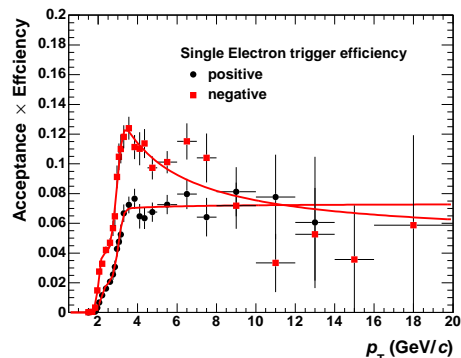


Figure 1: TRD trigger efficiency for the single electrons and positrons.

The event rejection of HSE and HQU triggers reduces the events down to 1/170 and 1/240, respectively. To reject the events triggered by the late conversions, which are created at larger radii (~ 2.5 -3 m from the collision point), online TRD tracks are associated with the offline global tracks reconstructed with the Inner Tracking System (ITS) and the Time Projection Chamber (TPC) [8]. This online-offline track matching further rejects the events by a factor of 20.

Figure 1 shows the trigger efficiency calculated as the number of triggered electrons divided by the minimum bias electron samples. The online tracking performance of TRD depends on the charge sign due to the effects between Lorentz angle of drift electrons and electron/positron trajectories. The trigger efficiency of negative and positive tracks including the online-offline track matching efficiency and the TRD acceptance is about 10% and 7%, respectively.

3. Electron identification

In the central barrel of the ALICE detector, charged tracks are reconstructed by ITS and TPC [9]. Electrons are identified by dE/dx in the TPC and contamination of hadrons is suppressed by the ToF detector. The hadron contamination is less than 3% up to 10 GeV/ c [10].

4. Pair analysis

All reconstructed electrons and positrons are taken to calculate pairs. Therefore there is a combinatorial background in the electron-positron pair distribution. The background is estimated using the same event like-sign pairs. They should contain not only the combinatorial background but also correlated pairs such as cross pairs which are produced from hadron decays with two e^+e^- pairs in the final state, Jet contribution, and $B\bar{B}$ oscillation. Figure 2 shows the subtracted yield in p -Pb collisions.

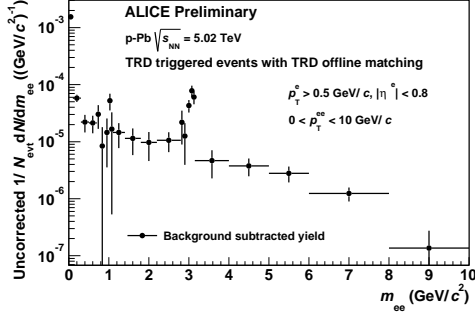


Figure 2: The dielectron spectrum after background subtraction for the TRD triggered data.

Pair acceptance and detection efficiency are evaluated with the Monte Carlo simulations. Firstly, the single electron efficiency is obtained from the full Monte Carlo calculation using the DPMJET event generator and GEANT3 simulations. Pair efficiency is extracted by the product of the single electron efficiencies, where the pairs are produced according to known hadronic decays. Dielectrons from light meson decays ($\pi^0, \eta, \rho, \omega, \eta', \phi$) are generated from EXODUS according to the measured charged pion spectrum in p -Pb collisions and m_T scaling [11]. For heavy quark contributions, dielectrons are generated using PYTHIA with the parametrization tuned for the Next-to-Leading order calculation [5]. Figure 3 shows the pair efficiency as a function of invariant mass, where circles and boxes correspond to the pair reconstruction efficiency and TRD trigger efficiency for pairs, respectively. TRD trigger efficiency for pairs is extracted according to Eq 1.

$$\epsilon_{trig}^{pair}(m_{ee}, p_T^{ee}) = 1 - [1 - \epsilon_{trig}^{single}(p_{T1})][1 - \epsilon_{trig}^{single}(p_{T2})] \quad (1)$$

Figure 4 shows the inclusive invariant yield of dielectrons as a function of invariant mass.

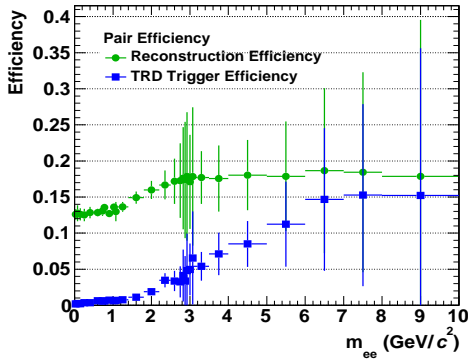


Figure 3: p_T integrated pair efficiency as a function of invariant mass. Circles and boxes correspond to the pair reconstruction efficiency and TRD trigger efficiency for pairs, respectively.

5. Summary and outlook

The corrected yield up to $m_{ee} = 10 \text{ GeV}/c^2$ is obtained with the TRD triggered data. As the next step, $c\bar{c}$ and $b\bar{b}$ cross section will be extracted by using PYTHIA, MC@NLO, POWHEG, and some other theoretical models.

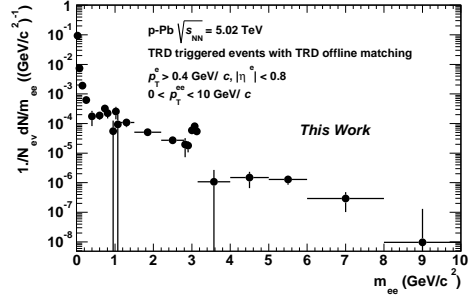


Figure 4: Corrected dielectron yield per inelastic p -Pb collision as a function of invariant mass.

References

- [1] M. Nahrgang *et al.*, PRC 90 (2014), 024907, S. Cao *et al.*, arXiv: 1505.01869 (2015).
- [2] H. Fuji, K. Watanabe, NPA 920, 78-93 (2013)
- [3] B. Abelev *et al.* (ALICE Collaboration), Phys. Rev. Letter 113, (2014) 232301.
- [4] K. Eskola, H. Paukkunen, and C. Salgado, J. High Energy Phys. 04 (2009) 065. D. Stump, *et al.*, J. High Energy Phys. 10 (2003) 046
- [5] M. Mangano, *et al.*, Nucl. Phys. B373, 295 (1992).
- [6] E. Pereira de Oliveira Filho, arXiv:1404.3983v2 (2013) NPA in press.
- [7] J. Klein, NIMA 706 23-28 (2013).
- [8] ALICE TRD Technical Design Report, Tech. Rep. CERN/LHCC 2001-021 (2001).
- [9] F. Carminati *et al.*, J. Phys. G: Nucl. Part. Phys. 30 1517 1763 (2004).
- [10] S. Hayashi *et al.*, CNS Annual Report 2013 (2015) 39-40.
- [11] K. Jiang, *et al.*, Phys. Rev. C. 91, 024910 (2015),

Two particle correlations of V^0 particles in p -Pb collisions with the ALICE detector

Y. Sekiguchi, H. Hamagaki, and T. Gunji for the ALICE Collaboration

Center for Nuclear Study, Graduate School of Science, The University of Tokyo

1. introduction

Measurement of the correlations in the particle production as a function of the azimuthal angle and rapidity is very useful for investigating particle production in high-energy nucleus-nucleus collisions. The long-range correlations in the rapidity space in near-side angular pairs of dihadrons were firstly observed in Au-Au collisions at $\sqrt{s_{NN}}=200$ GeV at RHIC [1, 2]. This long-range correlations are derived from the collective expansion of the initial geometry fluctuations. Unexpectedly, a similar structure has also been observed in high-multiplicity pp collisions at 7 TeV by the LHC-CMS experiment [3]. The high-density gluon fields in small x of nucleus and the collision of two high-density gluon sheets can explain the long-range correlations [4]. It is very interesting to study the correlations in p -Pb collisions since the initial gluon density and magnitude of the collective expansion are very different from those in other collision systems (pp and Pb-Pb). The azimuthal anisotropy parameter, v_2 , of K, π , and p shows mass ordering at low transverse momentum (p_T) and the trend is similar to Pb-Pb collisions [5]. The mass ordering is a characteristic feature of collective expansion. This analysis aims to further explore the partonic collectivity by extracting v_2 of K_s^0 and Λ in p -Pb collisions at $\sqrt{s_{NN}}=5.02$ TeV.

2. Analysis

The minimum bias data of p -Pb collisions at $\sqrt{s_{NN}}=5.02$ TeV in 2013 are used (~ 100 M events). The main subsystems in ALICE used in this analysis are the inner tracking system (ITS), time projection chamber (TPC), and time of flight (TOF). The ITS consists of 6 layers of silicon detectors for vertex finding and tracking. The TPC is the main tracking detector and is used for particle identification by measuring the specific energy loss. The TOF is used to identify particles by measuring the time of flight. They have a common pseudorapidity acceptance $|\eta| < 0.9$. To define centrality, VZERO-A, which is located in the Pb-going direction ($2.8 < \eta < 5.1$), is used. The position of the reconstructed vertex along the beam direction is required to be within 10 cm from the detector center. The correlations between trigger particles and associated particles are measured as a function of the azimuthal angle difference $\Delta\phi$ and pseudo-rapidity difference $\Delta\eta$. The trigger particles are unidentified charged hadrons, while K_s^0 and $\Lambda(\bar{\Lambda})$ are used as associated particles. K_s^0 and Λ decay into $\pi^+ + \pi^-$ and $p^+ + \pi^-$ with a characteristic decay pattern, called V^0 . Topological cuts are required to reduce the combinatorial background. The correlation function as a function of $\Delta\eta$ and $\Delta\phi$ between two charged particles is defined as:

$$\frac{1}{N_{\text{trig}}} \frac{d^2 N_{\text{asso}}}{d\Delta\eta d\Delta\phi} = \frac{S(\Delta\eta, \Delta\phi)}{B(\Delta\eta, \Delta\phi)}, \quad (1)$$

where N_{trig} is the total number of triggered particles in the event class and p_T interval, the signal distribution ($S(\Delta\eta, \Delta\phi) = \frac{1}{N_{\text{trig}}} \frac{d^2 N_{\text{same}}}{d\Delta\eta d\Delta\phi}$) and the background distribution

($B(\Delta\eta, \Delta\phi) = \alpha \frac{d^2 N_{\text{mixed}}}{d\Delta\eta d\Delta\phi}$) are the associated yield per trigger particle from the same events and from different events within the similar event multiplicities, respectively. The signal distribution is divided by the background distribution to account for pair acceptance and pair efficiency. The α factor is chosen so that it is unity at $\Delta\eta \sim 0$ because the acceptance is flat along $\Delta\phi$. This correlation function is studied for different p_T intervals and different event multiplicities. Left and right of Fig. 1 show the associated K_s^0 yield per unidentified hadron trigger particles with $1.5 < p_{T,\text{trig}}, p_{T,\text{asso}} < 2.5$ GeV for the 0-20% (central collisions) and 60-100% (peripheral collisions) event multiplicity classes, respectively.

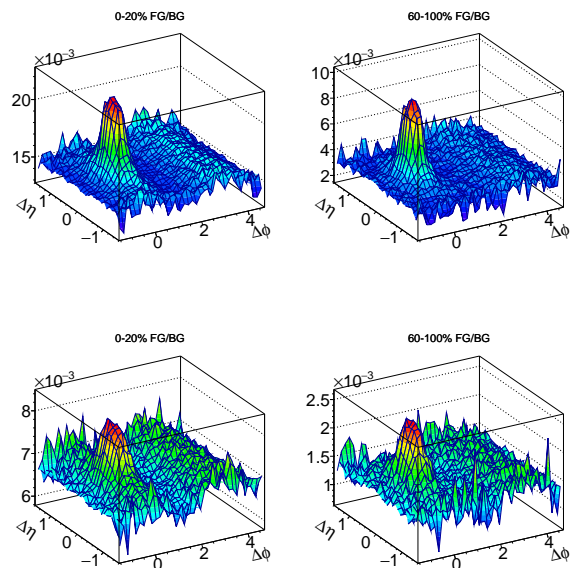


Figure 1: Associated K_s^0 (top) and Λ (bottom) yield per trigger particle with $1.5 < p_{T,\text{trig}}, p_{T,\text{asso}} < 2.5$ GeV for the 0-20% (left) and 60-100% (right) event classes.

The correlation function in peripheral collisions (60-100%) is subtracted from that in central collisions (0-20%) to remove the auto-correlations from jets. Figure 2 shows the subtracted correlations for $1.5 < p_{T,\text{trig}}, p_{T,\text{asso}} < 2.5$ GeV. The projection onto $\Delta\phi$, where the entries in $0.8 < |\Delta\eta| < 1.6$ on the near side and $|\Delta\eta| < 1.6$ on the away side are projected, is shown in Fig. 3. The region $|\Delta\eta| < 0.8$ on the near side is excluded to eliminate the jet yield which could not be completely subtracted. Long range structure on both the near and away side is observed.

To quantify the azimuthal anisotropy (v_2), the Fourier coefficients are extracted by fitting with the following function.

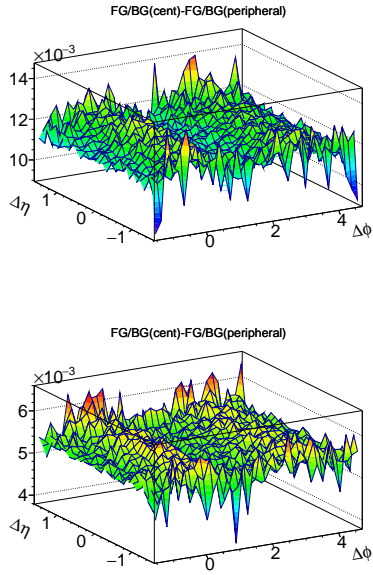


Figure 2: Associated K_s^0 (top) and Λ (bottom) yield per trigger particle with $1.5 < p_{T,\text{trig}}, p_{T,\text{asso}} < 2.5$ GeV for the 0-20% event class after the subtraction of the 60-100% (left) event class.

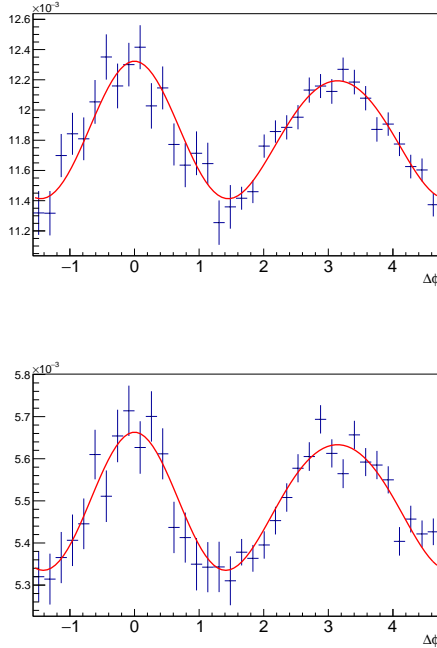


Figure 3: Projection of the subtracted correlation functions of the associated K_s^0 (top) and Λ (bottom) yield per trigger particle with $1.5 < p_{T,\text{trig}}, p_{T,\text{asso}} < 2.5$ GeV.

$$\frac{1}{N_{\text{trig}}} \frac{dN_{\text{asso}}}{d\Delta\phi} = a_0 + 2a_1 \cos(\Delta\phi) + 2a_2 \cos(2\Delta\phi) + 2a_3 \cos(3\Delta\phi) \quad (2)$$

The v_n coefficient can be obtained as:

$$V_n^i = \frac{a_n^i}{a_0^i + b^i}, v_n^{K_s^0, \Lambda} = \frac{V_n^{K_s^0, \Lambda}}{\sqrt{V_n^{h-h}}} \quad (3)$$

where i is the index of h-h or h-V0 pairs (h denotes unidentified hadrons) and b is the baseline which is determined by averaging over $1.2 < |\Delta\eta| < 1.6$ on the near side of the 60-100% event class. Figure 3 shows the extracted v_2 coefficient for K_s^0 and Λ compared p and K as function of p_T . Mass ordering between the v_2 of K_s^0 and Λ as well as kaon and proton is observed.

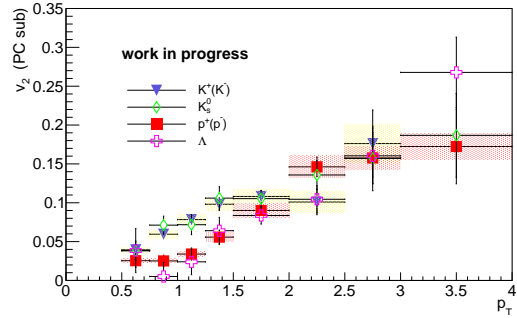


Figure 4: v_2 of K_s^0 , Λ compared with one of kaon and proton. Error bars and shaded bands show statistical uncertainties and systematic uncertainties, respectively.

3. Summary and Outlook

Two-particle correlations between unidentified charged hadrons and V^0 particles in p -Pb collisions at $\sqrt{s_{NN}}=5.02$ TeV are measured. Long range correlations are visible even at $0.8 < |\Delta\eta| < 1.6$. The measurements of the particle productions with large rapidity gaps and the centrality dependence are important for quantifying the collective expansion. Measurements of the correlation function with larger rapidity gap using forward detectors are ongoing.

References

- [1] STAR Collaboration, Phys. Rev. C80 (2009) 064912
- [2] PHOBOS Collaboration, Phys. Rev. Lett. 104 (2010) 062301
- [3] CMS Collaboration, JHEP 09 (2010) 091
- [4] K. Dusling and R. Venugopalan, Phys. Rev. D 87 (2013) 054014
- [5] ALICE Collaboration, Phys. Lett. B, 726 (2013) 164-177

Dielectron measurements in Au+Au collisions at $\sqrt{s_{NN}} = 200$ GeV using the PHENIX detector

Y. S. Watanabe for the PHENIX collaboration

Center for Nuclear Study, Graduate School of Science, University of Tokyo

1. Introduction

High-energy heavy ion collisions provide an unique opportunity to study the properties of Quantum ChromoDynamics at extreme temperature and/or density in the laboratory. One of the most intriguing phenomena at such extreme condition is “chiral symmetry restoration”. Chiral symmetry, which is spontaneously broken under normal condition, is expected to get restored [1]. As a result, the chiral partners, such as the ρ and a_1 mesons, become degenerate in mass. Since this degeneracy is very difficult to observe experimentally, extensive experimental efforts have been made to measure the spectral function of the ρ meson.

Dilepton decays of the ρ meson is particularly suited for this study because electrons are not subject to the final state interaction and carry information at the time of their production.

In 2010, PHENIX has installed a new detector, Hadron Blind Detector (HBD), to perform a precise dielectron measurement in Au+Au collisions at $\sqrt{s_{NN}} = 200$ GeV. In this report, the results of dielectron analysis using the data set and its implications are presented.

2. HBD

The HBD is a new Cherenkov detector consisting of a 50 cm long radiator operated with pure CF_4 and directly couple to a triple Gas Electron Multiplier (GEM) photon detection element. The detailed description of the HBD can be found in Ref. [2].

The HBD aims at rejecting the electrons originating from π^0 Dalitz decays and γ conversions, which are major background sources in dielectron measurements. This is achieved by exploiting the fact that the opening angle of such background pairs is small compared to those of other sources like the ρ meson. The HBD is placed in a field-free region around the beam axis and the opening angle is preserved in the HBD. Thus, a background pair produces two overlapping hits, resulting in a double charge amplitude compared to that of a single hit. The HBD responses of the single and double electron hits in the 2010 RHIC run are shown in Fig. 1.

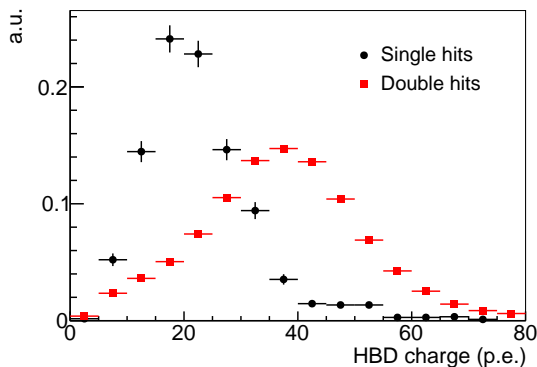


Figure 1: HBD responses to single hits and double hits [3].

3. Data analysis

This analysis uses 5.6×10^9 minimum bias events collected during the 2010 RHIC run. Only the key ingredients of the analysis, electron identification and pair background subtraction, are discussed here. A more detailed description can be found in Ref. [3].

Electron identification is performed by the Ring Imaging Cherenkov Detector (RICH), Electromagnetic calorimeter (EMCal), Time-of-flight East detector (TOFE) and HBD. Each detector has several variables useful for electron identification, resulting in 14 relevant variables in total. To combine these variables in an efficient way, an electron identification procedure based on neural networks has been developed. The hadron contamination in the final electron sample is as low as 5% even for the most central events.

After the electron identification, all electrons and positrons in the same event are combined to form “foreground” pairs. A large background of unphysical pairs is still present in such inclusive foreground pairs and needs to be subtracted statistically. The background of unphysical pairs consists of the following types:

- Cross pairs: The cross pairs are the pairs coming from two different parents but having a common grand parent. For example, in π^0 Dalitz decays followed by a conversion of photons, two e^+e^- pairs are produced in the final states. The electrons from Dalitz decays and the electrons from the subsequent conversions have different parents, but they are correlated through the primary π^0 .
- Jet pairs: The jet pairs are two electrons generated in the same or opposite jets.
- Electron-hadron pairs: The electron-hadron pairs are residual detector induced correlations.
- Combinatorial pairs: The combinatorial pairs are random combinations of electrons and positrons from two different sources.

The validity of our background description is confirmed using the likesign, e^+e^+ and e^-e^- , mass spectra, which have contributions from only “unphysical pairs”. Figure 2 shows a comparison of the likesign foreground spectra and the calculated background spectra for the minimum bias events. The top panel shows the foreground spectrum together with each background source. The bottom panel shows the ratio of the foreground spectrum to the sum of all the background sources.

4. Results

Figure 3 shows the invariant mass spectra of e^+e^- pairs in the PHENIX acceptance for the minimum bias events. The spectra are subject to a p_T cut of 0.2 GeV/c on the single electron tracks and an opening angle cut of 100 mrad on pairs. The opening angle cut is applied to avoid the hit sharing between tracks in HBD. The statistical uncertainties and systematic uncertainties are shown as vertical

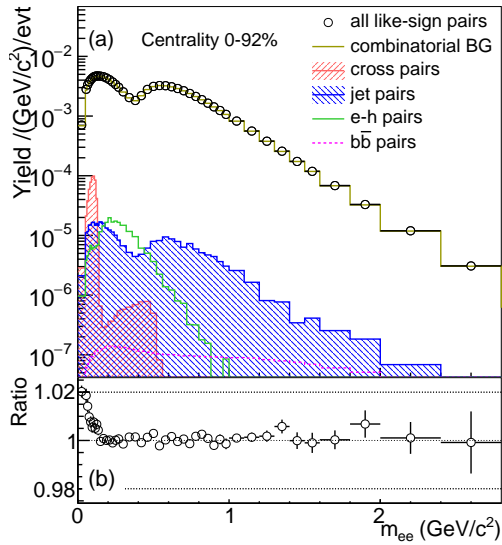


Figure 2: (a) Likesign foreground spectrum shown together with the calculated background sources. (b) Ratio of the foreground to the sum of calculated background sources [3].

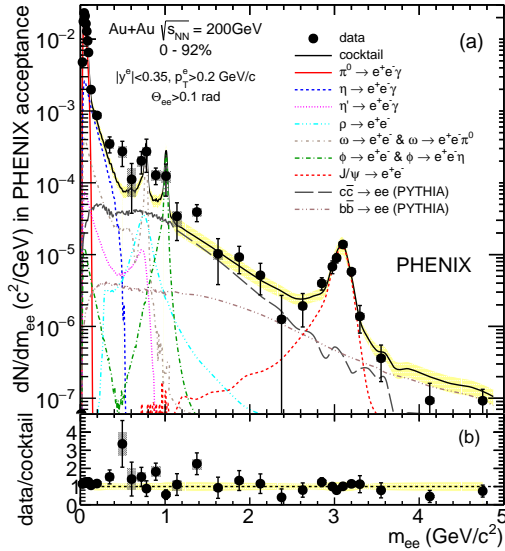


Figure 3: Invariant mass spectra of e^+e^- pairs in the PHENIX acceptance for minimum bias events. The experimental results are compared to the expected yield from hadronic sources [3].

bars and boxes, respectively. In the figure, the experimental results are compared to the expected yield from the cocktail of hadronic sources. An enhancement from the cocktail is observed at $m_{ee} \sim 0.5 \text{ GeV}/c^2$. The enhancement factor amounts to $2.3 \pm 0.4(\text{stat}) \pm 0.4(\text{syst}) \pm 0.2(\text{model})$ in the mass region, $0.3 < m_{ee} < 0.76 \text{ GeV}/c^2$. This value is consistent with the enhancement factor reported by STAR, $1.76 \pm 0.06(\text{stat}) \pm 0.26(\text{syst}) \pm 0.29(\text{cocktail})$ [4].

5. Summary

The HBD was installed in PHENIX in the 2010 RHIC run and successfully operated. This report presented the results of the dielectron measurement at midrapidity using the HBD in Au+Au collisions at $\sqrt{s_{NN}} = 200 \text{ GeV}$.

An enhancement of e^+e^- is observed at $m_{ee} \sim 0.5 \text{ GeV}/c^2$ with respect to the expected yields from hadronic decays. The enhancement factor amounts to

$2.3 \pm 0.4(\text{stat}) \pm 0.4(\text{syst}) \pm 0.2(\text{model})$ in the mass region, $0.3 < m_{ee} < 0.76 \text{ GeV}/c^2$, for minimum bias collisions.

References

- [1] C. A. Dominguez, M. Loewe, and Y. Zhang, Phys. Rev. D **86** (2012) 034030.
- [2] W. Anderson *et al*, Nucl. Instrum. Methods Phys. Res., Sec. **646** (2011) 35.
- [3] A. Adare *et al*, arXiv:1509.04667
- [4] L. Adamczyk *et al*, Phys. Rev. C **92** (2015) 024912

Accelerator and Instrumentation

Construction of OEDO beamline

S. Michimasa, S. Shimoura, M. Matsushita, N. Imai, H. Yamaguchi, S. Ota, E. Ideguchi^a, and K. Yamada^b

Center for Nuclear Study, Graduate School of Science, University of Tokyo

^a*Research Center for Nuclear Physics, Osaka University*

^b*RIKEN Nishina Center*

The OEDO system is a new beamline being proposed for high-quality slow-down RI beams [1]. The OEDO is an abbreviation of **Optimized Energy Degrading Optics** for RI beam: 大江戸, which is the old name of the Tokyo metropolitan area. Its novel idea is to manipulate timing degree-of-freedom in phase space for RI beam transport. To obtain high-quality beam with a small spot size and a small energy spread, the OEDO system shifts spreads of positions and angles to timing spread of the beam, which corresponds to rotation of phase space ellipse on the position- (angle-)timing plane to get a small position (angle) spread. Radiofrequency (RF) electric ion-optical elements can rotate a phase space ellipse of spatial and timing components, since beams provided by a cyclotron have an RF bunch structure.

Main components of the OEDO system are: A RF deflector [2] with is synchronized with the cyclotron's RF; 2 sets of triplet quadrupole magnets to build point-to-parallel/parallel-to-point ion optics. The OEDO system is to be installed downstream of a momentum-dispersive focus. For construction of the system, the rearrangement of BigRIPS [3] and High-Resolution (HR) beamline [4] will be made. In FY2014, a main part of construction budget was funded and the OEDO project was launched. We are iteratively improving the design of the beamline in respects of a magnet arrangement and an ion-optical design.

1. Arrangement of ion-optical elements

In order to implement the OEDO system to the HR beamline while maintaining the performance for intermediate-energy beams, we plan construction of new ion-optical elements and rearrangements of the magnets in the HR beamline. We call here the altered beamline OEDO beamline. Figure 1 shows magnet arrangement for the OEDO beamline downstream of the F6 focal plane of BigRIPS. The foci FE7, FE8, RF(FH9) and FE9 are newly set up for operation of the new beamline. Actually, for completion of the OEDO beamline, several construction works are necessary in sites indicated by (a)–(d):

- (a) Switching system of a STQ between STQ14 (for BigRIPS) and STQ14H (for OEDO-SHARAQ). Or construction of a new STQ is planned, depending on the FY2016 budget;
- (b) Relocation of two normal-conducting magnets and a vacuum chamber; The equipment is originally installed at FH9 of the HR beamline, although the power supplies for the magnets are necessary to be revised;
- (c) Relocation of a STQ, which will be moved from STQ14H;
- (d) Construction of OEDO system consisting of 2 STQs and a RF deflector. One STQ is put up by relocation of STQ15H. The another STQ and a RF deflector are newly manufactured.



Figure 1: Designed magnet arrangements for the OEDO beamline, comparing with the HR beamline

The construction budget for manufacture of STQ and RF deflector has been approved. Construction of the OEDO beamline will be completed in March, 2017.

2. Beam optics

Figure 2 shows how ion-optical elements change phase space ellipse along the beamline:

1. RI beam at 250 MeV/u is transported from F3 to F6 with the BigRIPS standard optics;
2. FE8 is set to be an momentum dispersion of 1 m, which is tuned between F6 to FE8. A mono-energetic degrader is installed at FE8, where the RI beam is slowed down to 50 MeV/u. The degrader is used for a rotation of the phase space ellipse on the plane of beam energy (δ) and flight time (t), as shown in Fig. 2(a);
3. The first half of the OEDO system, where is set to be point-to-parallel optics, rotates the phase space ellipse on the plane of horizontal position (x) and horizontal angle (a);
4. The RF deflector lessens a timing (t) dependence of angle (a), as shown in in Fig. 2(b);
5. The second half of the OEDO system, where is also set to be parallel-to-point optics, rotates phase space ellipse on the x - a plane. Finally, a small beam spot and a small energy spread are achieved at the FE9 and S0 foci (Fig. 2(c)).

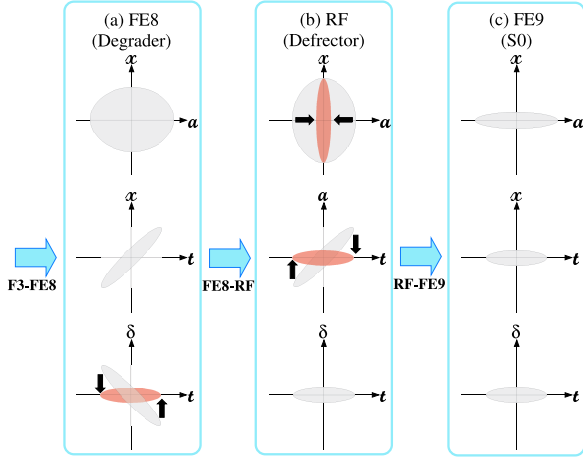
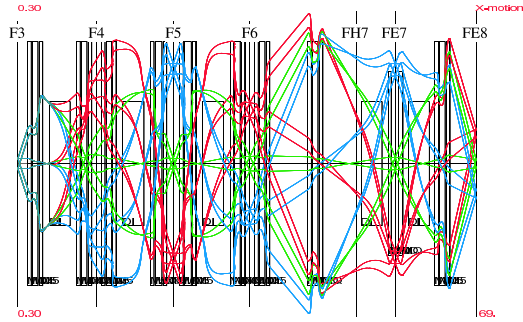
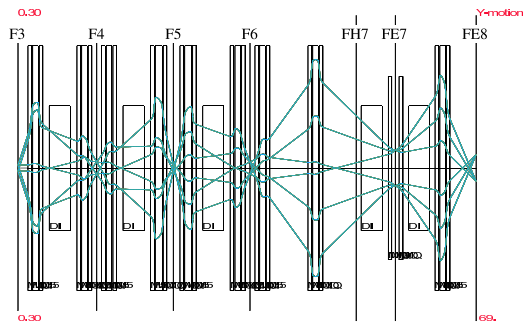


Figure 2: Phase space evolution along the OEDO beamline. Subset (a)–(c) respectively shows (a) Function of a FE8 mono-energetic degrader, (b) Function of the RF deflector, and (c) the final phase space ellipse at FE9 and S0.

We found a solution of ion-optical setting that realize the OEDO scheme. Figures 3 and 4 show the ion-optical solution for the OEDO operation.



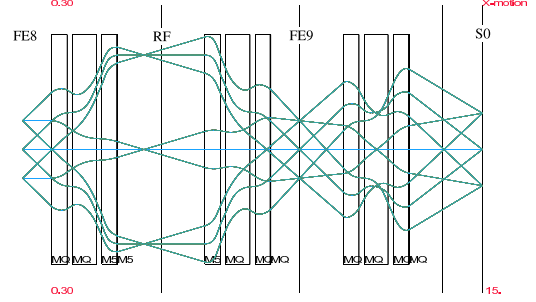
(a) Horizontal trajectory on F3-FE8



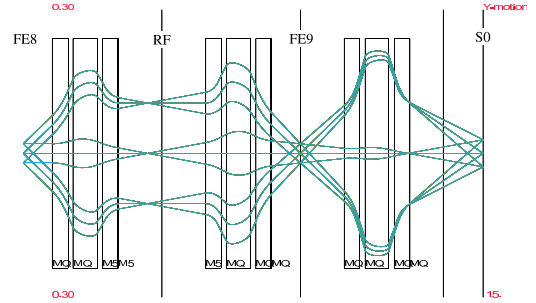
(b) Vertical trajectory on F3-FE8

Figure 3: Ion trajectory from F3 to FE8. Spreads of x , θ , y , ϕ and δ_p (momentum) were respectively 5 mm, 20 mrad, 3 mm, 20 mrad and 3 % at F3.

Based on the result, we started to estimate the higher order aberrations of the OEDO beamline using a Monte-Carlo simulation [5]. A practical solution for reducing higher-order components is to tune the sextupole magnets installed with STQs. We continue to study how effective sextupole elements are, including development of their tuning methods.



(a) Horizontal trajectory on FE8-S0



(b) Vertical trajectory on FE8-S0

Figure 4: Ion trajectory from FE8 to S0. Spreads of x , θ , y , ϕ and δ_p (momentum) were respectively 30 mm, 30 mrad, 10 mm, 30 mrad and 5 % at FE8.

References

- [1] S. Shimoura *et al.*, CNS Annual Report 2013, CNS-REP-93, (2015) 56.
- [2] K. Yamada *et al.*, Nucl. Phys. A **746** (2004) 156c.
- [3] T. Kubo *et al.*, Nucl. Instrum. Meth. in Phys. Res. **B204** (2003) 97.
- [4] S. Michimasa *et al.*, Nucl. Instrum. Meth. in Phys. Res. **B317** (2013) 305.
- [5] M. Matsushita *et al.*, somewhere in this report, CNS Annual Report 2014.

Simulation study of a new energy-degrading beamline, OEDO

M. Matsushita, S. Shimoura, S. Michimasa, S. Ota, K. Yako, H. Yamaguchi, N. Imai, E. Ideguchi^a,
and K. Yamada^b

Center for Nuclear Study, Graduate School of Science, University of Tokyo

^aResearch Center for Nuclear Physics, Osaka University

^bRIKEN Nishina Center

OEDO (Optimized Energy Degrading Optics for RI beam) beamline is one of the solutions to degrade an intense RI beams provided in RIBF, which will make possible the further research of exotic nuclei/states using the transfer reaction in the energy region of a few ten MeV, fusion reaction in a few MeV and others [1]. The application of a material energy degrader is a general method to degrade a fast beam, while it induces momentum- and angular aberrations that lead to broadenings of beam spot [2]. In the OEDO beamline, an RF electric deflector is employed to cancel the aberrations based on the time structure of the secondary beams. Simulation of this beamline has been performed to examine energy distributions, beam spot size, charge-state distributions, beam purification capability and transmission of energy decelerated beams.

In this work, beam transport by magnetic devices was reconstructed by beam transfer matrix obtained in COSY infinity [3], while interactions with materials and electric field were simulated by the code based on GEANT4 [4]. Conditions of the simulation are schematically shown in Figure 1, where a neutron-rich nucleus ^{132}Sn and neutron-deficient nucleus ^{56}Ni were used as typical examples. In case of ^{132}Sn , initial momentum and angular distributions were generated to enumerate the production via projectile-fission reaction of ^{238}U primary beam with an energy of 345A MeV, using the LISE++ code. After passing through a thin energy degrader installed at F1 focus in BigRIPS, ^{132}Sn beam with an energy of 250A MeV ($\Delta P/P = \pm 3\%$) was obtained. Thickness of the energy degrader was determined by considering a matching between energy of beam and phase of RF deflector. In case of ^{56}Ni , production via projectile-fragmentation reaction of ^{124}Xe primary beam with an energy of 345A MeV was assumed. Its energy of 210A MeV ($\Delta P/P = \pm 3\%$) at F3 focus was obtained. In the OEDO beamline following BigRIPS separator, a scheme of two-staged deceleration is considered. Secondary beams are degraded to ~ 50 A MeV by a mono-energetic degrader located at FE8 focus, and transported to the RF deflector with a point-to-parallel optics so as to convert from position- to angular dispersion. In order to make beams focused at FE9, the RF deflector compensates the angular aberrations by its dynamic electric field oscillating with a cyclotron resonance frequency. If an additional deceleration is required, another energy degrader is employed. In this simulation study, a wedge-shaped energy degrader with an appropriate thickness located at FE9 is used to decelerate to around 20A, 10A or 5A MeV. There is a correlation between energy and position (dispersion) at FE9 caused by a finite image size for the same δ (momentum), *i.e.* the ions with the same momentum and different position pass through different thickness of the wedge degrader at FE8. A proper wedge angle cancel out aberrations induced by this dispersion and compress energy spread of degraded beams. Figure 2 shows energy distributions of ^{132}Sn and ^{56}Ni after decelerations to

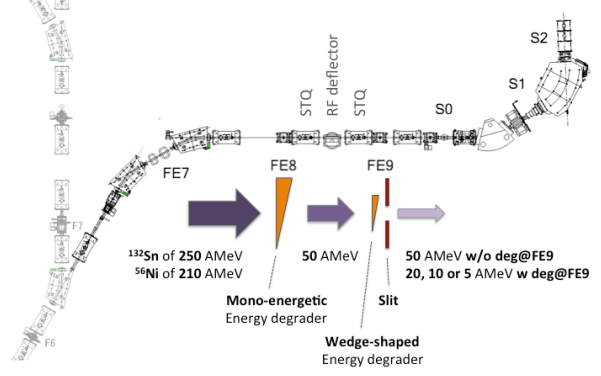


Figure 1: A scheme of energy deceleration in OEDO beamline. Secondary beams of ^{132}Sn and ^{56}Ni produced in BigRIPS were used in this simulation study.

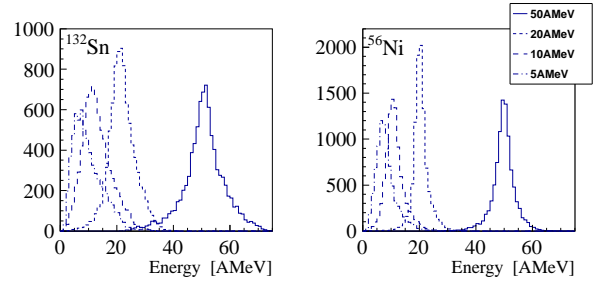


Figure 2: Energy distribution at S0 focus where a reaction target assumed to be install. Energy broadenings of ^{132}Sn in decelerations to 50, 20, 10 and 5A MeV is exhibited as different lines in left panel. Same spectra of ^{56}Ni in right panel.

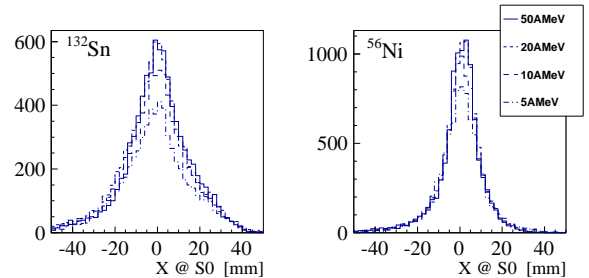


Figure 3: Horizontal position distributions of ^{132}Sn and ^{56}Ni at S0 focus are shown in a left and right panel, respectively. Line-indication follows the same rule as in Figure 2.

50, 20, 10 and 5A MeV. Larger broadenings for ^{132}Sn , compared with ones for ^{56}Ni , is as expected from the A/Z dependence of energy straggling. Position distribution at S0 focus demonstrates the focusing effect of the RF deflector. As shown in Figure 3, typical widths of beam spot size are ~ 24 and ~ 30 mm in FWHM for ^{132}Sn beam with energies of 10 - 50 A and 5 A MeV, respectively, and ~ 19 mm for

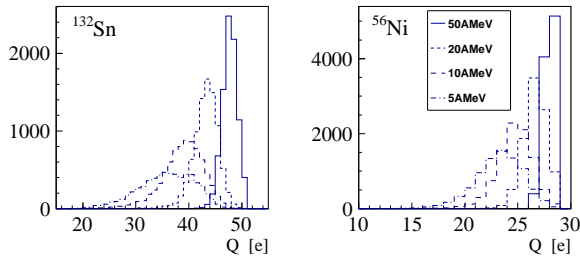


Figure 4: Charge-state distributions of ^{132}Sn and ^{56}Ni are indicated in the same manner as in Figure 2.

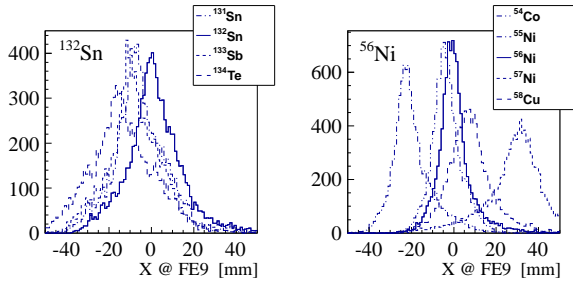


Figure 5: Isotopic and isotonic separation in horizontal position at FE9 focus are exhibited. Neighboring isotopes and isotones of ^{132}Sn and ^{56}Ni are indicated as different lines in a left and right panel, respectively.

^{56}Ni beam, which can be considered to be acceptable for experimental use.

Since a deflection angle depends on mass-to-charge ratio (A/Q) of particle passing through the electric field in the RF deflector, charge state of each isotope after deceleration has been investigated. Figure 4 shows charge state distributions of ^{56}Ni and ^{132}Sn with energies of 50A, 20A, 10A and 5A MeV. Due to the effect of charge stripping/pick-up in material energy degrader, distributions shift lower and broaden after deceleration to lower energy below 50A MeV. In order to minimize the loss of the focusing power of the RF deflector, energy of interested isotopes ^{56}Ni and ^{132}Sn at the RF deflector has been adjusted around 50A MeV and additional deceleration below 50A MeV has been operated after the RF deflector. It should be specially mentioned that OEDO consisting of a straight beamline can be free from transmission loss resulting from charge state shift and available beam includes multiple charge state.

Secondary beams are usually cocktail beams and have some contaminants especially for nuclei in medium/heavy mass region. In OEDO beamline, timing differences from the focusing phase of the RF deflector are transformed to position differences in the downstream focus. As shown in Figure 5, a clear separation in position distribution at FE9 focus were obtained for Nickel isotopes. This is due to the large enough difference in time-of-flight (TOF) caused by the velocity differences among the Nickel isotopes with the same rigidity and different momentum kicks consequently given by the RF deflector. It is thus verified that beams of nuclei with $A/Z = 2$ can be purified by optimizing the width of beam slit at FE9 focus. In the case of ^{132}Sn , on the other hand, clear separation cannot be obtained due to insufficient TOF differences between neighboring isotopes/isotones and bending power of RF deflector against particle with large A/Q ratio. Development of other beam transport optics which consciously enhance the capability of beam purifica-

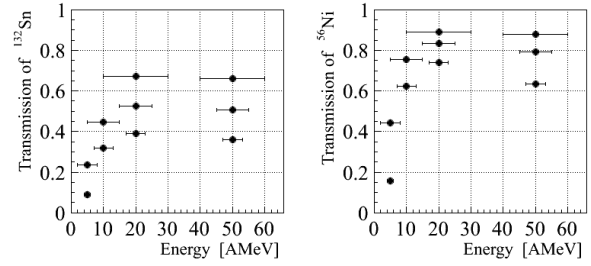


Figure 6: Transmission ratios of ^{132}Sn and ^{56}Ni as a function of beam energy are shown in left and right panel, respectively, in which error bars indicate width of a gate imposed on each energy distribution.

tion for neutron-rich nuclei in medium/heavy mass region, such as ^{132}Sn , is on going. Transmissions of ^{132}Sn and ^{56}Ni have been also investigated as shown in Figure 6. Most of beam loss attribute to beams completely stop in material degraders or come outside of the gated scope of position or energy at S0 focus.

In summary, we have performed simulation study for OEDO beamline. Acceptable beam spot size can be achieved by this new scheme of energy deceleration. Transmission depends on energy-broadenings of degraded beam while purification from neighboring isotopes depends on an A/Q ratio. Beam transport investigated in this work is considered to be the transmission-optimized optics. An alternative scheme of beam transport, separation-optimized optics, is under development to enhance capability of beam purification.

This work was funded by ImPACT Program of Council for Science, Technology and Innovation (Cabinet Office, Government of Japan).

References

- [1] S. Shimoura et al., CNS Annual Rep. **2013**, 55 (2013)
- [2] E. Ideguchi, Prog. Theor. Exp. Phys. **2012**, 03C005 (2012)
- [3] COSY Infinity, http://www.bt.pa.msu.edu/index_cosy.htm
- [4] GEANT4, <http://geant4.cern.ch/>

High intensity heavy-ion beam injection in CNS Active Target (CAT) and measurement of $^{132}\text{Xe}(d,d')$

S. Ota^a, C.S. Lee^{a,b}, H. Tokieda^a, Y.N. Watanabe^c, Y. Aramaki^a, M. Dozono^a, U. Garg^d, Y. Gupta^d, N. Imai^a, S. Kawakami^e, S. Kawase^a, Y. Kiyokawa^a, M. Kobayashi^a, Y. Kubota^{a,b}, M. Matsushita^a, S. Michimasa^a, N. Nakatsuka^{b,f}, T. Peach^d, R. Saiseau^{b,g}, M. Takaki^a, K. Wimmer^c, J. Zenihiro^b, E. Takada^h

^a Center for Nuclear Study, Graduate School of Science, University of Tokyo

^b Nishina Center for Accelerator-Based Science, RIKEN

^c Department of Physics, the University of Tokyo

^d Department of Physics, the University of Notre Dame

^e Department of Applied Physics, Miyazaki University

^f Department of Physics, Kyoto University

^g Orsay Fundamental Physics Magistere, University Paris-Sud, France

^h Heavy Ion Medical Accelerator in Chiba, National Institute of Radiological Science

Equation of State (EoS) of nuclear matter governs the bulk property of nuclei in femto-scale and the property of neutron stars in universe at the same footing. Isoscalar Giant Monopole Resonance (ISGMR) is related to the incompressibility of the nucleus, which is one of the parameters in the EoS. The ISGMR can be studied via the inelastic scattering (d, d'). To extract the ISGMR strength, the differential cross-section at the forward angle is important since the monopole strength has peak at the forward angle. As well as the forward angle scattering, the wide angular acceptance is required for the multipole decomposition analysis to deduce the ISGMR strength distribution in the continuum region above the particle emission threshold.

We are developing the gaseous active target system, CNS Active Target (CAT) to measure the low-energy recoil particles corresponding to the forward angle scattering [1]. The CAT consisted of the time projection chamber (TPC) and Silicon (or NaI) detector array surrounding the field cage of TPC. We are aiming at the series of the measurement of ISGMR in $A = 132$ isobars in order to determine the K_T parameter in the EoS. In FY2013, we modified the multiplication part of the CAT. In order to measure the low-energy deuteron inelastically scattered from the $A = 132$ isobars, we replaced thin GEM by thick GEM (THGEM) [2]. For the injection of the high-intensity beams, we introduced the mesh grid between the drift region and the multiplication part to reduce the large current after the multiplication along the beam path while the effective gas gain in the recoil region just beside the beam path was kept high enough to detect the recoil particles. The effective gas gain below 100 was achieved. However, the energy resolution became much worse than 10% since the number of primary electrons (just before multiplication) was reduced. In order to improve the energy resolution, which also determines the position resolution because the position is deduced using the charge division, we tried to reduce the effective gain with keeping the number of primary electrons. In this paper, we briefly summarize the new method to reduce the effective gain [3] and report the first measurement of the (d, d') on ^{132}Xe .

The effective gas gain using THGEM can be controlled by changing the voltage supplied to each electrode. In order to change the effective gas gains in beam region and recoil regions independently, the electrode of THGEM was seg-

mented into three region, namely one electrode of the beam region and two electrodes of the recoil regions. Figure 1 shows the photo of the THGEM with segmented electrodes called dual gain THGEM (DGTHGEM). Three electrodes of the widths of 4 cm, 2 cm and 4 cm are formed. The diameter and the pitch of the hole are $300\ \mu\text{m}$ and $700\ \mu\text{m}$, respectively, in the three regions, and they are exactly same as the original (single electrode) THGEM.

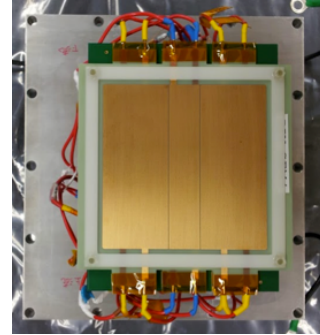


Figure 1: Photo of the segmented-electrode THGEM called dual gain THGEM (DGTHGEM). Three electrodes are of width of 4 cm, 2 cm and 4 cm.

We measured the effective gas gain and the energy resolution at the beam region of the DGTHGEM using $100\text{-MeV/u } ^{132}\text{Xe}$ primary beam at the HIMAC in Chiba. The CAT was operated with 0.4-atm deuterium gas and three layers of DGTHGEMs. Figure 2 shows the correlation between measured gain and resolution. The horizontal and vertical axes show the effective gas gain and energy resolution, respectively. The filled circles indicate the data taken with fixing ratio among the applied voltages to the electrodes while the open circles indicate the data taken with changing only the voltage applied to the electrode nearest to the readout pads. The effective gas gain is the ratio between the measured charge and the initial charge assuming the calculated energy deposition. The energy resolution was evaluated for the sum of the charges measured at three neighboring readout pads along the beam path for the simplicity. The effective gas gain was successfully suppressed below 100 at the beam region while the effective gas gain at

the recoil region was more than 2000. The measured energy resolution was below 10%, which is better than the achieved resolution by using mesh grid. The CAT was stable under the irradiation of the 10^6 -particle-per-pulse beam of ^{132}Xe .

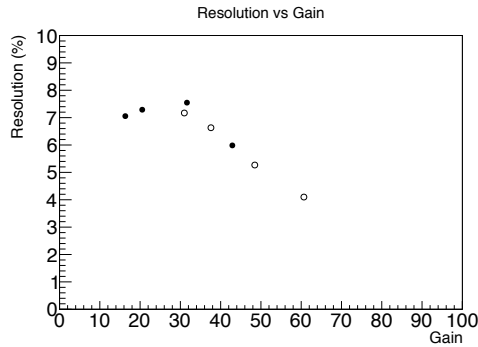


Figure 2: The correlation between the effective gas gain and the energy resolution for the beam region of DGTHGEM.

The experiment of the deuteron inelastic scattering from ^{132}Xe was performed at HIMAC (HIMAC collaborative research 12H307). The CAT consisted of the TPC and silicon detectors and was operated with 0.4-atm. deuterium gas. The silicon detectors were covered by 110- μm aluminized Mylar in order to reduce the noise from a large number of delta rays. Diamond detector was located in the air upstream of the CAT. An entrance window of 100- μm aluminized Mylar, 56-cm long beam pipe and 20-mm thick collimator was attached to the entrance of the CAT. The beam particles went through the CAT and stopped at the beam dump located more than 5-m downstream of the CAT. Figure 3 and 4 show the hit pattern of the same event. In Fig. 3, the threshold was set as low as possible and all the recorded pulses are filled. The color indicates the number hits in each readout pad. In this case, almost all the pads are fired by the cloud of delta rays. On the other hand, in Fig. 4, the threshold to find the pulse is set to be higher. Then, the clear trajectory of recoil particle can be extracted from the cloud of delta rays. The further analysis is in progress.

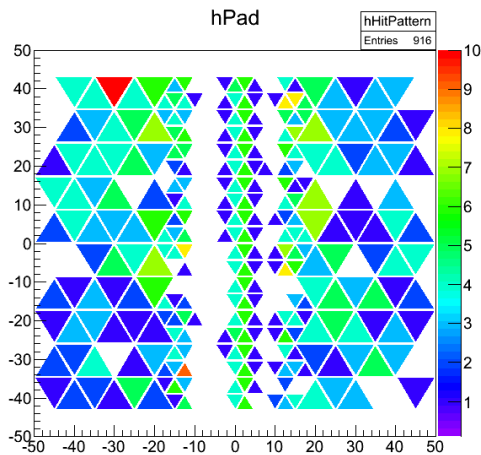


Figure 3: Hit pattern of one event of (d, d') on ^{132}Xe . Color indicates the number of recorded pulses in each readout pad. Beam particle travels from bottom to top.

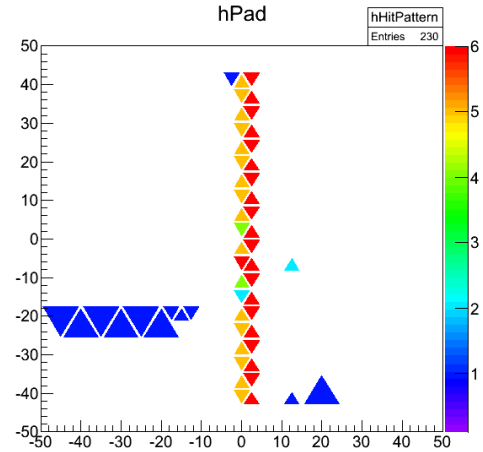


Figure 4: Same event as Fig. 3 but the pulses are refined by setting higher threshold by software. Clear trajectory of recoil particle can be found.

References

- [1] S. Ota *et al.*, CNS Annual Report 2011, (2013), 70-71.
- [2] C.S. Lee *et al.*, JINST 9, C05014 (2014)
- [3] S. Ota *et al.*, Journal of Radioanalytical and Nuclear Chemistry, 305, 907-911 (2015)

Study of Track Finding Algorithm for CNS Active Target

H. Tokieda^a, S. Ota^a, C. S. Lee^{a,b}, Y. N. Watanabe^c, and T. Uesaka^b

^aCenter for Nuclear Study, Graduate School of Science, University of Tokyo

^bNishina Center RIKEN (The Institute of Physical and Chemical Research)

^cDepartment of Physics, the University of Tokyo

We are developing a gaseous active target, called CNS Active Target (CAT). The CAT consists of a Time Projection Chamber (TPC) and NaI or Si detectors surrounding the field cage of TPC. As an electron multiplier of the CAT, Gas Electron Multipliers (GEMs) are employed. Readout pads are of regular triangular shape with 5-mm and 10-mm side and total number of readout pads is 400. Figure 1 shows a schematic view of the readout pads. An area consisting of 5-mm pads (small pads) is referred to as a beam region, areas of 10-mm pads (large pads) are referred to as recoil regions. One column in the beam region and recoil region are consisted of 20 pads and 10 pads, respectively. The current status of the CAT is reported by Ota *et al.* [1]. In this report, a track finding algorithm of the CAT will be presented.

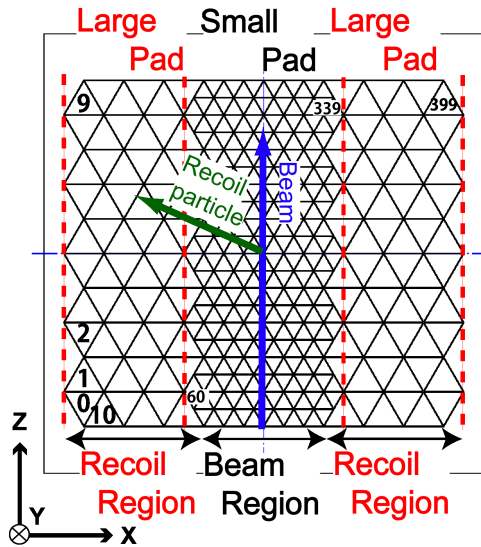


Figure 1: A schematic view of the readout pads of the CAT, which are of regular triangular shape with 5-mm and 10-mm side and total number of readout pads is 400. An area consisting of 5-mm pads (small pads) is referred to as a beam region, areas of 10-mm pads (large pads) are referred to as recoil regions.

Incident beam particle reacts with a target nucleus in the gas, and the target nucleus is recoiled. Non-reacting beam particle penetrates the active area of the CAT (Fig. 1). Beam and recoil particles ionize nuclei in the gas, releasing electrons. These electrons drift towards the GEMs and readout pads in an electric field. In the analysis, trajectory in the X-Z plane and in the X-Y plane are determined by using a charge distribution on readout pads and the electron drift time, respectively.

After a detection timing and charge are deduced by the pulse shape analysis, a track finding algorithm of the CAT is applied in two steps: hit collections (clusters) in which each hit is relevant are searched; and events included beam and

recoil particles are picked out from the hit clusters. Below, details of this two steps are described.

First step is to cluster the hits. In order to define a cluster, two conditions are required: (1) two or more hits at pads in neighboring columns and (2) the drift time of the hit is within a certain time range respect to that of the neighboring pad. Typical dynamic range of a ϕ direction of recoil particles is within 45 degrees. Since the drift velocity was about 0.6 cm/ μ s/atm, the difference between the drift time of hits on 10-mm pads was around 200 ns. However, a software time range of the drift time was needed to be 400 ns. Whether this time range of 400 ns can be contracted is currently being investigated.

If the number of hits in a cluster is less than 17, the cluster will be removed, because a beam fires typically more than 17 hits. Figure 2 shows an example of a result of this clustering. A horizontal and vertical axis are the detection timing and a pad ID, respectively. The pad IDs in the beam region are 60 – 339 (Fig. 1). The lines represent pulses (hits) and circles represent hit clusters obtained in the clustering.

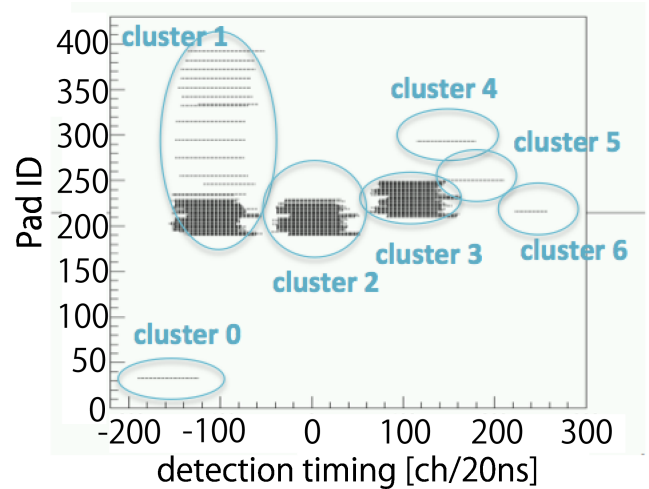


Figure 2: An example of a result of the clustering. The horizontal and vertical axis are the detection timing and pad ID, respectively. Lines show pulses (hits) and circles show hit clusters obtained in the clustering.

Second step is to search reaction events. The purpose of this search is that events including hits of the beam and recoil particles are extracted from hit clusters obtained in the first step. In one hit cluster, if fired pads in one column are more than 17, these hits of this column are defined as beam hits. Typically, the beam particle fired two columns. The other hits in same hit cluster are candidates of recoil hits. The candidates of recoil hits are clustered on the basis of position condition. This position condition is that two or more hits at pads are within neighboring pads. This is because true hits of one event should be spatially continuous. Figure 3 shows this position conditions. Under the condi-

tion, gray pads meet requirements for a black pad. If there are several recoil clusters in one hit cluster, the recoil cluster of the longest range parallel to the X-axis are chosen. Farther development for the treatment of recoil multi-cluster events is on going.

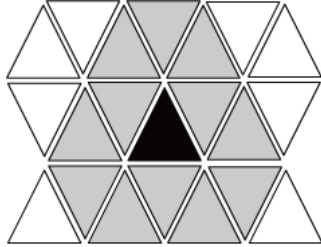


Figure 3: Position conditions of the clustering of recoil particles. Under the condition, gray pads meet requirements for black pad.

Range and recoil angle were determined using charge division method for the selected events. The position between two neighboring pads in the X-Z plane is deduced for every neighboring pads, while in the X-Y plane the positions of both ends of beam and recoil track are used. Figure 4 shows the TKE of recoil particles as functions of the angle in the laboratory system (θ_{lab}), except for the recoil cluster in which the number of hits is less than 8. The lines (curves) in this figure is a result from kinematics calculation. Here, θ_{cm} and E_x are the angle in the center of mass system and excitation energy, respectively. The data points around 120 deg. or 0.2 MeV seem to be misidentification of tracks. We will quantitatively investigate about this issue.

References

[1] S. Ota *et al.*: CNS Annual Report 2014.

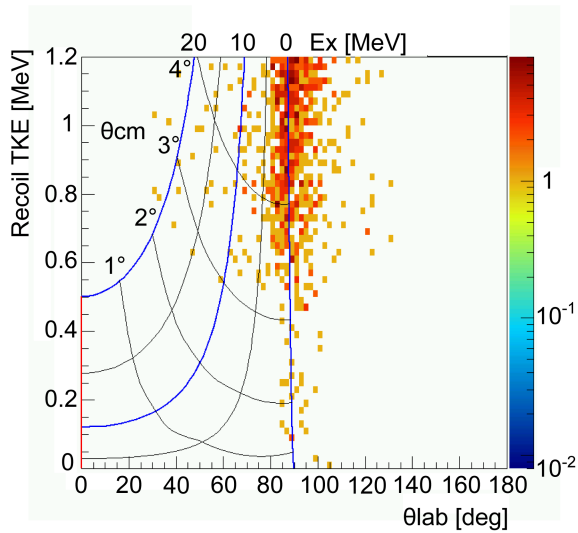


Figure 4: The TKE of recoil particles as functions of the angle in the laboratory system. The line is a result from kinematics calculation.

In summary, we developed a track finding algorithm of the CAT. This algorithm is composed of two steps: the hit cluster search and event search. This analysis is not supported to the multi-beam and recoil multi-particle. We intend to continue this development and increase the accuracy of track finding. Also, we plan to investigate the misidentification of tracks. These analyses are currently in progress.

Pressure dependence and long-term stability of effective gas gain of THGEM in deuterium gas

C. S. Lee^{a,b}, S. Ota^a, H. Tokieda^a, R. Kojima^a, Y.N. Watanabe^c, R. Saiseau^d and T. Uesaka^b

^aCenter for Nuclear Study, Graduate School of Science, The University of Tokyo

^bNishina Center for Accelerator-based Science, RIKEN

^cDepartment of Physics, The University of Tokyo

^dUniversity Paris-Sud

1. Introduction

A low-pressure gaseous active target called CNS Active Target (CAT) has been developed for a deuteron inelastic scattering off unstable nuclei [1]. The CAT consists of a combination of Gas Electron Multiplier (GEM) and Time Projection Chamber (TPC) as a vertex tracker, and Si detectors as a total kinetic energy detector for high momentum recoil particles. Three 400 μm -thick Thick Gas Electron Multipliers (THGEMs) are employed for the amplification inside TPC in order to achieve an effective gas gain of 10^4 at 0.4 atm deuterium gas. This gas gain of 10^4 fulfils the detection of the minimum energy deposition of our interest, 5 keV/cm, which is the energy loss per centimeter of a recoiling deuteron to 9° in the centre-of-mass frame from $^{132}\text{Sn}(d, d')$ reaction at 100 MeV/nucleon. Properties of a double THGEM configuration in 0.2-, 0.3- and 0.4-atm deuterium were investigated for the first time by corresponding authors [2]. In addition to the previous work, the pressure dependence and the long-term stability of the effective gas gain were investigated by using a triple THGEM configuration.

2. Experimental Setup and Measurement

A schematic view of the experimental setup is shown in Figure 1. The collected electrons on the readout pad was integrated with a charge-sensitive preamplifier which has a conversion gain of 200 mV/pC and a time-constant of 80 ns. The output signal from the preamplifier was treated by a shaping amplifier (ORTEC 571) and the pulse height of the shaped signal was recorded by a multi-channel analyser (MCA) (Kromek 102). The effective gas gain G_{eff} is derived

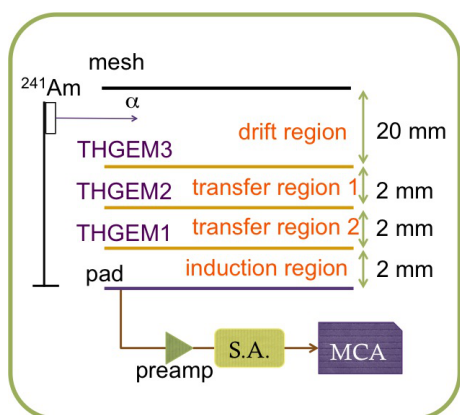


Figure 1: Experimental setup of this work. Voltages to THGEMs are supplied from a single channel of a HV module, by using a register chain where each ΔV_{THGEM} is equally provided.

from the equation:

$$G_{\text{eff}} = \frac{Q_{\text{pads}}}{q_e \cdot \Delta E / W_i} \quad (1)$$

where G_{eff} is the effective gas gain of GEM, ΔE is the energy loss of particle, W_i is mean energy for ion-electron pair creation of certain gas, q_e , the elementary charge and Q_{pads} is the collected charges on the readout pad.

3. Results and Summary

Figure 2 shows the obtained gain curves including the achievable gain from a triple THGEM configuration for 0.18-0.5 atm D_2 as a function of the voltage between the upper and the lower electrodes of THGEM, ΔV_{THGEM} . A triple THGEM configuration provides the effective gas gain of more than 10^4 for every pressure, and even more than 10^5 for under 0.35-atm. Every set of measurements for each

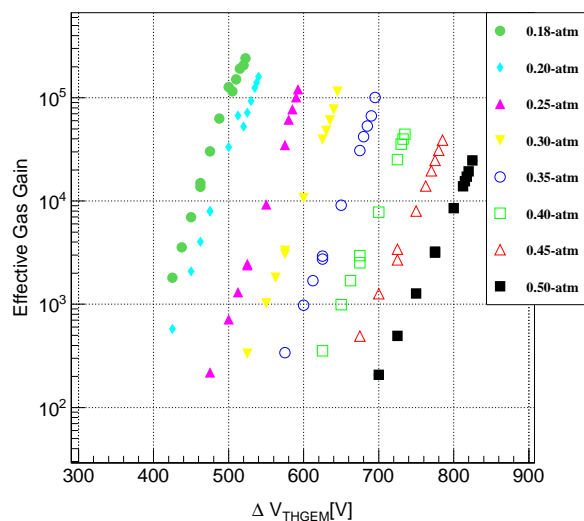


Figure 2: Gain curves of a triple THGEM configuration at 0.18-0.5 atm D_2 as a function of ΔV_{THGEM} .

pressure was suspended when a normal spectrum can hardly be taken due to the discharge problem. In this measurement, the ratio of the voltages on each electrode of THGEMs was retained in constant by using a resistance chain.

A long term stability of the effective gas gain of THGEMs was investigated with hydrogen gas, assuming that hydrogen and deuterium have same chemical properties. Time evolution of the G_{eff} in 0.4-atm hydrogen gas for a triple THGEM configuration was measured for 75 hours with a continuous alpha source irradiation. Figure 3 shows the

time dependence of the relative gas gain with and without a correction based on pressure and temperature described later. The initial drop of the gain seems to be caused by the charge-up of the overall insulator [3].

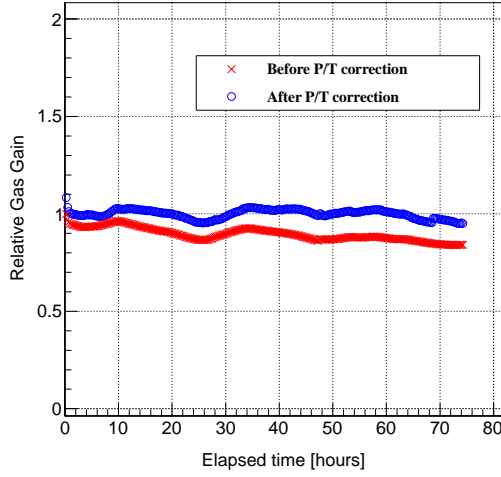


Figure 3: Time dependence of relative gas gain in 0.4-atm pressure H_2 .

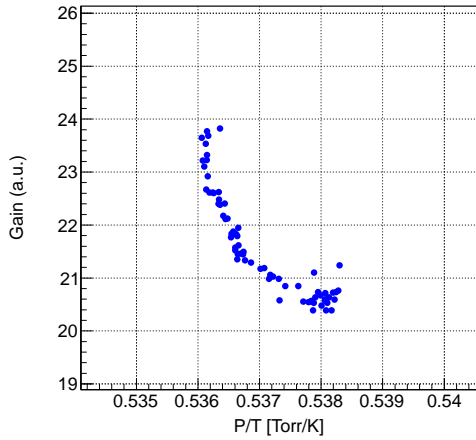


Figure 4: P/T correlation of gas gain in 0.4-atm pressure H_2 .

The high voltage to the THGEMs was supplied just before the start of the measurement and maintained stably until the end. ΔV_{THGEM} was 682.93 V and the drift field strength E_{drift} was 1.09 kV/cm/atm, the transfer field strengths $E_{\text{transfer}1,2}$ were 2.56 kV/cm/atm and the induction field strength $E_{\text{induction}}$ was 3.41 kV/cm/atm. In order to keep the temperature inside the chamber constant, the ambient room temperature was kept fixed with a standard air conditioning unit during the measurement. However, some changes of gas pressure P and temperature T were observed (see Figure 4) and the P/T correction was applied by using the P/T correlation of G_{eff} as $f(P/T) = \exp(\alpha + \beta \cdot P/T)$, where α and β are the fitting parameters. After the P/T correction, it turned out that the gas gain of THGEM has 2 hours or less of the relaxation time which is significantly

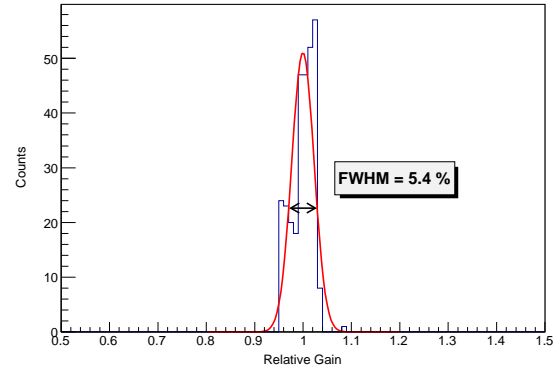


Figure 5: The gain deviation during the measurement.

shorter than our previous study [2], and the deviation after the relaxation was about 5% (FWHM) (see Figure 5).

References

- [1] S. Ota *et al.*, CNS Annual Report **2011** CNS-REP-90(2013) 70-71.
- [2] C.S. Lee *et al.*, JINST **9** (2014) C05014.
- [3] M. Tokuda *et al.*, JINST **7** (2012) C04006.

Performance Evaluation of the MICROMEAS for the Application of the TPC

K. Terasaki, H. Hamagaki, and T. Gunji

Center for Nuclear Study, Graduate School of Science, University of Tokyo

Table 1: The geometries of MICROMEAS.

	Gap	Fineness	Mesh pitch
MMG128	128 μm	400LPI	63.5 μm
MMG90	90 μm	780LPI	32.6 μm

1. Introduction

ALICE is a dedicated experiment to study the heavy-ion physics at LHC, especially the Quark Gluon Plasma (QGP). The ALICE Time Projection Chamber (ALICE-TPC) [1], which is the main device in the central barrel for charged particle tracking and particle identification, consists of a 90 m³ cylinder filled with Ne/CO₂/N₂ (90/10/5).

Secondary ions generated in an electron-avalanche process in the TPC move back to the drift space, known as ‘‘Ion Backflow (IBF).’’ Because IBF distorts the electric field in the drift space, reduction of IBF is essential to achieve good performance of the TPC. A gating grid system is widely employed to reduce IBF; however, it limits the data acquisition rate to the order of kHz. The rate of heavy-ion collisions at the LHC will be 50 kHz since 2021. The ALICE-TPC will be upgraded to read out data of Pb-Pb collisions continuously, which requires IBF to be less than 1.0% at the gain of 2000 in Ne-based gas mixtures [2]. Energy resolution for ⁵⁵Fe needs to be better than 12% to preserve current performance of the particle identification.

The performance of quadruple GEM stacks as a readout chamber is being investigated for this upgrade. In addition, investigations with 2GEMs + MICROMEAS are being carried out as reported in this article.

2. MICROMEAS

Figure 1 shows a schematic view of a cross section of MICRO-MESH-Gaseous Structure (MICROMEAS) [3]. MICROMEAS has a micromesh which is supported by

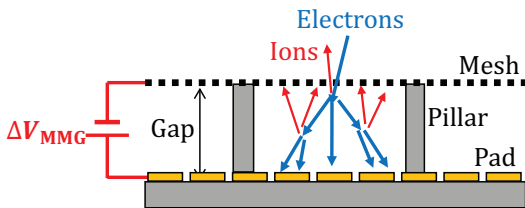


Figure 1: A schematic view of a cross section of MICROMEAS.

pillars $\sim 100 \mu\text{m}$ above a readout pad. Electrons are multiplied by a potential difference between the mesh and the readout (ΔV_{MMG}). Secondary ions are absorbed efficiently on the mesh when the electric field above the mesh is considerably smaller ($\sim 1/100$) than that below the mesh.

Two types of MICROMEASs have been developed; One has a 400 LPI (Lines Per Inch) mesh located 128 μm above the readout pad (MMG128) and the other has 780 LPI mesh and 90 μm gap (MMG90). Their geometries are summarized in Table 1.

3. Measurement Setup

A schematic view of the measurement setup with 2GEMs + MICROMEAS is shown in Fig. 2. Two 50 μm -thick

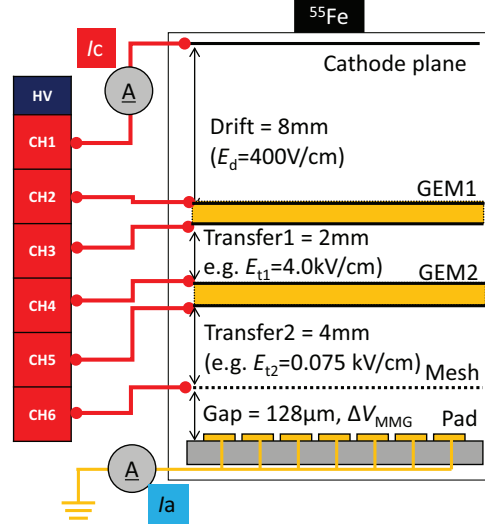


Figure 2: A schematic view of measurement setup with 2GEMs + MICROMEAS.

GEMs are placed above MICROMEAS to meet the requirements on IBF and energy resolution for the ALICE-TPC. They are removed when the characteristics of MICROMEAS is measured. The readout plate is divided into 120 pads ($8 \times 10 \text{ mm}^2$) and induced currents from all the readout pads are summed up.

IBF is defined as I_c/I_a , where I_c and I_a are currents at the cathode plane and at the anode pads, respectively. Gain is calculated as $I_a/(N_{\text{seed}} \times R \times e)$, where N_{seed} , R , and e are the number of seed electrons for ⁵⁵Fe in Ne gas, the rate of X-ray from ⁵⁵Fe, and the charge of an electron, respectively.

The electric field in the drift region (E_d) is fixed to 0.4 kV/cm, as is used in the ALICE-TPC. A high electric field ($\sim 4.0 \text{ kV/cm}$) is applied to the transfer1 region between GEM1 and GEM2 in order to extract the electrons multiplied in GEM1 efficiently. On the other hand, the electric field in transfer2 between GEM2 and the mesh is kept low ($< 0.1 \text{ kV/cm}$) for reducing IBF from MICROMEAS.

4. Results with the single MICROMEAS

Figure 3 shows gain and IBF of MMG128 and MMG90 for Ne/CO₂/N₂ (90/10/5). Gain can reach 2000, however, IBF is not less than 1.0% at gain ~ 2000 (see also Fig. 4). IBF reaches to the field ratio (E_d/E_{MMG}) at higher ΔV_{MMG} , where E_{MMG} is the electric field in MMG. IBF and energy resolution of MMG128 and MMG90 as a function of gain are shown in Fig. 4. MMG90 has a better IBF than MMG128 at the same gain because of the mesh fineness and the low field ratio. Still, their energy resolutions are nearly the same value. IBF at gain ~ 2000 with the single MMG doesn't satisfy the requirement for the upgrade.

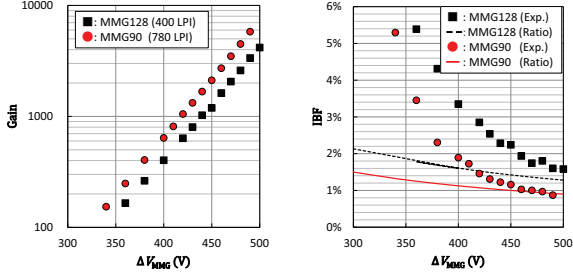


Figure 3: Gain (left) and IBF (right) with the single MMG configuration as a function of ΔV_{MMG} . Black squares and red circles show the result of MMG128 and MMG90, respectively. Dashed curve and solid curve in the right figure show the field ratio (E_d/E_{MMG}) of MMG128 and MMG90, respectively.

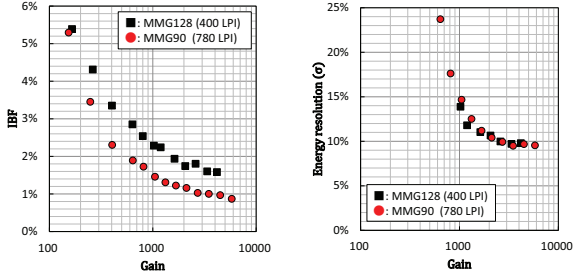


Figure 4: IBF (left) and energy resolution (right) as a function of gain. Black squares and red circles show the result of MMG128 and MMG90, respectively.

5. Results with the stack configuration

Figure 5 shows IBF and energy resolution for $\Delta V_{\text{GEM1}} - \Delta V_{\text{GEM2}}$ scan with the stack configuration of MMG128. This scan was performed for three different ΔV_{MMG} .

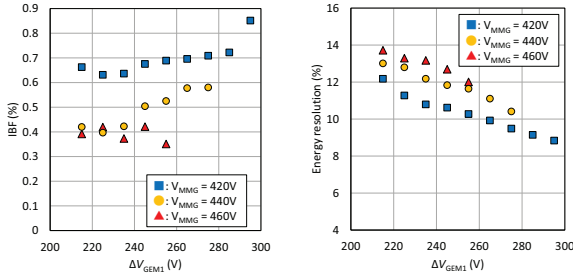


Figure 5: IBF (left) and energy resolution (right) for Ne/CO₂/N₂ (90/10/5) as a function of ΔV_{GEM1} . Blue squares, yellow circles, and red triangles show the result of $\Delta V_{\text{MMG}} = 420$ V, 440 V, and 460 V, respectively.

ΔV_{GEM1} and ΔV_{GEM2} were changed at fixed ΔV_{MMG} , E_d , E_{t1} and E_{t2} while gain is kept to ~ 2000 . A setup with larger MMG gain and smaller 2GEM gain leads to better IBF. Smaller gain of GEM1 causes worse energy resolution because of the worse electron-collection efficiency of GEM1 (i.e. smaller ΔV_{GEM1}). The correlation between energy resolution and IBF for Ne/CO₂ (90/10) and Ne/CO₂/N₂ (90/10/5) with the stack configuration of MMG128 is shown in Fig. 6. Additional nitrogen to Ne/CO₂ (90/10) leads to better IBF because a larger potential difference is required to achieve the gain of 2000 and subsequently the field ratio of MICROMEAS decreases. There are some points which have less than 1% IBF and better than 12% energy resolution. The correlation with the stack configuration of MMG90 was also evaluated, and it

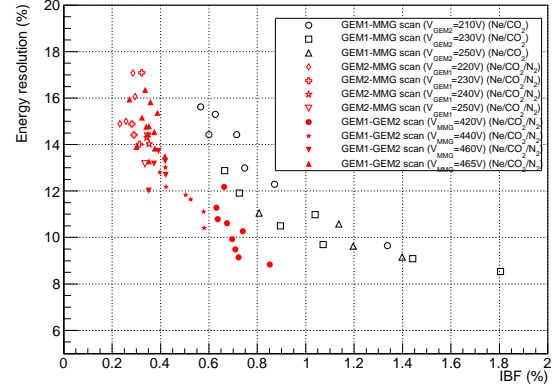


Figure 6: Energy resolution as a function of IBF for Ne/CO₂ (black) and Ne/CO₂/N₂ (red) with the stack configuration of MMG128 with different voltage setups.

was almost the same as the result of MMG128 because ions coming from MMG is only $\sim 20\%$ of the total number of ions going back to the drift region from GEM1-MMG.

6. Summary and outlooks

The performance of two types of MICROMEAS and 2GEM-MMG were evaluated for the application of the TPC. IBF and energy resolution with the single MICROMEAS configuration don't satisfy the requirement for the upgrade. Eventually, less than 1.0% IBF and better than 12% energy resolution were achieved with the 2GEMs + MICROMEAS configuration. This result fulfills the requirements for the ALICE-TPC, however, further investigations of gain stability, discharge property, and spatial resolution are required.

References

- [1] CERN-LHCC-2000-001 (2000).
- [2] CERN-LHCC-2013-020 (2013).
- [3] Y. Giomataris et al.: Nucl. Instr. and Meth. **A 376**, 29 (1996).

Emittance measurement of mixed ion beam in Hyper ECR ion source

Y. Ohshiro, Y. Kotaka, S. Watanabe, H. Muto^a, H. Yamaguchi, N. Imai and S. Shimoura

Center for Nuclear Study, Graduate School of Science, University of Tokyo

^aCenter of General Education, Tokyo University of Science, Suwa

1. Introduction

An analyzed ion beam from the Hyper ECR ion source is injected to RIKEN AVF cyclotron in order to supply for the nuclear physics experiment, RI production and biological irradiation [1,2,3]. The transmission efficiency of the gaseous ion beam from the ion source to the cyclotron extraction is typically 10% or less. The transmission depends on the beam emittance which varies with ion species and beam energy. For this reason, the beam emittance of the extraction region of the ion source was measured in this year.

Generally, various ionic species of the beam, called “mixed ion beam”, are pulled out at the same time from the extraction region of the ion source. The emittance of a specific ion beam to be identified is measured by a method of dividing and separating the mixed ion beam, called “mixed beam analysis method”. We describe the method of the emittance measurement of the mixed ion beam below.

2. Emittance measurement

A schematic of emittance measurement with the mixed beam analysis method is shown in Fig. 1. Beams from the ion source go through the slit (E1) are separated by the analyzing magnet (AM), and are measured with a beam monitor (FC). The beam intensity at FC decreases when the beam is hidden by gradually inserting the beam cover (E2). Then, beam profiles are obtained as shown in Fig. 2. Each profile represents the beam reduction rate at FC that is varied according with the insertion position of E2.

Angle (X') of the emittance is determined from the profile and the distance between E1 and E2. Emittance is calculated by the X and X' where X is a distance that has moved perpendicularly E1 to the direction of the beam. The initial emittance was measured by moving E2 in 2.5 mm step while inserting E1 in 0.7 mm step. The slit width of E1 is 0.2 mm, and the distance between E1 and E2 is 830 mm. By moving E1 and E2, we measured the emittance of the ion beam at 308 mm downstream from the beam starting point of the ion source.

3. Initial beam emittance diagram

An example of multiple beam profile at E2 separated at E1 is shown in Fig. 2. In this case, the beam at E1 is divided into seven profiles at E2. The peak of the profile at E2 of the beam emitted from $X = -4.9$ mm at

E1 is identified at -21 mm.

Figure 3 shows an example of beam emittance obtained from information above. In this case, the beam

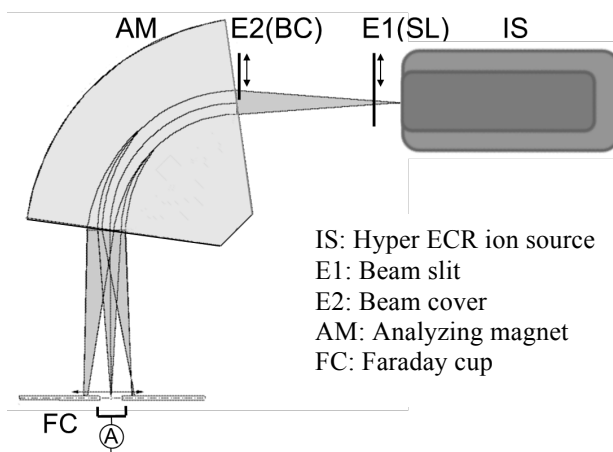


Fig. 1: A schematic of emittance measurement with the mixed beam analysis method. The emittance at E1 is measured by using E2, AM and FC.

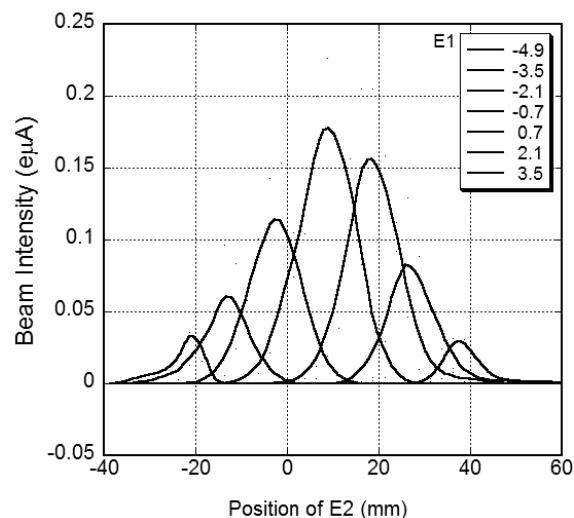


Fig 2: An example of multiple beam profile separated at E1. Beam at E1 is divided into seven profiles at E2.

was $^{12}\text{C}^{4+}$ and the extraction voltage and the intensity were 11.14 kV and 40 μA , respectively. The transmission efficiency from the ion source to the cyclotron extraction was 23%, which was relatively high. The emittance with 95% was calculated using the

14 split profiles measured at E2, when E1 is moved from -8 mm to 8 mm. From the emittance, we found that the beam has a spread of $169.9 \pi\text{mm}\cdot\text{mrad}$, and the beam axis is shifted in the positive direction from the center of the beam duct.

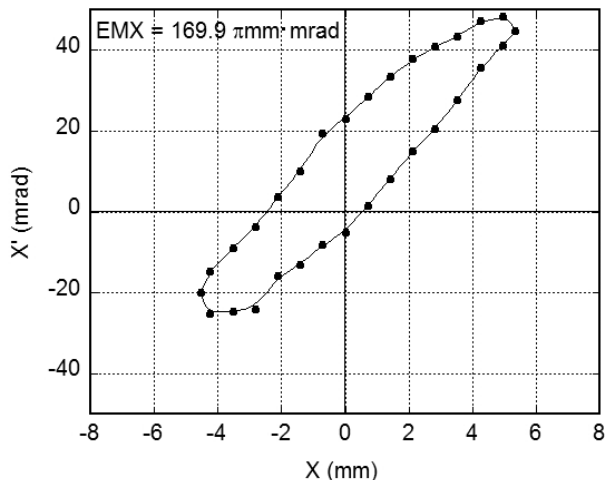


Fig. 3: An example of $^{12}\text{C}^{4+}$ ion beam emittance at E1. X and X' are obtained by dividing a beam at E1 to 14 profiles.

We also measured the emittance of the $^{12}\text{C}^{4+}$ beam when we changed the extraction voltage and beam intensity of the ion source (see Table 1). The left side of Table 1 shows the beam emittance when the extraction voltage applied were 6.34 kV, 8 kV and 11.14 kV while the intensity was kept constant at $80 \mu\text{A}$. The right side of Table 1 gives the emittance when the beam intensity were $40 \mu\text{A}$, $80 \mu\text{A}$ and $200 \mu\text{A}$ while the voltage was kept constant at 11.14 kV. This table suggests that the emittance is improved by a lower beam intensity and higher extraction voltage.

4. Estimation of plasma boundary

Schematic diagram of the extraction system of Hyper ECR ion source is shown in Fig. 4 together with the beam trajectory [4]. Beam trajectory is a bundle of ray trace drawn from E1 to the plasma electrode (PE), based on the emittance of Fig. 3. From this figure, various beam information of the ray traces in the extraction system are described as following criterion of 1) to 2),

- 1) Deviation of the axis of the beam is about 2.8 mm from the center of the beam duct.
- 2) Beam emitted from the PE is converged at approximately 24 mrad, is focused to 195 mm position (FP).

Plasma boundary (PB) is concave, strongly convergent beams are extracted. In this way, we were able to predict an ideal surface structure of the PB of the ECR ion source, called "ideal PB" when the AVF cyclotron achieved the transmission efficiency of 23%.

Table 1. Emittances of $^{12}\text{C}^{4+}$ ion beam when measured by changing the extraction voltage and the beam intensity of the ion source.

Extraction voltage (kV)	Beam emittance ($\pi\text{mm}\cdot\text{mrad}$)	Beam intensity (μA)	Beam emittance ($\pi\text{mm}\cdot\text{mrad}$)
6.34	273.7	40	169.9
8	218.5	80	175.1
11.14	175.1	200	270.4

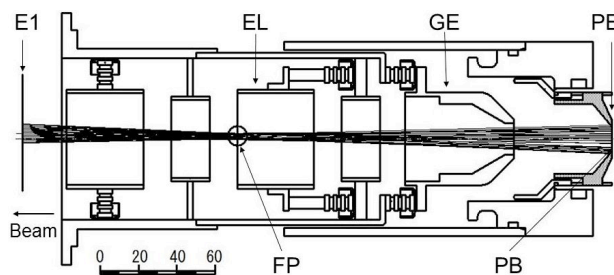


Fig. 4: Schematic view of the extraction system of Hyper ECR ion source that contains the beam ray trace. PE: Plasma electrode GE: Ground electrode EL: Einzel lens E1: Beam slit PB: Plasma boundary FP: Focus point of the beam

In order to constantly reproduce this ideal PB, we are planning to Remodeling of the beam extraction system assisted with a diagnostic system which is based on the mixed beam analytical method.

5. Summary

Emittance of the specific ion beams in a mixed beam extracted from the ion source was measured. Measured beam emittances show the tendency of that a higher extraction voltage and a lower ion beam intensity of the ion source lead to good transmission efficiency. In the high extraction voltage and low intensity, the beam profile at a starting point of the ion source becomes narrow due to a good emittance along with the focal position. We have enhanced the reliability of the measurement method; we hope that will be used to remodel the extraction system of the ion source.

References

- [1] Y. Ohshiro, S. Yamaka, S. Watanabe, K. Kobayashi, Y. Kotaka *et al.*, Rev. Sci. Instrum. **85** (2014) 02A912.
- [2] Y. Yanagisawa, S. Kubono, T. Teranishi *et al.*, Nucl. Instrum. Methods Phys. Res. **A539** (2005) 74-83.
- [3] Y. Ohshiro, S. Yamaka *et al.*, RIKEN Accel. Prog. Rep. **39** (2006) 231.
- [4] Y. Ohshiro, S. Watanabe *et al.*, CNS Annual Report 2004 (2003) 71.

THE PEFFORMANCE OF PEEPER-POT EMITTANCE MONITOR

Y. Kotaka, Y. Ohshiro, S. Watanabe, H. Muto^a, H. Yamaguchi, N. Imai, S. Shimoura, K. Kase^b, and K.Hatanaka^b

Center for Nuclear Study, Graduate School of Science, University of Tokyo

^a*Center of General Education, Tokyo University of Science, Suwa*

^b*Riken Nishina Center*

^c*Research Center for Nuclear Physics, Osaka University*

1. Introduction

The upgrade of AVF cyclotron has been conducted by a collaboration of CNS and RIKEN Nishina Center. One of the upgrades is to increase beam intensity supplied to CRIB [1]. One way for this purpose is to increase the transmission efficiency from AVF cyclotron to CRIB, which is currently 6%. This efficiency is composed of four sections. The transmission efficiency of first section from ECRIS to the center of AVF cyclotron is 19%. That of second from the center to the outermost orbit of AVF cyclotron is 63%. That of third from the outermost orbit to the outside of AVF cyclotron is 73%. That of last from the outside of AVF cyclotron to CRIB is 70%. We focused on the first section because it is the lowest.

There are three solenoid coils and two Glaser coils exist in the injection beam line. This means horizontal (x) and vertical (y) beam elements are coupled. Considering this, we focused on a four-dimensional phase space (x, x', y, y'). At first, we started the beam simulation of Hyper ECRIS and then a pepper-pot emittance measurement [2].

2. The measurement principle and the developed pepper-pot emittance monitor

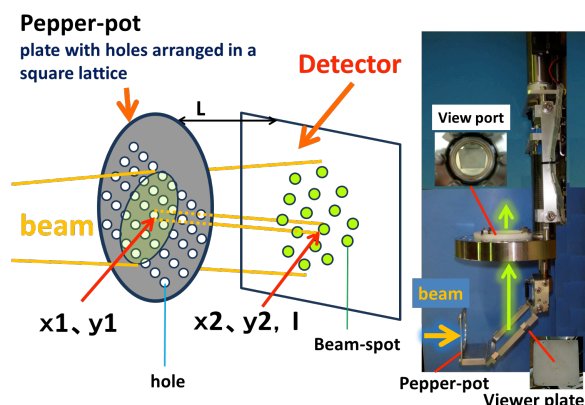


Figure 1: The schematic view of pepper-pot emittance measurement (left) and developed monitor (right).

The measurement principle is indicated in the left of Fig.1. A pepper-pot which is a plate with holes arranged in a square lattice shape is set perpendicular

to beam axis. The beam passing through the holes reaches Detector set at the back. Each beam-spot measured by Detector can have a certain corresponding hole of the pepper-pot like (x1, y1) and (x2, y2). The angle can be calculated with the distance (L) between the pepper-pot and Detector.

We have developed a pepper-pot emittance monitor indicated in the right picture of Fig.1. The diameter of the hole is 0.3 mm. Each distance of the adjacent holes is 3 mm.

Since we selected the viewer plate coated by KBr phosphor as Detector, the beam image can be recorded by digital camera. We assume the beam intensity would be proportional to pixel size of the digital image. The viewer plate is inclined at 45 degrees against the beam axis because the beam image is seen through the view port. L is 55 mm.

3. Measurement Set up

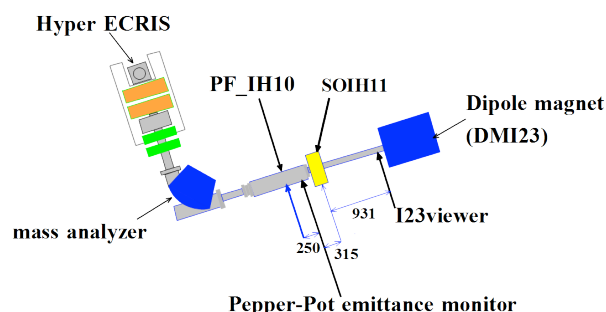


Figure 2: Top view of Hyper ECRIS and the beam line.

Figure 2 shows the test set to see the performance of the pepper-pot emittance monitor. This is a top view of the beam line from Hyper ECRIS to DMI23. The desired ion beam to be analyzed by mass analyzer goes straight to DMI23. On this straight line, a beam profile monitor (PF_IH10), a pepper-pot emittance monitor, a solenoid coil (SOIH11) and a viewer plate (I23viewer) exist in order from upstream. The distance between PF_IH10 and pepper-pot emittance monitor is 250 mm. The distance between pepper-pot emittance monitor and SOIH11 is 315 mm. The distance between SOIH11 and I23viewer is 931 mm.

The mechanism of I23viewer is the same as pepper-pot emittance monitor without the part of pepper-pot. Its height of viewer plate is 80 mm and

its width is 60 mm. It is also inclined at 45 degrees against beam axis.

4. Beam test and Analysis

We irradiated this monitor with ${}^7\text{Li}^{2+}$ 20.88 keV ion beam (160 eμA). The beam image on the viewer plate of the pepper-pot emittance monitor is indicated in the Fig.3. Many beam-spots are found to be separated. Connecting each beam-spot with a certain corresponding hole of pepper-pot, the beam angle is calculated so that the vector distribution indicated in the Fig.4 is made.

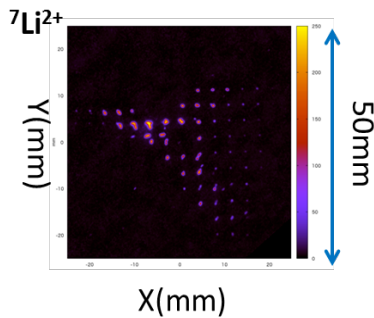


Figure 3: the beam image of the pepper-pot emittance monitor

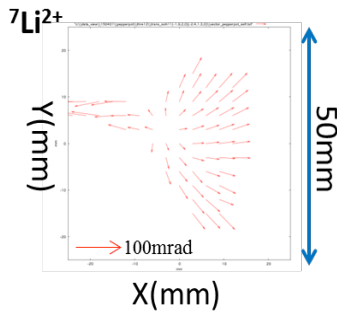


Figure 4: the distribution of vector by the pepper-pot emittance monitor

In order to align the pepper-pot emittance monitor, we transfer the four-dimensional phase space to the position where PF_IH10 is located and make profiles onto the horizontal (x) and vertical (y) axis. Then, we compare the profiles of PF_IH10 indicated in the Fig.5 with the profiles of the transferred four-dimensional phase space indicated in the Fig.6. After alignment, we can find both positions and shapes of the profiles are close in part. However, the proportion of height of the x-axis profiles against the y-axis is different between Fig.5 and Fig.6. We think this is why the gain of the x-axis amplifier of PF_IH10 is different from that of the y-axis. Then, we transfer the four-dimensional phase space to the position where I23viewer exists through the SOIH1 and show it as the image on this x-y plane in the Fig.7. The real solenoid model [3] is adopted as the transfer matrix of SOIH1. The left parts of the Fig.7 are found to be lost. The left part is the beam loss we estimate in view of the barrier of beam duct. Fig.8 shows the beam image of I23viewer.

The top part of this image is undetectable area beyond the I23viewer. Considering these, we compare the beam images measured by I23viewer indicated in Fig.8 with the image of Fig.7 and find both shapes and positions are close in part. This means our pepper-pot emittance monitor has the performance to be useful for analysis.

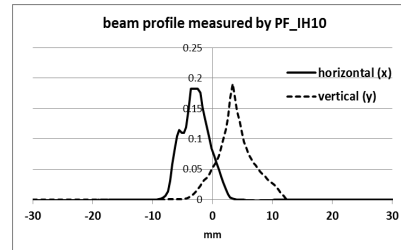


Figure 5: the profiles measured by PF_IH10

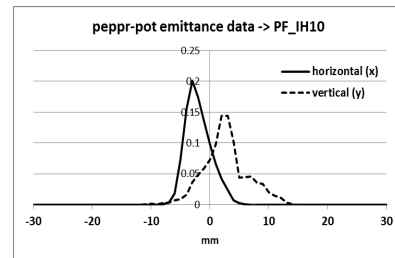


Figure 6: the transferred profile of pepper-pot emittance monitor

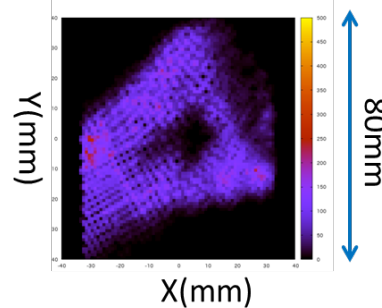


Figure 7 the image of the transferred distribution to the position of I23viewer

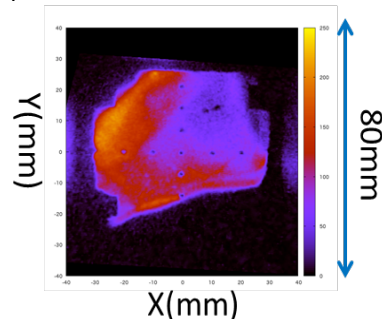


Figure 8: the beam image of I23viewer

REFERENCE

- [1] Y.Yanagisawa et al., Nucl. Instr. and Meth. Phys. Res., **A539** (2005) 74.
- [2] T.Hoffmann et al., Proc. 9th BIW 2000, Cambridge, USA, PP.432-439.
- [3] H. Wiedemann, Particle Accelerator Physics, 3rd ed., Berlin, Springer, 2007.

Observation of Ti getter pump effect by a grating monochromator

H. Muto^{a,b,c}, Y. Ohshiro^b, Y. Kotaka^b, S. Yamaka^b, S. Watanabe^{b,c}, M. Oyaizu^d, H. Yamaguchi^b, K. Kobayashi^c, M. Nichimura^c, S. Kubono^{c,e}, M. Kase^a, T. Hattori^{e,f}, and S. Shimoura^b

^aCenter of General Education, Tokyo University of Science, Suwa, ^bCenter for Nuclear Study, University of Tokyo,

^cNishina Center for Accelerator-Based Science, RIKEN ^dInstitute of Particle and Nuclear Studies, High Energy Accelerator Research Organization ^eInstitute of Modern Physics, Chinese Academy of Sciences, ^fHeavy Ion Cancer Therapy Center, National Institute of Radiological Sciences

1. Introduction

Light intensities of a grating monochromator during plasma chamber baking, $^{48}\text{Ti}^{13+}$ beam operation was observed at the Hyper-Electron Cyclotron Resonance (ECR) ion source. Titanium is famous for its high reactivity toward oxygen, nitrogen, and other gases and is used in titanium sublimation pumps. During the operation of $^{48}\text{Ti}^{13+}$ beam of the Hyper ECR ion source we observed the sublimation pump effect of Ti ions through measurement of light intensities with a grating monochromator. In this paper we describe such effect during chamber baking and beam tuning. In this paper we describe the sublimation pump effect of Ti ions of ECR ion source during chamber baking and beam tuning.

2. Experimental

$^{48}\text{Ti}^{13+}$ ions were produced in the 14.2 GHz Hyper-ECR ion source [1, 2]. The structure and present operation condition of the ion source are described in Ref. 3. A grating monochromator (JASCO CT-25C) and a photomultiplier (Photosensor module H11462-031, Hamamatsu Photonics) were used for a light intensity observation during chamber baking and beam operation [4]. Beam resolution of the grating is 0.1 nm (FWHM). L-37 and R-64 filters were used for preventing both second and third order light signals. Wavelengths of the observed lines were determined in accordance with the NIST Atomic Spectra Database [5]. At the beginning of the chamber baking RF power of ~ 100 W was fed to the residual gas of the plasma chamber made of stainless steel. Extraction voltage was set to 10 kV. Then a vacuum gauge reading rapidly dropped down to less than 10^{-4} Pa from 10^{-5} Pa order, and a brake-down of the high voltage power supply happened because of a huge extraction current. Several hours later the extraction voltage was recovered, and vacuum gauge reading also reached 10^{-5} Pa order. RF power gradually increased to ~ 600 W until obtaining a required vacuum condition ($1\sim 5 \times 10^{-5}$ Pa) and a row extraction current of less than 2 mA.

After baking of the plasma chamber, a pure metal or an oxidized metal rod was gradually inserted into the chamber without an excessive heat. An excessive heat causes a brake-down of the power supply because of a

huge extraction current. The applied RF power was ranging between 500 and 600W for a highly multi-charged ion production. Argon, Neon, Oxygen and Helium gases were used as supporting gases to keep the plasma condition stable.

3. Results

Figure 1 shows the optical line spectrum of the Hyper-ECR ion source under plasma chamber baking after three hours of baking of the plasma chamber. A vacuum gauge reading was 5.7×10^{-5} Pa. The drain current (an extraction current) was 12 mA. The applied RF power was 100 W. In this figure almost all the peaks are due to Fe I and Fe II. There were some C, N and O optical lines in the spectrum. However, those lines are all disturbed by the strong Fe I and Fe II lights, and therefore it was difficult to separate those. Relative intensities of those Fe I and Fe II are quite strong. Figure 2 shows light intensity spectrum of residual gas plasma just after inserting TiO_2 rod. Vacuum condition became stable after insertion of TiO_2 rod. However, a sublimation effect is too strong, and a production of highly multi-charged Ti ions was complex. Then, a pure Ti rod instead of TiO_2 rod was used to make $^{48}\text{Ti}^{13+}$ beam.

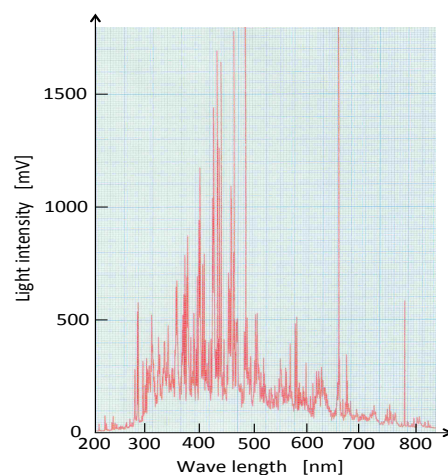


Figure 1. Light intensity spectrum of the residual gas ions after baking for three hours. The peaks of the spectrum are mostly Fe I and Fe II. The pressure and microwave power were 5.7×10^{-5} Pa and 100 W, respectively.

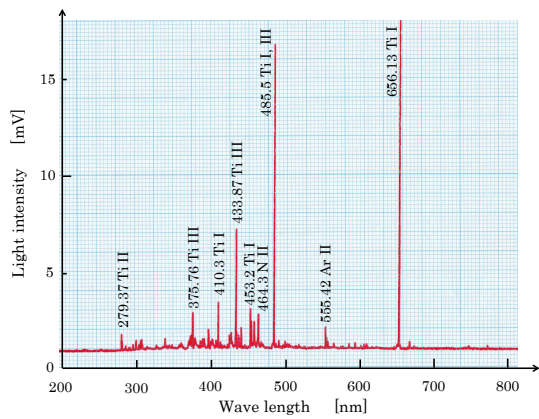


Figure 2 Optical line spectrum of residual gas plasma just after inserting TiO_2 rod. The vacuum gauge reading was 1.9×10^{-5} Pa and RF power was 100 W.

Figure 3 shows the light intensity spectrum during $^{48}\text{Ti}^{13+}$ ion beam tuning with He supporting gas. The RF power was 350 W. Vacuum gauge reading was 3.5×10^{-5} Pa. Ti XIII line was clearly observed and $^{48}\text{Ti}^{13+}$ and $^{48}\text{Ti}^{11+}$ beam intensities were $1.0 \mu\text{A}$ and $9.6 \mu\text{A}$ respectively. From these results sublimation pump effect of Titanium ions was visually demonstrated by the grating monochromator with photomultiplier.

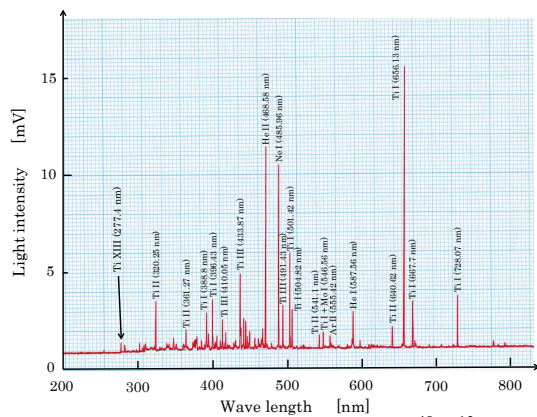


Figure 3. Optical line spectrum during $^{48}\text{Ti}^{13+}$ ion beam tuning with He supporting gas. The RF power was 350 W. Ti XIII line was clearly observed and $1.0 \mu\text{A}$ of $^{48}\text{Ti}^{13+}$ ion beam was obtained.

4. Conclusions

During plasma chamber baking observed light intensities were mostly Fe I and Fe II. Fe ions were relatively heavy and not easy to remove from the plasma chamber. Those atoms were present for a long time in the vacuum chamber. Therefore, stainless steel is thought to be an unsuitable material for a plasma chamber to extract multi-charged ions. Aluminum or Magnesium based light alloy is better for plasma

chamber materials for degassing and extraction.

References

- [1] H. Muto et al., Rev. Sci. Instrum. 84, (2013) 073304.
- [2] H. Muto et al., Rev. Sci. Instrum. 85, (2014) 02A905.
- [3] Y. Ohshiro et al., Rev. Sci. Instrum. 85, (2014) 02A912.
- [4] H. Muto et al., Rev. Sci. Instrum. 85 (2014) 126107.
- [5] www.nist.gov/pml/data/asd.cfm for NIST Atomic Spectra Data base

Theoretical Nuclear Physics

Shell Model Study of Triaxial Deformation in Xenon and Barium Isotopes

N. Shimizu, T. Otsuka^a, T. Mizusaki^b, Y. Utsuno^c, and M. Honma^d

Center for Nuclear Study, Graduate School of Science, the University of Tokyo

^a*Department of Physics, Graduate School of Science, the University of Tokyo*

^b*Institute of Natural Sciences, Department of Physics, Senshu University*

^c*Advanced Science Research Center, Japan Atomic Energy Agency*

^d*Center for Mathematical Sciences, Aizu University*

The nuclear quadrupole collective motion has been one of the most intriguing and characteristic problems of many-body physics. In order to investigate it, we performed shell-model calculations of Xe and Ba isotopes, whose masses are around 134. This report is a part of the future publication [1].

In the present shell model calculations, $50 < Z, N < 82$ valence shells are taken as a model space. The two-body interaction is assumed to consist of the monopole pairing, quadrupole pairing, and quadrupole-quadrupole interactions for identical particles and the quadrupole-quadrupole interaction for a proton-neutron interaction. The strengths of these interactions are determined for reproducing the 2_1^+ , 4_1^+ excitation energies of semi-magic nuclei. The strengths of the proton-proton interaction are particularly taken from Ref. [2]. The adopted values for neutrons (protons) are $g^0 = 0.15(0.21)\text{MeV}$, $g^2 = 0.16(0.22)\text{MeV}$, and $f^{(2)} = -0.0017(-0.0002)\text{MeV/fm}^4$, respectively. The strength of the proton-neutron quadrupole-quadrupole interaction is 0.0017MeV/fm^4 . This phenomenological interaction has sufficient capability for the description of the quadrupole collective states, and is simple enough for determining the strengths. The effective charges are taken as $e_p = 1.5e$ and $e_n = 1.0e$ for protons and neutrons, respectively. We performed large-scale shell-model calculations about the nuclei whose M -scheme dimension is tractable by the conventional Lanczos method. Concerning the nuclei beyond its feasibility, we performed the Monte Carlo shell model (MCSM) calculations [3].

Here, we introduce the MCSM method combined with energy-variance extrapolation [3, 4]. The original MCSM provides us with a linear combination of the angular-momentum (J) projected Slater determinants, which are selected from many candidates generated stochastically, utilizing the auxiliary field Monte Carlo technique. In practice, the MCSM wave function is written as

$$|\Psi^{(N)}\rangle = \sum_{i=1}^N f_{iK}^{(N)} P_{MK}^J |\phi_i\rangle \quad (1)$$

where P_{MK}^J and $|\phi_i\rangle$ are angular-momentum projector and deformed Slater determinant. The coefficient $f_{iK}^{(N)}$ is determined by solving the Hill-Wheeler equation under the condition of $\langle\Psi^{(N)}|\Psi^{(N)}\rangle = 1$. By using the set of Slater determinants, we take a sequence of the approximated wave functions as a function of N . We evaluate energy and its variance of each approximated wave function, and fit the energy ($\langle\Psi^{(N)}|H|\Psi^{(N)}\rangle$) as a function of the corresponding energy variance ($\langle\Psi^{(N)}|H^2|\Psi^{(N)}\rangle - \langle\Psi^{(N)}|H|\Psi^{(N)}\rangle^2$). Since the energy variance of the exact eigenstate is zero, we can obtain the estimated energy as the energy with zero energy variance extrapolation. In order to decrease the computa-

tion time of the energy variance, which are proportional to the N squared, we optimize the energy expectation value of the MCSM wave function by varying the coefficients of the Slater determinants by the conjugate gradient method [5].

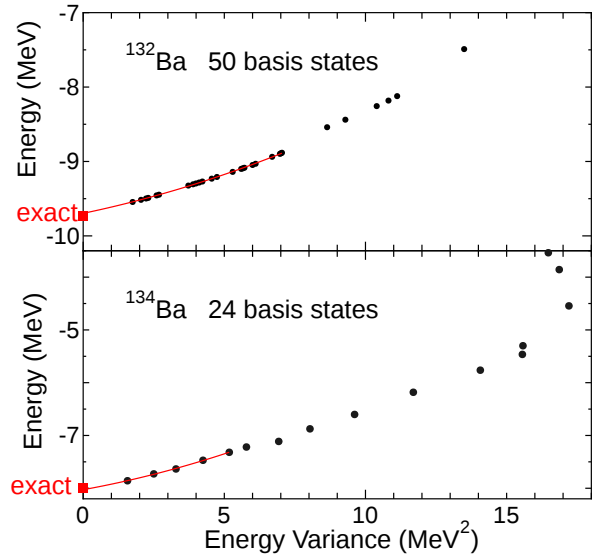


Figure 1: Energy vs. energy variance plot of the ground state energy of ^{134}Ba and ^{132}Ba . The red lines are drawn by chi-square fitting for the extrapolation.

We demonstrate how the extrapolation method works in Fig. 1. In order to discuss the low-lying spectroscopy, it is especially important to estimate the ground state energy precisely, because the ground state energy affects all the excitation energies. It shows the extrapolation plot following the idea of Ref. [4]. The lower panel of Fig. 1 shows the extrapolation plot of ^{134}Ba with 24 J -projected Slater determinants. The extrapolated energy, or the y-intercept of fitted line, agrees quite well with the exact value obtained by the conventional Lanczos method. The upper panel shows that of ^{132}Ba obtained by the same manner as the case of ^{134}Ba . The MCSM wave function is expressed as a linear combination of 50 J -projected Slater determinants. By using this method, we obtained the low-lying spectra of ^{130}Ba , whose M -scheme dimension is 2.2×10^{11} and is beyond the limitation of Lanczos method.

The structure of ^{134}Ba is quite interesting since it is located in between triaxially deformed isotope (^{132}Ba) and spherical nuclei ($^{136,138}\text{Ba}$). Figure 2 shows the energy spectra and $B(E2)$ transition probabilities obtained by the present shell model calculation, experiments, and the critical point symmetry E(5), respectively. The present result shows good agreement with the experimental values. The ^{134}Ba is considered to be a candidate of the microscopic

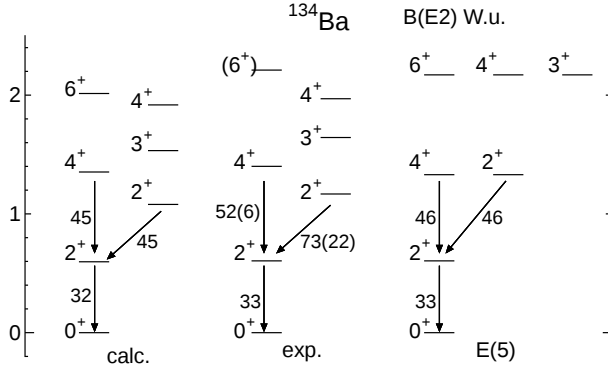


Figure 2: Energy spectra of ^{134}Ba . Left: the present SM calculation result. Center: experimental values [6]. Right: the values from the critical point symmetry E(5) [7] B(E2) values are also shown in Weisskopf unit.

realization of the E(5) symmetry by examining the level scheme and transition probabilities [7]. The present SM calculation shows consistent results with this prediction. Especially, the 2_2^+ excitation energy is rather low and the values of $B(E2; 4_1^+ \rightarrow 2_1^+)$ and $B(E2; 2_2^+ \rightarrow 2_1^+)$ are similar to each other. They indicate features of triaxial deformation.

This work has been supported by Grants-in-Aids (20740127, 25870168, 20244022, 20105003) from JSPS, MEXT, Japan. It has also been supported in part by HPCI Strategic Program (hp130024, hp140210) and the CNS-RIKEN joint project for large-scale nuclear structure calculations. A part of the numerical calculations was performed on the T2K Open Supercomputers at the University of Tokyo and University of Tsukuba.

References

- [1] N. Shimizu, T. Otsuka, T. Mizusaki, Y. Utsuno, M. Honma and Y. Tsunoda, submitted.
- [2] N. Shimizu, T. Otsuka, T. Mizusaki and M. Honma, Phys. Rev. Lett. **86**, 1171 (2001).
- [3] N. Shimizu, T. Abe, Y. Tsunoda, Y. Utsuno, T. Yoshida, T. Mizusaki, M. Honma, and T. Otsuka, Prog. Theor. Exp. Phys. **2012(1)**, 01A205 (2012).
- [4] N. Shimizu, Y. Utsuno, T. Mizusaki, T. Otsuka, T. Abe and M. Honma, Phys. Rev. C **82**, 061305(R) (2010).
- [5] N. Shimizu, Y. Utsuno, T. Mizusaki, M. Honma, Y. Tsunoda, and T. Otsuka, Phys. Rev. C **85**, 054301 (2012).
- [6] Nudat 2.5, <http://www.nndc.bnl.gov/nudat2/>
- [7] F. Iachello, Phys. Rev. Lett. **87**, 052502 (2001); R. F. Casten and N. V. Zamfir, Phys. Rev. Lett. **87**, 052503 (2001).

Shell-model calculation for first-forbidden beta decay in neutron-rich K isotopes

Y. Utsuno^{a,b}, N. Shimizu^b, T. Togashi^b, T. Otsuka^{c,b,d,e}, T. Suzuki^f, and M. Honma^g

^aAdvanced Science Research Center, Japan Atomic Energy Agency

^bCenter for Nuclear Study, Graduate School of Science, University of Tokyo

^cDepartment of Physics, University of Tokyo

^dDepartment of Physics and Astronomy and National Superconducting Cyclotron Laboratory, Michigan State University

^eKU Leuven, Instituut voor Kern-en Stralingsfysica

^fDepartment of Physics, College of Humanities and Sciences, Nihon University

^gCenter for Mathematical Sciences, University of Aizu

Shell evolution in neutron-rich Ca isotopes has attracted much attention since a new $N = 34$ magic number was predicted to occur at ^{54}Ca in 2001 [1]. After a number of experimental investigations of exotic nuclei around ^{54}Ca , the first excited level in ^{54}Ca has finally been measured in RIBF [2] to lie as high as 2.04 MeV, strongly supporting the theoretical prediction. The measured 2^+ energy level is well described not only with a shell-model calculation using an empirical interaction [2] but also with recent microscopic calculations [3,4]. Those calculations, however, predict different mass systematics beyond $N = 34$ [5]: the empirical and microscopic shell-model approaches [2, 4] predict the decrease of two-neutron separation energy at $N = 35$, which is a typical behavior across the magic numbers, whereas the coupled-cluster theory [3] predicts this value to increase. Further investigation of neutron-rich Ca isotopes is thus needed for deeper understanding of shell evolution in this region.

In this study, we calculate first-forbidden β -decay probabilities for the decays of neutron-rich K to Ca isotopes with the shell model. The β -decay probability is a quite useful tool for probing dominant configurations of nuclear states and hence shell structure. Since the natural-parity states of neutron-rich K and Ca isotopes for the same mass number have the opposite parity, most of the low-lying states in neutron-rich Ca isotopes are populated with the first-forbidden β decay. The first-forbidden β -decay probabilities are calculated following the formulation presented in Ref. [6]. In short, they are evaluated with phase-space integrals which involve six nuclear matrix elements (two for rank 0, three for rank 1, and one for rank 2) in a somewhat complicated way. We introduce effective operators by scaling the strengths of the transition operators. Although all the six transition operators should be properly scaled in principle, here we restrict ourselves only to two operators (one for rank 0 and one for rank 2) which are sensitive to the decay probabilities for using effective operators. These effective operators are determined to well reproduce the $\log ft$ values of the 0_1^+ state and the $2_{1,2,3}^+$ states in ^{50}Ca . The shell-model calculation is carried out in the $0\hbar\omega$ valence space with the SDPF-MU interaction [7]. The calculated energy levels in Ca isotopes are almost identical with those of the pf -shell calculation with the GXPF1B interaction [8] because the pf -shell interaction of SDPF-MU is based on GXPF1B. On the other hand, proton-neutron correlation is taken into account for the K levels.

The energy levels and their $\log ft$ values in $^{50-53}\text{Ca}$ are compared between experiment and theory in Figs. 1-4, respectively. The experimental $\log ft$ values are evaluated

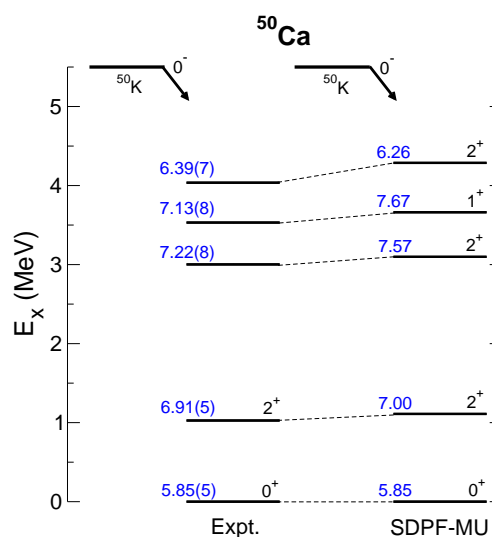


Figure 1: Energy levels in ^{50}Ca and their $\log ft$ values (on the left side of each level) for the first-forbidden β transition from ^{50}K compared between experiment (Expt.) and the present calculation (SDPF-MU).

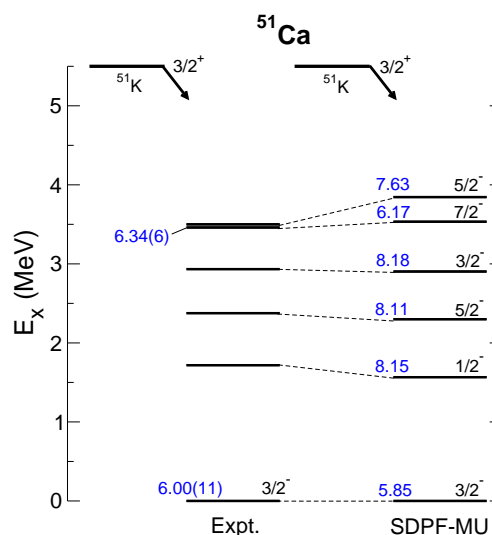


Figure 2: Same as Fig. 1 but for ^{51}Ca .

with the partial decay probabilities shown in [9, 10] and the atomic masses measured recently [5, 11]. The present calculation well reproduces the experimental $\log ft$ values especially for strongly populated states with $\log ft \lesssim 6$. This good agreement suggests that the present shell-model calcu-

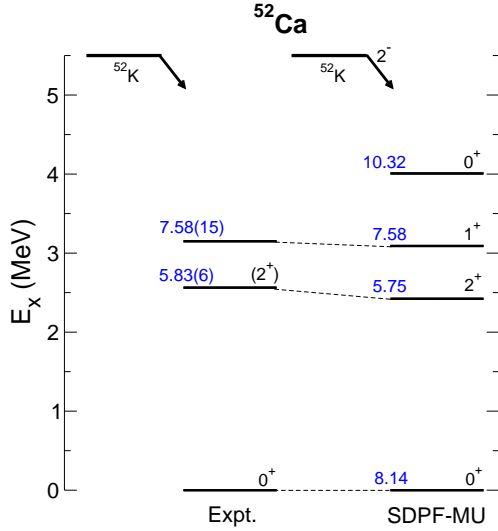


Figure 3: Same as Fig. 1 but for ^{52}Ca . The calculated $\log ft$ values are presented for the decay from the 2_1^- state in ^{52}K .

lation appropriately describes the structure of neutron-rich Ca isotopes which is strongly influenced by neutron shell structure.

We move on to each nucleus. For ^{50}Ca , the order of $\log ft$ among three 2^+ levels is correctly reproduced. This is nothing to do with the choice of the effective operator because the scaling of the rank 2 effective operator can only change the overall $\log ft$ values. From the analysis of the wave functions, the 2_3^+ , the one having the largest $[rY_1 \otimes \sigma]^{(2)}$ transition matrix element, is dominated by the $\nu(0f_{7/2})^{-1} \otimes \nu(1p_{3/2})^{-1}$ configuration on top of the ^{52}Ca core. For ^{51}Ca , only two levels are observed with direct β feeding. From the comparison between experiment and theory, the 3460 keV level with $\log ft = 6.34(6)$ must be the $7/2^-$ state dominated by the $\nu(0f_{7/2})^{-1}$ configuration on top of the ^{52}Ca core. The calculation shows that the $1/2_1^-$, $5/2_1^-$, $3/2_2^-$ and $5/2_2^-$ levels are very weakly populated, which is consistent with experiment. For the decay to ^{52}Ca , the spin-parity of the parent nucleus ^{52}K has not been known experimentally. The ground-state spin of ^{52}K should be either 0^- , 1^- or 2^- according to the possible coupling of the last proton ($0d_{3/2}$ or $1s_{1/2}$) and the last neutron ($1p_{1/2}$). The calculation can clearly exclude the possibilities of the 0^- or 1^- assignment on the basis of the comparison of the $\log ft$ values. The only possibility is the 2^- state, from which the $\log ft$ values are excellently reproduced. For ^{53}Ca , two low-lying excited levels are expected: the $5/2^-$ level dominated by the $\nu(0f_{5/2})^1$ configuration and the $3/2^-$ level dominated by the $\nu(1p_{1/2})^2 \otimes \nu(1p_{3/2})^{-1}$ configuration on top of the ^{52}Ca core. While two excited levels located at 1.753(15) MeV and 2.227(19) are observed from in-beam γ spectroscopy, only the latter level is observed from β decay. The present calculation shows that only the $3/2^-$ level is strongly populated with β decay. Thus, the 2.227(19) and 1.753(15) MeV levels are most likely the $3/2^-$ and $5/2^-$ levels, respectively. The position of the $5/2^-$ level is not correctly reproduced with the SDPF-MU (GXPF1B) interaction as shown in Fig. 4. This interaction also overestimates the 2_1^+ level in ^{54}Ca by 0.5 MeV. Very interestingly, those two discrepancies are simultaneously corrected by tuning the effective $N = 34$ shell gap

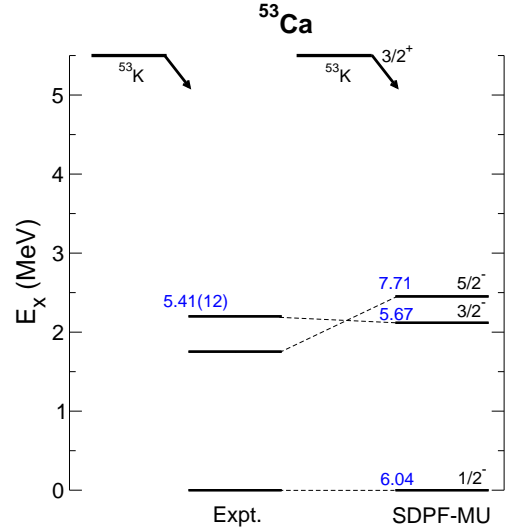


Figure 4: Same as Fig. 1 but for ^{53}Ca . The calculated $\log ft$ values are presented for the decay from the $3/2_1^+$ state in ^{53}K .

as indicated in Ref. [2]. From the analysis of the $5/2^-$ level in ^{53}Ca and the 2^+ level in ^{54}Ca , the $N = 34$ shell gap can be quantified to be ~ 2.5 MeV, which is comparable to the $N = 32$ shell gap for ^{52}Ca .

References

- [1] T. Otsuka *et al.*, Phys. Rev. Lett. **87** (2001) 082502.
- [2] D. Steppenbeck *et al.*, Nature **502** (2013) 207.
- [3] G. Hagen *et al.*, Phys. Rev. Lett. **109** (2012) 032502.
- [4] J. D. Holt *et al.*, J. Phys. G **39** (2012) 085111.
- [5] F. Wienholtz *et al.*, Nature **498** (2013) 346.
- [6] E. K. Warburton *et al.*, Ann. Phys. **187** (1988) 471.
- [7] Y. Utsuno *et al.*, Phys. Rev. C **86** (2012) 051301(R).
- [8] M. Honma *et al.*, RIKEN Accelerator Progress Report **41** (2008) 32.
- [9] P. Baumann *et al.*, Phys. Rev. C **58** (1998) 1970.
- [10] F. Perrot *et al.*, Phys. Rev. C **74** (2006) 014313.
- [11] M. Rosenbusch *et al.*, Phys. Rev. Lett. **114** (2015) 202501.

Fundamentals of matrix element for neutrinoless double beta decay

Y. Iwata^a, J. Menéndez^b, N. Shimizu^a, T. Otsuka^{a,b,c,d}, Y. Utsuno^e, M. Honma^f, T. Abe^b

^aCenter for Nuclear Study, The University of Tokyo

^bDepartment of Physics, The University of Tokyo

^cNational Superconducting Cyclotron Laboratory, Michigan State University

^dInstituut voor Kern- en Stralingsfysica, Katholieke Universiteit Leuven

^eAdvanced Science Research Center, Japan Atomic Energy Agency

^fCenter for Mathematical Sciences, University of Aizu

1. Introduction

In this review a theoretical work for the nuclear matrix element of neutrinoless double beta decay is presented. A description of how to obtain the nuclear matrix element for neutrinoless double beta decay is given.

The matrix element consists of three parts, depending on the spin structure of the operator: Gamow-Teller ($M_{GT}^{0\nu}$), Fermi ($M_F^{0\nu}$) and tensor ($M_T^{0\nu}$) parts.

$$M^{0\nu} = M_{GT}^{0\nu} - \frac{g_V^2}{g_A^2} M_F^{0\nu} + M_T^{0\nu}, \quad (1)$$

where g_V and g_A denote vector and axial coupling constants, respectively. The matrix element reads

$$M_\alpha^{0\nu} = \langle 0_f^+ | \hat{O}_\alpha^{0\nu} | 0_i^+ \rangle = \langle 0_f^+ | \tau_1^- \tau_2^- \hat{S}_\alpha \hat{H}_\alpha(r) | 0_i^+ \rangle, \quad (2)$$

where $\alpha = \text{GT, F, or T}$. The spin operators are

$$\hat{S}_{\text{GT}} = \sigma_1 \sigma_2, \quad \hat{S}_{\text{F}} = 1, \quad \hat{S}_{\text{T}} = 3(\sigma_1 \cdot r)(\sigma_2 \cdot r) - \sigma_1 \sigma_2,$$

where 0_i^+ and 0_f^+ denote initial and final states of the decay, respectively. The radial part of the operator comes from the so called neutrino potential $\hat{H}_\alpha(r)$, with r the relative distance between the decaying neutrons, and τ_i^- is the isospin-lowering operator transforming neutrons into protons.

2. Nuclear matrix element

The nuclear matrix element can be calculated from the wavefunctions of the initial and final nuclei (or the two-body transition density) and the antisymmetrized two-body matrix element of the operator (cf. Eq. (7)). Let the two-body matrix element be denoted by

$$\langle n'_1 l'_1 j'_1 t'_1, n'_2 l'_2 j'_2 t'_2; J | O_\alpha | n_1 l_1 j_1 t_1, n_2 l_2 j_2 t_2; J \rangle \quad (3)$$

where n, l, j , and t denote the principal, angular momentum, total angular momentum and isospin, respectively, j_1 and j_2 (or j'_1 and j'_2) are coupled to J , and similarly l_1 and l_2 (or l'_1 and l'_2) are coupled to λ (or λ'). Because neutrons decay into protons (Fig. 1), $t_1 = t_2 = 1/2$ (neutrons), and $t'_1 = t'_2 = -1/2$ (protons). Equation (3) can be written as (Ref. [1])

$$\text{Eq. (3)} = 2 \sum_{S, S', \lambda', \lambda} \sqrt{j'_1 j'_2 S' \lambda'} \sqrt{j_1 j_2 S \lambda} \langle l'_1 l'_2 \lambda' S'; J | S_\alpha | l_1 l_2 \lambda S; J \rangle \langle n'_1 l'_1, n'_2 l'_2 | H_\alpha(r) | n_1 l_1, n_2 l_2 \rangle$$

$$\left\{ \begin{array}{ccc} l'_1 & 1/2 & j'_1 \\ l'_2 & 1/2 & j'_2 \\ \lambda' & S' & J \end{array} \right\} \left\{ \begin{array}{ccc} l_1 & 1/2 & j_1 \\ l_2 & 1/2 & j_2 \\ \lambda & S & J \end{array} \right\},$$

where S and S' mean the two-body spins and $\{\cdot\}$ including nine numbers denotes the $9j$ -symbol [1]. In the following the calculation of each component of Eq. (3) is discussed step by step.

3. Two-body matrix element

3.1. Talmi-Moshinsky transformation

The Talmi-Moshinsky transformation [2] transforms from the single-particle harmonic oscillator basis to the center-of-mass / relative system, this is, from r_1 and r_2 (cf. $|n_1 l_1, n_2 l_2\rangle$) to $R = (r_1 + r_2)/\sqrt{2}$, and $\rho = (r_1 - r_2)/\sqrt{2}$ (cf. $|nl, NL\rangle$). Using the Talmi-Moshinsky transformation,

$$\begin{aligned} & \langle l'_1 l'_2 \lambda' S'; J | S_\alpha | l_1 l_2 \lambda S; J \rangle \langle n'_1 l'_1, n'_2 l'_2 | H_\alpha(r) | n_1 l_1, n_2 l_2 \rangle \\ &= \sum_{\text{mos1}} \langle nl, NL | n_1 l_1, n_2 l_2 \rangle_\lambda \langle n' l', N' L' | n'_1 l'_1, n'_2 l'_2 \rangle_{\lambda'} \\ & \langle l' l' \lambda' S'; J | S_\alpha | l l \lambda S; J \rangle \langle n' l' N' L' | H_\alpha(r) | n l N L \rangle \\ &= \sum_{\text{mos2}} \langle nl, NL | n_1 l_1, n_2 l_2 \rangle_\lambda \langle n' l', N' L' | n'_1 l'_1, n'_2 l'_2 \rangle_{\lambda'} \\ & \langle l' l \lambda' S'; J | S_\alpha | l l \lambda S; J \rangle \langle n' l' | H_\alpha(\sqrt{2}\rho) | n l \rangle, \end{aligned}$$

where “mos1” and “mos2” mean that the sum is taken over $(n, n', l, l', N, N', L, L')$ and (n, n', l, l', N, N') , respectively. $\langle N' L' | N L \rangle = \delta_{N, N'}$ due to the orthogonality of the Laguerre polynomials. Consequently the relative-motion is picked out, and the two-body matrix element is written in terms of the normalized relative coordinate ρ .

3.2. Spin-dependent part

As indicated in the previous discussion, the center-of-mass angular momentum L in the spin dependent part of the operator is conserved during the process. Here we calculate the spin part of the two-body matrix elements. The Fermi type is calculated as

$$\langle l' l \lambda' S'; J | S_{\text{F}} | l l \lambda S; J \rangle = \delta_{S, S'} \delta_{\lambda, \lambda'} \delta_{l, l'} \quad (4)$$

due to the orthogonality, where $\delta_{x,y}$ means the Kronecker delta. The Gamow-Teller type is calculated as

$$\begin{aligned} & \langle l' l \lambda' S'; J | S_{\text{GT}} | l l \lambda S; J \rangle \\ &= \langle S | \sigma_1 \sigma_2 | S \rangle \delta_{S, S'} \delta_{\lambda, \lambda'} \delta_{l, l'} \\ &= \{2S(S+1) - 3\} \delta_{S, S'} \delta_{\lambda, \lambda'} \delta_{l, l'}. \end{aligned} \quad (5)$$

Finally the Tensor type is calculated as

$$\begin{aligned} & \langle l' l \lambda' S'; J | S_{\text{T}} | l l \lambda S; J \rangle \\ &= \langle l' l \lambda' S'; J | \sqrt{24\pi} [Y^2(r) [\sigma_1 \sigma_2]^2]^0 | l l \lambda S; J \rangle \\ &= (-1)^{1+J+L} \sqrt{120 \lambda \lambda' l l'} \delta_{S, 1} \delta_{S', 1} \\ & \left\{ \begin{array}{ccc} J & 1 & \lambda' \\ 2 & \lambda & 1 \end{array} \right\} \left\{ \begin{array}{ccc} l' & \lambda' & L \\ \lambda & l & 2 \end{array} \right\} \left(\begin{array}{ccc} l' & 2 & l \\ 0 & 0 & 0 \end{array} \right) \end{aligned} \quad (6)$$

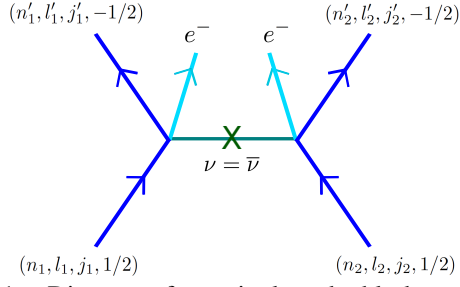


Figure 1: Diagram of neutrinoless double beta decay in which the neutrino and anti-neutrino (shown in green) are identical. The situation shown in Eq. (3) is explained by assuming a contact interaction. Nucleons are shown in dark-blue lines and electrons are shown in light-blue lines.

where $\{\cdot\}$ including six numbers denotes the $6j$ -symbol, (\cdot) including six numbers denotes the $3j$ -symbol, and $\langle l' || Y^2(r) || l \rangle = (-1)^l \sqrt{(5/4\pi)} \sqrt{l'l'}$ is used.

3.3. Neutrino potential part

The neutrino potential in general depends on the four quantum numbers n, n', l and l' , so that the representation for tensor part is represented by

$$\langle n'l' | H_T(\sqrt{2}\rho) | nl \rangle.$$

On the other hand, the representations for Fermi and Gamow-Teller parts become rather simple

$$\langle n'l | H_{F,GT}(\sqrt{2}\rho) | nl \rangle,$$

since $\delta_{l,l'}$ appears for Eqs. (4) and (5).

3.4. Antisymmetrization

Using Eq. (3), the antisymmetrized two body matrix element is represented by

$$\begin{aligned} & \langle n'_1 l'_1 j'_1 t'_1, n'_2 l'_2 j'_2 t'_2; J | O_\alpha | n_1 l_1 j_1 t_1, n_2 l_2 j_2 t_2; J \rangle_{AS} \\ &= \frac{1}{\sqrt{(1+\delta_{j_1, j_2})} \sqrt{(1+\delta_{j'_1, j'_2})}} \\ & [\langle n'_1 l'_1 j'_1 t'_1, n'_2 l'_2 j'_2 t'_2; J | O_\alpha | n_1 l_1 j_1 t_1, n_2 l_2 j_2 t_2; J \rangle \\ & - (-1)^{j_1 + j_2 + J} \\ & \langle n'_1 l'_1 j'_1 t'_1, n'_2 l'_2 j'_2 t'_2; J | O_\alpha | n_2 l_2 j_2 t_2, n_1 l_1 j_1 t_1; J \rangle]. \end{aligned} \quad (7)$$

The anti-symmetrization effect can be different depending on whether the channel holds an odd $j_1 + j_2 + J$ or not, $j_1 = j_2$ or not, and $j'_1 = j'_2$ or not.

4. Summary

As a result the obtained representation is summarized. Each term of the nuclear matrix element

$$M^{0v} = M_{GT}^{0v} - \frac{g_V^2}{g_A^2} M_F^{0v} + M_T^{0v},$$

is represented by the sum consisting of two-body transition density (TBSD) and antisymmetrized two-body matrix elements.

$$\begin{aligned} M_\alpha^{0v} &= \langle 0_f^+ | \hat{O}_\alpha^{0v} | 0_i^+ \rangle \\ &= \sum \text{TBSD}(n'_1 l'_1 j'_1 t'_1, n'_2 l'_2 j'_2 t'_2, n_1 l_1 j_1 t_1, n_2 l_2 j_2 t_2; J) \\ & \langle n'_1 l'_1 j'_1 t'_1, n'_2 l'_2 j'_2 t'_2; J | O_\alpha | n_1 l_1 j_1 t_1, n_2 l_2 j_2 t_2; J \rangle_{AS}, \end{aligned}$$

where the sum is taken over indices $(n_i, l_i, j_i, t_i, n'_j, l'_j, j'_j, t'_j)$ with $i, j = 1, 2$. The antisymmetrized two-body matrix element is

$$\begin{aligned} & \langle n'_1 l'_1 j'_1 t'_1, n'_2 l'_2 j'_2 t'_2; J | O_\alpha | n_1 l_1 j_1 t_1, n_2 l_2 j_2 t_2; J \rangle_{AS} \\ &= \frac{1}{\sqrt{(1+\delta_{j_1, j_2})} \sqrt{(1+\delta_{j'_1, j'_2})}} \\ & [\langle n'_1 l'_1 j'_1 t'_1, n'_2 l'_2 j'_2 t'_2; J | O_\alpha | n_1 l_1 j_1 t_1, n_2 l_2 j_2 t_2; J \rangle \\ & - (-1)^{j_1 + j_2 + J} \\ & \langle n'_1 l'_1 j'_1 t'_1, n'_2 l'_2 j'_2 t'_2; J | O_\alpha | n_2 l_2 j_2 t_2, n_1 l_1 j_1 t_1; J \rangle], \end{aligned}$$

where each two-body matrix element is given by

$$\begin{aligned} & \langle n'_1 l'_1 j'_1 t'_1, n'_2 l'_2 j'_2 t'_2; J | O_\alpha | n_1 l_1 j_1 t_1, n_2 l_2 j_2 t_2; J \rangle \\ &= 2 \sum_{s, s', \lambda', \lambda''} \sqrt{j'_1 j'_2 s' \lambda'} \sqrt{j_1 j_2 s \lambda} \\ & \left\{ \begin{matrix} l'_1 & 1/2 & j'_1 \\ l'_2 & 1/2 & j'_2 \\ \lambda' & s' & J \end{matrix} \right\} \left\{ \begin{matrix} l_1 & 1/2 & j_1 \\ l_2 & 1/2 & j_2 \\ \lambda & s & J \end{matrix} \right\} \\ & \langle l'_1 l'_2 \lambda' s'; J | S_\alpha | l_1 l_2 \lambda s; J \rangle \\ & \langle n'_1 l'_1, n'_2 l'_2 | H_\alpha(r) | n_1 l_1, n_2 l_2 \rangle, \end{aligned}$$

with the spin-dependent part

$$\begin{aligned} & \langle l' L \lambda' s'; J | S_F | l L \lambda s; J \rangle = \delta_{s, s'} \delta_{\lambda, \lambda'} \delta_{l, l'} \\ & \langle l' L \lambda' s'; J | S_{GT} | l L \lambda s; J \rangle \\ &= \{2S(S+1) - 3\} \delta_{s, s'} \delta_{\lambda, \lambda'} \delta_{l, l'} \\ & \langle l' L \lambda' s'; J | S_T | l L \lambda s; J \rangle \\ &= (-1)^{1+J+L} \sqrt{120 \lambda \lambda' l l'} \delta_{s, 1} \delta_{s', 1} \\ & \left\{ \begin{matrix} J & 1 & \lambda' \\ 2 & \lambda & 1 \end{matrix} \right\} \left\{ \begin{matrix} l' & \lambda' & L \\ \lambda & l & 2 \end{matrix} \right\} \begin{pmatrix} l' & 2 & l \\ 0 & 0 & 0 \end{pmatrix} \end{aligned}$$

and with the neutrino potential part

$$\begin{aligned} & \langle n'_1 l'_1, n'_2 l'_2 | H_{F,GT}(r) | n_1 l_1, n_2 l_2 \rangle = \langle n'l | H_{F,GT}(\sqrt{2}\rho) | nl \rangle, \\ & \langle n'_1 l'_1, n'_2 l'_2 | H_T(r) | n_1 l_1, n_2 l_2 \rangle = \langle n'l' | H_T(\sqrt{2}\rho) | nl \rangle. \end{aligned}$$

References

- [1] A. R. Edmonds, Angular momentum in quantum mechanics, Princeton University Press, 1996.
- [2] I. Talmi, Simple Models of Complex Nuclei, Harwood, 1993.

Microscopic description of shell model Hamiltonian and neutron-rich nuclei

N. Tsunoda, T. Otsuka^{a b}, N. Shimizu^a

Center for Nuclear Study, Graduate School of Science, University of Tokyo

^a*Department of Physics, University of Tokyo*

^b*National Superconducting Cyclotron Laboratory, Michigan State University*

One of the major goal of theoretical nuclear physics is understand nuclear structure based on basic nuclear force as a many body problem. Ab-initio method and developments of computational facilities made it possible to approach this goal, mainly for light mass nuclei. On the experimental side, the great progress and interest took place on radioactive beam, which can explore wide range of nuclear chart, including unstable nuclei. To investigate such a frontier, it is of great importance to construct our theory based only on fundamental components, in this case, nuclear force and many body theories. In this report, we discuss on the new many body theory based on nuclear force and its application to neutron-rich unstable nuclei.

Nuclear shell model is one of the most reliable theories to describe basic properties of the nuclei. Once we have a reliable effective interaction, we can calculate wavefunction of the many body states, by diagonalizing many body Hamiltonian. Our approach is to derive those Hamiltonian by many body perturbation theory [1]. The effective interaction is defined in a subspace P of whole Hilbert space $P + Q$, yielding the same physical quantities. The effective interaction is given by the following iterative formula,

$$V_{\text{eff}}^{(n)} = \hat{Q}(\epsilon_0) + \sum_{k=1}^{\infty} \frac{1}{k!} \frac{d^k \hat{Q}(\epsilon_0)}{d\epsilon^k} \{V_{\text{eff}}^{(n-1)}\}^k. \quad (1)$$

$$\hat{Q}(E) = PVP + PVQ \frac{1}{E - QHQ} QVP, \quad (2)$$

where ϵ_0 is the unperturbed energy of the original Hamiltonian. However, conventional many body theory has a strong limitation, that is, the model space has to be degenerate, because of i) the divergence of \hat{Q} -box, ii) the divergence of the iteration. To investigate neutron-rich nuclei, we have to deal with at least two-major shells. As we will show later, the physics on the island of inversion is one of the best example to see how important they are. Then, to deal with more general case, we proposed instead EKK method [2] as follows,

$$H_{\text{eff}}^{(n)} = H_{\text{BH}}(E) + \sum_{k=1}^{\infty} \frac{1}{k!} \frac{d^k \hat{Q}(E)}{dE^k} \{H_{\text{eff}}^{(n-1)} - E\}^k \quad (3)$$

$$H_{\text{BH}}(E) = PHP + PVQ \frac{1}{E - QHQ} QVP, \quad (4)$$

where the new parameter E is introduced, which can be chosen arbitrarily without changing the final results within the accuracy of the approximation.

We applied this new method to neutron-rich system. Here we will discuss on the physics of island of inversion and its neighbors, $10 < Z < 14$, $10 < N < 40$. The computational set up is as follows; we start from $V_{\text{low}k}$ iteration of $\chi\text{N}^3\text{LO}$ potential with cutoff $\Lambda = 2.0 \text{ fm}^{-1}$. The \hat{Q} -box in Eq. 3 is calculated perturbatively up to third order in $V_{\text{low}k}$ and the 17 major shells in harmonic oscillator basis are taken into account as the original Hilbert space. The effect of

three body force is also added as effective two body force, originated from Fujita-Miyazawa type three body force [3]. Effective interaction H_{eff} is defined in $sdpf$ -shell model space. Then, Lanczos diagonalization and Monte Carlo Shell Model calculation is performed with the Hamiltonian obtained with Eq. 3.

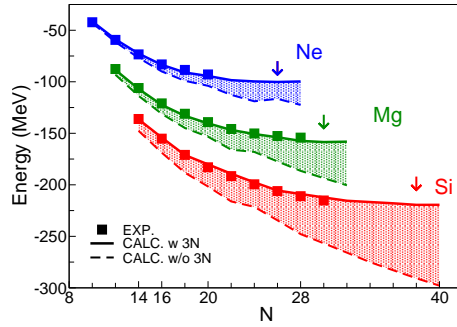


Figure 1: Ground state energies of Ne, Mg and Si isotope. Shadow shows the effect of three body force and the arrows indicate the driplines, respectively.

Figure. 1 shows the ground state energies of Ne, Mg and Si isotopes. The agreement of calculation and experiment is remarkable. One should also notice that the effect of three body force is significant as neutron number and proton number increases. This observation agrees with the previous findings shown in ref. [3], for example. With this large model space, we can predict the driplines as well, shown as arrows in Fig. 1, ^{36}Ne , ^{42}Mg and ^{52}Si , respectively.

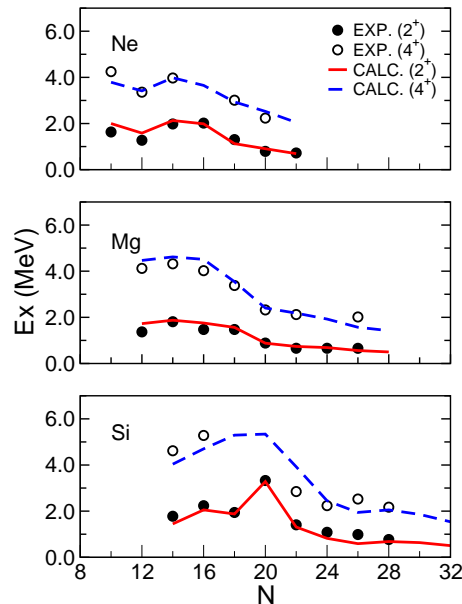


Figure 2: $E(2^+)$ and $E(4^+)$ of Ne, Mg and Si isotopes.

Next we present a brief view of the shell structure of those nuclei. Figure. 2 shows the $E^{(2+)}$ and $E^{(4+)}$ of the same nuclei. First of all, shell model calculation based on nuclear force agrees with experimental values remarkably well. By looking at excited states, we can discuss on the shell structure. It is clearly shown that the $N = 20$ major gap disappears in Ne and Mg case, which is the main feature of the island of inversion. On the other hand, ^{34}Si shows the magic structure. This is because neutron $N = 20$ gap grows as proton number increases from $Z = 10$ to $Z = 16$ by proton-neutron interaction. Although we do not show all the details of this work in this reports, we can analyzed this results more in detail, because we start from nuclear force and microscopic theories. A discussion derived from the analysis is the effect of the tensor force and three body force. We calculated the same quantities with switching off tensor force or three body force and showed that both tensor force and three body force plays a crucial role to reproduce this shell gap of ^{34}Si .

In conclusion, we proposed a powerful new method to derive the shell model Hamiltonian not only in one major shell but also in multi major shells. We applied this method to neutron-rich system, in this case, island of inversion physics. The reproduction of the experimental data is remarkable and with this prescription we can make a reliable prediction, as well as the microscopic analysis of the force, which derive the important physical consequences.

The content of this report will be submitted to peer-review article.

References

- [1] T. Kuo, E. Osnes, Lecture Notes in Physics, **364**, 1 170 (1990).
- [2] N. Tsunoda, K. Takayanagi, M. Hjorth-Jensen, T. Otsuka, Phys. Rev. C, **89**, 024313 (2014).
- [3] T. Otsuka, T. Suzuki, J. D. Holt, A. Schwenk, and Y. Akaishi, Phys. Rev. Lett. **105**, 032501 (2010).

Study of unnatural-parity states in neutron-rich Cr and Fe isotopes by large-scale shell-model calculations

T. Togashi^a, N. Shimizu^a, Y. Utsuno^{a,b}, T. Otsuka^{a,c}, and M. Honma^d

^aCenter for Nuclear Study, University of Tokyo

^bJapan Atomic Energy Agency

^cDepartment of Physics, University of Tokyo

^dUniversity of Aizu

The shell structure in neutron-rich nuclei is one of the main interests of modern nuclear physics. In the neutron-rich fp -shell region, new magic numbers have recently been established [1]. The appearance of the $N = 32$ and $N = 34$ subshell magic numbers is attributed to the tensor-force driven shell evolution [2]. For more neutron-rich nuclei near $N = 40$, the experimental development provides us a novel feature of nuclei. The abnormally small excitation energy of $9/2_1^+$ and large $B(E2, 0_1^+ \rightarrow 2_1^+)$ are reported for even-mass $^{60-64}\text{Cr}$ [3–6] and $^{66-68}\text{Fe}$ [3, 6, 7], which indicates the large collectivity. Theoretical calculations suggested the important role of $\nu 0g_{9/2}$ in the collectivity and demonstrated that the above abnormality cannot be reproduced without considerable neutron excitation across the $N = 40$ shell gap [8–10]. While the $N = 40$ magicity seems to be rather stable in Ni isotopes [11–13], the study of [14] suggested that the small observed $B(E2, 0_1^+ \rightarrow 2_1^+)$ value in ^{68}Ni is explained by a fragmentation of the $B(E2)$ strength. According to their study, this $B(E2)$ strength is mainly distributed in higher excited states due to neutron excitations to $0g_{9/2}$. The structure change from Ni to lower- Z isotopes in the neutron-rich $N \sim 40$ region is analogous to the “island of inversion” in the region around ^{32}Mg [15] where neutron excitation across the shell gap induces large deformation. The $N = 40$ shell gap is expected to be deeply involved with the formation of the island of inversion in neutron-rich Cr and Fe isotopes.

Practically, it is difficult and complicated to directly deduce the $N = 40$ shell gap of the nuclei in the island of inversion because low-lying states of those nuclei are dominated by multi-particle and multi-hole excitations. On the other hand, the states dominated by one-particle one-hole ($1p-1h$) excitation provide more direct information on the shell gap, when those levels are compared to the $0p-0h$ states. For Cr and Fe isotopes, low-lying unnatural-parity states with $N \leq 35$ are regarded as such $1p-1h$ states because low-lying natural-parity states in this region are excellently described within the fp -shell configurations. Recent experiments indicate a sharp drop of the $9/2_1^+$ levels in going from $N = 29$ to $N = 35$ observed in Cr and Fe isotopes [16–20]. If this change in energy level is an indication of a sharp evolution of the $0g_{9/2}$ orbit with an increasing neutron number as suggested in [8], the driving force of the evolution needs to be clarified. In this work, we focus on the unnatural positive-parity states in odd-mass Cr and Fe isotopes with $N \leq 35$ and examine the feasibility to systematically describe both the $0p-0h$ and $1p-1h$ states across the $N = 40$ shell gap by large-scale shell-model calculation.

In the present shell-model calculation, we adopt the model space composed of fp -shell ($0f_{7/2}$, $0f_{5/2}$, $1p_{3/2}$, $1p_{1/2}$) + $0g_{9/2}$ + $1d_{5/2}$ orbits to describe both the natural negative-parity and unnatural positive-parity state in odd-

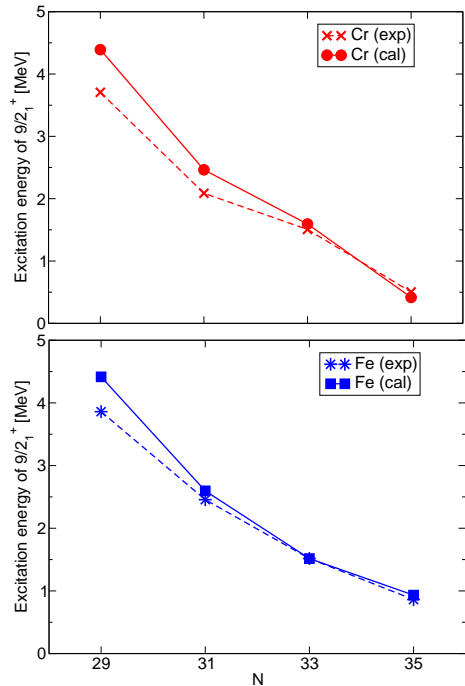


Figure 1: Excitation energy of $9/2_1^+$. Experimental data labeled “exp” are taken from [22].

mass Cr and Fe nuclei with $N \leq 35$. To focus on the states dominated by $1p-1h$ excitation across the $N = 40$ shell gap for the unnatural positive-parity states, the truncation is introduced that one neutron is allowed to occupy the $0g_{9/2}$ or $1d_{5/2}$ orbit, which means that the $1\hbar\omega$ excitation of a neutron occurs in only unnatural-parity states. As the effective Hamiltonian, we apply GXPF1Br [1] for fp -shell orbits. For the neutron $1\hbar\omega$ excitation to a $0g_{9/2}$ or $1d_{5/2}$ orbit, we create the cross-shell two-body interaction between fp -shell and gds -shell orbits from V_{MU} [21] with the modification to improve the energy intervals of positive-parity states.

We examine what causes the sharp drop in the $9/2_1^+$ level with increasing neutron number observed in Cr and Fe isotopes. A particular attention is paid to the relation to the evolution of the $\nu 0g_{9/2}$ orbit. Figure 1 shows the results of the excitation energy of $9/2_1^+$ from $N = 29$ to $N = 35$. The sharp drop in $9/2_1^+$ is reproduced quite well in the present calculations. This shows wide applicability of the present Hamiltonian in this mass region. The neutron single-particle properties of these odd-mass nuclei are probed from the spectroscopic factors for neutron transfer reactions. The present calculation well reproduces their systematic behavior of the measured spectroscopic factors: ~ 0.5 for $9/2_1^+$ states. This indicates that these $9/2_1^+$ states are single-particle-like states and that the excitation energy

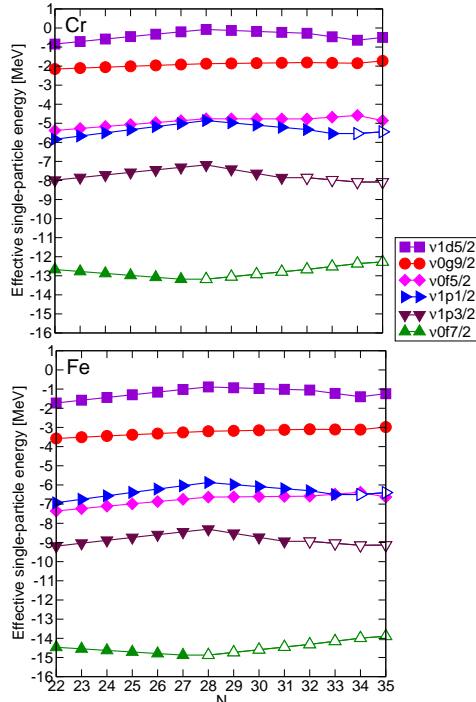


Figure 2: Effective single-particle energies of a neutron. Open symbols represent ESPEs calculated as the hole states to specify the occupied states.

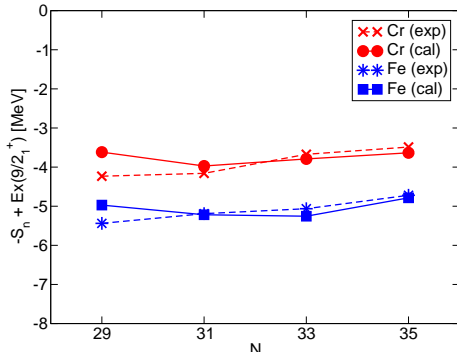


Figure 3: Plots of $-S_n + E_x(9/2_1^+)$. Experimental values labeled “exp” are taken from [22].

of $9/2_1^+$ in these nuclei is influenced directly by the location of the $v0g_{9/2}$ orbit.

Neutron effective single-particle energies in Cr and Fe isotopes are shown in Fig. 2 using the present Hamiltonian. The ESPEs of $v0g_{9/2}$ are rather constant with increasing neutron number, and so are the shell gaps between the fp shell and $v0g_{9/2}$. This indicates that the evolution of the $9/2_1^+$ level is explained by the Fermi surface approaching the $v0g_{9/2}$ orbit with increasing neutron number.

This evolution of the $v0g_{9/2}$ orbit can be probed through experimental energies. Namely, in the independent-particle limit, the $v0g_{9/2}$ single-particle energy is identical to the energy of the $9/2_1^+$ state measured from the adjacent even-even core nucleus, $-S_n + E_x(9/2_1^+)$, where S_n is one-neutron separation energy. In Fig. 3, the $-S_n + E_x(9/2_1^+)$ values are compared between the experimental data and the present calculation. The observed stabilities in $-S_n + E_x(9/2_1^+)$ along the Cr and Fe isotopic chains suggest that the $v0g_{9/2}$ single-particle energies are kept nearly constant as shown in Fig. 2.

The other unnatural positive-parity states described as $1p-1h$ states in odd-mass Cr and Fe nuclei with $N \leq 35$ are discussed in detail in [23]. This work was supported in part by MEXT SPIRE Field 5 “The origin of matter and the universe” and the RIKEN-CNS joint research project on large-scale nuclear-structure calculations.

References

- [1] D. Steppenbeck *et al.*, Nature **502** (2013) 207.
- [2] T. Otsuka *et al.*, Phys. Rev. Lett. **95** (2005) 232502.
- [3] B. Pritychenko *et al.*, At. Data Nucl. Data Tables **98** (2012) 798.
- [4] N. Aoi *et al.*, Phys. Rev. Lett. **102** (2009) 012502.
- [5] T. Baugher *et al.*, Phys. Rev. C **86** (2012) 011305(R).
- [6] H. L. Crawford *et al.*, Phys. Rev. Lett. **110** (2013) 242701.
- [7] W. Rother *et al.*, Phys. Rev. Lett. **106** (2011) 022502.
- [8] K. Kaneko *et al.*, Phys. Rev. C **78** (2008) 064312.
- [9] H. Oba and M. Matsuo, Prog. Theor. Phys. **120** (2008) 143.
- [10] S. M. Lenzi *et al.*, Phys. Rev. C **82** (2010) 054301.
- [11] R. Broda *et al.*, Phys. Rev. Lett. **74** (1995) 868.
- [12] T. Ishii *et al.*, Phys. Rev. Lett. **84** (2000) 39.
- [13] O. Sorlin *et al.*, Phys. Rev. Lett. **88** (2002) 092501.
- [14] K. Langanke *et al.*, Phys. Rev. C **67** (2003) 044314.
- [15] E. K. Warburton *et al.*, Phys. Rev. C **41** (1990) 1147.
- [16] D. E. Appelbe *et al.*, Phys. Rev. C **67** (2003) 034309.
- [17] A. N. Deacon *et al.*, Phys. Lett. B **622** (2005) 151.
- [18] S. J. Freeman *et al.*, Phys. Rev. C **69** (2004) 064301.
- [19] A. N. Deacon *et al.*, Phys. Rev. C **76** (2007) 054303.
- [20] N. Hoteling *et al.*, Phys. Rev. C **77** (2008) 044314.
- [21] Y. Utsuno *et al.*, Phys. Rev. C **86** (2012) 051301(R).
- [22] National Nuclear Data Center (NNDC), information extracted from the NuDat2 database, <http://www.nndc.bnl.gov/nudat2/>.
- [23] T. Togashi *et al.*, Phys. Rev. C **91** (2015) 024320.

Structure of Be isotopes based on Monte Carlo shell model with $N_{\text{shell}} > 4$ model space

T. Yoshida^a, N. Shimizu^a, T. Abe^b and T. Otsuka^{a, b, c, d}

^a Center for Nuclear Study, Graduate School of Science, University of Tokyo

^b Department of Physics, University of Tokyo

^c National Superconducting Cyclotron Laboratory, Michigan State University
, East Lansing, Michigan, USA

^d Instituut voor Kern- en Stralingsfysica, Katholieke Universiteit Leuven

In Be isotopes, $B(E2)$ s and energies for the 2_1^+ states have been studied [1–4]. Be isotopes have already been studied by using Monte Carlo shell model (MCSM). The model space has been truncated with $N_{\text{shell}} = 4$ by using unitary correlation operator method (UCOM) and the energies and $B(E2)$ s have been discussed [5]. In our previous study, we have adapted the JISP16 interaction with $N_{\text{shell}} = 4$ [6–8]. The JISP16 NN interaction reproduces NN scattering data and properties of deuteron and other light nuclei [9]. The physical observables of Be isotopes have been discussed in association with the properties of α cluster structure and orbits of valence neutrons [11]. We have confirmed that the cluster like configuration can be taken into account within the model space of shell model for $N_{\text{shell}} = 4$ by using the intrinsic densities. In the present study, we see the energies of 2_1^+ states and the development of cluster configuration for larger model space than before. We use the MCSM with model space for $N_{\text{shell}} = 6$. This truncation means that the all orbits up to sdg shells are taken into account. The formulation for MCSM wave function shown below is the same as before. The basis state of the MCSM wave function is described by a Slater determinant, $|\phi_n\rangle$, which is given as

$$|\phi_n(D)\rangle = \prod_{\alpha=1}^{N_p} a_{\alpha}^{\dagger} |-\rangle, \quad (1)$$

where $|-\rangle$ shows a vacuum state and a_{α}^{\dagger} shows the canonical basis of the Hartree-Fock theory: $a_{\alpha}^{\dagger} = \sum_{i=1}^{N_{sp}} c_i^{\dagger} D_{i\alpha}^{(n)}$. Here, single-particle orbit, i , is specified by t_z, n, l, j (denoting quanta for the isospin, radial node, orbital angular momentum and total angular momentum, respectively). N_p and N_{sp} denote the numbers of nucleons and single-particle orbits, respectively. The resultant wave function is given by a superposition of N_b Slater determinants as follows,

$$|\Psi(J^{\pi})\rangle = \sum_{K=-J}^J P_{MK}^{J^{\pi}} |\Phi_K\rangle, \quad |\Phi_K\rangle = \sum_{n=1}^{N_b} f_K^n |\phi_n\rangle. \quad (2)$$

Here, $P_{MK}^{J^{\pi}}$ is the parity and angular-momentum projection operator. In the present work, the Coulomb interaction is neglected for simplicity. The center of mass motion is treated by the Lawson's procedure [10]. The numerical calculation was performed on the K computer (RIKEN AICS) and FX10 (the University of Tokyo). For the harmonic oscillator width parameter, $\hbar\omega$, (which appears in $|\phi_n\rangle$) we use $\hbar\omega = 20$ MeV, simply because it is closer to the optimized value with respect to the energy. In Fig. 1, 2_1^+ energies for Be isotopes are shown. In the red empty diamond symbols, the results for N_b around 100 are shown. Although the calculation cost for such N_b value is large, the model space is not sufficient to obtain the converged value. To obtain the

true eigen energy, the extrapolation method of the energy by using the energy variance is adapted [6,12,13]. Here, results for the MCSM, No-Core Full Configuration (NCFC) [14], Green's function Monte Carlo (GFMC) [18] and experiments are shown for comparison. We notice that the JISP16 with the Coulomb force is adopted for the NCFC and the Argonne v_{18} two-nucleon and Illinois7 three-nucleon potentials are adopted for the GFMC. A good agreement between the two for $^{8,10}\text{Be}$ (red triangle) are found compared with the other results. For ^{12}Be , there are still uncertainties in the extrapolation due to the limitation of the present model space. The main reason is considered to be the limitation of the number of the basis states.

Although there are uncertainties with respect to the N_b value, we check the value of $B(E2; 2_1^+ \rightarrow 0_1^+)$ to discuss the correspondence between the distribution of the valence neutrons and the $B(E2)$ value. The values for $A = 8, 10$, and 12 are around $12, 5$, and $2 \text{ e}^2\text{fm}^4$, respectively. The A dependence observed by the experiment is not reproduced in the present results. The value for $A = 12$ are much smaller than the experiment values, $6\text{-}10 \text{ e}^2\text{fm}^4$. The value for $A = 8$ and 10 are also smaller than GFMC and experimental results, respectively. As discussed in Ref [15], the mixing of p and sd orbits for the two valence neutrons are important for the large $B(E2)$ for $A=12$. This could be seen by the occupation number of the four valence neutrons. To discuss the valence neutron occupation numbers, we neglect the α cluster contribution in the occupation number by subtracting the proton occupation number from the total occupation number for each orbit. The p and sd orbit for the valence neutrons occupy about 85 and 15% for the 0_1^+ state. On the other hand, the percentages are about 70 and 30% for the 0_2^+ state. As a result of the change of the mixing ratio, we find the larger $B(E2)$ value, $B(E2; 2_1^+ \rightarrow 0_2^+) \sim 5 \text{ e}^2\text{fm}^4$ than for the 0_1^+ state.

We discuss the development of the cluster structure for the intrinsic density. As we already discussed for the intrinsic wave function [6], the intrinsic wave function is defined by the wave function before the J^{π} projection. To use the aligned basis state, we rotate each Slater determinant by diagonalizing the quadrupole moment. The superposition of these are used as the intrinsic state. To focus on the relative two α distance, angular momentum projection with respect to the z -axis have been taken into account when we see the intrinsic wave function. In Fig. 2, the relative α - α distance (S) of the intrinsic state of Be isotopes are shown. The length S is defined by the distance of the two local maximum peaks of the intrinsic density. We can see that for $N_{\text{shell}} = 4$, S decreases with respect to the mass number. For $N_{\text{shell}} = 6$, S increases for $A=8, 12$ compared with $N_{\text{shell}}=4$ results. The shrunk S value in $A=10$ is en-

hanced. This is well explained by the effect of the glue-like role of π orbit which has been discussed by using cluster model [11, 19, 20].

In summary, we perform MCSM calculation with JISP16 interaction. Observable such as 2_1^+ energy and $B(E2)$ are investigated. We find that the extrapolation is essential to obtain the 2_1^+ energies. The energy convergence for the ^{12}Be need further study by increasing the model space. Appearance of α cluster in the intrinsic state has been discussed. Results are compared with AMD and cluster model. For ^{12}Be , the mixing of sd orbit for the ground state seems to be not sufficiently large to cause the developed α - α distance and observed large $B(E2)$. One possible reason is that the choice of the $\hbar\omega$ parameter. The value $N_{shell} = 6$ might not be large enough for the present choice of $\hbar\omega$. In the future study, we need to see the different choice of $\hbar\omega$ such as an empirical one and investigate the N_{shell} dependence for the better description of the model space. This work has

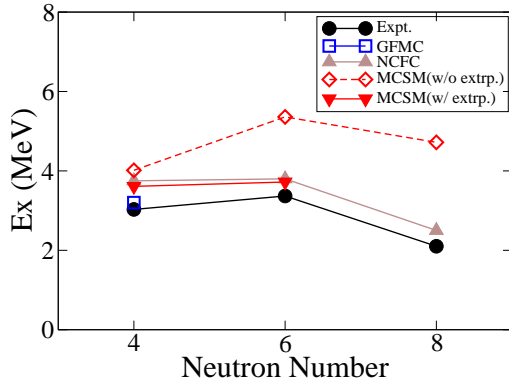


Figure 1: The 2_1^+ energies are shown for each isotope are shown. The results both before and after the extrapolations are shown with red dots. The values are compared with other method, such as GFMC (blue open squares), NCFC(brown triangles), and the experiments (black filled circles).

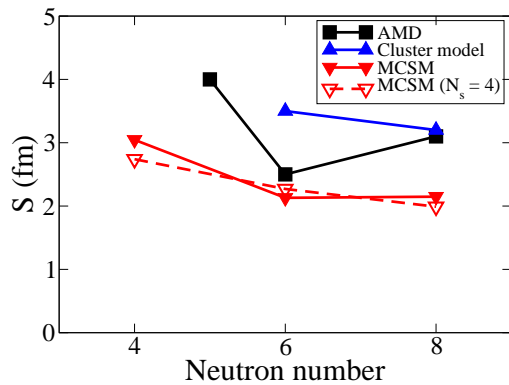


Figure 2: The distance between the centers of two α clusters are shown. The vertical axis (S) shows the relative distance between the two α clusters of the intrinsic density for each nucleus. The results for AMD [16, 17] and Cluster model [19, 20] are also shown.

been supported by the SPIRE Field 5 from MEXT, and the CNS-RIKEN joint project for large-scale nuclear structure calculations.

References

- [1] S. Shimoura, et al. *Phys. Lett. B* **654** 87 (2007).
- [2] N. Imai, et al. *Phys. Lett. B* **673** 179 (2009).
- [3] F. Barker, *J. Phys. G* **2** L45 (1976).
- [4] S. Shimoura, et al. *Phys. Lett. B* **560** 31 (2003).
- [5] L. Liu, T. Otsuka, N. Shimizu, Y. Utsuno, and R. Roth *Phys. Rev. C* **86**, 014302 (2012).
- [6] N. Shimizu, T. Abe, Y. Tsunoda, Y. Utsuno, T. Yoshida, T. Mizusaki, M. Honma and T. Otsuka, *Prog. Theor. Exp. Phys.* **2012**, 01A205 (2012).
- [7] T. Yoshida, N. Shimizu, T. Abe, and T. Otsuka, *Few-Body Systems* **54**, Nos. 7-10, 1465 (2013).
- [8] T. Yoshida, N. Shimizu, T. Abe and T. Otsuka, *JPS Conf. Proc.* **6**, 030028 (2015).
- [9] A.M. Shirokov, J.P. Vary, A.I. Mazur, S.A. Zaytsev, and T.A. Weber, *Phys. Lett. B* **621**, 96 (2005).
- [10] D. Gloeckner and R. Lawson, *Phys. Lett. B* **53**, 313 (1974).
- [11] N. Itagaki and S. Okabe, *Phys. Rev. C* **61**, 044306 (2000).
- [12] T. Mizusaki and M. Imada, *Phys. Rev. C* **65**, 064319 (2002).
- [13] N. Shimizu, Y. Utsuno, T. Mizusaki, T. Otsuka, T. Abe, and M. Honma, *Phys. Rev. C* **82**, 061305(R) (2010).
- [14] P. Maris, J.P. Vary, A.M. Shirokov, *Phys. Rev. C* **79**, 014308 (2009); P. Maris, A.M. Shirokov, and J.P. Vary, *ibid.*, **81**, 021301(R) (2010).
- [15] A. Navin, et al., *Phys. Rev. Lett.* **85**, 266 (2000).
- [16] Y. Kanada-En'yo and H. Horiuchi, *Prog. Theor. Phys. Suppl.* **142**, 205 (2001).
- [17] Y. Kanada-En'yo and H. Horiuchi, *Phys. Rev. C* **68**, 014319 (2003).
- [18] R. B. Wiringa, S. C. Pieper, J. Carlson and V. R. Pandharipande, *Phys. Rev. C* **62**, 014001 (2000).
- [19] M. Ito, N. Itagaki, H. Sakurai and K. Ikeda, *Phys. Rev. Lett.* **100**, 182502 (2008).
- [20] M. Ito and K. Ikeda, *Rep. Prog. Phys.* **77**, 096301 (2014).

Other Activities

Laboratory Exercise for Undergraduate Students

S. Ota, M. Niikura^a, S. Koyama^a, Y. Kiyokawa, K. Yako, H. Sakurai^{a,b} and S. Shimoura

Center for Nuclear Study, Graduate School of Science, University of Tokyo

^a*Department of Physics, University of Tokyo*

^b*RIKEN Nishina Center*

Nuclear scattering experiments were performed as a laboratory exercise for undergraduate students of the University of Tokyo. This program was aiming at providing undergraduate students with an opportunity to learn how to study subatomic physics by using an ion beam from an accelerator. In 2014, 32 students attended this program.

The four beam times were scheduled in the second semester for third-year students, and 8 students participated in each beam time. The experiments were performed at the RIBF using a 26-MeV alpha beam accelerated by the AVF cyclotron. The alpha beam extracted from the AVF cyclotron was transported to the E7B beam line in the E7 experimental hall. The scattering chamber has two separate target ports which enable us to perform two independent experiments without opening the chamber during the beam time. In each beam time, the students were divided into two groups and took one of the following two subjects:

1. Measurement of elastic scattering of incident alpha particle with ^{197}Au , to learn how to determine nuclear size.
2. Measurement of gamma rays emitted from the cascade decay of highly excited ^{154}Gd and ^{184}Os , to learn the nuclear deformation.

Before the experiment, the students took a course on the basic handling of the semiconductor detectors and electronic circuits at the Hongo campus, and attended a radiation safety lecture at RIKEN. They also joined a tour to the RI beam factory at RIKEN.

In the $\alpha+^{197}\text{Au}$ measurement, α particles scattered with the Au target with a thickness of 1 μm were detected using a silicon PIN-diode located 15-cm away from the target. A collimator with a diameter of 6 mm was attached on the silicon detector. The energy spectrum of the scattered α particles was recorded by a multi-channel analyzer (MCA) system. The beam was stopped by a Faraday cup located downstream of the scattering chamber. The cross section for the alpha elastic scattering was measured in the angular range of $\theta_{\text{lab}} = 20 - 150^\circ$.

The measured cross section was compared with the calculated cross section of the Rutherford scattering. The cross section was also analyzed by the potential model calculation, and the radius of the ^{197}Au nucleus was discussed. Some students obtained the radius of ~ 10 fm by using a classical model where the trajectory of the α particle in the nuclear potential is obtained using the Runge-Kutta method. Others tried to understand the scattering process by calculating the angular distribution using the distorted wave Born approximation method with a Coulomb wave function and a realistic nuclear potential.

In the measurement of gamma rays, excited states in ^{154}Gd and ^{184}Os nuclei were populated by the $^{152}\text{Sm}(\alpha,2n)$ and $^{182}\text{W}(\alpha,2n)$ reactions, respectively. The gamma rays emitted from the cascade decay of the rotational bands were

measured by a high-purity germanium detector located 30-cm away from the target. The energy of the gamma ray were recorded by the MCA system. The gain and the efficiency of the detector system had been calibrated using standard gamma-ray sources of ^{22}Na , ^{60}Co , ^{133}Ba , and ^{137}Cs . The gamma rays from the 10^+ and 8^+ states in ^{154}Gd and ^{184}Os , respectively, were successfully identified. Based on the energies of the gamma rays, the moment of inertia and the deformation parameters of the excited states were discussed by using a classical rigid rotor model and a irrotational fluid model. The students found that the reality lies between the two extreme models. The initial population among the levels in the rotational band was also discussed by taking the effect of the internal conversion into account.

It was the first time for most of the students to use large experimental equipments. They learned basic things about the experimental nuclear physics and how to extract physics from the data. We believe this program was very impressive for the students. The authors would like to thank Dr. Y. Uwamino, the CNS accelerator group, and the RIBF cyclotron crew for their helpful effort in the present program.

The 13th CNS International Summer School (CNSSS14)

S. Michimasa^a, Y. Iwata^a, S. Ota^a, T. Gunji^a, S. Shimoura^a, T. Otsuka^{a,b}, H. Sakai^c,
H. Hamagaki^a, T. Nakatsukasa^d, H. Sakurai^{b,c}, N. Shimizu^a, T. Uesaka^b, Y. Utsuno^{a,e},
H. Utsunomiya^{a,f}, K. Yako^a, and N. Imai^a

^aCenter for Nuclear Study, Graduate School of Science, University of Tokyo

^bDepartment of Physics, Graduate School of Science, University of Tokyo

^cRIKEN Nishina Center

^dDepartment of Physics, University of Tsukuba

^eJapan Atomic Energy Agency (JAEA)

^fDepartment of Physics, Konan University

The 13th CNS International Summer School (CNSSS14) was organized jointly by the Center for Nuclear Study (CNS), the University of Tokyo in the period of August 21–27, 2014. The summer school was held at the Nishina hall in the Wako campus of RIKEN.

This summer school was the thirteenth one in the series which aimed at providing graduate students and post docs with basic knowledge and perspectives of nuclear physics. It consisted of lectures by leading scientists in the fields of both experimental and theoretical nuclear physics. Each lecture started with an introductory talk from the fundamental point of view and ended with up-to-date topics in the relevant field.

The list of lecturers and the title of lectures are shown below.

David Brink (Oxford University, UK),

“Discovering nuclear physics”

Nigel Orr (University of Caen, France),

“Direct Reaction Studies of Light Neutron-Rich Nuclei”

Thomas Papenbrock (University of Tennessee, USA),

“Effective theories, nuclear interactions, and calculations of atomic nuclei”

Hiroaki Utsunomiya (Konan University and CNS, Japan),

“Toward New Era of Photonuclear Reaction”

Kyoichiro Ozawa (KEK, Japan),

“Hadron physics experiments at J-PARC”

Kiyoshi Kato (Hokkaido University, Japan),

“Many-Body Resonances of Nuclear Systems and Unstable Nuclei”

Shigehiro Nagataki (RIKEN, Japan),

“Supernovae and Nucleosynthesis”

Masaki Sasano (RIKEN Nishina Center, Japan),

“How can we see nuclear spin isospin symmetry?”

This year, 8 lecturers and 91 participants attended from fourteen countries. Three lecturers and twenty participants were from foreign institutes. Attendances communicated with each other in the free discussion time between the lectures and in the welcome and farewell parties in a relaxed atmosphere.

The Student and Post Doc sessions were also held in the school. Twenty-two talks and seventeen posters were presented by graduate students and post docs.

All the information concerning the summer school is open for access at the following URL:

<http://www.cns.s.u-tokyo.ac.jp/summerschool/cnss14>

This summer school was supported in part by the International Exchange Program of the Graduate School of Science, the University of Tokyo. The financial support from the program was indispensable to successfully organize this summer school. The organizers deeply appreciate various accommodations provided by RIKEN Nishina center for the school. They are also grateful to administration staffs of the CNS and the Graduate School of Science for their helpful supports. They thank graduate students and postdocs in the CNS for their dedicated efforts. Finally, the organizers acknowledge all the lecturers and participants for their contributions to this summer school.

Appendices

**Symposium, Workshop, Seminar, PAC and
External Review**

CNS Reports

Publication List

Talks and Presentations

Personnel

Symposium, Workshop, Seminar, Colloquium, and PAC

A. Symposium and Workshop

1. Advances in Radioactive Isotope Science (Jointly organized by the RIKEN Nishina Center and the CNS):
<https://ribf.riken.jp/ARIS2014/index.html>,
June 1-6, 2014, Hongo, The University of Tokyo
2. The first Sicily-East Asia Workshop for Low-energy Nuclear Physics:
<https://agenda.infn.it/conferenceDisplay.py?confId=8300>,
July 28-31, 2014, Sicily, Italy
3. Progress in nuclear shell-model calculations in CNS-RIKEN collaboration:
<http://indico.cns.s.u-tokyo.ac.jp/conferenceDisplay.py?confId=180>,
Nov. 26-28, 2014, Saitama, RIKEN
4. 第一回放射線によるイメージングの展望:
<http://indico.cns.s.u-tokyo.ac.jp/conferenceDisplay.py?confId=195>,
Nov. 29, 2014, Hongo, The University of Tokyo
5. 第二回放射線によるイメージングの展望:
<http://indico.cns.s.u-tokyo.ac.jp/conferenceDisplay.py?confId=204>,
Jan. 24, 2015, Hongo, The University of Tokyo

B. CNS Seminar

1. Dr. Javier Menendez (Department of Physics, The University of Tokyo): "From nuclear structure to neutrinos and dark matter", Dec. 16, 2014, Hongo, The University of Tokyo
2. Dr. Kathrin Wimmer (Department of Physics, UT / CNS): "In-beam gamma-ray spectroscopy with GREY at the NSCL", Dec. 1, 2014, Hongo, The University of Tokyo
3. Prof. Tetsuya Sakurai (Department of Computer Science, University of Tsukuba): "A Scalable Parallel Eigensolver for Large-scale Simulations on Petascale Computing Environment", Jan. 19, 2015, Hongo, The University of Tokyo

C. Program Advisory Committee for Nuclear-Physics Experiments at RI Beam Factory

1. The 14th NP-PAC meeting
Date: June 27-28, 2014
Place: RIBF Conference Hall on the 2nd floor of the RIBF Building
2. The 15th NP-PAC meeting
Date: December 12-13, 2014, 2013
Place: RIBF Conference Hall on the 2nd floor of the RIBF Building

CNS Reports

#93 “CNS Annual Report 2013”

Edited by S. Ota, T. Gunji, and Y. Kushi March, 2015

Publication List

A. Original Papers

1. N. Matsuda, S. Mikami, S. Shimoura, J. Takahashi, M. Nakano, K. Shimada, K. Uno, S. Hagiwara, K. Saito: “Depth profiles of radioactive cesium in soil using a scraper plate over a wide area surrounding the Fukushima Dai-ichi Nuclear Power Plant, Japan” *J. Environ. Radioact.* **139** 427–434 (2015)
2. K. Saito, I. Tanihata, M. Fujiwara, T. Saito, S. Shimoura, T. Otsuka, Y. Onda, M. Hoshi, Y. Ikeuchi, F. Takahashi, N. Kinouchi, J. Saegusa, A. Seki, H. Takemiya, T. Shibata: “Detailed deposition density maps constructed by large-scale soil sampling for gamma-ray emitting radioactive nuclides from the Fukushima Dai-ichi Nuclear Power Plant accident”, *J. Environ. Radioact.* **139**, 308–319 (2015)
3. H. Baba, T. Ichihara, T. Ohnishi, S. Takeuchi, K. Yoshida, Y. Watanabe, S. Ota, S. Shimoura, K. Yoshinaga: “Time-stamping system for nuclear physics experiments at RIKEN RIBF”, *Nucl. Instr. Meth. A* **777**, 75–79 (2015)
4. K. Tshoo, Y. Satou, C.A. Bertulani, H. Bhang, S. Choi, T. Nakamura, Y. Kondo, S. Deguchi, Y. Kawada, Y. Nakayama, K.N. Tanaka, N. Tanaka, Y. Togano, N. Kobayashi, N. Aoi, M. Ishihara, T. Motobayashi, H. Otsu, H. Sakurai, S. Takeuchi, K. Yoneda, F. Delaunay, J. Gibelin, F.M. Marques, N.A. Orr, T. Honda, T. Kobayashi, T. Sumikama, Y. Miyashita, K. Yoshinaga, M. Matsushita, S. Shimoura, D. Sohler, J.W. Hwang, T. Zheng, Z.H. Li, Z.X. Cao: “Neutron occupancy of the $0d_{5/2}$ orbital and the $N = 16$ shell closure in ^{24}O ”, *Phys. Lett. B* **739**, 19–22 (2014)
5. H. Muto, Y. Ohshiro, S. Yamaka, S. Watanabe, M. Oyaizu, H. Yamaguchi, K. Kobayashi, Y. Kotaka, M. Nishimura, S. Kubono, M. Kase, T. Hattori, S. Shimoura: “Note: ^6Li III light intensity observation for $^6\text{Li}^{3+}$ ion beam operation at Hyper-Electron Cyclotron Resonance ion source”, *Rev. Sci. Instrum* **85**, 126107 (2014)
6. H.L. Crawford, P. Fallon, A.O. Macchiavelli, R.M. Clark, B.A. Brown, J.A. Tostevin, D. Bazin, N. Aoi, P. Doornenbal, M. Matsushita, H. Scheit, D. Steppenbeck, S. Takeuchi, H. Baba, C.M. Campbell, M. Cromaz, E. Ideguchi, N. Kobayashi, Y. Kondo, G. Lee, I.Y. Lee, J. Lee, K. Li, S. Michimasa, T. Motobayashi, T. Nakamura, S. Ota, S. Paschalis, M. Petri, T. Sako, H. Sakurai, S. Shimoura, M. Takechi, Y. Togano, H. Wang, K. Yoneda: “Shell and shape evolution at $N=28$: The 40Mg ground state”, *Phys. Rev. C* **89**, 41303 (2014)
7. Z. Patel, P.-A. Söderström, Zs. Podolyák, P.H. Regan, P.M. Walker, H. Watanabe, E. Ideguchi, G.S. Simpson, H.L. Liu, S. Nishimura, Q. Wu, F.R. Xu, F. Browne, P. Doornenbal, G. Lorusso, S. Rice, L. Sinclair, T. Sumikama, J. Wu, Z.Y. Xu, N. Aoi, H. Baba, F.L. Bello Garrote, G. Benzoni, R. Daido, Y. Fang, N. Fukuda, G. Gey, S. Go, A. Gottardo, N. Inabe, T. Isobe, D. Kameda, K. Kobayashi, M. Kobayashi, T. Komatsubara, I. Kojouharov, T. Kubo, N. Kurz, I. Kuti, Z. Li, M. Matsushita, S. Michimasa, C.-B. Moon, H. Nishibata, I. Nishizuka, A. Odahara, E. ahin, H. Sakurai, H. Schaffner, H. Suzuki, H. Takeda, M. Tanaka, J. Taprogge, Zs. Vajta, A. Yagi, and R. Yokoyama: “Isomer Decay Spectroscopy of ^{164}Sm and ^{166}Gd : Midshell Collectivity Around $N = 100$ ”, *Phys. Rev.Lett.* **113** 262502 (2014)
8. S. Michimasa, Y. Yanagisawa, K. Inafuku, N. Aoi, Z. Elekes, Zs. Fülöp, Y. Ichikawa, N. Iwasa, K. Kurita, M. Kurokawa, T. Machida, T. Motobayashi, T. Nakamura, T. Nakabayashi, M. Notani, H.J. Ong, T. Onishi, H. Otsu, H. Sakurai, M. Shinohara, T. Sumikama, S. Takeuchi, K. Tanaka, Y. Togano, K. Yamada, M. Yamaguchi, and K. Yoneda: “Quadrupole collectivity in island-of-inversion nuclei $^{28,30}\text{Ne}$ and $^{34,36}\text{Mg}$ ”, *Phys. Rev. C* **89**, 054307 (2014)
9. P. Doornenbal, H. Scheit, S. Takeuchi, Y. Utsuno, N. Aoi, K. Li, M. Matsushita, D. Steppenbeck, H. Wang, H. Baba, E. Ideguchi, N. Kobayashi, Y. Kondo, J. Lee, S. Michimasa, T. Motobayashi, T. Otsuka, H. Sakurai, M. Takechi, Y. Togano and K. Yoneda: “Rotational level structure of sodium isotopes inside the “island of inversion”, *Prog. Theor. Exp. Phys.* **2014**, 053D01 (2014)
10. N. Kobayashi, T. Nakamura, Y. Kondo, J. A. Tostevin, Y. Utsuno, N. Aoi, H. Baba, R. Barthelemy, M. A. Famiano, N. Fukuda, N. Inabe, M. Ishihara, R. Kanungo, S. Kim, T. Kubo, G. S. Lee, H. S. Lee, M. Matsushita, T. Motobayashi, T. Ohnishi, N. A. Orr, H. Otsu, T. Otsuka, T. Sako, H. Sakurai, Y. Satou, T. Sumikama, H. Takeda, S. Takeuchi, R. Tanaka, Y. Togano, K. Yoneda: “Observation of a p-Wave One-Neutron Halo Configuration in ^{37}Mg ”, *Phys. Rev.Lett.* **112** 242501 (2014)
11. B. B. Abelev *et al.* [ALICE Collaboration]: “ $K^*(892)^0$ and $\phi(1020)$ production in Pb-Pb collisions at $\sqrt{s_{NN}}=2.76$ TeV”, *Phys. Rev. C* **91**, no. 2, 024609 (2015)
12. B. B. Abelev *et al.* [ALICE Collaboration]: “Freeze-out radii extracted from three-pion cumulants in pp, pPb and PbPb collisions at the LHC”, *Phys. Lett. B* **739**, 139 (2014)

13. A. Adare *et al.* [PHENIX Collaboration]: “Measurement of $\Upsilon(1S + 2S + 3S)$ production in $p + p$ and Au+Au collisions at $\sqrt{s_{NN}} = 200$ GeV”, Phys. Rev. C **91**, no. 2, 024913 (2015)
14. B. B. Abelev *et al.* [ALICE Collaboration]: “Measurement of visible cross sections in proton-lead collisions at $\sqrt{s_{NN}} = 5.02$ TeV in van der Meer scans with the ALICE detector”, JINST **9**, no. 11, P11003 (2014)
15. B. B. Abelev *et al.* [ALICE Collaboration]: “Azimuthal anisotropy of D meson production in Pb-Pb collisions at $\sqrt{s_{NN}} = 2.76$ TeV”, Phys. Rev. C **90**, no. 3, 034904 (2014)
16. B. B. Abelev *et al.* [ALICE Collaboration]: “Transverse momentum dependence of inclusive primary charged-particle production in p-Pb collisions at $\sqrt{s_{NN}} = 5.02$ TeV”, Eur. Phys. J. C **74**, no. 9, 3054 (2014)
17. B. B. Abelev *et al.* [ALICE Collaboration]: “Measurement of prompt D-meson production in $p - Pb$ collisions at $\sqrt{s_{NN}} = 5.02$ TeV”, Phys. Rev. Lett. **113**, no. 23, 232301 (2014)
18. A. Adare *et al.* [PHENIX Collaboration]: “Measurement of K_S^0 and K^{*0} in $p + p$, $d + Au$, and $Cu + Cu$ collisions at $\sqrt{s_{NN}} = 200$ GeV”, Phys. Rev. C **90**, no. 5, 054905 (2014)
19. B. B. Abelev *et al.* [ALICE Collaboration]: “Neutral pion production at midrapidity in pp and Pb-Pb collisions at $\sqrt{s_{NN}} = 2.76$ TeV”, Eur. Phys. J. C **74**, no. 10, 3108 (2014)
20. B. B. Abelev *et al.* [ALICE Collaboration]: “Suppression of $\psi(2S)$ production in p-Pb collisions at $\sqrt{s_{NN}} = 5.02$ TeV”, JHEP **1412**, 073 (2014)
21. A. Adare *et al.* [PHENIX Collaboration]: “Low-mass vector-meson production at forward rapidity in $p+p$ collisions at $\sqrt{s} = 200$ GeV”, Phys. Rev. D **90**, no. 5, 052002 (2014)
22. A. Adare *et al.* [PHENIX Collaboration]: “Cross section for $b\bar{b}$ production via dielectrons in d+Au collisions at $\sqrt{s_{NN}} = 200$ GeV”, Phys. Rev. C **91**, no. 1, 014907 (2015)
23. B. B. Abelev *et al.* [ALICE Collaboration]: “Measurement of electrons from semileptonic heavy-flavor hadron decays in pp collisions at $\sqrt{s} = 2.76$ TeV”, Phys. Rev. D **91**, no. 1, 012001 (2015)
24. B. B. Abelev *et al.* [ALICE Collaboration]: “Beauty production in pp collisions at $\sqrt{s} = 2.76$ TeV measured via semi-electronic decays”, Phys. Lett. B **738**, 97 (2014)
25. B. B. Abelev *et al.* [ALICE Collaboration]: “Suppression of $\Upsilon(1S)$ at forward rapidity in Pb-Pb collisions at $\sqrt{s_{NN}} = 2.76$ TeV”, Phys. Lett. B **738**, 361 (2014)
26. B. B. Abelev *et al.* [ALICE Collaboration]: “Multiparticle azimuthal correlations in p -Pb and Pb-Pb collisions at the CERN Large Hadron Collider”, Phys. Rev. C **90**, no. 5, 054901 (2014)
27. B. B. Abelev *et al.* [ALICE Collaboration]: “Production of $\Sigma(1385)^\pm$ and $\Xi(1530)^0$ in proton-proton collisions at $\sqrt{s} = 7$ TeV”, Eur. Phys. J. C **75**, no. 1, 1 (2015)
28. A. Adare *et al.* [PHENIX Collaboration]: “Cross section and transverse single-spin asymmetry of η mesons in $p^\uparrow + p$ collisions at $\sqrt{s} = 200$ GeV at forward rapidity”, Phys. Rev. D **90**, no. 7, 072008 (2014)
29. B. B. Abelev *et al.* [ALICE Collaboration]: “Multiplicity dependence of jet-like two-particle correlations in p-Pb collisions at $\sqrt{s_{NN}} = 5.02$ TeV”, Phys. Lett. B **741**, 38 (2015)
30. B. B. Abelev *et al.* [ALICE Collaboration]: “Exclusive J/ψ photoproduction off protons in ultra-peripheral p-Pb collisions at $\sqrt{s_{NN}} = 5.02$ TeV”, Phys. Rev. Lett. **113**, no. 23, 232504 (2014)
31. B. Abelev *et al.* [ALICE Collaboration]: “Upgrade of the ALICE Experiment: Letter Of Intent”, J. Phys. G **41**, 087001 (2014)
32. B. Abelev *et al.* [ALICE Collaboration]: “Technical Design Report for the Upgrade of the ALICE Inner Tracking System”, J. Phys. G **41**, 087002 (2014)
33. B. B. Abelev *et al.* [ALICE Collaboration]: “Event-by-event mean p_T fluctuations in pp and Pb-Pb collisions at the LHC”, Eur. Phys. J. C **74**, no. 10, 3077 (2014)
34. A. Adare *et al.* [PHENIX Collaboration]: “Search for dark photons from neutral meson decays in $p + p$ and $d + Au$ collisions at $\sqrt{s_{NN}} = 200$ GeV”, Phys. Rev. C **91**, no. 3, 031901 (2015)
35. A. Adare *et al.* [PHENIX Collaboration]: “Charged-pion cross sections and double-helicity asymmetries in polarized p+p collisions at $\sqrt{s}=200$ GeV”, Phys. Rev. D **91**, no. 3, 032001 (2015)

36. B. B. Abelev *et al.* [ALICE Collaboration]: “Production of inclusive $\Upsilon(1S)$ and $\Upsilon(2S)$ in p-Pb collisions at $\sqrt{s_{NN}} = 5.02$ TeV”, *Phys. Lett. B* **740**, 105 (2015)
37. B. Abelev *et al.* [ALICE Collaboration]: “Inclusive photon production at forward rapidities in proton-proton collisions at $\sqrt{s} = 0.9, 2.76$ and 7 TeV”, *Eur. Phys. J. C* **75**, no. 4, 146 (2015)
38. J. Adam *et al.* [ALICE Collaboration]: “Two-pion femtoscopy in p-Pb collisions at $\sqrt{s_{NN}} = 5.02$ TeV”, *Phys. Rev. C* **91**, 034906 (2015)
39. P. Doornenbal, S. Takeuchi, N. Aoi, M. Matsushita, A. Obertelli, D. Steppenbeck, H. Wang, L. Audirac, H. Baba, P. Bednarczyk, S. Boissinot, M. Ciemala, A. Corsi, T. Furumoto, T. Isobe, A. Jungclaus, V. Lapoux, J. Lee, K. Matsui, T. Motobayashi, D. Nishimura, S. Ota, E.C. Pollacco, H. Sakurai, C. Santamaria, Y. Shiga, D. Sohler, R. Taniuchi: “Intermediate-energy Coulomb excitation of Sn-104: Moderate E2 strength decrease approaching Sn-100”, *Phys. Rev. C* **90**, 061302 (2014)
40. J. Hu, J. J. He, A. Parikh, S. W. Xu, H. Yamaguchi, D. Kahl, P. Ma, J. Su, H. W. Wang, T. Nakao, Y. Wakabayashi, T. Teranishi, K. I. Hahn, J. Y. Moon, H. S. Jung, T. Hashimoto, A. A. Chen, D. Irvine, C. S. Lee, and S. Kubono” “Examination of the role of the $14O(\alpha, p)17F$ reaction rate in type-I x-ray bursts”, *Phys. Rev. C* **90**, 025803 (2014)
41. E. Mcneice, K. Setoodehnia, B. Singh, Y. Abe, D. Binh, A. Chen, J. Chen, S. Cherubini, S. Fukuoka, T. Hashimoto, T. Hayakawa, Y. Ishibashi, Y. Ito, D. Kahl, T. Komatsubara, S. Kubono, T. Moriguchi, D. Nagae, R. Nishikiori, T. Niwa, A. Ozawa, T. Shizuma, H. Suzuki, H. Yamaguchi, and T. Yuasa: “In-beam γ -ray spectroscopy of ^{30}P via the $^{28}Si(3He, p\gamma)^{30}P$ reaction”, *Nuclear Data Sheets* **120**, 88–90 (2014)
42. N. Imai, M. Mukai, J. Cederkäll, H. Aghai, P. Golubev, H. T. Johansson, D. Kahl, J. Kurcewics, T. Teranishi, and Y. X. Watanabe: “Isobaric analog resonances of ^{31}Mg and the border of the island of inversion”, *Phys. Rev. C* **90**, 011302 (2014)
43. T. Komatsubara, S. Kubono, T. Hayakawa, T. Shizuma, A. Ozawa, Y. Ito, Y. Ishibashi, T. Moriguchi, H. Yamaguchi, D. Kahl, S. Hayakawa, Dam Nguyen Binh, A. A. Chen, J. Chen, K. Setoodehnia and T. Kajino: “Excited states above the proton threshold in ^{26}Si ”, *Eur. Phys. J. A* **50**, 136 (2014)
44. C. Spitaleri, L. Lamia, S. M. R. Puglia, S. Romano, M. La Cognata, V. Crucilla, R. G. Pizzone, G. G. Rapisarda, M. L. Sergi, M. G. Del Santo, N. Carlin, M. G. Munhoz, F. A. Souza, A. Szanto de Toledo, A. Tumino, B. Irgaziev, A. Mukhamedzhanov, G. Tabacaru, V. Burjan, V. Kroha, Z. Hons, J. Mrazek, S.-H. Zhou, C. Li, Q. Wen, Y. Wakabayashi, H. Yamaguchi, E. Somorjai: “Measurement of the 10 keV resonance in the $^{10}B(p, \alpha_0)^7Be$ reaction via the trojan horse method”, *Phys. Rev. C* **90**, 035801 (2014)
45. H. S. Jung, C. S. Lee, Y. K. Kwon, J. Y. Moon, J. H. Lee, C. C. Yun, M. J. Kim, T. Hashimoto, H. Yamaguchi, D. Kahl, S. Kubono, Y. Wakabayashi, Y. Togano, S. Choi, Y. H. Kim, Y. K. Kim, J. S. Park, E. J. Kim, C.-B. Moon, T. Teranishi, N. Iwasa, T. Yamada, S. Kato, S. Cherubini, S. Hayakawa, G. G. Rapisarda: “Elastic scattering of $^{25}Al+p$ to explore the resonance structure in ^{26}Si ”, *Phys. Rev. C* **90** 035805 (2014)
46. H. Muto, Y. Ohshiro, S. Yamaka, S. Watanabe, M. Oyaizu, H. Yamaguchi, K. Kobayashi, Y. Kotaka, M. Nishimura, S. Kubono, M. Kase, T. Hattori, and S. Shimoura: “ 6Li III light intensity observation for $^6Li^{3+}$ ion beam operation at Hyper-Electron Cyclotron Resonance ion source”, *Review of Scientific Instruments* **85**, 126107 (2014)
47. C. Yuan, C. Qi, F. Xu, T. Suzuki, and T. Otsuka: “Mirror energy difference and the structure of loosely bound proton-rich nuclei”, *Phys. Rev. C* **89**, 044327 (2014).
48. K. Saito, I. Tanihata, M. Fujiwara, *et al.* : “Detailed deposition density maps constructed by large-scale soil sampling for gamma-ray emitting radioactive nuclides from the Fukushima Dai-ichi Nuclear Power Plant accident”, *J. Environ. Radioact.* **139**, 308 (2015).
49. H. Watanabe, G. Lorusso, S. Nishimura, T. Otsuka, K. Ogawa, Z.Y. Xu, T. Sumikama, P. A. Soderstrom, P. Doornenbal, Z. Li, F. Browne, G. Gey, H.S. Jung, J. Taprogge, Zs. Vajta, J. Wu, A. Yagi, H. Baba, G. Benzoni, K.Y. Chae, F.C.L. Crespi, N. Fukuda, R. Gernhauser, N. Inabe, T. Isobe, A. Jungclaus, D. Kameda, G.D. Kim, Y.K. Kim, I. Kojouharov, F.G. Kondev, T. Kubo, N. Kurz, Y.K. Kwon, G.J. Lane, C.B. Moon, A. Montaner-Piza, K. Moschner, F. Naqvi, M. Niikura, H. Nishibata, D. Nishimura, A. Odahara, R. Orlandi, Z. Patel, Zs. Podolyak, H. Sakurai, H. Schaffner, G.S. Simpson, K. Steiger, H. Suzuki, H. Takeda, A. Wendt, and K. Yoshinaga: “Monopole-Driven Shell Evolution below the Doubly Magic Nucleus Sn 132 Explored with the Long-Lived Isomer in Pd 126”. *Physical review letters*, **113** (4), 042502.
50. Y. Utsuno, N. Shimizu, T. Otsuka, T. Yoshida, Y. Tsunoda: “Nature of Isomerism in Exotic Sulfur Isotopes”, *Phys. Rev. Lett.* **114**, 032501 (2015).

51. P. Doornenbal, H. Scheit, S. Takeuchi, Y. Utsuno, N. Aoi, K. Li, M. Matsushita, D. Steppenbeck, H. Wang, H. Baba, E. Ideguchi, N. Kobayashi, Y. Kondo, J. Lee, S. Michimasa, T. Motobayashi, T. Otsuka, H. Sakurai, M. Takechi, Y. Togano, and K. Yoneda: “Rotational level structure of sodium isotopes inside the ”island of inversion”, *Prog. Theor. Exp. Phys.* **2014**, 053D01 (2014).
52. N. Kobayashi, T. Nakamura, Y. Kondo, J.A. Tostevin, Y. Utsuno, N. Aoi, H. Baba, R. Barthelemy, M.A. Famiano, N. Fukuda, N. Inabe, M. Ishihara, R. Kanungo, S. Kim, T. Kubo, G.S. Lee, H. S. Lee, M. Matsushita, T. Motobayashi, T. Ohnishi, N. A. Orr, H. Otsu, T. Otsuka, T. Sako, H. Sakurai, Y. Satou, T. Sumikama, H. Takeda, S. Takeuchi, R. Tanaka, Y. Togano, and K. Yoneda: “Observation of a p-Wave One-Neutron Halo Configuration in ^{37}Mg ”, *Phys. Rev. Lett.* **112**, 242501 (2014).
53. T. Nakamura, N. Kobayashi, Y. Kondo, Y. Satou, J.A. Tostevin, Y. Utsuno, N. Aoi, H. Baba, N. Fukuda, J. Gibelin, N. Inabe, M. Ishihara, D. Kameda, T. Kubo, T. Motobayashi, T. Ohnishi, N.A. Orr, H. Otsu, T. Otsuka, H. Sakurai, T. Sumikama, H. Takeda, E. Takeshita, M. Takechi, S. Takeuchi, Y. Togano, and K. Yoneda: “Deformation-Driven p-Wave Halos at the Drip Line: ^{31}Ne ”, *Phys. Rev. Lett.* **112**, 142501 (2014).
54. A. Sanetullaev, M.B. Tsang, W.G. Lynch, D. Lee Jenny, D. Bazin, K.P. Chan, D. Coupland, V. Henzl, D. Henzlova, M. Kilburn, A.M. Rogers, Z.Y. Sun, M. Youngs, R.J. Charity, L.G. Sobotka, M. Famiano, S. Hudan, D. Shapira, W.A. Peters, C. Barbieri, M. Hjorth-Jensen, M. Horoi, T. Otsuka, T. Suzuki, Y. Utsuno: “Neutron spectroscopic factors of ^{55}Ni hole-states from image transfer reactions”, *Phys. Lett. B* **736**, 137 (2014).
55. T. Togashi, N. Shimizu, Y. Utsuno, T. Otsuka, and M. Honma: “Large-scale shell-model calculations for unnatural-parity high-spin states in neutron-rich Cr and Fe isotopes”, *Phys. Rev. C* **91**, 024320 (2015).
56. F. Flavigny, D. Pauwels, D. Radulov, I.J. Darby, H. De Witte, J. Diriken, D.V. Fedorov, V.N. Fedosseev, L.M. Fraile, M. Huyse, V.S. Ivanov, U. Koster, B.A. Marsh, T. Otsuka, L. Popescu, R. Raabe, M.D. Seliverstov, N. Shimizu, A.M. Sjodin, Y. Tsunoda, P. Van den Bergh, P. Van Duppen, J. Van de Walle, M. Venhart, W.B. Walters, and K. Wimmer: “Characterization of the low-lying 0^+ and 2^+ states in ^{68}Ni via decay of the low-spin ^{68}Co isomer”, *Phys. Rev. C* **91**, 034310 (2015).
57. Y. Iwata: “Energy-dependent existence of soliton in the synthesis of chemical elements”, *Mod. Phys. Lett. A* **30**, 155008 (2015).

B. Proceedings

1. N. N. Ajitanand *et al.* [PHENIX Collaboration]: “Comparison of the space-time extent of the emission source in $d+\text{Au}$ and $\text{Au}+\text{Au}$ collisions at $\sqrt{s_{NN}} = 200$ GeV”, *Nucl. Phys. A* **931**, 1082 (2014)
2. M. Ball *et al.* [ALICE TPC Collaboration]: “Ion backflow studies for the ALICE TPC upgrade with GEMs”, *JINST* **9**, C04025 (2014)
3. T. Gunji [ALICE Collaboration]: “Future Upgrade and Physics Perspectives of the ALICE TPC”, *Nucl. Phys. A* **931**, 1152 (2014)
4. H. Sako, T. Chujo, T. Gunji, H. Harada, K. Imai, M. Kaneta, M. Kinsho and Y. Liu *et al.*: “Towards the heavy-ion program at J-PARC”, *Nucl. Phys. A* **931**, 1158 (2014)
5. Y. Maeda, T. Saito, H. Miyasako, T. Uesaka, S. Ota, S. Kawase, T. Kikuchi, H. Tokieda, T. Kawabata, K. Yako, T. Wakasa, S. Sakaguchi, R. Chen, H. Sakaguchi, T. Shima, T. Suzuki, A. Tamii: “Measurement of the H-2(p,n) Breakup Reaction at 170 MeV and the Three-Nucleon Force Effects”, *Few-Body Systems*, **55**, 729-732 (2014)
6. D. Kahl, T. Hashimoto, N. N. Duy, S. Kubono, H. Yamaguchi, D. N. Binh, A. A. Chen, S. Cherubini, S. Hayakawa, J. J. He, H. Ishiyama, N. Iwasa, L. H. Khiem, Y. K. Kwon, S. Michimasa, T. Nakao, S. Ota, T. Teranishi, H. Tokieda, Y. Wakabayashi, T. Yamada, L. Y. Zhang: “Active target studies of the αp -process at CRIB”, *AIP Conference Proceedings* **1594**, 163–170 (2014)
7. J. J. He, J. Hu, L. Y. Zhang, S. W. Xu, A. Parikh, H. Yamaguchi, D. Kahl, P. Ma, S. Z. Chen, J. Su, Y. Wakabayashi, Y. Togano, S. Hayakawa, H. W. Wang, W. D. Tian, R. F. Chen, B. Guo, T. Nakao, T. Teranishi, J. Y. Moon, H. S. Jung, T. Hashimoto, A. A. Chen, D. Irvine, K. I. Hahn, N. Iwasa, T. Yamada, T. Komatsubara, C. S. Lee, S. Kubono: “Astrophysics studies relevant to stellar X-ray bursts”, *AIP Conference Proceedings* **1594**, 176–183 (2014)
8. S. Cherubini, M. Gulino, C. Spitaleri, M. La Cognata, L. Lamia, S. Puglia, G. Rapisarda, S. Romano, S. Kubono, H. Yamaguchi, D. Binh, S. Hayakawa, Y. Kurihara, Y. Wakabayashi, S. Bishop, A. Coc, N. De Séréville, F. Hammache: “First results of trojan horse method using radioactive ion beams: $^{18}\text{F}(p,\alpha)$ at astrophysical energies”, *AIP Conference Proceedings* **1594**, 184–189 (2014)

9. H. Yamaguchi, D. Kahl, T. Nakao, Y. Wakabayashi, S. Kubano, T. Hashimoto, S. Hayakawa, T. Kawabata, N. Iwasa, T. Teranishi, Y. K. Kwon, D. N. Binh, L. H. Khiem, N. G. Duy: “Alpha resonant scattering for astrophysical reaction studies”, AIP Conference Proceedings **1594**, 220–225 (2014)
10. H. Yamaguchi, D. Kahl, T. Nakao, Y. Wakabayashi, T. Hashimoto, S. Hayakawa, T. Kawabata, T. Teranishi, Y.K. Kwon, D.N. Binh, L.H. Khiem, N.N. Duy, S. Kubono, T. Suhara, Y. Kanada-En’yo, J.Y. Moon, A. Kim, N. Iwasa, P.S. Lee, K.Y. Chae, S.M. Cha, M.S. Gwak, D.H. Kim and E. Milman: “Nuclear clusters studied with alpha resonant scatterings using RI beams at CRIB”, Journal of Physics: Conference Series **569**, 012019 (2014)
11. Pilsoo Lee, Chun Sik Lee, Jun Young Moon, Kyung Yuk Chae, Soo Mi Cha, Hidetoshi Yamaguchi, Taro Nakao, David M. Kahl, Shigeru Kubono, Silvio Cherubini, Seiya Hayakawa, and Cosimo Signorini: “Development and performance test of the analysis software for the CRIB active target”, Journal of the Korean Physical Society **66**, 459–464 (2015).
12. T. Otsuka: “Perspectives of Physics of Exotic Nuclei Beyond the Shell Evolution”, Exotic Nuclei (IASEN-2013)-Proceedings of the First International African Symposium on Exotic Nuclei. Edited by PENIONZHKEVICH YURI ERASTOVICH ET AL. Published by World Scientific Publishing Co. Pte. Ltd., 2015. pp. 399-407. Vol. **1**. 2015
13. T. Suzuki, T. Otsuka, M. Honma, and N. Tsunoda: “Shell-model study of spin modes in nuclei and nuclear forces”, Journal of Physics: Conference Series (Vol. **580**, No. 1, pp. 12032-12037). (2015, February).
14. N. Shimizu, T. Abe, M. Honma, T. Otsuka, Y. Tsunoda, Y. Utsuno, and T. Yoshida: “Frontier of nuclear shell-model calculations and high performance computing”, accepted, JPS conference proceedings, ARIS2014
15. Y. Utsuno, T. Otsuka, Y. Tsunoda, N. Shimizu, M. Honma, T. Togashi, and T. Mizusaki: “Recent Advances in Shell Evolution with Shell-Model calculations”, arXiv:1409.4506[nucl-th], accepted, JPS conference proceedings, ARIS2014
16. T. Togashi, N. Shimizu, Y. Utsuno, T. Abe, and T. Otsuka: “GPGPU Application to the Computation of Hamiltonian Matrix Elements between Non-orthogonal Slater Determinants in Monte Carlo Shell Model”, Proc. Comp. Sci. **29**, 1711 (2014)
17. Y. Utsuno, N. Shimizu, T. Otsuka, S. Ebata, and M. Honma: “Photonuclear reactions of calcium isotopes calculated with the nuclear shell model”, Progress in Nuclear Energy, accepted.
18. T. Abe, P. Maris, T. Otsuka, N. Shimizu, Y. Utsuno, and J.P. Vary: “Monte Carlo Shell Model for ab initio nuclear structure”, EPJ Web Conf. **66**, 02001 (2014)
19. Y. Tsunoda, T. Otsuka, N. Shimizu, M. Honma, and Y. Utsuno: “Study of nuclei around $Z = 28$ by large-scale shell model calculations”, EPJ Web Conf. **66**, 02105 (2014)
20. Y. Utsuno, T. Otsuka, N. Shimizu, M. Honma, T. Mizusaki, Y. Tsunoda, and T. Abe: “Recent shell-model results for exotic nuclei”, EPJ Web Conf. **66**, 02106 (2014)
21. T. Yoshida, N. Shimizu, T. Abe, and T. Otsuka: “Density profiles of light nuclei in Monte Carlo shell-model calculation”, EPJ Web Conf. **66**, 02113 (2014)
22. Y. Iwata: “Co-existence of states in quantum systems”, J. Phys. Conf. Ser. **569** (2014) 012029
23. Y. Iwata: “Present Status of Fission Research Based on TDDFT”, The proceedings of the 2014 symposium on nuclear data, to appear.
24. Y. Iwata, N. Shimizu, Y. Utsuno, M. Honma, T. Abe, and T. Otsuka: “Ingredients of nuclear matrix element for two-neutrino double-beta decay of ^{48}Ca ”, JPS Conf. Proc. Volume **6** (2015), to appear.
25. T. Yoshida, N. Shimizu, T. Abe, and T. Otsuka: “Appearance of α -cluster structure in Be isotopes based on Monte Carlo shell model”, Journal of Physics: Conference Series, **569**, 012063 (2014)

C. Theses

1. K. Kizamori: “Study of tetra-neutron system via the exothermic double-charge exchange reaction $^4\text{He}(^8\text{He}, ^8\text{Be})4n$ ” Doctor Thesis, the University of Tokyo, March 2015
2. K. Yukawa: “GEM と Micromegs 検出器におけるイオンバックフローの研究” Master Thesis, the University of Tokyo, March 2015

D. Other Publications

1. 大塚孝治: “テンソル力とエキゾチック核の構造進化”, 原子核研究, 59 巻, pp86-100, (2014).
2. 大塚孝治: “ ^{54}Ca で発見した新しい魔法数”, Isotope News, No.720, 4 月号, 2014 年.

Talks and Presentations

A. Conferences

1. S. Shimoura (invited): “Nuclear responses via inelastic scatterings of exotic nuclei”, Advances in Nuclear Structure at Extreme Conditions, Feb. 19–22, 2014, Bormio, Italy.
2. M. Takaki (Oral): “New type of spectroscopy via Heavy-Ion Double Charge eXchange reaction”, Advances in Nuclear Structure at Extreme Conditions, Feb. 19–22, 2014, Bormio, Italy.
3. S. Michimasa, Y. Yanagisawa, K. Inafuku, N. Aoi, Z. Elekes, Zs. Fülöp, Y. Ichikawa, N. Iwasa, K. Kurita, M. Kurokawa, T. Machida, T. Motobayashi, T. Nakamura, T. Nakabayashi, M. Notani, H.J. Ong, T. Onishi, H. Otsu, H. Sakurai, M. Shinohara, T. Sumikama, S. Takeuchi, K. Tanaka, Y. Togano, K. Yamada, M. Yamaguchi, and K. Yoneda (oral): “Proton inelastic scattering on Island-of-inversion nuclei” The 2nd Conference on “Advances in Radioactive Isotope Science”(ARIS2014), June 1–6, 2014, Tokyo, Japan.
4. K. Kisamori, S. Shimoura, M. Assie, H. Baba, T. Baba, D. Beumel, M. Dozono, T. Fujii, N. Fukuda, S. Go, F. Hammache, E. Ideguchi, N. Inabe, M. Itoh, D. Kameda, S. Kawase, T. Kawabata, M. Kobayashi, Y. Kondo, T. Kubo, Y. Kubota, M. Kurata-Nishimura, C. S. Lee, Y. Maeda, H. Matsubara, S. Michimasa, K. Miki, H. Miya, T. Nishi, S. Noji, S. Ota, S. Sakaguchi, H. Sakai, Y. Sasamoto, M. Sasano, H. Sato, Y. Shimizu, A. Stolz, H. Suzuki, M. Takaki, H. Takeda, S. Takeuchi, A. Tamii, L. Tang, H. Tokieda, M. Tsumura, T. Uesaka, K. Yako, Y. Yanagisawa and R. Yokoyama (poster): “Missing-mass Spectroscopy of the $4n$ System by Exothermic Double-charge Exchange Reaction ${}^4\text{He}({}^8\text{He}, {}^8\text{Be})4n$ ” The 2nd Conference on “Advances in Radioactive Isotope Science”(ARIS2014), June 1–6, 2014, Tokyo, Japan.
5. R. Yokoyama, E. Ideguchi, G. Simpson, Mn. Tanaka, S. Nishimura, P. Doornenbal, P.-A. Sderstrm, G. Lorusso, Z. Y. Xu, J. Wu, T. Sumikama, N. Aoi, H. Baba, F. Bello, F. Brown, R. Daido, Y. Fang, N. Fukuda, G. Gey, S. Go, N. Inabe, T. Isobe, D. Kameda, K. Kobayashi, M. Kobayashi, T. Komatsubara, T. Kubo, I. Kuti, Z. Li, M. Matsushita, S. Michimasa, C.-B. Moon, H. Nishibata, I. Nishizuka, A. Odahara, Z. Patel, S. Rice, E. Sahin, L. Sinclair, H. Suzuki, H. Takeda, J. Taprogge, Zs. Vajta, H. Watanabe, A. Yagi (oral): “Isomers in Pm isotopes on the neutron-rich frontier of largely deformed $Z \sim 60$ region”, at the 2nd Conference on Advances in Radioactive Isotope Science, Jun. 1-6, 2014, ITO International Research Center in the University of Tokyo, Japan.
6. K. Kisamori, S. Shimoura, S. Michimasa, H. Miya, M. Assie, H. Baba, T. Baba, D. Beumel, M. Dozono, T. Fujii, N. Fukuda, S. Go, F. Hammache, E. Ideguchi, N. Inabe, M. Itoh, D. Kameda, S. Kawase, T. Kawabata, M. Kobayashi, Y. Kondo, T. Kubo, Y. Kubota, M. Kurata-Nishimura, C. S. Lee, Y. Maeda, H. Matsubara, K. Miki, H. Miya, T. Nishi, S. Noji, S. Ota, S. Sakaguchi, H. Sakai, Y. Sasamoto, M. Sasano, H. Sato, Y. Shimizu, A. Stolz, H. Suzuki, M. Takaki, H. Takeda, S. Takeuchi, A. Tamii, L. Tang, H. Tokieda, M. Tsumura, T. Uesaka, K. Yako, Y. Yanagisawa and R. Yokoyama (oral): “Missin- mass spectroscopy of the $4n$ system by exothermic double-charge exchange reaction ${}^4\text{He}({}^8\text{He}, {}^8\text{Be})4n$ ” at the 8th International Workshop on “Direct Reactions with Exotic Beams - DREB2014”, June 30–July 4, 2014, Darmstadt, Germany
7. K. Kisamori, M. Sasano, T. Uesaka, Y. Kikuchi (oral): “Tetra-neutron study via four neutron decay of superheavy hydrogen ${}^7\text{H}$ ” SAMURAI international collaboration workshop 2014, September 8–9, 2014, Sendai, Japan.
8. S. Michimasa (oral): “Quadrupole Colletivity in Island-of-Inversion Nuclei “ The 3rd SUNFLOWER Workshop, September 15–16, 2014, Tokyo, Japan.
9. M. Matsushita (oral): “New Energy-Degrading Beamline for Low-Energy Reaction Measurements of RI beam” The 3rd SUNFLOWER Workshop, September 15–16, 2014, Tokyo, Japan.
10. S. Shimoura (invited): “Charge exchange reactions of RI-beams using SHARAQ spectrometer”, NUBA Conference Series-1: Nuclear Physics and Astrophysics in Antalya, September 15–21, 2014, Adrasan, Turkey.
11. K. Kisamori, S. Shimoura, M. Assie, H. Baba, T. Baba, D. Beumel, M. Dozono, T. Fujii, N. Fukuda, S. Go, F. Hammache, E. Ideguchi, N. Inabe, M. Itoh, D. Kameda, S. Kawase, T. Kawabata, M. Kobayashi, Y. Kondo, T. Kubo, Y. Kubota, M. Kurata-Nishimura, C. S. Lee, Y. Maeda, H. Matsubara, S. Michimasa, K. Miki, H. Miya, T. Nishi, S. Noji, S. Ota, S. Sakaguchi, H. Sakai, Y. Sasamoto, M. Sasano, H. Sato, Y. Shimizu, A. Stolz, H. Suzuki, M. Takaki, H. Takeda, S. Takeuchi, A. Tamii, L. Tang, H. Tokieda, M. Tsumura, T. Uesaka, K. Yako, Y. Yanagisawa and R. Yokoyama (poster): “Study of tetra-neutron system by the exothermic double-charge exchange reaction ${}^4\text{He}({}^8\text{He}, {}^8\text{Be})4n$ ”

12. M. Dozono (Oral) : “The ($^{16}\text{O},4^{16}\text{F}$) reaction as a novel probe for studying the spin-dipole excitations in nuclei”, Neutrino Nuclear Reponses for Neutrino Studies in Nuclei (NNR14), Nov. 5-6, 2014, RCNP, Osaka University, Japan.
S. Shimoura (invited): “Nucleon transfer reactions at intermediate energy to exotic nuclei using inverse kinematics”, ECT* Workshop on ‘From nuclear structure to particle-transfer reactions and back II’, November 10–14, 2014, Trento, Italy.
13. S. Michimasa (invited): “In-beam gamma spectroscopy using direct reactions for probing shell evolution”, Progress in nuclear shell-model calculations in CNS-RIKEN collaboration, Nov. 26–28, 2014, Wako, Saitama, Japan.
14. K. Kisamori, S. Shimoura, M. Assie, H. Baba, T. Baba, D. Beaumel, M. Dozono, T. Fujii, N. Fukuda, S. Go, F. Hammache, E. Ideguchi, N. Inabe, M. Itoh, D. Kameda, S. Kawase, T. Kawabata, M. Kobayashi, Y. Kondo, T. Kubo, Y. Kubota, M. Kurata-Nishimura, C. S. Lee, Y. Maeda, H. Matsubara, S. Michimasa, K. Miki, H. Miya, T. Nishi, S. Noji, S. Ota, S. Sakaguchi, H. Sakai, Y. Sasamoto, M. Sasano, H. Sato, Y. Shimizu, A. Stolz, H. Suzuki, M. Takaki, H. Takeda, S. Takeuchi, A. Tamii, L. Tang, H. Tokieda, M. Tsumura, T. Uesaka, K. Yako, Y. Yanagisawa and R. Yokoyama (oral): “Study of tetra-neutron system via the exothermic double-charge exchange reaction $4\text{He}(8\text{He}, 8\text{Be})4\text{n}$ ” International Workshop on “Critical Stability in Few-Body System”, January 26–30, 2015, Wako, Saitama, Japan.
15. T. Gunji for the ALICE Collaboration (Oral): “Future upgrade and physics perspectives of the ALICE TPC”, XXIV International Conference on Ultrarelativistic Nucleus-Nucleus Collisions (QM2014), May 19 - 24, 2014, Darmstat, Germany
16. T. Gunji for the ALICE Collaboration (Invited): “Dark Photon searches in ALICE for the ALICE Collaboration”, International workshop on Dark Interactions: Perspectives from Theory and Experiment, June 11-13, 2014, Brookhaven National Laboratory
17. T. Gunji (Oral): “LHC-ALICE 実験用 MPGD を用いた TPC 検出器開発の現状”, MicroPattern Gas Detector 研究会, 東北大学, 12/19-20, 2014
18. K. Yukawa (oral): “GEM と MICROMEAS におけるイオンバックフローの研究”, MicroPattern Gas Detector 研究会, 東北大学, 12/19-20, 2014
19. T. Gunji (Poster): “Future Upgrade and Physics Perspectives of the LHC-ALICE Experiment”, Hadron Physics Symposium, April 17-19, 2014, Nagoya University, Japan
20. T. Gunji (Oral): “Dielectron Measurements, TPC upgrade, and activities of CNS”, France-Japan workshop on physics analysis in the ALICE experiment, Mar. 14–17, 2015, VVF Villages, Sainte-Maxime, France
21. T. Gunji (Oral): “高エネルギー重イオン衝突における重クォークとクォークoniumの物理”, チュートリアル研究会「重イオン衝突の物理」, March 25–27, 2-15, Wako, Japan
22. Y. Watanabe (Oral): “Measurements of di-electron production in Au+Au collisions at RHIC-PHENIX”, The 5th Asian Triangle Heavy Ion Conference (ATHIC2014), August 5-8, 2014, Osaka, Japan
23. Y. Watanabe: “HF measurements in Run1”, France-Japan workshop on physics analysis in the ALICE experiment, Mar. 14–17, 2015, VVF Villages, Sainte-Maxime, France
24. Y. Watanabe (Poster): “Dielectron measurement in PHENIX and charm baryon measurement in ALICE ”, チュートリアル研究会「重イオン衝突の物理」, March 25–27, 2-15, Wako, Japan
S. Hayashi on behalf of the ALICE Collaboration (Poster): “ Study of dielectron production in p-Pb collisions at $\sqrt{s_{NN}} = 5.02$ TeV using Transition Radiation Detector triggers with the ALICE detector ”, Quark Matter 2014, May 19-24, 2014 Darmstadt, German
25. S. Hayashi on behalf of the ALICE Collaboration (poster), “Dielectron measurement in p-Pb collisions at $\sqrt{s_{NN}} = 5.02$ TeV”, チュートリアル研究会「重イオン衝突の物理」, March 25-27, Wako, Japan
26. S. Hayshi (invited): “ Review of Quark Matter 2014(Heavy Flavor) ”, Heavy Ion Pub and Heavy Ion Cafe 合同研究会, June 6, Nagoya, Japan
27. S. Hayashi on behalf of the ALICE Collaboration (oral): “ Dielectron measurement in p-Pb collisions at $\sqrt{s_{NN}} = 5.02$ TeV with the ALICE detector ”, The 5th Asian Triangle Heavy Ion Conference (ATHIC2014), August 5-8, 2014, Osaka, Japan
28. S. Hayashi on behalf of the ALICE Collaboration (oral): “Dielectrons production from heavy quark decays in p-Pb collisions at $\sqrt{s_{NN}} = 5.02$ TeV”, September 22-26, High Energy Strong Interactions: A School for Young Asian Scientists, Wuhan, China

29. S. Hayashi, “LHC での p-Pb 衝突における粒子相関”, Heavy Ion Pub, December 5, Osaka, Japan
30. Yuko Sekiguchi (oral): “Two particle correlations in pPb collisions”, at France-Japan workshop on physics analysis in the ALICE experiment, Mar. 14-17, 2015, VVF Villages, Sainte-Maxime, France
31. Yuko Sekiguchi (poster): “h-V0 correlations in pPb collisions at $\sqrt{s_{NN}} = 5.02$ TeV with the ALICE detector”, チュートリアル研究会「重イオン衝突の物理」, March 25-27, Wako, Japan
32. K. Terasaki, H. Hamagaki, T. Gunji (Oral): “Ion backflow measurements with 2GEMs + MICROMEAS for the TPC upgrade”, at France-Japan workshop on physics analysis in the ALICE experiment, Mar. 14-17, 2015, VVF Villages, Sainte-Maxime, France
33. S. Ota, T. Tokieda, C.S. Lee, Y.N. Watanabe, for CAT collaboration (Invited) “CNS Active Target (CAT) for Missing Mass Spectroscopy with Intense Beams”, 27th International Conference of the International Nuclear Target Development Society (INTDS-2014), Aug. 31 - Sep. 5, 2014, Tokyo, Japan
34. Shinsuke OTA, H. Tokieda, C.S. Lee, R. Kojima, Y.N. Watanabe, A. Corsi, M. Dozono, J. Gibelin, T. Hashimoto, T. Kawabata, S. Kawase, S. Kubono, Y. Kubota, Y. Maeda, H. Matsubara, Y. Matsuda, S. Michimasa, T. Nakao, T. Nishi, A. Obertelli, H. Otsu, C. Santamaria, M. Sasano, M. Takaki, Y. Tanaka, T. Leung, T. Uesaka, K. Yako, H. Yamaguchi, J. Zenihiro, and E. Takada (Poster), “Development of CNS Active Target for Deuteron Induced Reactions with High Intensity Exotic Beam”, The 2nd conference on “Advances in Radioactive Isotope Science” (ARIS2014), Jun. 1-6, 2014, Tokyo, Japan
35. CheongSoo LEE, Shinsuke OTA, Hiroshi TOKIEDA, Reiko KOJIMA, Yuni, WATANABE, Raphael SAISEAU, and Tomohiro UESAKA, “Property of THGEM in Low-Pressure Deuterium for a Low-Pressure Gaseous Active Target”, The 2nd conference on “Advances in Radioactive Isotope Science” (ARIS2014), Jun. 1-6, 2014, Tokyo, Japan
36. H. Yamaguchi (invited): “Studying alpha-cluster structure using low-energy RI beam”, 3rd International Workshop on State of the Art in Nuclear Cluster Physics (SOTANCP3) May 26-30, 2014, KGU Kannai Media Center, Kanto Gakuin University, Yokohama, Japan.
37. H. Yamaguchi (oral): “Proton resonance elastic scattering of ^7Be at CRIB”, RIBF-ULIC mini workshop: ‘The way to evaluate the inelastic channel in the proton resonance elastic scattering’, May 31, 2014, RIKEN Nishina Center, Wako, Saitama, Japan.
38. H. Yamaguchi (invited): “Studies on Nuclear Astrophysics and Exotic Structure at the Low-Energy RI beam Facility CRIB”, The 2nd Conference on Advances in Radioactive Isotope Science (ARIS2014) Ito International Center, Jun 2-6, 2014, Tokyo, Japan.
39. D. Kahl (poster): “ $^{30}\text{S}+\alpha$ Resonant Elastic Scattering with an Active Target”, The 2nd Conference on Advances in Radioactive Isotope Science (ARIS2014) Ito International Center, Jun 2-6, 2014, Tokyo, Japan.
40. H. Yamaguchi (oral): “Studies on Nuclear Astrophysics and Exotic Structure at the Low-Energy RI Beam Facility CRIB”, Sicily-East Asia Workshop for Low-energy Nuclear Physics, Catania University, Ortygia island, Siracusa, July 28–31, 2014,
41. D. Kahl (oral): “ $^{30}\text{S}+\alpha$ Resonant Elastic Scattering with an Active Target”, Sicily-East Asia Workshop for Low-energy Nuclear Physics, Catania University, Ortygia island, Siracusa, July 28–31, 2014,
42. H. Yamaguchi (oral): “Search for cluster states by measurements of alpha resonant scattering”, The 10th RIBF Discussion ‘Cluster states probed by reaction experiments’, Sep. 25, 2014, Yukawa institute for theoretical physics, Kyoto Univ.
43. H. Yamaguchi (invited): “Nuclear astrophysics, reaction, and structure studies at the low-energy RI beam separator CRIB”, The International Symposium on Physics of Unstable Nuclei 2014 (ISPUN14) Hotel New World Saigon, Ho Chi Minh City, Vietnam, November 3–8, 2014.
44. T. Otsuka (invited): “Dual Fermi liquid, critical point and ^{68}Ni ”, Workshop on “The structure of ^{68}Ni : current knowledge and open questions”, Leuven, Belgium, April 23-24, 2014.
45. T. Otsuka (invited): “Shape evolution, shape coexistence and shell evolution in exotic nuclei”, 11th INT. SPRING SEMINAR ON NUCLEAR PHYSICS, Ischia, Italy, May 12-16, 2014.
46. T. Otsuka (invited): “Shell model and nuclear shapes”, French-US Theory Institute for Physics with Exotic Nuclei (FUSTIPEN) Topical Meeting, GANIL, France, July 19-20, 2014.

47. T. Otsuka (invited): “Shapes of exotic nuclei and quantum liquid picture”, Fourth Workshop of the European Gamma and Ancillary Detectors Network, GSI, Germany, July 23-25, 2014.
48. T. Otsuka (invited): “Shapes of exotic nuclei and shell evolution”, Fifteenth International Symposium on Capture Gamma-Ray Spectroscopy and Related Topics (CGS15), Dresden, Germany, August 25-29, 2014.
49. T. Otsuka (invited): “Dual quantum liquids and shell evolutions in exotic nuclei”, INTERNATIONAL SCHOOL OF NUCLEAR PHYSICS 36th Course, Erice, Italy, September 16-24, 2014.
50. T. Otsuka (invited): “Dual quantum liquids and shell evolution in exotic nuclei”, International Symposium on Physics of Unstable Nuclei, Ho Chiming, Vietnam, November 2-8, 2014.
51. T. Otsuka (invited): “Two-neutrino Double Beta Decay from ^{48}Ca calculated with sd and pf shells”, EMMI Rapid Reaction Task Force on matrix elements of neutrinoless double beta decay, Darmstadt, Germany, November 10-21, 2014.
52. N. Shimizu (invited), T. Abe, M. Honma, T. Otsuka, T. Togashi, Y. Tsunoda, Y. Utsuno, and T. Yoshida: “Exotic nuclear structure by nuclear shell model calculations and Monte Carlo shell model”, CMSI International Workshop on “New Frontier of Numerical Methods for Many-Body Correlations — Methodologies and Algorithms for Fermion Many-Body Problems”, Univ. of Tokyo, Tokyo, Japan, Feb. 18-21, 2015.
53. N. Shimizu (invited), T. Abe, M. Honma, T. Mizusaki, T. Otsuka, T. Togashi, Y. Tsunoda, Y. Utsuno, and T. Yoshida: “Frontier of nuclear shell-model calculations and high performance computing”, Advances in Radioactive Isotope Science (ARIS2014), Univ. of Tokyo, Tokyo, Japan, Jun. 05, 2014.
54. Y. Utsuno (invited), T. Otsuka, Y. Tsunoda, N. Shimizu, M. Honma, T. Togashi, T. Mizusaki: “Recent Advances in shell evolution with shell-model calculations”, 2nd International Conference “Advances in Radioactive Isotope Science”, Tokyo, Japan, Jun. 2-6, 2014.
55. Y. Utsuno (invited), T. Otsuka, N. Shimizu, Y. Tsunoda, M. Honma, T. Abe, T. Mizusaki, T. Togashi and B.A. Brown: “Large-scale shell-model studies for exotic nuclei: probing shell evolution”, International Conference “Nuclear Theory in the Supercomputing Era 2014 (NTSE-2014)”, Khabarovsk, Russia, Jun. 23-27, 2014.
56. Y. Utsuno (invited) : “Exploring shell evolution with alphalet collaborations”, Workshop “Progress in nuclear shell-model calculations in CNS-RIKEN collaboration”, Wako, Japan, Nov. 26-28, 2014.
57. Y. Iwata (invited) : “Present status of fission research based on TDDFT”, Symposium on Nuclear Data, Hokkaido University, Japan, Nov 2014.
58. Y. Iwata (invited) : “Nuclear matrix element of ^{48}Ca ”, NNR14, RCNP, Osaka University, Japan, Nov 2014.
59. Y. Iwata: “Large-scale shell model calculation project for double-beta decay”, Workshop on “Progress in nuclear shell-model calculations in CNS-RIKEN collaboration”, RIKEN, Japan, Nov. 2014.
60. Y. Iwata (Poster), N. Shimizu, Y. Utsuno, M. Honma, T. Abe, and T. Otsuka: “Large-scale shell model calculations for double beta decay of ^{48}Ca ”, ARIS 2014, Tokyo, Japan, Jun. 2014.
61. Y. Iwata: “Shape transition induced by rotation”, 3rd International Workshop on “ State of the Art in Nuclear Cluster Physics ” (SOTANCP3), Yokohama, Japan, May 2014.
62. N. Tsunoda (invited) : “Many-body perturbation theory in nuclei and its application to the neutron-rich nuclei”, CMSI International Workshop on “New Frontier of Numerical Methods for Many-Body Correlations — Methodologies and Algorithms for Fermion Many-Body Problems”, Univ. of Tokyo, Tokyo, Japan, Feb. 18-21, 2015.
63. N. Tsunoda (invited) : “Microscopic description of neutron-rich nuclei from the nuclear force”, Progress in nuclear shell-model calculation in CNS-RIKEN collaboration, Nov. 26-28, 2014, RIKEN, Wako.
64. T. Yoshida (Poster), N. Shimizu, T. Abe, T. Otsuka: “Cluster Structure of Be Isotopes based on Monte Carlo Shell Model”, The 2nd Conference on “Advances in Radioactive Isotope Science” (ARIS2014), Tokyo, Japan. Jun. 1-6, 2014.
65. T. Yoshida, N. Shimizu, T. Abe, and T. Otsuka: “Cluster structure of Be isotopes based on Monte Carlo shell model”, ICNT workshop “Physics of exotic nuclei: Theoretical advances and challenges”, RIKEN Wako Campus, Japan, Jun. 9-13, 2014.
66. T. Togashi, N. Shimizu, Y. Utsuno, T. Abe and T. Otsuka: “GPGPU Application to the Computation of Hamiltonian Matrix Elements between Non-orthogonal Slater Determinants in the Monte Carlo Shell Model”, , ICCS2014, Pullman Cairns International, Cairns, Australia, Jun. 11, 2014.

67. T. Togashi (Poster), N. Shimizu, Y. Utsuno, T. Otsuka and M. Honma: “Shell-model calculation of high-spin states in neutron-rich Cr and Fe isotopes”, Advances in Radioactive Isotope Science (ARIS2014), Univ. of Tokyo, Tokyo, Japan, Jun. 05, 2014.
68. T. Yoshida, N. Shimizu, T. Abe, T. Otsuka: “Appearance of alpha-cluster structure in Be isotopes based on Monte Carlo shell model”, 3rd International Workshop on “ State of the Art in Nuclear Cluster Physics ” (SOTANCP3), KGU Kannai Media Center, Kanto Gakuin University, Yokohama, Japan, May 26-30, 2014.
69. T. Yoshida (Poster), N. Shimizu, T. Abe, T. Otsuka: “Study of even-mass Be nuclei based on Monte Carlo shell model”, CMSI International Workshop on “New Frontier of Numerical Methods for Many-Body Correlations — Methodologies and Algorithms for Fermion Many-Body Problems”, Univ. of Tokyo, Tokyo, Japan, Feb. 18-21, 2015.
70. N. Shimizu: “Overview of Alphleet collaboration project and Monte Carlo shell model”, International workshop on “Progress in nuclear shell-model calculations in CNS-RIKEN collaboration”, RIKEN Nishina hall, Wako, Japan, November 26, 2014.
71. N. Shimizu: “Introduction to shell-model code, KSHELL”, International workshop on “Progress in nuclear shell-model calculations in CNS-RIKEN collaboration”, RIKEN Nishina hall, Wako, Japan, November 27, 2014.
72. Y. Iwata (Poster): “Neutrino potential for the large-scale shell model calculations of double-beta decay”, CMSI International Workshop on “New Frontier of Numerical Methods for Many-Body Correlations — Methodologies and Algorithms for Fermion Many-Body Problems”, Univ. of Tokyo, Tokyo, Japan, Feb. 18-21, 2015.
73. T. Togashi, N. Shimizu, T. Otsuka, and Y. Utsuno: “Electric dipole transitions in medium-heavy nuclei described with Monte Carlo shell model”, CMSI International Workshop on “New Frontier of Numerical Methods for Many-Body Correlations — Methodologies and Algorithms for Fermion Many-Body Problems”, Univ. of Tokyo, Tokyo, Japan, Feb. 18-21, 2015.

B. JPS Meetings

1. T. Gunji (invited): “Experimental upgrades at RHIC and LHC”, JPS-DNP at Hawaii2014. Workshop on “Quark Gluon Plasma and Future Directions in Heavy Ion Physics at RHIC and LHC”, Hawaii 2014, half-day workshop, Oct. 7, 2014
2. Y. Watanabe (Oral): “ Measurements of di-electron production in Au+Au collisions at $\sqrt{s_{NN}} = 200$ GeV by RHIC-PHENIX using Hadron Blind Detector ”, 4th Joint Meeting of the APS Division of Nuclear Physics and the Physical Society of Japan, Oct. 7 – 11, 2014, Hawaii, USA
3. S. Hayashi on behalf of the ALICE Collaboration (oral): “Dielectrons from Charm and Bottom meson decays in p-Pb collisions at $\sqrt{s_{NN}} = 5.02$ TeV measured with the ALICE detector”, Fourth Joint Meeting of the Nuclear Physics Divisions of the American Physical Society and The Physical Society of Japan, October 7-11, Hawaii, USA
4. Yuko Sekiguchi for ALICE collaboration (oral): “Long range correlation in p-Pb collisions at $\sqrt{s_{NN}} = 5.02$ TeV with the ALICE detector”, at 4th Joint Meeting of the APS Division of Nuclear Physics and the Physical Society of Japan, Oct. 7-11, 2014, Waikoloa, Hawaii, USA
5. K. Terasaki, H. Hamagaki, T. Gunji, Y. Yamaguchi (Oral): “Performance Evaluation of the COBRA GEM for the Application of the TPC”, at 4th Joint Meeting of the APS Division of Nuclear Physics and the Physical Society of Japan, Oct. 7-11, 2014, Waikoloa, Hawaii, USA
6. S. Shimoura (invited): “New energy degraded beam project at RIBF OEDO project “ Fourth Joint Meeting of the Nuclear Physics Divisions of the American Physical Society and The Physical Society of Japan, October 7–11, 2014, Waikoloa, Hawaii, USA
7. S. Michimasa (invited): “RI-induced reaction studies by new energy-degrading beam line, OEDO” Fourth Joint Meeting of the Nuclear Physics Divisions of the American Physical Society and The Physical Society of Japan, October 7–11, 2014, Waikoloa, Hawaii, USA
8. M. Dozono (Oral) : “The parity-transfer reaction ($^{16}\text{O}, ^{16}\text{F}$) for studies of pionic 0^- mode”, 4th Joint Meeting of the APS Division of Nuclear Physics and the Physical Society of Japan, Oct. 7-11, 2014, Hilton Waikoloa village, Hawaii, USA.

9. K. Kisamori, S. Shimoura, M. Assie, H. Baba, T. Baba, D. Beaumel, M. Dozono, T. Fujii, N. Fukuda, S. Go, F. Hammache, E. Ideguchi, N. Inabe, M. Itoh, D. Kameda, S. Kawase, T. Kawabata, M. Kobayashi, Y. Kondo, T. Kubo, Y. Kubota, M. Kurata-Nishimura, C. S. Lee, Y. Maeda, H. Matsubara, S. Michimasa, K. Miki, H. Miya, T. Nishi, S. Noji, S. Ota, S. Sakaguchi, H. Sakai, Y. Sasamoto, M. Sasano, H. Sato, Y. Shimizu, A. Stolz, H. Suzuki, M. Takaki, H. Takeda, S. Takeuchi, A. Tamii, L. Tang, H. Tokieda, M. Tsumura, T. Uesaka, K. Yako, Y. Yanagisawa and R. Yokoyama (oral): “Tetra-neutron system studied by exothermic double-charge exchange reaction $^4\text{He}(^8\text{He}, ^8\text{Be})4n$ ” The 4th Joint Meeting of the Nuclear Physics Divisions of the APS and JPS, October 7–11, 2014, Hawaii, USA.
10. M. Kobayashi, K. Yako, S. Shimoura, M. Dozono, S. Kawase, K. Kisamori, Y. Kubota, C.S. Lee, S. Michimasa, H. Miya, S. Ota, H. Sakai, M. Sasano, M. Takaki (Oral): “Spin-isospin response of neutron-rich nuclei ^8He via (p, n) reaction in inverse kinematics”, Fourth Joint Meeting of the Nuclear Physics Divisions of the American Physical Society and The Physical Society of Japan (Hawaii2014), Oct. 7–11, 2014, Hilton Waikoloa Village, Hawaii, US.
11. H. Miya, S. Shimoura, K. Kisamori, H. Baba, T. Baba, M. Dozono, N. Fukuda, T. Fujii, S. Go, E. Ideguchi, N. Inabe, M. Ito, D. Kameda, T. Kawabata, S. Kawase, Y. Kikuchi, T. Kubo, Y. Kubota, M. Kobayashi, Y. Kondo, C. S. Lee, Y. Maeda, H. Matsubara, K. Miki, S. Michimasa, T. Nishi, M. Nishimura, S. Ota, S. Sakaguchi, H. Sakai, M. Sasano, H. Sato, Y. Shimizu, H. Suzuki, M. Takaki, H. Takeda, S. Takeuchi, A. Tamii, H. Tokieda, M. Tsumura, T. Uesaka, Y. Yanagisawa, K. Yako, R. Yokoyama, K. Yoshida, M. Assie, D. Beaumel, H. Fariouz and A. Stolz (oral): “Missing mass spectroscopy of ^4H via exothermic charge exchange reaction $(^8\text{He}, ^8\text{Li}\gamma)$ ”, The 4th Joint Meeting of the Nuclear Physics Divisions of the APS and JPS, October 7–11, 2014, Hawaii, USA.
12. C.S. Lee, S. Ota, Y. Aramaki, R. Saiseau, H. Tokieda, Y. Watanabe (Oral): “Development of a dual-gain multiplication in CNS Active Target for high-intensity heavy-ion beam injection”, The 4th Joint Meeting of the Nuclear Physics Divisions of the APS and JPS, October 7–11, 2014, Hawaii, USA.
13. S. Ota (Oral): “CNS Active Target for deuteron induced reactions with high intensity beams”, The 4th Joint Meeting of the Nuclear Physics Divisions of the APS and JPS, October 7–11, 2014, Hawaii, USA.
14. N. Imai, M. Mukai, J. Cederkall, H. Aghai, P. Golubev, H. Johansson, D. Kahl, J. Kurcewics, T. Teranishi, Y. Watanabe (Oral): “Small spectroscopic factors of low-lying positive parity states in ^{31}Mg ”, The 4th Joint Meeting of the Nuclear Physics Divisions of the APS and JPS, October 7–11, 2014, Hawaii, USA.
15. T. Otsuka (invited): “What can we learn from large-scale MCSM calculations?”, Fourth Joint Meeting of the Nuclear Physics Divisions of the American Physical Society and The Physical Society of Japan, Waikoloa, USA, Oct. (2014).
16. Y. Utsuno (invited): “Shells and shapes in exotic nuclei”, Fourth Joint Meeting of the Nuclear Physics Divisions of the American Physical Society and The Physical Society of Japan, Waikoloa, USA, Oct. (2014).
17. N. Shimizu, Y. Utsuno, T. Togashi, T. Otsuka, and M. Honma: “Shell-model description of E1 excitation”, Fourth Joint Meeting of the Nuclear Physics Divisions of the American Physical Society and The Physical Society of Japan, Waikoloa, USA, Oct. (2014).
18. T. Iwata, N. Shimizu, Y. Utsuno, M. Honma, T. Abe, and T. Otsuka: “Large-scale shell model calculations for two-neutrino double-beta decay of ^{48}Ca ”, Fourth Joint Meeting of the Nuclear Physics Divisions of the American Physical Society and The Physical Society of Japan, Waikoloa, USA, Oct. (2014).
19. T. Yoshida, N. Shimizu, T. Abe, and T. Otsuka: “Structure of Be isotopes based on Monte Carlo shell model”, Fourth Joint Meeting of the Nuclear Physics Divisions of the American Physical Society and The Physical Society of Japan, Waikoloa, USA, Oct. (2014).
20. N. Tsunoda: “Neutron-rich nuclei from the nuclear force a new Many-body perturbation theory with 3N force and its first application”, Fourth Joint Meeting of the Nuclear Physics Divisions of the American Physical Society and The Physical Society of Japan, Waikoloa, USA, Oct. (2014).
21. T. Togashi, N. Shimizu, Y. Utsuno, T. Otsuka and M. Honma: “Large-scale shell-model calculation of unnatural parity high-spin states in neutron-rich Cr and Fe isotopes”, Fourth Joint Meeting of the Nuclear Physics Divisions of the American Physical Society and The Physical Society of Japan, Waikoloa, USA, Oct. (2014).
22. 宇都野穰: “ポスト京における大規模核構造計算”, HPCI 戦略プログラム分野 5 全体シンポジウム・素粒子・原子核・宇宙「京からポスト京に向けて」(紀尾井フォーラム) 3 月 (2015).
23. 清水則孝: “原子核殻模型計算による E1 励起の記述”, HPCI 戦略プログラム分野 5 全体シンポジウム・素粒子・原子核・宇宙「京からポスト京に向けて」(紀尾井フォーラム) 3 月 (2015).
24. 富樫智章, 清水則孝, 吉田亨, 宇都野穰, 阿部喬, 大塚孝治: “モンテカルロ殻模型計算のマルチ GPGPU への適用と開発状況”, 第 6 回「学際計算科学による新たな知の発見・統合・創出」シンポジウム.

25. 富樫智章, 清水則孝, 大塚孝治, 宇都野穰: “ポスト京における核変換の基礎研究” HPCI 戦略プログラム分野 5 全体シンポジウム・素粒子・原子核・宇宙「京からポスト京に向けて」(紀尾井フォーラム) 3 月 (2015).
26. 角田直文: “核力から出発した有効相互作用の構築とその応用” HPCI 戦略プログラム分野 5 全体シンポジウム・素粒子・原子核・宇宙「京からポスト京に向けて」(紀尾井フォーラム) 3 月 (2015).
27. R. Yokoyama, E. Ideguchi, G. Simpson, Mn. Tanaka, S. Nishimura, P. Doornenbal, P.-A. Sderstrm, G. Lorusso, Z. Y. Xu, J. Wu, T. Sumikama, N. Aoi, H. Baba, F. Bello, F. Brown, R. Daido, Y. Fang, N. Fukuda, G. Gey, S. Go, N. Inabe, T. Isobe, D. Kameda, K. Kobayashi, M. Kobayashi, T. Komatsubara, T. Kubo, I. Kuti, Z. Li, M. Matsushita, S. Michimasa, C.-B. Moon, H. Nishibata, I. Nishizuka, A. Odahara, Z. Patel, S. Rice, E. Sahin, L. Sinclair, H. Suzuki, H. Takeda, J. Taprogge, Zs. Vajta, H. Watanabe, A. Yagi (oral): “Investigation of the octupole correlation of neutron-rich $Z \sim 56$ isotopes by β - γ spectroscopy”, at the JPS Spring meeting, Mar. 21-24, 2015, Waseda University, Japan.
28. K. Kisamori, S. Shimoura, M. Assie, H. Baba, T. Baba, D. Beaumel, M. Dozono, T. Fujii, N. Fukuda, S. Go, F. Hammache, E. Ideguchi, N. Inabe, M. Itoh, D. Kameda, S. Kawase, T. Kawabata, M. Kobayashi, Y. Kondo, T. Kubo, Y. Kubota, M. Kurata-Nishimura, C. S. Lee, Y. Maeda, H. Matsubara, S. Michimasa, K. Miki, H. Miya, T. Nishi, S. Noji, S. Ota, S. Sakaguchi, H. Sakai, Y. Sasamoto, M. Sasano, H. Sato, Y. Shimizu, A. Stolz, H. Suzuki, M. Takaki, H. Takeda, S. Takeuchi, A. Tamii, L. Tang, H. Tokieda, M. Tsumura, T. Uesaka, K. Yako, Y. Yanagisawa and R. Yokoyama (oral): “Study of tetra-neutron system via exothermic double-charge exchange reaction ${}^4\text{He}({}^8\text{He}, {}^8\text{Be})4n$ ” at the JPS Spring meeting, Mar. 21-24, 2015, Waseda University, Japan.
29. 岩田順敬, 清水則孝, 宇都野穰, 本間道雄, 阿部喬, 大塚孝治: “ ${}^{48}\text{Ca}$ の二重ベータ崩壊の殻模型計算による記述 II”, 日本物理学会 第 70 回年次大会 (早稲田大学) 3 月 (2015).
30. 富樫智章, 清水則孝, 大塚孝治, 宇都野穰: “モンテカルロ殻模型計算によるストロンチウム 90 の E1 励起状態の記述” 日本物理学会 第 70 回年次大会 (早稲田大学) 3 月 (2015).
31. 吉田亨, 清水則孝, 阿部喬, 大塚孝治: “ ${}^{12}\text{Be}$ における殻構造のモンテカルロ殻模型による研究” 日本物理学会 第 70 回年次大会 (早稲田大学) 3 月 (2015).

C. Lectures

D. Seminars

1. Y. Iwata: “Fission Dynamics of $A=240$ Nuclei Based on Time-Dependent Density Functional Calculations”, Colloquium at Tokyo Institute of Technology, Sep. (2014).
2. 下浦 享: 「エキゾチック原子核の世界」, June 9–11, July 8–9, 2014, Konan University, Kobe, Japan.

Personnel

Director

OTSUKA, Takaharu *Professor, Department of Physics,
Graduate School of Science*

Scientific Staff

SHIMOURA, Susumu *Professor*
HAMAGAKI, Hideki *Associate Professor*
YAKO, Kentaro *Associate Professor*
IMAI, Nobuaki *Associate Professor*
SHIMIZU, Noritaka *Project Associate Professor*
YAMAGUCHI, Hidetoshi *Lecturer*
MICHIMASA, Shin'ichiro *Assistant Professor*
GUNJI, Taku *Assistant Professor*
OTA, Shinsuke *Assistant Professor*

Guest Professors

UTSUNOMIYA, Hiroaki *Konan University*
UTSUNO, Yutaka *JAEA*

Technical Staff

OHSIRO, Yukimitsu *KOTAKA, Yasuteru*

Technical Assistants

KUREI, Hiroshi
YOSHIMURA, Kazuyuki
YOSHINO, Akira

YAMAHA, Shoichi
KATAYANAGI, Mamoru
TANAKA Masahiro

Post Doctoral Associates

YOSHIDA, Toru
IWATA, Yoritaka
TSUNOAD, Naofumi
MATSUSHITA, Masafumi
WATANABE, Yosuke
DOZONO, Masanori

NAKAO, Taro
TOGASHI, Tomoaki
STEPHENBECK, David
ARAMAKI, Yoki
HAYAKAWA, Seiya
YAMAGUCHI, Yorito

Graduate Students

KAHL, David
TOKIEDA, Hiroshi
KAWASE, Shoichiro
KISAMORI, KenIchi
SEKIGUCHI, Yuko
KUBOTA, Yuki
TERASAKI, Kohei
YUKAWA, Kentaro
SAKAGUCHI, Yuji

MIYA, Hiroyuki
TSUJI, Tomoya
HAYASHI, ShinIchi
TAKAKI, Motonobu
YOKOYAMA, Rin
LEE, CheongSoo
KOBAYASHI, Motoki
KIYOKAWA, Yu

Administration Staff

YOSHIMURA, Hiroshi
YAMAMOTO, Ikuko
ENDO, Takako

KISHI, Yukino
ITAGAKI, Toshiko
SOMA, Yuko

Committees

Steering Committee

AIHARA, Hiroaki	<i>Department of Physics, Graduate School of Science, UT</i>
HOSHINO, Masahiro	<i>Department of Earth and Planetary Science, Graduate School of Science, UT</i>
MIYASHITA, Seiji	<i>Department of Physics, Graduate School of Science, UT</i>
OTSUKA, Takaharu	<i>Department of Physics, Graduate School of Science, UT</i>
SHIMOURA, Susumu	<i>Center for Nuclear Study, Graduate School of Science, UT</i>
HAMAGAKI, Hideki	<i>Center for Nuclear Study, Graduate School of Science, UT</i>
GONOKAMI, Makoto	<i>Department of Physics, Graduate School of Science, UT</i>
NAGAMIYA, Shoji	<i>J-PARC Center, KEK and JAEA</i>
KOBAYASHI, Tomio	<i>International Center for Elementary Particle Physics, UT</i>
TAKAHASHI, Hiroyuki	<i>Department of Nuclear Engineering and Management, Graduate School of Engineering, UT</i>

